Spectral Editing for Detection of Oncologically Relevant Metabolites with *In-Vivo* Magnetic Resonance Spectroscopy at 9.4 T

by

Brennen Jay Dobberthien

A thesis submitted in partial fulfillment of the requirements for the degree of

Doctor of Philosophy

in

Medical Physics

Department of Oncology
University of Alberta

© Brennen Jay Dobberthien, 2019

Abstract

Short echo time (TE) magnetic resonance spectroscopy (MRS) techniques with spectral fitting are commonly employed approaches for brain metabolite quantification at 9.4 T. However, there is a significant overlap of peaks in short-TE spectra, even at 9.4 T. To better resolve resonances, spectral editing by optimal-TE Point RESolved Spectroscopy (PRESS), a readily available *in-vivo* MRS sequence, was used to improve the detection of some oncologically relevant brain metabolites in rat brain at 9.4 T. The metabolites include glycine (Gly), glutamine (Gln), glutamate (Glu), and γ-aminobutyric acid (GABA). $^{13}C_4$-Glu was also measured with indirect ^{13}C detection, using optimized PRESS timings, during [U-$^{13}C_6$]-glucose infusions. For Gly, a PRESS (TE_1, TE_2) combination of (60 ms, 100 ms) was found numerically to minimize the *myo*-inositol signal in the Gly spectral region resulting in a well resolved Gly resonance. LCModel was employed to analyze *in-vivo* spectra. Average Gly concentration (over three rats) was found to be 1.35 mM with an average Cramér-Rao Lower Bound (CRLB) of 17.5 %, agreeing with values in the literature. To simultaneously quantify Gln, Glu and GABA, a (TE_1, TE_2) combination of (106 ms, 16 ms) minimized the NAA signal in the Gln spectral region, while retaining macromolecule-free Gln, Glu, and GABA peaks. The efficacy of the timings were verified on phantom solutions and on rat brain *in vivo*. Average Gln, Glu, and GABA concentrations were found over five rats to be 3.39 mM, 11.43 mM, and 2.20 mM, with average CRLBs of 15.4 %, 5.0 %, and 17.8 %, respectively, within error of literature values. In addition, we evaluated short-TE spectra obtained from phantoms of known Gln, Glu and GABA concentrations, and demonstrated that errors can result due to overlapping signals. Specifically, concentrations were estimated from phantoms of known varying glutamine (Gln) concentrations, with other metabolites present in fixed known physiological concentration ratios, and it was found that errors in estimation were >39 %. The

errors were reduced with the long-TE PRESS sequence. For the dynamic ^{13}C indirect measures, a (TE_1, TE_2) combination of (20 ms, 106 ms) was found to be suitable for minimizing NAA signal in the ≈ 2.51 ppm $^{13}C_4$-Glu proton spectral region, while retaining the ≈ 2.51 ppm $^{13}C_4$-Glu proton satellite peak. The efficacy of the technique was verified on phantom solutions and on rat brain *in vivo* during an infusion of [U-$^{13}C_6$]-glucose. LCModel was again employed for analysis of the *in-vivo* spectra to quantify the ≈ 2.51 ppm proton $^{13}C_4$-Glu signal to obtain Glu C4 fractional enrichment (FE) time courses during the infusions. Glutamate FE was found to be, on average, 0.59, for two rats at the end of infusion. The indirect ^{13}C detection with optimized PRESS provides an alternative to subtraction techniques and techniques that require additional ^{13}C capability.

In addition, rat kidney MRS was also investigated with short-TE PRESS at 9.4 T to non-invasively obtain *in-vivo* spectra of the kidney and quantify levels of Glx (Glu + Gln), *myo*-inositol, and taurine, relative to choline + betaine. The relative concentrations, found over four rats, were found to be, on average, 2.16, 1.40, and 2.17, for Glx, *myo*-inositol, and taurine, respectively. Previous MRS of rat kidney *in vivo* relied on surgical exposure.

Preface

A version of Chapter 3 of the thesis has been published in the journal *Biomedical Physics and Engineering Express*:

Dobberthien, B. J., Tessier, A. G., Fallone, B. G., & Yahya, A. (2016). Optimized PRESS sequence timings for measuring glycine at 9.4 T: demonstration *in vivo* in rat brain. Biomedical Physics & Engineering Express, 2(2), 027003.

A version of Chapter 4 of the thesis has been published in the journal *NMR in Biomedicine*:

Dobberthien, B. J., Tessier, A. G., & Yahya, A. (2018). Improved resolution of glutamate, glutamine and γ-aminobutyric acid with optimized point-resolved spectroscopy sequence timings for their simultaneous quantification at 9.4 T. NMR in Biomedicine, 31(1), e3851.

A version of Chapter 5 of the thesis has been submitted for publication to the journal *NMR in Biomedicine*:

Dobberthien, B. J., Tessier, A. G., Stanislaus, A. E., Sawyer, M. B, Fallone, B. G., & Yahya, A. PRESS timings for resolving $^{13}C_4$-glutamate ^{1}H signal at 9.4 T: demonstration in rat with uniformly-labelled-^{13}C-glucose.

A version of Chapter 6 of the thesis has been provisionally accepted for publication by the journal *Biomedical Physics and Engineering Express*:

Dobberthien, B. J., Volotovskyy, V., Tessier, A. G., & Yahya, A. Magnetic Resonance Spectroscopy of Rat Kidney *In Vivo* at 9.4 T.

For both published journal articles, I, Brennen J. Dobberthien, contributed to the project conceptualization, and was responsible for all experimental data acquisition, data analysis, and manuscript writing. Dr. B.G. Fallone contributed to manuscript review and editing for the chapter 3 article. Mr. A.G. Tessier contributed to experimental planning, data analysis procedures, as well as manuscript review for both articles. Dr. A. Yahya, the principal investigator, was involved with project formation, the experimental approach, and manuscript review and editing for both articles.

Chapters 5 and 6 are based on original work performed by me, Brennen J. Dobberthien, where my contributions are indicated as above. Contributions by others are as follows. For both Chapters, the roles of Mr. A.G. Tessier and Dr. A. Yahya are as described above. For Chapter 5, additional contributions were provided by Dr. Avalyn Stanislaus, who performed liquid chromatography – mass spectrometry on blood samples; Dr. B.G. Fallone and Dr. Michael B. Sawyer were involved in manuscript review and editing. For Chapter 6, the coil design and construction was performed by Dr. Vyacheslav Volotovskyy.

The research project, of which this thesis is a part, received ethics approval from the Cross Cancer Institute's Animal Care Committee under the following two protocols:

- AC12202 "Nuclear Magnetic Resonance Spectroscopy Techniques for Measuring Oncologically Relevant Metabolites in Rat Brain at 9.4 T", October 24, 2012
- AC16228 "Nuclear Magnetic Resonance Spectroscopy Techniques for Measuring Oncologically Relevant Metabolites in Rat Brain at 9.4 T", July 4, 2016

Acknowledgements

First and foremost, I would like to acknowledge my family. My mother, Deb, and my father, Jay, have shown me love and support throughout my life. They taught me the value of education from a young age and provided a positive learning environment. My siblings, Connor and Jenna, have always been encouraging of their older brother. Thank you to my loving life partner, Jacquelin, who has stood beside me through all of life's trials and celebrations alike. I could never have done it without you.

I would like to thank all of the esteemed members of my supervisory committee, including Dr. Gino Fallone, Dr. Matthew Larocque, Dr. Alan Wilman, and Dr. Jonathan Sharp. The expertise and feedback provided throughout my graduate studies was invaluable and truly strengthened my research. Thank you also to Dr. Terence Riauka and Dr. Satyapal Rathee for being a part of my candidacy examination, and to Dr. Riauka and Dr. Robert Bartha for being involved with my thesis defense.

I have made a number of close friends through the years, and I would like to thank them as well, especially Mat, Nick, and Gavin. Thanks also to my fellow students and trainees, including Brian, Hali, Dylan, Cam, Andrei, JD, Eugene, Jay, Mike, Devin, Radim, Hongwei, Bryson, Niri, Clara, Simon, Aaron, and Amanda, among others. I am looking forward to seeing what all of these bright minds can accomplish.

I also would like to thank the Natural Sciences and Engineering Research Council of Canada for grant funding of the research program of which this thesis was a part. In addition, I am grateful to the Kidney Foundation of Canada for supporting me with an Allied Health Doctoral

Fellowship, and to the University of Alberta and the Government of Alberta for various sources of student funding.

Thank you to all of the staff at the Cross Cancer Institute, especially Anthony Tessier, as well as Dan Mcginn and the rest of the vivarium staff.

Last but not least, a special thank you goes to my supervisor, Dr. Atiyah Yahya. I could not have asked for a more knowledgeable, dedicated, patient, and encouraging mentor, and I am forever grateful.

Table of Contents

List of Tables

List of Figures

Chapter 1 - Introduction

1.1 – INTRODUCTION TO THESIS

1.1.1 – Thesis Hypothesis

The detection and quantification of oncologically relevant rat brain metabolites with *in-vivo* magnetic resonance spectroscopy at 9.4 T is improved via spectral editing with optimal-echo-time point-resolved spectroscopy. In addition, the high magnetic field strength of 9.4 T can be exploited to enable *in-vivo* magnetic resonance spectroscopy of rat kidney non-invasively.

1.1.2 – General Overview of MRS

Nuclear Magnetic Resonance (NMR) is a phenomenon that can be used to measure information about chemical systems. Specifically-designed magnetic fields enable localized NMR signals to be measured *in-vivo* non-invasively. More specifically, NMR is the phenomenon whereby a nucleus precesses, or resonates, in the presence of an external magnetic field. Magnetic Resonance Spectroscopy (MRS) is one of a number of techniques within the field of NMR imaging, but it is unlike many others in that it can provide metabolic information. That is, it can provide biochemical information instead of just an anatomic appearance. MRS can be used to indirectly measure metabolism, the series of chemical processes that maintain life, by measuring metabolite concentrations. The chemical shift effect results in signature peaks for different metabolites (depending on their chemical structure) enabling relative levels of metabolite concentrations to be estimated. MRS can provide insight into both healthy and diseased tissue function.[1]

Prominent brain metabolite peaks in ^{1}H MRS include those from *N*-acetylaspartate (NAA), creatine (Cr), and choline (Cho), which are the three largest peaks, at chemical shifts of approximately 2 ppm, 3 ppm, and 3.2 ppm, respectively. The protons that give rise to the signals are not involved in J-coupling interactions; therefore, they appear as singlets. The absence of J-coupling also implies no temporal J-coupling modulation of the signal. There are a number of other metabolites that either exist in lower concentrations or have a lower signal due to the signal arising from fewer nuclei. Their peaks are not as distinct and hence more difficult to detect and quantify. Further complicating matters is that a number of metabolite protons have similar chemical shifts and exhibit peak splitting due to J-coupling interactions, leading to spectral overlap. The low signal and spectral overlap makes it challenging to detect and accurately quantify signals from those metabolites and the application of more sophisticated techniques is required. This is where the subfield of spectral editing comes in.

In spectral editing, various methods are used to improve the signal resolution and detectability of a number of metabolite signals, to aid in their quantification. Most methods rely on differences in J-coupling evolution of the protons of interest and the contaminating protons. Pulse sequence parameters or modifications to pulse sequences are made such that J-coupling evolution results in minimal signal from contaminating protons while retaining sufficient signal from protons of interest. An example of spectral editing is optimizing the echo time (TE) of either Point-RESolved Spectroscopy (PRESS)[2] or Stimulated Echo Acquisition Mode (STEAM)[3], two commonly employed single-shot *in-vivo* MRS pulse sequences. PRESS potentially offers twice the Signal-to-Noise Ratio (SNR) obtainable from STEAM. It is a single-shot, double-spin-echo technique, characterized by two TE values, namely, TE_1 and TE_2, which have been optimized for spectral editing purposes,[4-10] as J-coupling evolution occurs during both time periods.[11]

Alternatives to spectral editing include 2D NMR methods. However, their applicability *in vivo* is limited due to long acquisition times, low SNR, and susceptibility to scan instabilities.[12]

1.1.3 – Challenges in MRS Quantification of Some Relevant Metabolites

Four metabolites that can benefit from spectral editing are glycine (Gly), glutamine (Gln), glutamate (Glu), and γ-aminobutyric acid (GABA). The spectrum from Gly is a singlet peak at about 3.55 ppm, which does not experience J-coupling evolution.[13] *In vivo*, it is significantly overlapped by signal from the protons of *myo*-inositol (Ins) at about 3.52 and 3.61 ppm, which do experience J-coupling interactions.[13] Additionally, Ins exists at a much larger concentration than Gly in the brain, and, as such, has a much larger signal. Glutamine, Glu, and GABA have resonances at about 2.45 ppm, 2.35 ppm, and 2.28 ppm, resulting from protons that are all involved in J-coupling interactions.[13] Glutamate experiences signal overlap with both Gln and GABA, and Gln additionally experiences signal overlap with the signal of NAA at about 2.49 ppm, which also experiences J-coupling modulation.[13] The four metabolites play important biological roles in neurotransmission and energy metabolism,[14,15] and their altered concentration levels have been implicated in a number of disease states, including cancer.[8,16] Therefore, the ability to detect and quantify their levels *in vivo* is relevant both as a research tool and, potentially, as a clinical diagnostic one. Spectral editing to enable better detection and quantification of the MRS signals of the metabolites is a crucial step towards paving the way for advanced research and diagnosis of diseases such as cancer with MRS.

1.1.4 – ^{13}C MRS

While hydrogen-1 (^{1}H) is the most commonly utilized nucleus in MRS because of its high natural abundance and sensitivity, others of interest include carbon-13 (^{13}C). Performing research with ^{13}C has its own set of challenges, including lower sensitivity due to a lower gyromagnetic ratio (approximately one-fourth that of ^{1}H) and a lower natural isotopic abundance (around 1.1%, compared to 99% for ^{1}H). An additional cost is the extra hardware that is typically required to detect ^{13}C NMR signal on a scanner that is normally used for ^{1}H. However, some of the challenges can be mitigated or even turned to advantage. The natural isotopic abundance of ^{13}C can be leveraged by infusing a ^{13}C-enriched substrate, such as ^{13}C-labelled-glucose (Glc), into a living system. When Glc has been enriched with ^{13}C (up to 99% of Glc carbons can be ^{13}C-enriched) and injected into a human or animal, the products of Glc metabolism will incorporate the ^{13}C label, resulting in increased ^{13}C signal from those metabolites. By measuring the increase in the signal over time (the rate of ^{13}C accumulation into the metabolite pool), a measure of Glc energy metabolism can be obtained.[17] These are referred to as *dynamic* measurements, as opposed to typical *steady-state* MRS measurements.

One relevant product of glucose metabolism of which such dynamic measures can be obtained is Glu, which is linked to the tricarboxylic acid (TCA) cycle through α-ketoglutarate.[17] When ^{13}C-labelled-Glc is metabolized, the C4 carbon of Glu becomes ^{13}C labelled ($^{13}C_4$-Glu). Measuring the increase in signal over time can enable the measurement of V_{TCA}, the rate of the TCA cycle.[17] V_{TCA} is important to the study of a number of diseases, including cancer.[18,19] While $^{13}C_4$-Glu can be measured *directly* with ^{13}C MRS, it can also be measured *indirectly* with ^{1}H MRS through heteronuclear J-coupling interactions between the ^{1}H nuclei and the ^{13}C nuclei that results in peak splitting (can be referred to as satellite peaks).[20] The proton spectrum becomes modified

as ^{13}C label is incorporated due to the heteronuclear J-coupling. Techniques that can be used to measure $^{13}C_4$-Glu indirectly include Adiabatic Carbon Editing and Decoupling (ACED)-STEAM[21] and the Proton-Observed Carbon-Edited (POCE) Sequence.[22] The methods include both ^{13}C and ^{1}H pulses and, therefore, require hardware for both. Indirect ^{13}C detection has, however, been performed without additional ^{13}C hardware, using only a standard short-TE PRESS ^{1}H pulse sequence.[20] The work was performed at 3 T to obtain $^{13}C_4$-Glu measures from monkey brain during an infusion of uniformly-labelled-^{13}C-glucose ([U-$^{13}C_6$]-Glc).[20] Measures were obtained from satellite peak signals surrounding the nominal ^{1}H signal in the spectrum, which begin to grow as more ^{13}C label is incorporated. Subtraction from the baseline spectrum removes overlapping signals at each time point.

1.1.5 – High Field MRS

A large amount of MRS research in humans *in vivo* has been performed at clinical field strengths, such as 1.5 T or 3 T. Higher static magnetic field strengths, available for research, such as 7 T or 9.4 T, offer two key advantages for MRS. One major advantage is an increase in SNR; *in vivo,* there is approximately a linear increase in SNR with increasing field strength.[23] The increase in SNR results in better defined peaks in MRS, allowing for more accurate quantification. In some cases, this can enable the detection of peaks that would otherwise be undetectable.[24] The second benefit of a higher field strength is increased spectral resolution that results from an increased separation between peaks due to the increase in the frequency difference between them.

There are a number of challenges associated with high field magnets, including magnetic field homogeneity, rendering small bore magnets popular for research studies.[25-31] Such small bore

magnets are suitable for studying animal models such as the rat. While it is not a completely human equivalent model, valuable information learned from research on the rat model, for example, in disease states such as cancer, can potentially be translated to or justify human studies. The field strength of 9.4 T has been used to perform a number of rat brain MRS studies.[25-28,31-36] Many of the studies were performed with short-TE techniques and relied on spectral fitting for quantification.[25-28,31,34,35] However, it has been shown that when spectral overlap occurs, signal quantification with spectral fitting can be inaccurate, even when the Cramér-Rao Lower Bound (CRLB, a measure of fitting uncertainty) is low, for example, in the case of glutathione (GSH), which has overlap with a number of metabolites.[37] Even at 9.4 T, there is spectral overlap for Gly, Glu, Gln, GABA, and $^{13}C_4$-Glu. Only a limited number of spectral editing techniques have been implemented at 9.4 T. SPin ECho, full Intensity Acquired Localized (SPECIAL) spectroscopy has been optimized for Gly.[32,36] Subtraction editing has been utilized for GABA.[133] Optimal-TE STEAM has been optimized for Glu and Gln via simulation, but it has not been applied *in vivo*.[24]

1.1.6 – Thesis Objectives

The hypothesis of this thesis is that the detection and quantification of oncologically relevant rat brain metabolites with *in-vivo* magnetic resonance spectroscopy at 9.4 T is improved via spectral editing with optimal-TE PRESS. In addition, the high magnetic field strength of 9.4 T can be exploited to enable *in-vivo* magnetic resonance spectroscopy of rat kidney non-invasively. This is investigated throughout the thesis, with a few specific research objectives in mind. One objective is to optimize TE_1 and TE_2 of PRESS for the improved quantification of steady-state measures of Gly (concentration of ≈ 1 mM), Gln (≈ 4 mM), Glu (≈ 10 mM), and GABA (≈ 1 mM)

for rat brain ^{1}H MRS studies at 9.4 T. We evaluated short-TE spectra obtained from phantoms of known concentrations, and demonstrated that errors can result due to overlapping signals. Specifically, concentrations were estimated from phantoms of known varying glutamine (Gln) concentrations, with other metabolites present in fixed known physiological concentration ratios, and it was found that errors in estimation were >39 %. In addition, another objective is to optimize PRESS for the dynamic measures of $^{13}C_4$-Glu by indirect ^{13}C detection at 9.4 T, during rat [U-$^{13}C_6$]-Glc infusions. PRESS is a readily available MRS sequence and our optimizations provide a convenient alternative to spectral editing techniques presented in the literature for the measurement of Gly[32,36] and GABA[33] at 9.4 T. The former relies on the SPECIAL technique, which is not readily available on most scanners. Both techniques rely on subtraction of spectra, rendering them prone to subtraction errors. The subtraction technique for the detection of GABA removes the 2.35 ppm Glu and 2.45 ppm Gln signals. While STEAM timings have been optimized for Glu and Gln via simulation,[24] the optimizations have not been verified *in vivo*. In this thesis work, PRESS was optimized for the simultaneous measurement of Gln, Glu, and GABA in rat brain. We also optimize PRESS for indirect $^{13}C_4$-Glu measurements at 9.4 T that do not rely on subtraction or the need for additional ^{13}C hardware. Previous work that measured $^{13}C_4$-Glu without a ^{13}C channel relied on subtraction of spectra[20], which as mentioned already can be prone to subtraction errors. At 9.4 T, $^{13}C_4$-Glu results in a proton satellite peak at 2.51 ppm which suffers spectral overlap primarily with NAA (≈ 2.49 ppm). Our optimization reduced the contamination from NAA.

While MRS studies on rat brain have been common, work on other body structures such as kidney has been limited.[38] The study of metabolites such as Glu, Gln, Ins, taurine (Tau), betaine (Bet), and Cho has shown relevance to research on kidney cancers, including renal cell carcinoma.[39] Kidney MRS studies have been largely limited due to respiratory motion, which

makes any study of abdominal structures challenging due to motion artifacts. Previous rat kidney studies were performed at 2.0 T[40] and 7 T[41,42] on surgically exposed kidneys, which allows the kidney to be fixed, while also improving SNR due to the proximity of the radiofrequency (RF) coil. In this thesis, the final objective is to exploit the higher SNR at 9.4 T to obtain *in-vivo* MRS spectra of the rat kidney non-invasively to quantify levels of Glx (Glu + Gln), Ins, and Tau, relative to Cho + Bet.

1.1.7 - Overview of Thesis Organization

The presented thesis is organized into 7 chapters. The rest of chapter 1 includes background information on MRS, including the basics of NMR, NMR detection, the chemical shift effect, J-coupling, longitudinal and transverse relaxation, *in-vivo* MRS techniques, J-coupling evolution during PRESS, spectral editing, the benefits of high field NMR, as well as special considerations for ^{13}C MRS. Chapter 2 provides details on the relevant metabolites, numerical density matrix simulations, experimental design for phantom, rat brain, and rat kidney MRS experiments, and data analysis with LCModel peak fitting software. Chapter 3 presents the optimization of PRESS for Gly detection and quantification in rat brain at 9.4 T. The PRESS timings are chosen to minimize the overlapping Ins resonance, retaining sufficient Gly signal, the protons of which do not experience J-coupling interactions. The chapter discusses the methods and results obtained from numerical calculations and phantom experiments and demonstrated the efficacy of the sequence timings *in vivo* in the brains of four rats (published in Biomedical Physics and Engineering Express, 2016). Chapter 4 demonstrated how PRESS timings are selected for the simultaneous detection of Glu, Gln, and GABA in rat brain at 9.4 T. PRESS is optimized such that

the NAA resonance in the Gln spectral region is reduced, while the Glu, Gln, and GABA signals are preserved. The longer TE values also allow for the decay of short-T_2 macromolecule signals that overlap all three signals.[43-45] The chapter includes methods and results attained from simulations and experiments, from both phantom and five rat brains *in vivo* (published in NMR in Biomedicine, 2018). Chapter 5 describes the study on dynamic measurements of $^{13}C_4$-Glu in rat brain with optimal-TE ^{1}H PRESS at 9.4 T upon infusion of [U-$^{13}C_6$]-Glc. Optimizations were done numerically and verified in phantom solutions and *in vivo* in the brains of two rats during infusion (submitted to NMR in Biomedicine, 2019). Chapter 6 presents the outcome of non-invasive rat kidney MRS *in vivo* at 9.4 T with short-TE PRESS, including quantification of Glx (Glu + Gln), Ins, and Tau, relative to Cho + Bet, from four rat kidneys. Chapter 7 offers concluding remarks.

1.2 – NUCLEAR MAGNETIC RESONANCE

1.2.1 – Spin and Nuclear Magnetic Moments

The physical property of nuclei that enables them to have an NMR signal is spin, which not all nuclei have. Spin is a quantized intrinsic angular momentum that gives rise to a magnetic moment. Spin quantum number, s, is defined as:

$$s = \frac{n}{2} \tag{1.1}$$

n is any non-negative integer. For this thesis, the focus is on nuclei that have a spin of ½. Protons and neutrons, which are the particles that populate a nucleus, both have a spin of ½. If a nucleus contains one of these in an odd number, it will have a spin of ½. Such nuclei include ^{1}H, ^{13}C, nitrogen-15, fluorine-19, and phosphorus-31. This thesis will discuss ^{1}H and ^{13}C NMR. ^{1}H is the

most popular for a number of reasons, including the sheer number of hydrogen nuclei that exist in biological systems as a part of water, as well as the relative natural isotopic abundance of ^{1}H (around 99%). A ^{1}H nucleus is simply made up of one proton, so it is often referred to as such, and ^{1}H NMR is often referred to as proton NMR. Carbon-12 (^{12}C) is the most abundant form of carbon (around 98.9%), but it has no net spin, owing to the nuclear structure of six protons and six neutrons. ^{13}C is less abundant (around 1.1%), but because it contains seven neutrons, it has a spin of ½.

The total spin angular momentum, S, is described by:

$$S = \hbar\sqrt{s(s+1)} \tag{1.2}$$

ħ is the reduced Planck constant (1.054×10^{-34} J·s). For a spin-½ system:

$$S = \hbar\frac{\sqrt{3}}{2} \tag{1.3}$$

The z component is:

$$S_z = \pm\frac{\hbar}{2} \tag{1.4}$$

The spin gives rise to a magnetic moment, $\vec{\mu}$, which has a z component of:

$$\mu_z = \gamma S_z = \pm\frac{\gamma\hbar}{2} \tag{1.5}$$

γ is the gyromagnetic ratio ($2\pi \times 42.6 \times 10^{6}$ rad·s^{-1}·T^{-1} for ^{1}H).

1.2.2 – Effects of External Magnetic Fields – Zeeman Energy

When a magnetic moment is placed in an external magnetic field, $\vec{B}$, it gains an energy:

$$E = -\vec{\mu} \cdot \vec{B} \tag{1.6}$$

A spin-½ particle in a uniform magnetic field in the $\vec{z}$ direction will align with $\vec{B}_0$ and gain an energy:

$$E = \pm \frac{\gamma \hbar}{2} B_0 \tag{1.7}$$

Spins that are aligned parallel to $\vec{B}_0$ are in a lower energy state and have a negative E, while spins that are aligned anti-parallel to $\vec{B}_0$ are in a higher energy state and have a positive E. The difference between these two energies is:

$$\Delta E = \gamma \hbar B_0 \tag{1.8}$$

This is known as the Zeeman Energy, and it is illustrated in figure 1.1. This is the energy required for a spin to switch between the two states.

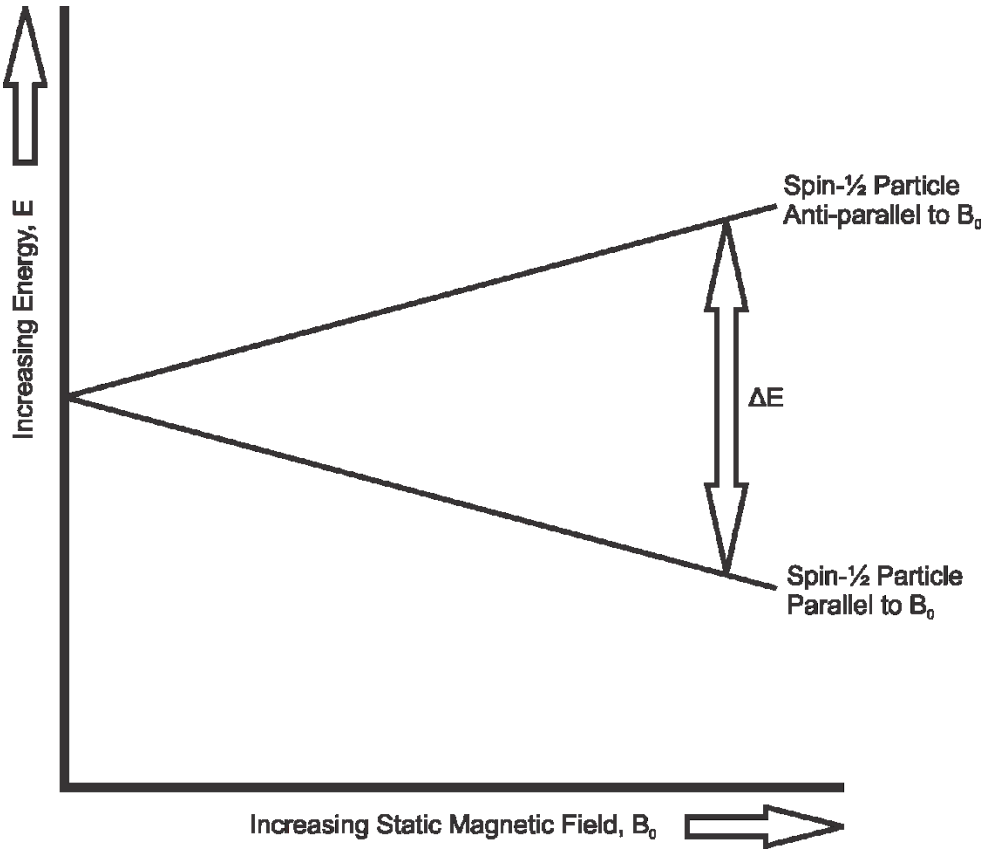

Figure 1.1: The Zeeman Energy for a spin-½ particle, which increases with increasing $\vec{\boldsymbol{B}}_{\boldsymbol{0}}$.

1.2.3 – Larmor Frequency

As the Zeeman energy is the energy required for a spin to switch between the two states, a photon of this energy can cause the transition. The frequency of such a photon would be given by:

$$\omega_0 = \frac{\Delta E}{\hbar} = \gamma B_0 \tag{1.9}$$

This is equivalent to the frequency of precession of a magnetic moment when a torque is exerted on it by an external magnetic field. This is referred to as the Larmor frequency, shown in figure 1.2.

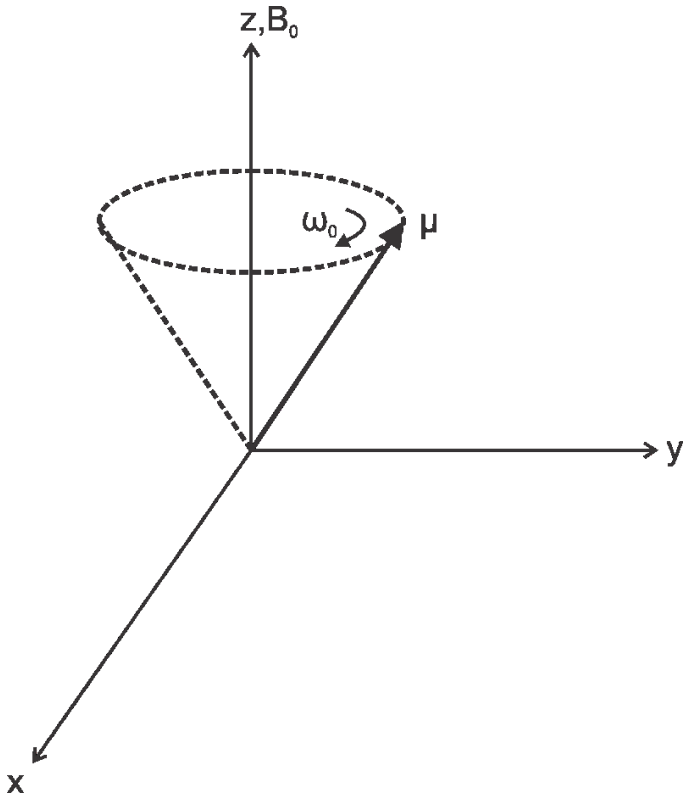

Figure 1.2: The precession of a magnetic moment $\vec{\boldsymbol{\mu}}$ placed in an external magnetic field $\vec{\boldsymbol{B}}$, which oscillates with the Larmor frequency $\boldsymbol{\omega_0}$.

1.2.4 – Population of Spin States

Prior to application of an external magnetic field, a given spin in a population will have a random orientation. When the field is added, the spins will align either parallel or anti-parallel as described above. In addition, since the spins that are parallel to $\vec{B}_0$ are in a lower energy state, this state is preferentially populated. The number of spins in this state, relative to the number of spins that are anti-parallel, follows the Boltzmann distribution, given by:

$$\frac{N_{parallel}}{N_{antiparallel}} = \exp\left(\frac{\Delta E}{kT}\right) = \exp\left(\frac{\gamma \hbar B_0}{kT}\right) \tag{1.10}$$

k is the Boltzmann constant (1.381 x 10^{-23} J·K^{-1}) and T is temperature in K.

1.2.5 – The Net Magnetization Vector

The preferential population of spins parallel to $\vec{B}_0$ results in a net magnetization, M_0. At room temperature:

$$kT \gg \gamma \hbar B_0 \tag{1.11}$$

A first order Taylor series approximation can be applied to the Boltzmann distribution in equation 1.10, yielding:

$$\frac{N_{parallel}}{N_{antiparallel}} \approx 1 + \frac{\gamma \hbar B_0}{kT} \tag{1.12}$$

Multiplying both sides by and then subtracting $N_{antiparallel}$ gives:

$$N_{parallel} - N_{antiparallel} \approx N_{antiparallel} \frac{\gamma \hbar B_0}{kT} \tag{1.13}$$

Since the difference between $N_{parallel}$ and $N_{antiparallel}$ is small, it can be assumed that:

$$N_{antiparallel} \approx \frac{N_s}{2} \tag{1.14}$$

N_s is the total number of spins. Therefore:

$$N_{parallel} - N_{antiparallel} \approx \frac{N_s}{2} \frac{\gamma \hbar B_0}{kT} \tag{1.15}$$

The resulting net magnetization is given by:

$$M_0 = \mu_z (N_{parallel} - N_{antiparallel}) = \frac{\gamma^2 \hbar^2 N_s B_0}{4kT} \tag{1.16}$$

The net magnetization vector will point along $\vec{B}_0$ at equilibrium.

1.3 – NMR DETECTION

1.3.1 – Radiofrequency (RF) Excitation

As mentioned above, a photon of frequency ω_0 will allow the spins to switch between their two states. For NMR, this is typically in the radiofrequency (RF) range of the spectrum. For example, for ^{1}H at 9.4 T:

$$\omega_0 = \gamma B_0 = (2\pi \times 42.6 \times 10^6\ rad \cdot s^{-1} \cdot T^{-1})(9.4\ T) = 2\pi \times 400.44 \times 10^6\ rad \cdot s^{-1} \quad (1.17)$$

When an RF pulse ($\vec{B}_1$ magnetic field) is applied, the orientation of the net magnetization vector can be modified. It is useful here to define the rotating reference frame, which is separate from the laboratory frame. The rotating reference frame rotates at the frequency of the applied RF pulse. $\vec{B}_1$, which oscillates in the laboratory frame, is static in the rotating frame on a fixed axis. This axis is referred to as a pulse's phase. The angle through which the magnetization vector, M, is flipped is related to the amplitude and duration of the $\vec{B}_1$ pulse. The phase of the RF pulse determines the direction in which the magnetization vector is tipped. For example, a $90°_X$ (the subscript refers to pulse phase direction in the rotating frame, in this case in the x-direction) pulse will tip the magnetization vector from along the z direction into to the x-y plane, along the y-axis. This is known as an excitation pulse, and it can be visualized in figure 1.3. A 180° pulse will invert the magnetization vector from the positive z direction to the negative z direction. This is known as an inversion pulse, which is demonstrated in figure 1.4. There is another type of 180° pulse called a refocusing pulse, which is discussed in section 1.7.2.

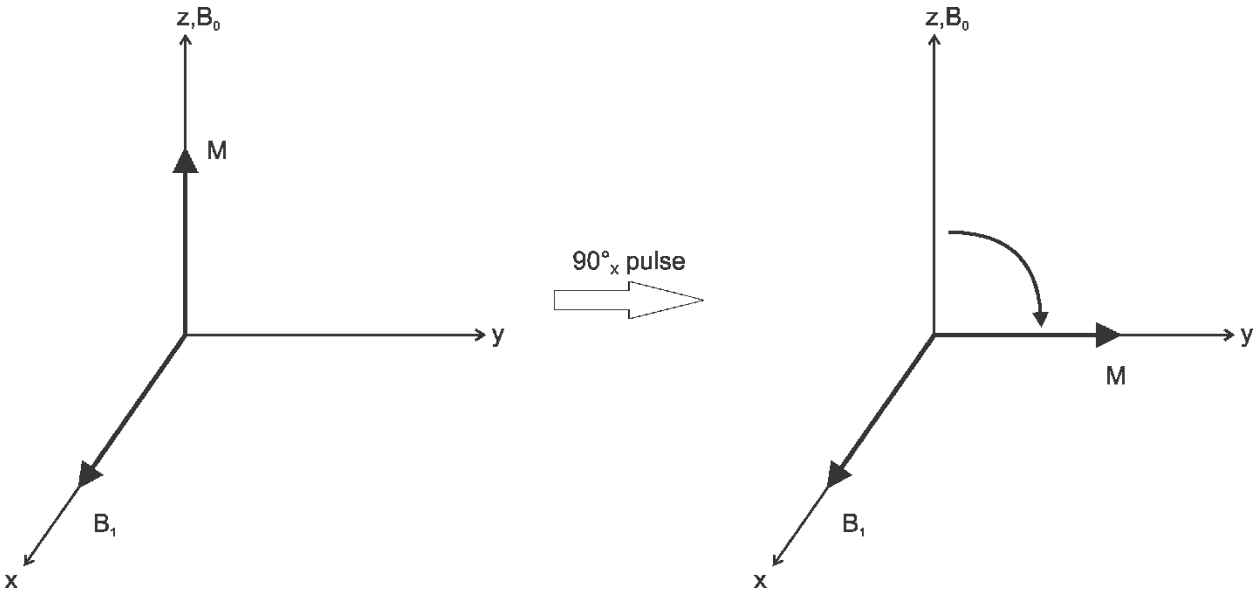

Figure 1.3: Diagram of a magnetization ***M*** being tipped from the z-direction (parallel to $\vec{\boldsymbol{B}}_{\boldsymbol{0}}$) into the xy-plane (perpendicular to $\vec{\boldsymbol{B}}_{\boldsymbol{0}}$) with a $90°_X$ excitation pulse in the rotating frame.

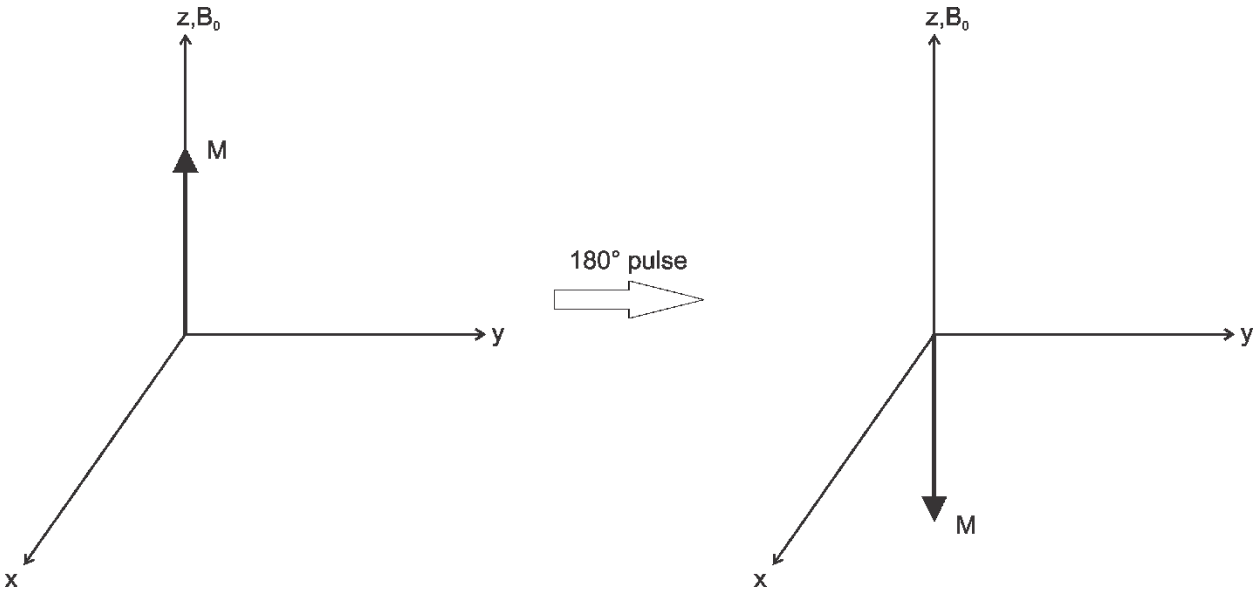

Figure 1.4: Diagram of a magnetization $\boldsymbol{M}$ being tipped from the z-direction (parallel to $\vec{\boldsymbol{B}}_{\boldsymbol{0}}$) into the negative z-direction (anti-parallel to $\vec{\boldsymbol{B}}_{\boldsymbol{0}}$) with a 180° inversion pulse.

1.3.2 – Detection via Faraday Induction

Faraday induction is the creation of an electromotive force (EMF), or voltage, in a closed circuit, due to a rate of change in the magnetic flux, $\frac{d\Phi_B}{dt}$, enclosed by the circuit. This is shown in figure 1.5. When the spins are excited, the magnetization vector, M_{xy}, now in the x-y plane, will precess around the z-axis with the Larmor frequency ω_0. As this happens, a magnetic flux that varies with this frequency will be created. An appropriately designed circuit can detect this via faraday induction, and the voltage can be detected and measured.

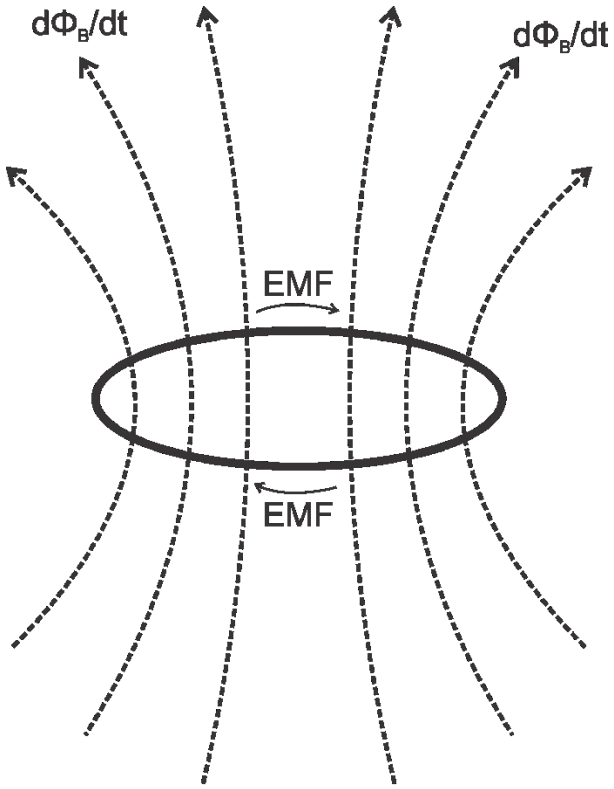

Figure 1.5: Illustration of Faraday induction.

RF coils are used to apply the excitation pulses and detect the varying magnetic field created by the resulting precession of the magnetization vector. There are different types of coils that can be used for these purposes. Two of the most common are surface coils and volume coils.

A surface coil is a simple LC circuit loop, shown in figure 1.6. The resonant frequency, given by:

$$\omega = \frac{1}{\sqrt{LC}} \tag{1.18}$$

ω is tuned to the Larmor frequency ω_0. The main advantage of surface coils is a better SNR, as the design allows for closer proximity of the coil to the region being imaged. However, the tradeoff is the inhomogeneity of the RF field and signal drop-off with depth.

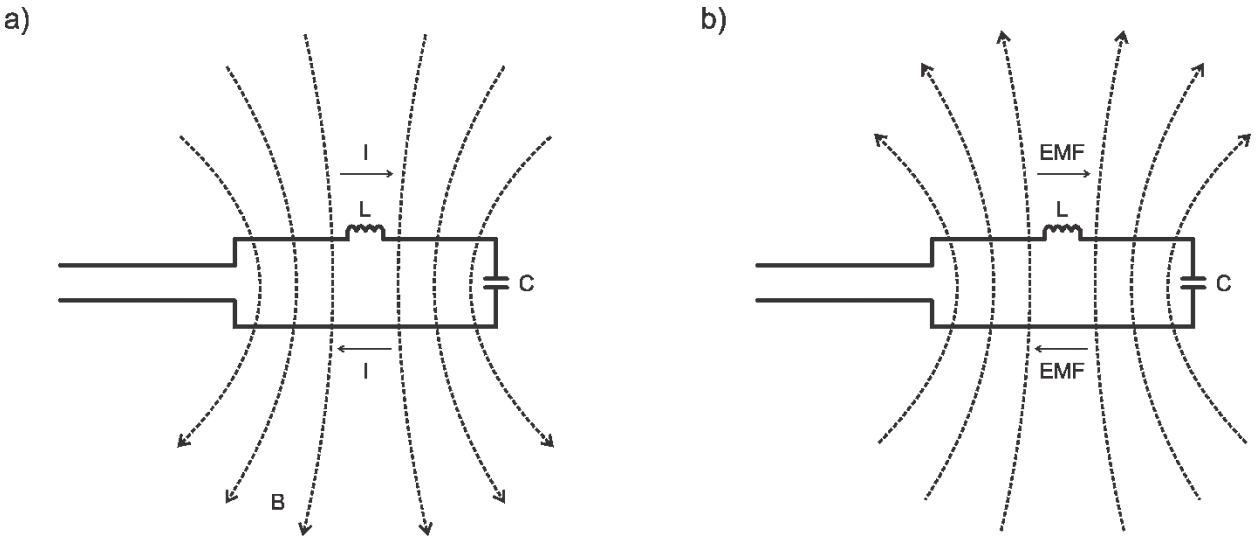

Figure 1.6: Basic surface coil design, which is an LC circuit. Panel a) shows $\vec{\boldsymbol{B}}$ (dashed arrows) generation from a current $\boldsymbol{I}$. Panel b) shows detection, with an EMF induced by the magnetic flux (dashed arrows) from the spins.

A birdcage coil, which is a type of volume coil, has a different and more complicated design. It involves a number of LC circuits connected in parallel to form a cylinder or "cage." Figure 1.7 illustrates this. This design ensures that there is more homogeneity of the RF field throughout the inside of the cylinder. The main disadvantage is that the geometry of the coil often results in a greater distance from the sample, which reduces the SNR.

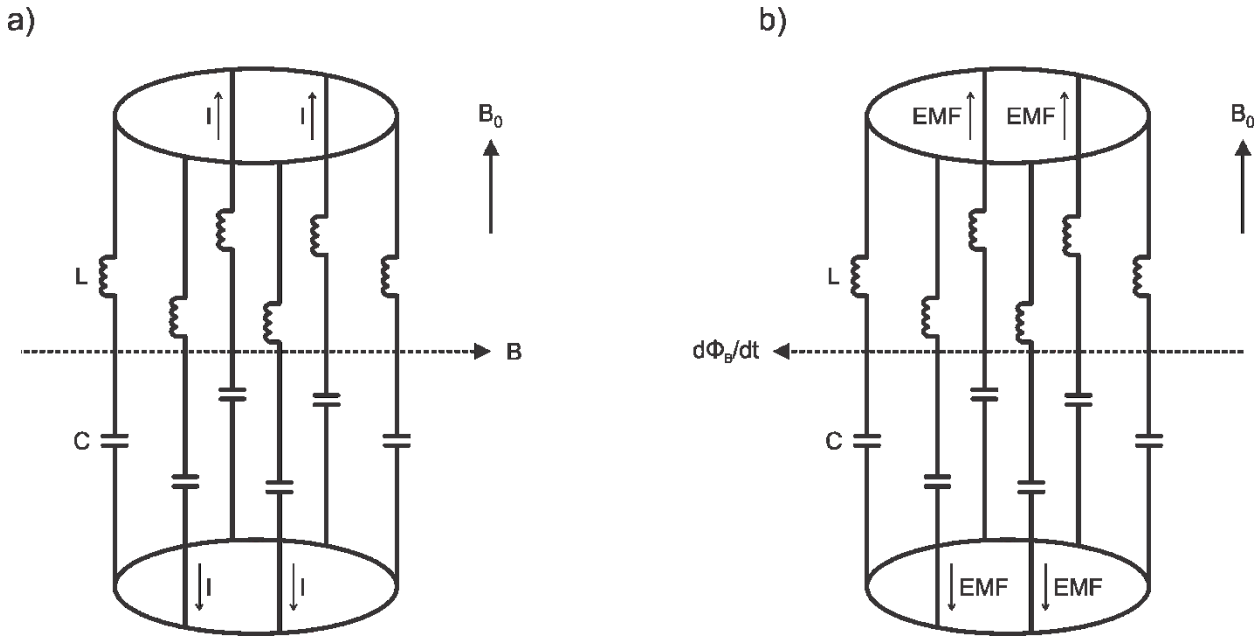

Figure 1.7: Birdcage coil, which is a number of LC circuits attached in parallel to form a cylinder. Panel a) shows $\vec{\boldsymbol{B}}$ generation from a current $\boldsymbol{I}$. Panel b) shows detection, with an EMF induced by the magnetic flux from the spins.

1.3.3 – Effect of Magnetic Field Gradients

By combining a static magnetic field with RF coils, it is possible to excite spins and then detect the resulting precession. However, there needs to be a way to determine where the signal originates. The mapping is important for imaging but is also crucial for spectroscopy where the signal needs to be spatially localized. Magnetic field gradients allows for this. By applying a linear, spatially varying magnetic field gradient to the existing static magnetic field, the Larmor frequency ω_0 of the spins can be varied linearly over space. As the local magnetic field of each spin changes, the resulting frequency changes, according to:

$$\omega = \gamma B \tag{1.19}$$

A gradient can be applied, which is given by:

$$G = \frac{\Delta B}{\Delta x} \tag{1.20}$$

A slice can be excited by applying a $\Delta\omega$ range of RF frequencies, or bandwidth, while the gradient is applied. The pulse is known as a slice-selective RF $\vec{B}_1$ pulse and will be discussed further in section 1.6.1. The slice will have dimension:

$$\Delta x = \frac{\Delta\omega}{\gamma G} \tag{1.21}$$

Slice-selection can be done with the field variation in all three dimensions, using three magnetic field gradients to achieve a cubic voxel for MRS. The fields all point along the z-axis.

1.3.4 – Free Induction Decay (FID)

The resulting signal detected by the coil is referred to as a Free Induction Decay (FID), which is shown in figure 1.8. It is detected as an induced voltage that changes with time.

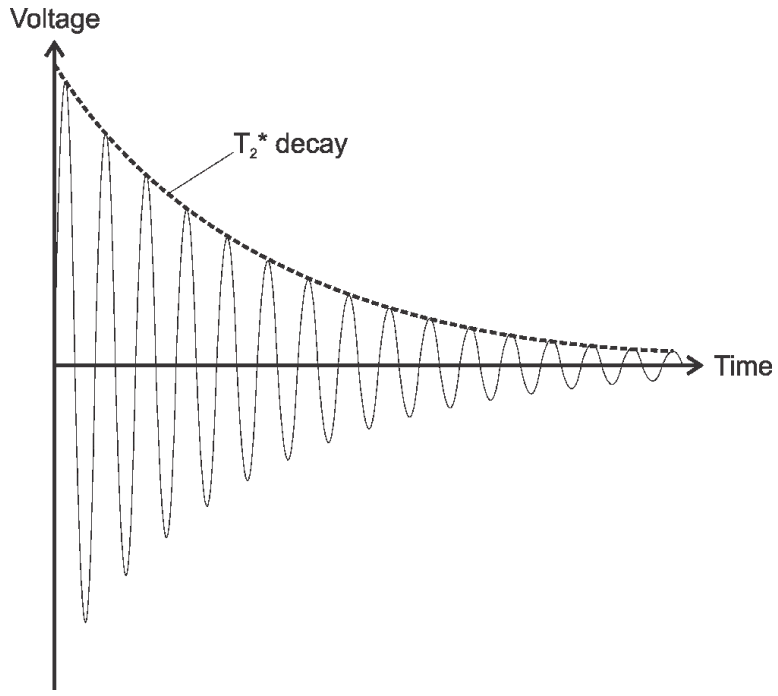

Figure 1.8: Free induction decay.

The oscillations in the FID match the Larmor frequency ω_0 of the spins. Applying a Fourier Transform to this time domain signal results in a frequency domain signal that consists of a peak at ω_0, which corresponds to a frequency of $\nu_0 = \frac{\omega_0}{2\pi}$ in Hz (see figure 1.9). The FID decays exponentially with a time parameter, T_2^*, following e^{-t/T_2^*}, and this results in a peak in the time domain that has a finite linewidth that is proportional to $\frac{1}{\pi T_2^*}$. T_2^* will be discussed further in section 1.5.2.

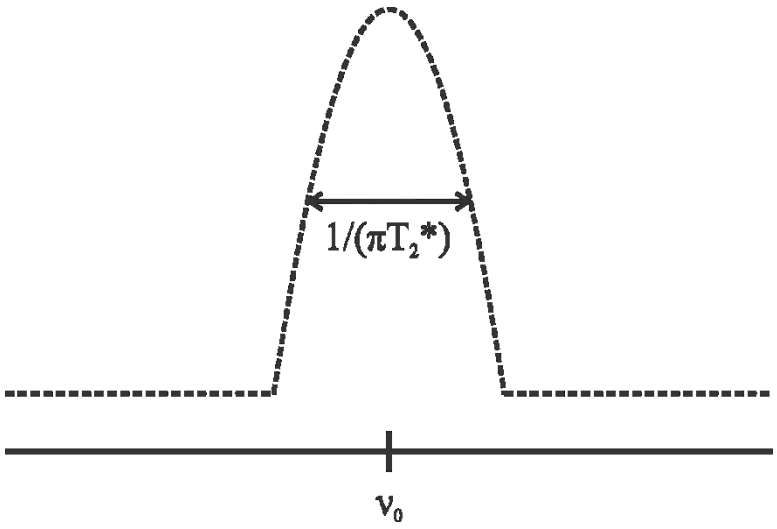

Figure 1.9: Peak in frequency domain associated with the FID.

1.4 – CHEMICAL SHIFT EFFECT

An isolated nucleus in a static magnetic field will precess at the Larmor frequency, as determined by the magnetic field strength, following equation 1.9. However, when the nucleus exists as a part of a molecule, the frequency depends on its chemical environment, as the precession of the electrons present in the molecule will alter the local magnetic field of the proton. This subtracts from the static magnetic field via shielding by these surrounding electrons, giving an effective field of:

$$B = B_0(1 - \sigma) \tag{1.22}$$

σ is the shielding constant. This results in a new resonant frequency of:

$$\omega = \gamma B = \gamma B_0(1 - \sigma) \tag{1.23}$$

As every functional group of each molecule has a different chemical environment and electron structure, each will have a slightly different σ. This results in a slightly different resonant frequency ω for nuclei that exist in these groups, giving a unique set of frequencies for each molecule. The shielding is known as the chemical shift effect, and it is what enables NMR spectroscopy to be a powerful tool. Figure 1.10 provides an example. As each metabolite has a unique spectral signature, it is possible to detect and quantify their specific signal peaks. The size, or strength, of the signal peaks is dependent on the number of nuclei at that frequency that are detected. In the case of a population of molecules, this corresponds to the concentration of that molecule in a sample. The number of nuclei within one moleculer group that contributes to the signal must also be accounted for. For example, signal from a CH_2 group will have twice the strength as signal from a CH group. For ^1H MRS, this is known as proton multiplicity.

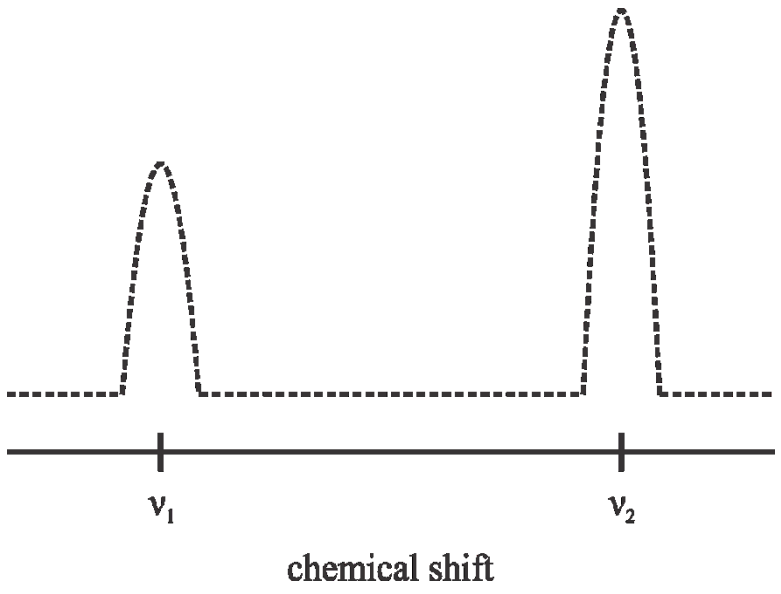

Figure 1.10: The chemical shift effect, with the frequency ν_1 greater than ν_2.

Chemical shift can be measured directly in Hz; however, this is dependent on field strength. For continuity between field strengths, ppm (parts per million) is used instead. The chemical shift, δ, in ppm, is determined by the formula:

$$\delta = \frac{\nu - \nu_{ref}}{\nu_{ref}} \tag{1.24}$$

ν is the resonance frequency in Hz and is given by:

$$\nu = \frac{\omega}{2\pi} \tag{1.25}$$

ν_{ref} is a reference frequency. One commonly used reference frequency is the resonance frequency of $Si(CH_3)_4$ or tetramethylsilane, which has 12 protons that resonate at the same frequency, resulting in a large singlet peak. They are magnetically equivalent, which means that they resonate at the same resonance frequency and experience the same J-coupling interactions. J-coupling interactions will be further discussion in section 1.7.

1.5 – RELAXATION

It is important to consider how the magnetization vector changes with time, especially following an excitation. This is known as relaxation, and there are two types of relaxation that are often discussed in NMR, longitudinal (or T_1) relaxation, and transverse (or T_2) relaxation. Each of these have separate, but equally important, effects in both imaging and spectroscopy.

1.5.1 – Longitudinal (T_1) Relaxation

Longitudinal (T_1) relaxation, also known as spin-lattice relaxation, describes the change in the z-component (along $\vec{B}_0$) of the magnetization with time, following an excitation. It has units of time (seconds, but it is commonly given in milliseconds), and it gives a measure of the time it takes the z-component of the magnetization to return to thermal equilibrium. Equilibrium refers to its state in the absence of RF excitation, where the magnetization is pointing along $\vec{z}$ with a magnitude of M_0. More specifically, T_1 is equal to the time it takes the magnetization vector to recover approximately 63% of its equilibrium value, following a 90° excitation pulse. This is equal to $1 - \frac{1}{e}$ and comes from:

$$M_z(t) = M_0 - (M_0 - M_z(0))e^{-t/T_1} \tag{1.26}$$

This describes T_1 relaxation following an excitation, which is illustrated in figure 1.11.

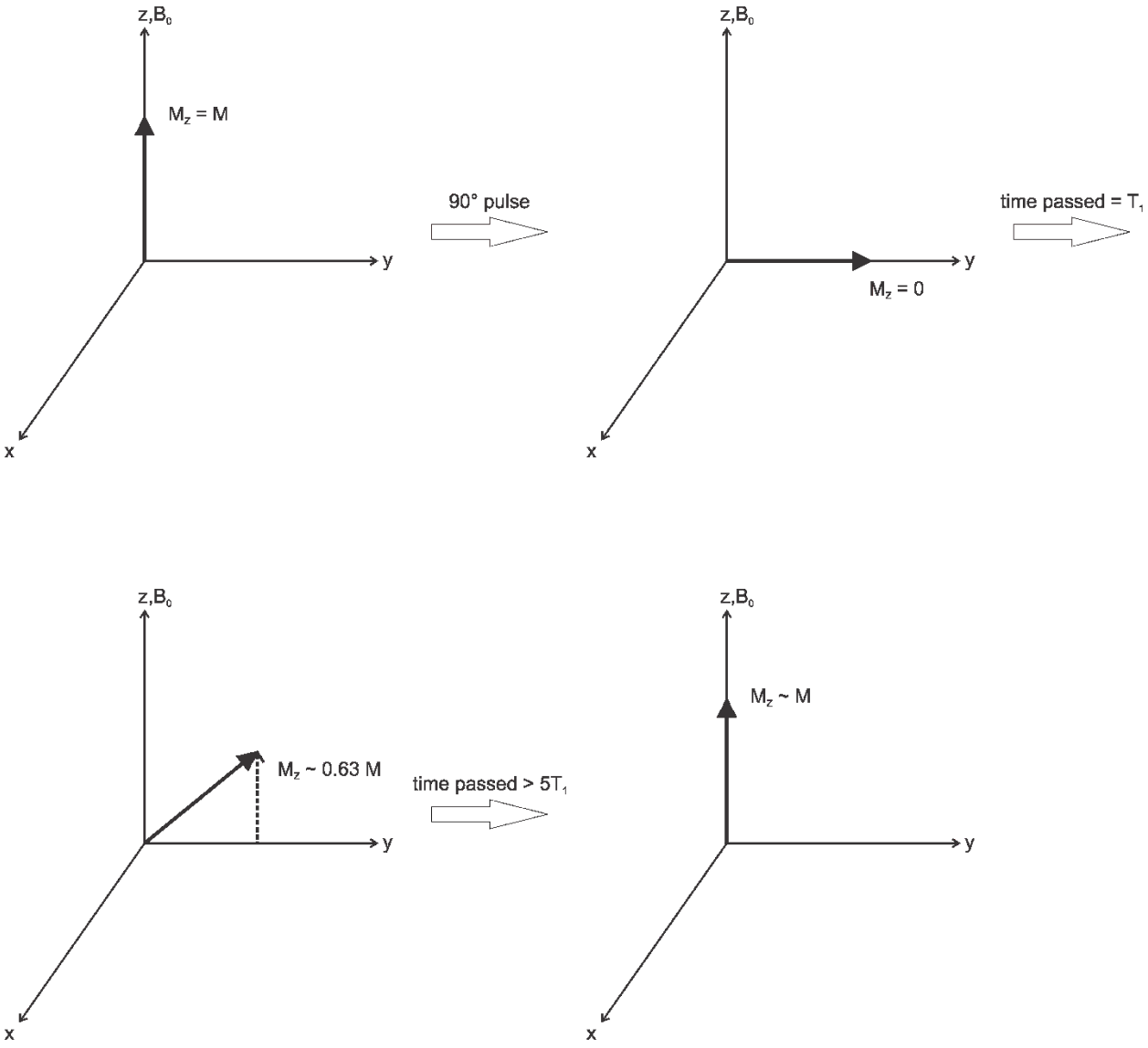

Figure 1.11: T_1 relaxation following a 90° excitation.

Longitudinal relaxation is caused by dipole-dipole interactions, which occur through space between the fields of magnetic dipoles, such as protons. This can allow for the transfer of energy from a dipole in a higher energy state, such as that of an excited nucleus, to a dipole in a lower energy state. The low energy dipoles that form the lattice (the surroundings of the excited nucleus),

therefore, absorb the energy given to the excited nucleus from the RF pulse. This allows the excited nucleus to return to a lower energy state and the z-component of the magnetization to return to equilibrium.

Spin-lattice relaxation is important for both MRI and MRS because it plays a role in determining the signal response. The amount that the longitudinal magnetization M_z recovers prior to an excitation will determine the amount of M_{xy} after excitation. If it fully recovers ($t > 5T_1$), a 90° excitation pulse will result in:

$$M_{xy} = M_z = M_0 \tag{1.27}$$

If not, a 90° excitation pulse will result in:

$$M_{xy} = M_z = M_0(1 - e^{-t/T_1}) \tag{1.28}$$

t is the amount of time that M_z has been allowed to recover. This loss in M_{xy} results in a loss in observed signal.

1.5.2 – Transverse (T_2) Relaxation

Transverse (T_2) relaxation, also known as spin-spin relaxation, describes the change in the xy-component (perpendicular to $\vec{B}_0$) of the magnetization with time, following an excitation. Like longitudinal relaxation, it has units of time, as it gives a measure of the time it takes the xy-component of the magnetization to return to equilibrium, which is equal to zero. Specifically, T_2 is equal to the time it takes the magnetization vector to decay to approximately 37% of its value. This is equal to $\frac{1}{e}$ and comes from:

$$M_{xy}(t) = M_{xy}(0)e^{-t/T_2} \tag{1.29}$$

This describes T_2 relaxation, which is shown in figure 1.12. It is worth noting that T_2 is always shorter than or equal to T_1.

Transverse relaxation is also caused by dipole-dipole interactions, but it is an entropy process. There is no net energy transfer while spins exchange energy between themselves. Instead, there is a loss of phase coherence (an increase of entropy). As a result, M_{xy} eventually returns to zero.

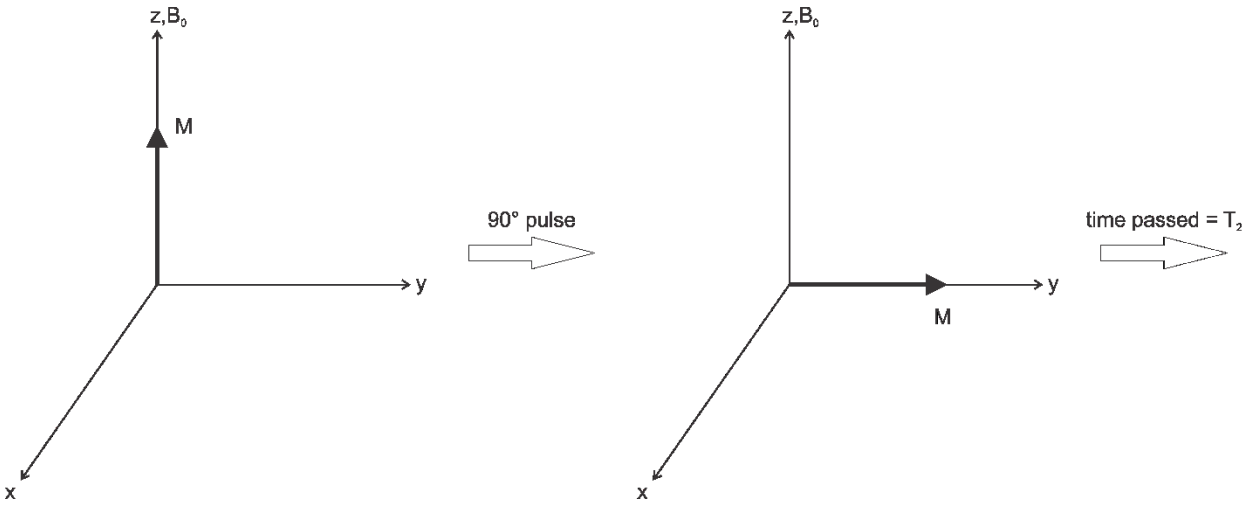

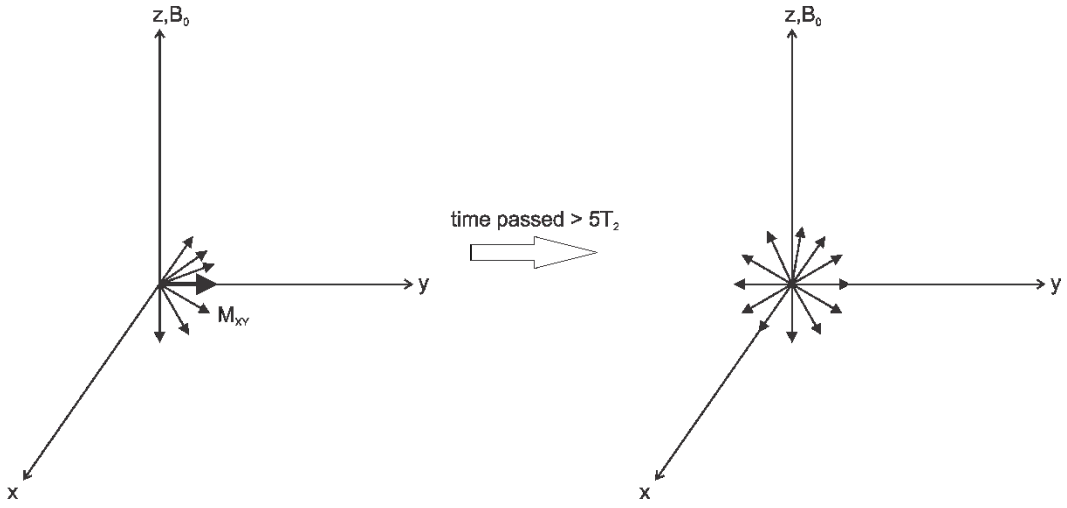

Figure 1.12: T_2 relaxation following a 90° excitation.

Spin-spin relaxation in both MRI and MRS plays a role in determining the signal response. The time between excitation and signal acquisition contributes to a loss in M_{xy}. If signal acquisition is directly after excitation, signal loss is minimized. However, in *in-vivo* MRS where pulse sequences require RF pulses of finite duration and gradients to play out, the time between excitation and reception is increased, resulting in a loss of M_{xy}, and, therefore, a loss in signal.

Another important aspect to consider is the presence of local magnetic field inhomogeneities. Since there are local changes in magnetic field strength B_0, the spins will experience slightly different Larmor frequencies ω_0, and will therefore precess at slightly different rates. This will cause excess dephasing, which means that some spins will acquire an excess positive or negative phase due to their increase or decrease in frequency relative to the expected nominal Larmor frequency. Dephasing causes M_{xy} to decay to zero quicker. The resulting relaxation is termed T_2^* relaxation, which is composed of the intrinsic T_2 relaxation, in addition to the effects of magnetic field inhomogeneities, ΔB_0, as follows:

$$\frac{1}{T_2^*} = \frac{1}{T_2} + \gamma \Delta B_0 \tag{1.30}$$

Fortunately, there is a way to reverse the dephasing due to the time independent field variations. By refocusing the magnetization with a spin echo pulse sequence, we can reduce the decay caused by $\gamma \Delta B_0$ effects, such that the system is only affected by T_2 relaxation.

As shown in figure 1.13, following spin excitation, the spins begin to dephase. Applying a refocusing $180°_X$ pulse rotates the transverse magnetization about the y-axis such that the spins "flip" to the opposite side. The spins that acquired a positive phase due to increased frequency will now have an equal negative phase, and vice-versa. As the spins continue to acquire phase, it will eventually return to zero during the same time delay. This is referred to as a spin echo. The total time from the initial excitation pulse to the height of the spin echo is referred to as the echo time (TE). It is defined as twice the time from the centre of the excitation pulse to the centre of the refocusing pulse.

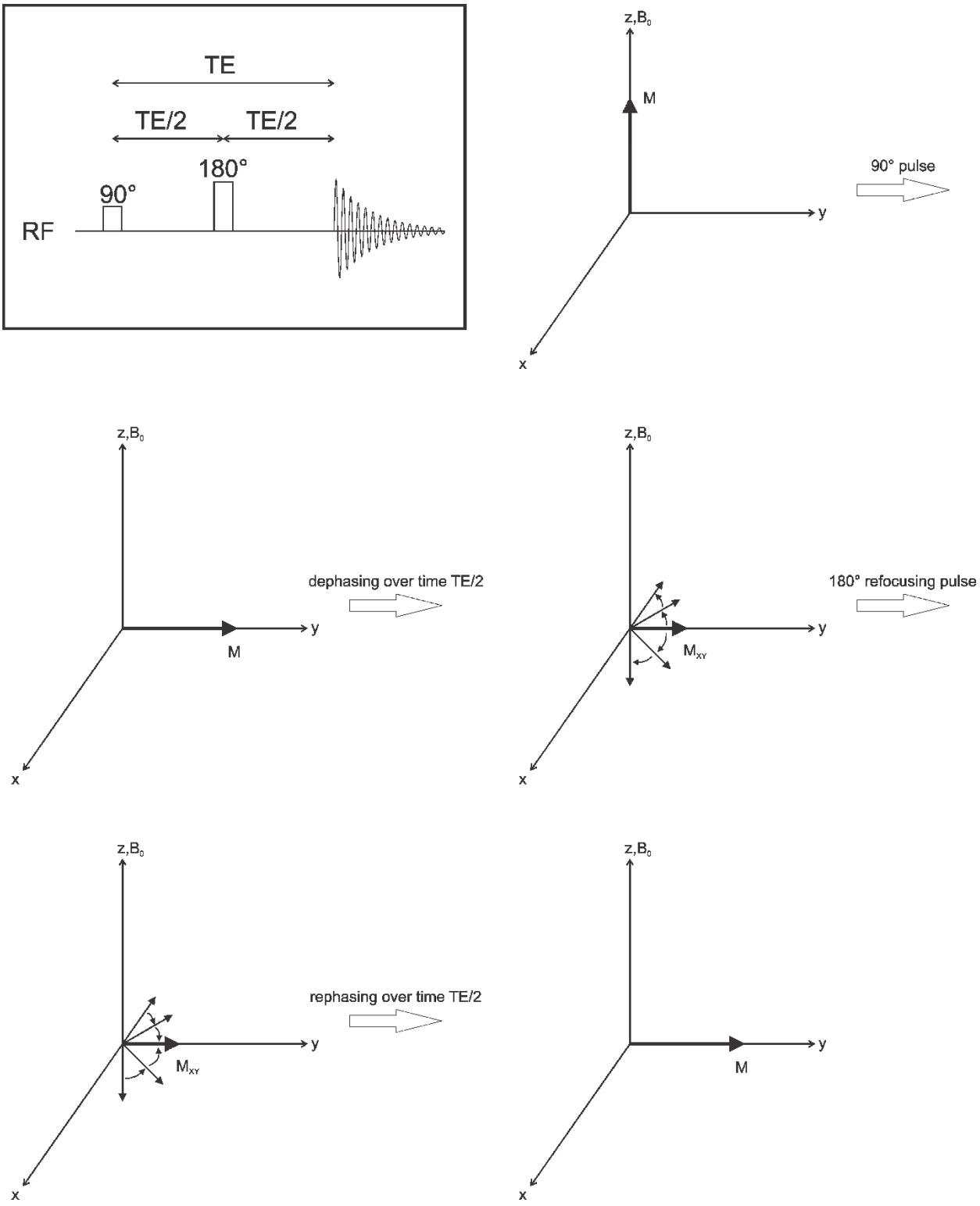

Figure 1.13: Illustration of a spin echo where dephasing due to time independent field variations are shown to be refocused.

1.6 – *IN-VIVO* NMR SPECTROSCOPY

When obtaining spectra *in vivo,* the signal needs to be localized to a specific region of interest, such as a cubic voxel in a certain brain location.

1.6.1 – Spatial Localization with Slice-Selective RF Pulses

As previously discussed, the Larmor frequency ω_0 of the spins can be changed in space by applying magnetic field gradients. Using slice-selective pulses along with magnetic field gradients enables us to selectively excite or refocus spins in a region of interest. By applying an amplitude-modulated RF pulse, we can excite only a specific range of frequencies that corresponds to the bandwidth of the pulse (determined by the Fourier transform). For example, a square pulse, known as a hard pulse, will excite all frequencies, but not equally. A Fourier transform of a square results in a sinc shape, therefore, a hard pulse will have a frequency profile that looks like a sinc wave, shown in figure 1.14.

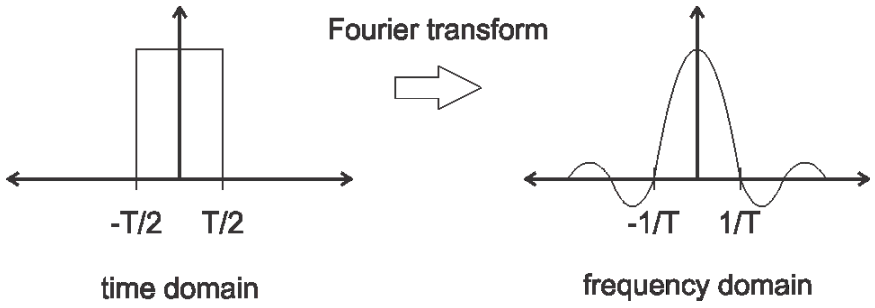

Figure 1.14: Fourier transform of a square-shaped hard pulse, which is a sinc wave in frequency domain.

If we apply the opposite, a sinc-shaped pulse, we can obtain a frequency profile that looks close to a square, as seen in figure 1.15. This is known as a frequency-selective pulse, and when it is combined with an appropriate magnetic field gradient, it can select a slice.

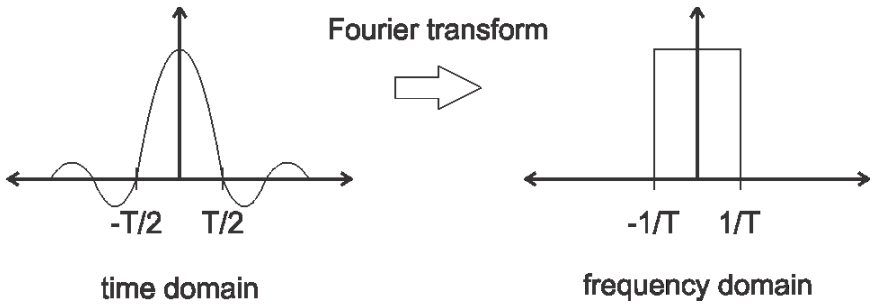

Figure 1.15: Fourier transform of a sinc-shaped pulse, which is a square in frequency domain.

1.6.2 – Single-Shot *In-Vivo* MRS Pulse Sequences

Point-Resolved Spectroscopy $(PRESS)^2$ is a commonly used pulse sequence in *in-vivo* MRS. It consists of three orthogonal slice-selective pulses, one 90° excitation pulse followed by two 180° refocusing pulses. Therefore, PRESS is a double spin echo sequence characterized by two separate echo times, TE_1 and TE_2, the sum of which is the total TE. The pulses are all slice-selective pulses, and they are all applied in conjunction with magnetic field gradients that are orthogonal to each other, creating three orthogonal slices. Spins in the first slice will be excited, and only those in a column will be refocused by the first refocusing pulse. Following that, only a cube of that column will be refocused by the second focusing pulse. This cube forms the voxel of

interest from which the signal is acquired. Spoiler gradients are used to dephase any signal that would come from outside of the voxel and from any spins experiencing imperfect 180 pulses. PRESS is visualized in figure 1.16.

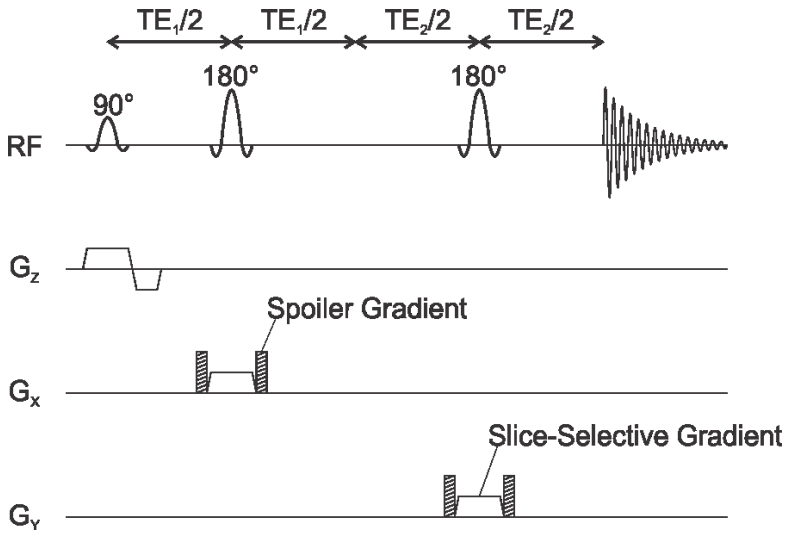

Figure 1.16: Diagram of PRESS.

Another popular *in-vivo* MRS technique is STimulated Echo Acquisition Mode (STEAM).[3] Like PRESS, STEAM is a single-shot sequence, that is, all the relevant information is acquired in each acquisition. It consists of three orthogonal 90° slice-selective pulses, which result in a stimulated echo that can be observed. Single-shot sequences allow shimming, the process of optimizing the homogeneity of B_0, directly on the voxel of interest.[46] In addition, they are less susceptible to any motion artifacts and using them with respiratory gating is straightforward. Assuming a steady-state, the signal acquired from a PRESS acquisition is governed by[47]:

$$M_{xy} = M_0(1 - 2e^{\frac{-\left(TR-\frac{TE}{2}\right)}{T_1}} + e^{\frac{-TR}{T_1}})e^{\frac{-TE}{T_2}} \quad (1.31)$$

When TR >> TE, equation 1.31 simplifies to:

$$M_{xy} = M_0(1 - e^{\frac{-TR}{T_1}})e^{\frac{-TE}{T_2}} \quad (1.32)$$

It is susceptible to losses due to both T_1 and T_2 relaxation. By ensuring that the repetition time, TR, is long enough, and the total echo time, TE, is short enough, the losses are minimized. By comparison, the signal acquired from a STEAM acquisition is governed by[48]:

$$M_{xy} = \frac{M_0}{2}(1 - e^{\frac{-(TR-TM-\frac{TE}{2})}{T_1}})e^{\frac{-TM}{T_1}+\frac{-TE}{T_2}} \quad (1.33)$$

Due to the nature of the stimulated echo, half of the magnetization is lost, giving rise to the $\frac{M_0}{2}$ term. When TR >> (TE + TM), equation 1.33 simplifies to:

$$M_{xy} = \frac{M_0}{2}(1 - e^{\frac{-TR}{T_1}})e^{\frac{-TM}{T_1}+\frac{-TE}{T_2}} \quad (1.34)$$

TM is referred to as the mixing time. It is apparent that STEAM provides half of the potential SNR of PRESS. The SNR can be boosted by increasing the number of acquisitions, or averages, as the SNR is proportional to the square root of the number of averages.

1.7 – J-COUPLING

1.7.1 – J-Coupling Basics

J-coupling, which is also known as scalar or spin-spin coupling, is the interaction between nuclei on the same molecule through their electronic bonds. Systems that are J-coupled can be referred to as weakly J-coupled or strongly J-coupled. This is determined by the inequality:

$$\frac{J}{\delta} \ll 1 \tag{1.35}$$

J, measured in Hz, is referred to as the J-coupling constant and δ is the chemical shift difference between the coupled nuclei in Hz. If the inequality holds, the system is weakly coupled, and if it does not, it is strongly coupled.

When a nucleus exhibits weak J-coupling, it experiences peak splitting with predictable relative amplitudes and periodic signal evolution. Strongly coupled systems have more complex spectral patterns.

To denote the difference between weak and strong J-coupling, a lettering system is used. Letters close together in the alphabet refer to nuclei that are strongly coupled to each other, and letters far apart in the alphabet refer to nuclei that are weakly coupled to each other. For example, an AB spin system has two nuclei that are strongly coupled to each other, while an AX spin system has two nuclei that are weakly coupled to each other.

J-coupling interactions, including peak splitting and signal evolution, are dependent on field strength. A system that is strongly coupled at one field strength may be weakly coupled at another. In addition, the location of the split peaks in ppm will be different at different field strengths, as the J constant is measured in Hz.

J-coupling is guided by a combination of Fermi contact and the Pauli exclusion principle.[49] Fermi contact is the magnetic interaction of a nucleus with a bound electron. S-orbital electrons have a non-zero electron density at the nucleus. Because of this, the electron magnetic moment interacts with the nuclear magnetic moment, which results in slight changes in the energy levels of the nucleus. The nuclear and electronic spins existing in an anti-parallel state is energetically preferred, which means that it has a lower energy.

The Pauli exclusion principle states that two or more spin-½ particles in a quantum system cannot occupy the same quantum state simultaneously. This means that two electrons in an electronic bond will not exist in the same spin state. They will be anti-parallel to each other. If a nucleus is connected to another via an electron bond, being anti-parallel to the other nucleus will be energetically preferred. This is because each nucleus and its bound electron being in an anti-parallel configuration is energetically preferred, and the two electrons must be in an anti-parallel configuration with each other. As a result, the energy state of the nucleus will be lower than if it was alone (no J-coupling). Additionally, the nucleus being parallel to the other nucleus will have a higher energy state than if there was no J-coupling. If the energy state is changed this way, the difference between states will also change, resulting in a change in the Larmor frequency ω_0. The energy diagram is shown in figure 1.17. The change in ω results in peak splitting. In a weakly-coupled system, the peaks will appear on either side of the frequency that the nuclei would have without J-coupling. Each peak will have half of the amplitude of the single peak that would exist without J-coupling. Peak splitting is shown in figure 1.18.

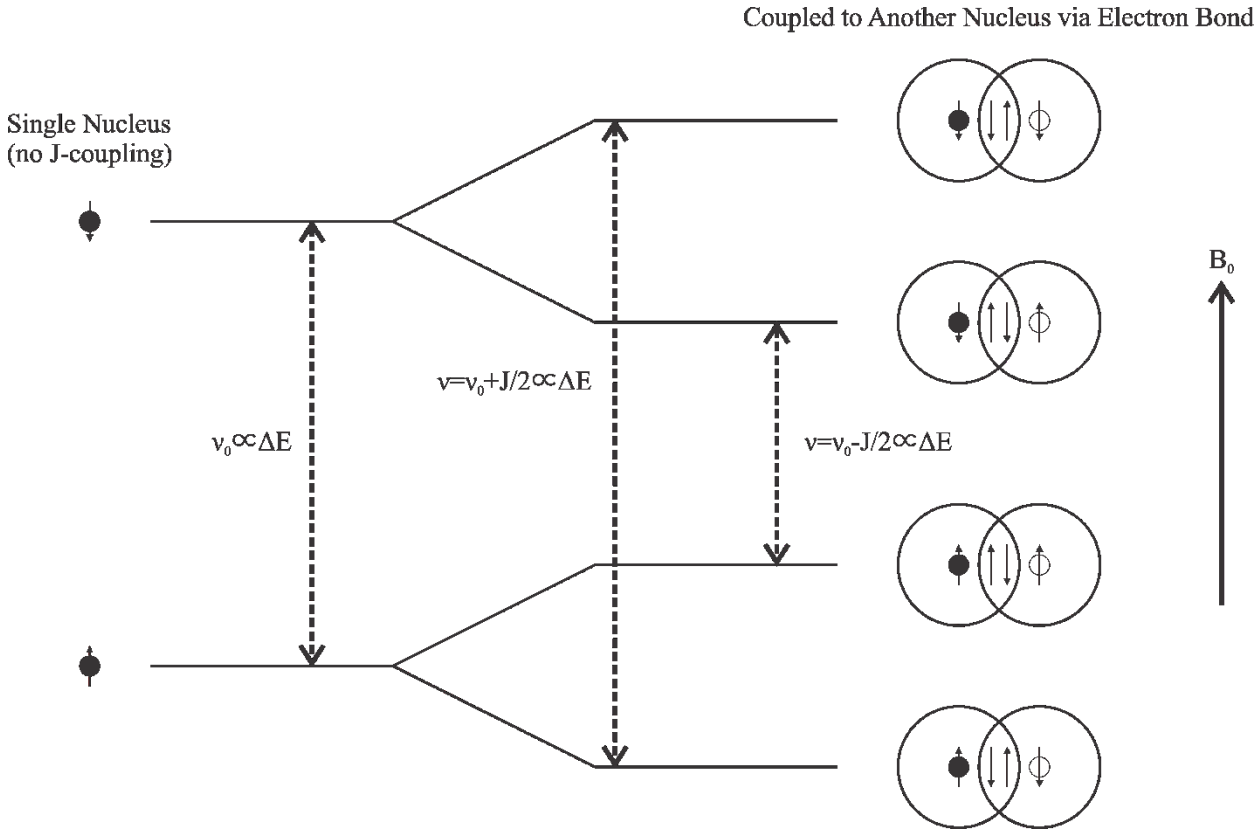

Figure 1.17: Energy level diagram of a single nucleus (no J-coupling), as well as a nucleus coupled to another nucleus via an electronic bond. (adapted from De Graaf[49])

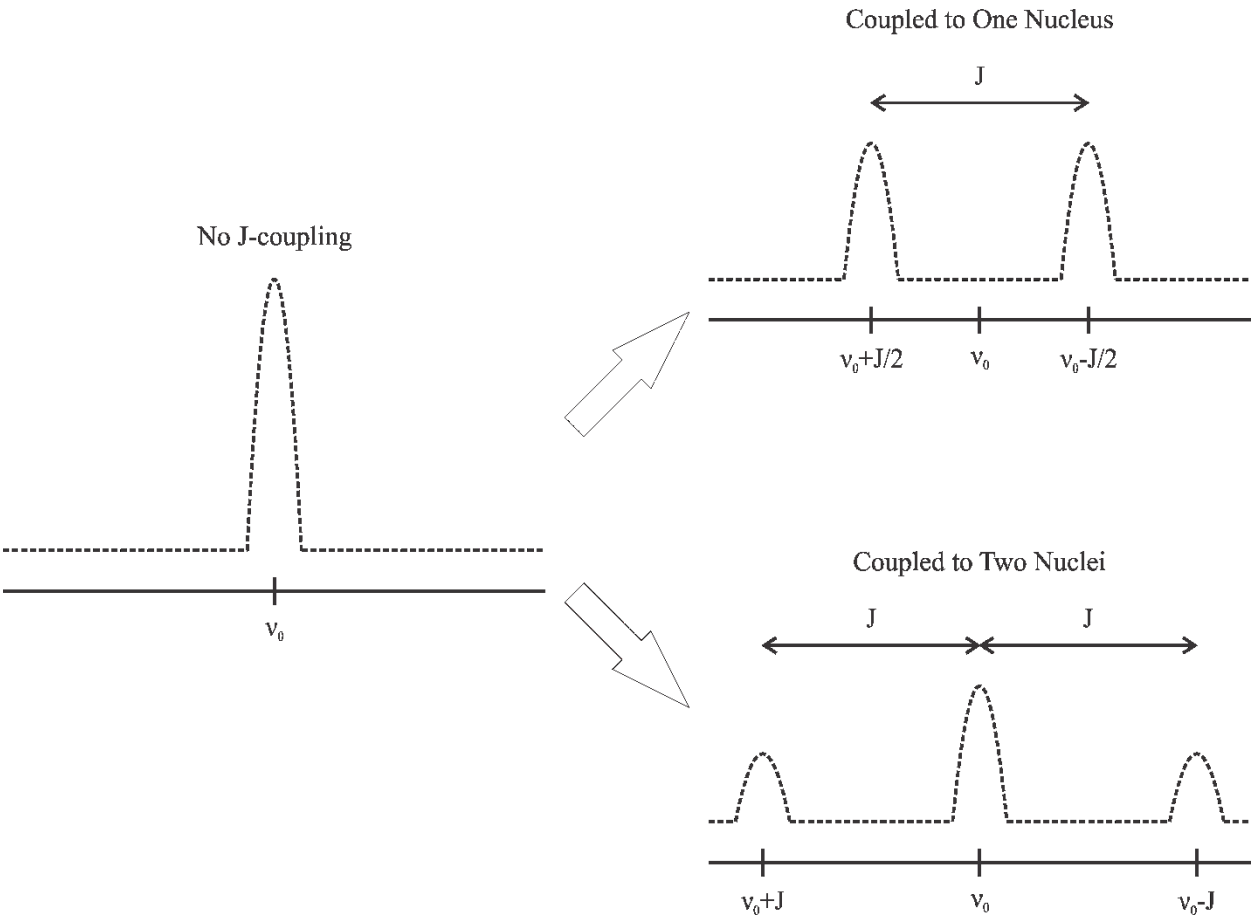

Figure 1.18: The spectra of a nucleus with no J-coupling, weak coupling to one other nucleus, and weak coupling to two other nuclei, shown with peak splitting associated with J-coupling.

If a nucleus is weakly coupled to more than one nucleus, the signal will split into $n + 1$ peaks, with n being the number of magnetically equivalent nuclei that it is coupled to. The amplitudes of the split peaks will follow a binomial distribution. For example, a nucleus coupled to 2 other nuclei will have 3 peaks, with relative amplitudes of 1-2-1.

In addition to peak splitting, J-coupling results in signal modulation with time. This is because the coherences (or magnetizations) that precess faster or slower (with a higher or lower

Larmor frequency ω_0) will continue to do so following an excitation pulse until they are out of phase, resulting in a smaller and, eventually, negative peak. A weakly coupled spin A, coupled to a spin X, will respond to a spin echo as follows after excitation with a 90°$_Y$ RF pulse[50]:

$$A_X \rightarrow A_X \cos(\pi J T_E) + 2A_Y X_Z \sin(\pi J T_E) \tag{1.36}$$

A_X is referred to as an in-phase coherence, in which the resonances are aligned along the same axis (x-axis). $2A_Y X_Z$ is referred to as an anti-phase A coherence with respect to X. This can be visualized as two resonances that are along opposite axes and 90° out of phase with A_X. At a T_E of odd multiples of $\frac{1}{2J}$, only $\pm 2A_Y X_Z$ remains, and at multiples of $\frac{1}{J}$, only $\pm A_X$ remains. Figure 1.19 demonstrates signal modulation with weak J-coupling.

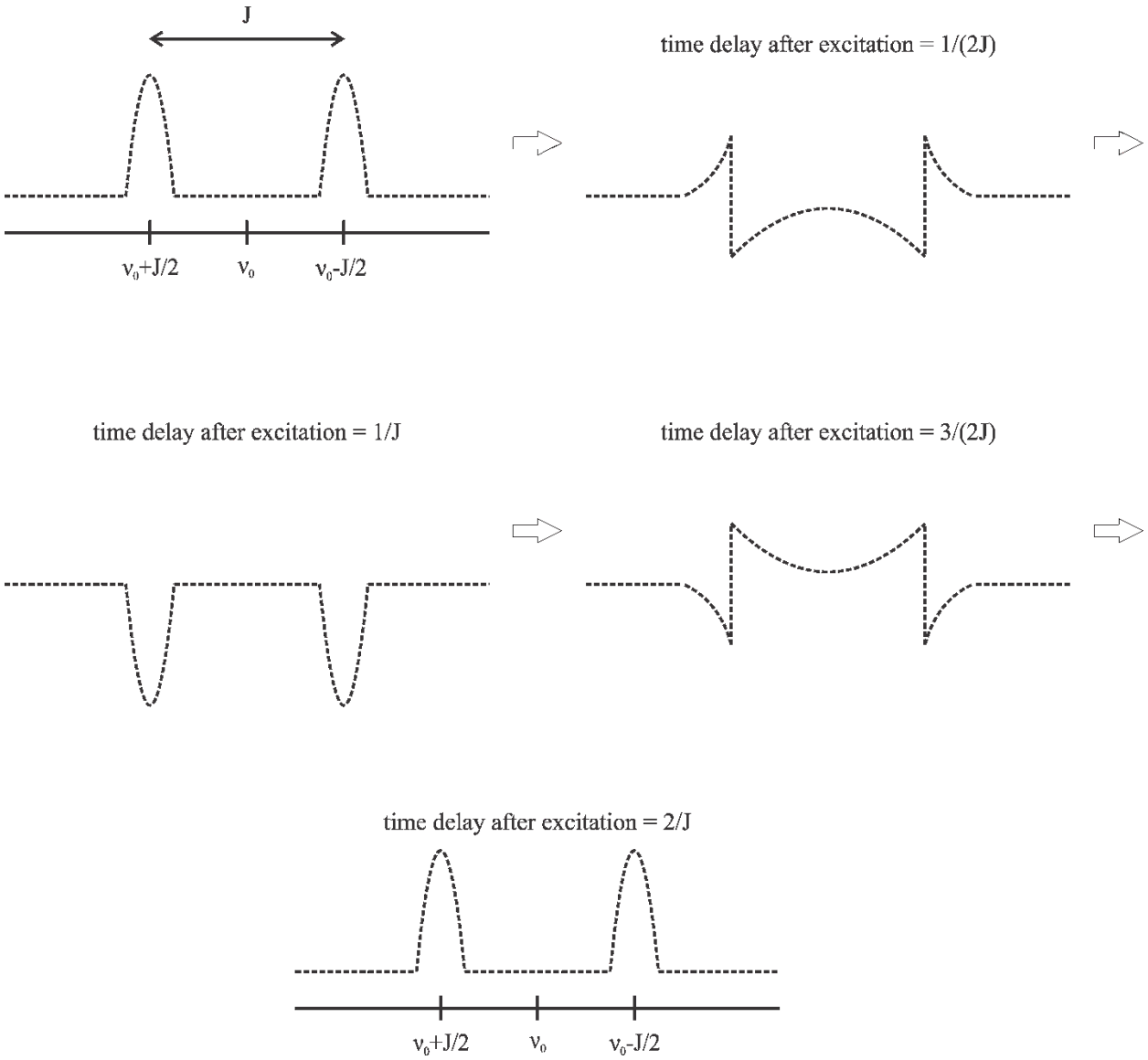

Figure 1.19: Signal modulation due to weak J-coupling.

The evolution of a strong coupled system is more complex because far more coherences can evolve.[51] For example, in an AB spin system, the coherence state A_X following a 90°$_Y$ RF pulse can evolve during a spin echo into $2A_ZB_X$, $2A_ZB_Y$, B_X and B_Y coherences, in addition to the A_X and $2A_YB_Z$ coherences. $2A_ZB_X$ and $2A_ZB_Y$ are anti-phase B coherences with respect to A. B_X

and B_Y are in-phase coherences for B. That is, polarization transfer occurs from the A spin to the B spin. As such, neither peak splitting nor temporal signal modulation are straightforward or easily predicted analytically. Advanced numerical techniques can be used to assess the responses of complex strongly-coupled spin systems, as discussed in chapter 2.

1.7.2 – Homonuclear vs Heteronuclear J-Coupling

Homonuclear J-coupling refers to coupling between two nuclei of the same species. For example, J-coupling between two ^{1}H nuclei is a case of homonuclear coupling (^{1}H-^{1}H J-coupling with J constant J_{HH}). Heteronuclear J-coupling refers to J-coupling between two different species of nuclei. For example, J-coupling between a ^{1}H nucleus and a ^{13}C nucleus would be a case of heteronuclear J-coupling (^{1}H-^{13}C J-coupling with J constant J_{CH}). Both homonuclear and heteronuclear J-coupling can happen simultaneously, and this will cause two splits in the signal peaks, one guided by J_{HH} and one guided by J_{CH} as shown in figure 1.20. It is also worth noting that homonuclear J-coupling evolution is not refocused by a spin echo sequence, whereas heteronuclear J-coupling evolution can be.

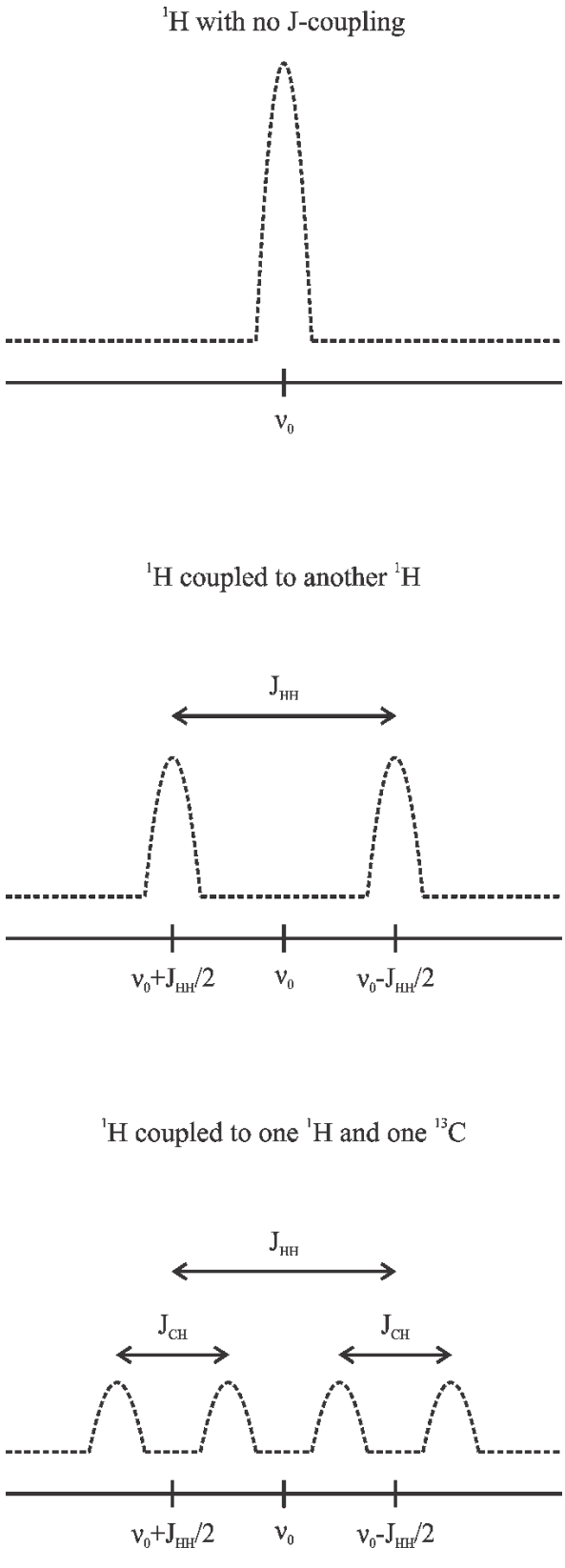

Figure 1.20: Heteronuclear J-coupling.

1.8 – J-COUPLING EVOLUTION DURING PRESS

J-coupling can cause changes in the NMR signal, both in peak splitting and in modulation of the signal. The latter is temporal in nature, as the more time has passed, the more modulation will occur. When it comes to PRESS, the relevant timing parameters are TE_1 and TE_2. As mentioned, homonuclear J-coupling is not refocused by a spin echo, so modulation will occur during both TE_1 and TE_2. In addition to that, for strongly coupled spin systems, modulation will happen differently during TE_1 than TE_2, ie. signal response can be different for a (TE_1, TE_2) combination of (20 ms, 40 ms) than for (40 ms, 20 ms), despite having the same total TE of 60 ms. This is due to polarization transfer that happens during strong J-coupling evolution. The spin response also depends on the length/bandwidth of the RF pulses, and on pulse shape imperfections. Perfectly square slice-selective pulses cannot be achieved, as a temporal sinc pulse cannot be made infinite in length. This causes irregularities in the slice-selection, resulting in changes in line shape and intensity.[11]

Spatial interference effects, also known as voxel shift effects, also affects the signal response.[52] When a voxel is excited with PRESS, each dimension Δx can be calculated as:

$$\Delta x = \frac{\Delta\omega}{\gamma G} \tag{1.37}$$

$\Delta\omega$ is the pulse bandwidth, and G is the gradient strength. This assumes a homogenous sample of spins that all have the same ω. However, the chemical shift effect causes the voxel location to shift slightly for nuclei of different chemical shifts. A chemical shift of δ will result in a slice or voxel shifted away from the expected location by ΔVS according to:

$$\frac{\Delta VS}{\Delta x} = \frac{\delta \gamma B_0}{\Delta \omega} \tag{1.38}$$

This effect is more pronounced for weakly-coupled spins because they have a larger δ. This comes from the inequality in equation 1.35, which holds true for weakly-coupled systems. For a spin A that is weakly coupled to spin X, the effective X voxel will be shifted. The shift also happens for strongly-coupled systems but to a lesser degree. This results in three distinct regions for each refocusing pulse: one in which only the A spin experiences the pulse, one in which only the X spin does, and one in which they both do. This results in a complex signal that is made up of different signals from each of the three regions, with the size of each one dependent on the δ, G, and $\Delta\omega$ of the RF pulses.

1.9 – SPECTRAL EDITING WITH OPTIMAL-TE PRESS

Spectral editing can alleviate the challenge of overlapping resonance by seeking to suppress one signal that is overlapping our signal of interest. Most spectral editing methods rely on a differences in J-coupling evolution of different spin systems. One such method is optimal-TE PRESS.[4] The timings TE_1 and TE_2 of PRESS can be selected such that J-coupling modulation of a contaminating signal results in minimal signal, while J-coupling modulation of the signal of interest results in adequate signal for quantification (in the case of an uncoupled spins, there will be no J-coupling modulation). The resulting spectrum will be mostly, or completely, composed of the signal of interest, which can then be measured directly. A simple example of spectral editing is shown in figure 1.21. In this figure, it is assumed that a timing was found in which the contaminating signal had a response that was close to zero.

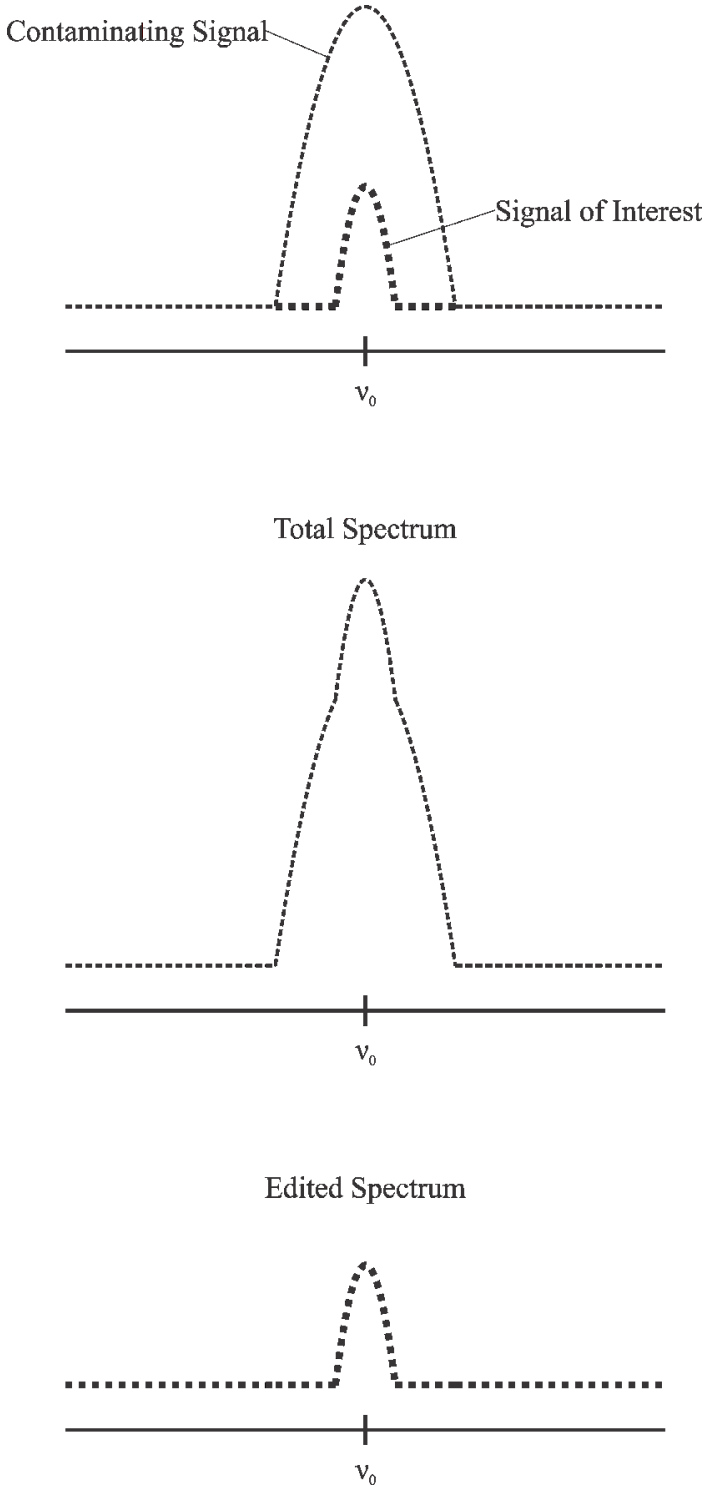

Figure 1.21: Illustration of spectral editing, with a large contaminating signal suppressed to reveal a smaller signal of interest. A timing that results in low signal for the contaminating signal is assumed.

1.10 – BENEFITS OF HIGH FIELD NMR

Clinical MRI magnets typically have field strengths 1.5 T, with some as high as 3.0 T. However, higher field strengths are in use for research purposes. With higher field strengths, it is advantageous to have a smaller bore, to minimize magnetic field inhomogeneities. As such, many high field magnets are restricted to use on animals, such as rats or mice. 9.4 T studies on rats are fairly common.[25-31]

The benefits of a higher magnetic field strength, B_0, includes improvements to *in-vivo* SNR and spectral resolution. The former comes from the fact that signal voltage is directly proportional to $M_0\omega_0$, which are each proportional to B_0. Assuming sample-dominated losses, noise voltage is proportional to $\sqrt{R}$, where R is the resistance of the sample as seen by the coil.[53] R is proportional to ${\omega_0}^2$, and ω_0 is proportional to B_0. This makes *in-vivo* SNR roughly linearly dependent on B_0. The improvement to spectral resolution comes from the chemical shift effect. Equation 1.23 shows that as B_0 goes up, the difference between the resonance frequencies of two peaks will go up proportionally.

1.11 – ^{13}C MRS

While ^{1}H is the most common nucleus in *in-vivo* MRS due to the abundance of ^{1}H nuclei in biological systems, other types of nuclei may also be utilized. Another option is ^{13}C, which is less often used. An advantage of ^{13}C MRS is the increase in spectral resolution due to a larger range of chemical shifts.[54] Challenges of ^{13}C include a lower natural isotopic abundance (around

1.1%, instead of 99% for ^{1}H), leading to a lower biological signal, as ^{12}C is the most common isotope and has no net spin, and, therefore, no NMR signal. This can, however, be turned to advantage. The natural isotopic abundance of ^{13}C can be exploited by injecting a ^{13}C-labelled substrate into a living system. Substrates can be enriched such that the fraction of ^{13}C isotopes on the substrate are much higher, up to 99 %. Infusing said substrate and measuring the increase of ^{13}C nuclei in the metabolic products over time allows for measures of metabolic rates to be attained.[3]

^{13}C has a lower inherent SNR owing to a lower gyromagnetic ratio of 2π x 10.7 x 10^6 rad·s^{-1}·T^{-1}, which is about one-fourth that of ^{1}H at 2π x 42.6 x 10^6 rad·s^{-1}·T^{-1}. As mentioned in section 1.10, signal voltage is directly proportional to $M_0\omega_0$. From equation 1.16, M_0 is directly proportional to γ^2, and from equation 1.9, ω_0 is directly proportional to γ. This gives signal voltage an overall dependence on γ^3. Assuming sample-dominated losses *in vivo*, noise voltage is dependent on γ, giving an overall dependence of SNR on γ^2. For ^{13}C, this is approximately $\frac{1}{16}$ of ^{1}H. This is an issue, but it can be improved with a few different techniques. Direct ^{13}C MRS can be improved by techniques such as Distortionless Enhancement by Polarization Transfer (DEPT).[55] DEPT is performed by exciting the ^{1}H nuclei that are coupled to ^{13}C nuclei of interest with a ^{1}H RF pulse. A combination of ^{1}H and ^{13}C pulses are then applied prior to signal acquisition. The result is a transfer of spin polarization from the ^{1}H nuclei to the ^{13}C nuclei, which increases the ^{13}C SNR by a factor related to the ratio of γ values (≈ 4).

Indirect methods can also be used to measure ^{13}C labelling where the signal comes from the ^{1}H nuclei coupled to the ^{13}C nuclei. One such method is Proton-Observed Carbon-Edited (POCE).[22] A ^{1}H pulse sequence, such as a simple spin echo is applied, and a ^{13}C channel is utilized

for editing. The 180° ^{1}H pulse is set with a time delay (TE/2) of $\frac{1}{2J}$ after the excitation pulse (alternatively, TE = $\frac{1}{J}$). A 180° ^{13}C pulse is applied simultaneously with the 180° ^{1}H pulse, alternating on and off between each acquisition. When it is on, J-coupling is not refocused, and the ^{13}C-coupled ^{1}H signal is inverted. When it is off, J-coupling is refocused, and the signal is upright. Subtraction then removes signal from any non-^{13}C-coupled ^{1}H signal, while doubling the ^{13}C-bonded signal.

Another consideration is the Larmor frequency of ^{13}C, which is 100.6 Hz at 9.4 T, compared to ^{1}H, which is 400.4 Hz at 9.4 T. On its own, this is not an issue, but if one wishes to study ^{13}C nuclei on an MRI system that does not have multinuclear capabilities, additional hardware including an RF amplifier and a ^{13}C coil will need to be added to the system. Adding ^{13}C capability is costly. However, indirect ^{13}C MRS can be done without a ^{13}C channel, by using the satellite peaks created from heteronuclear coupling between ^{1}H and ^{13}C.[20] This can be done by using a ^{1}H MRS sequence such as PRESS to acquire a baseline spectrum before starting the infusion. Subsequent spectra are then acquire throughout the infusion and subtracted from the baseline scan. The subtraction serves to remove any contaminating signals to reveal the increase in the ^{13}C-coupled signals or satellite peaks, as well as the decrease in the non-^{13}C-coupled signal. A simple illustration of this is shown in figure 1.22.

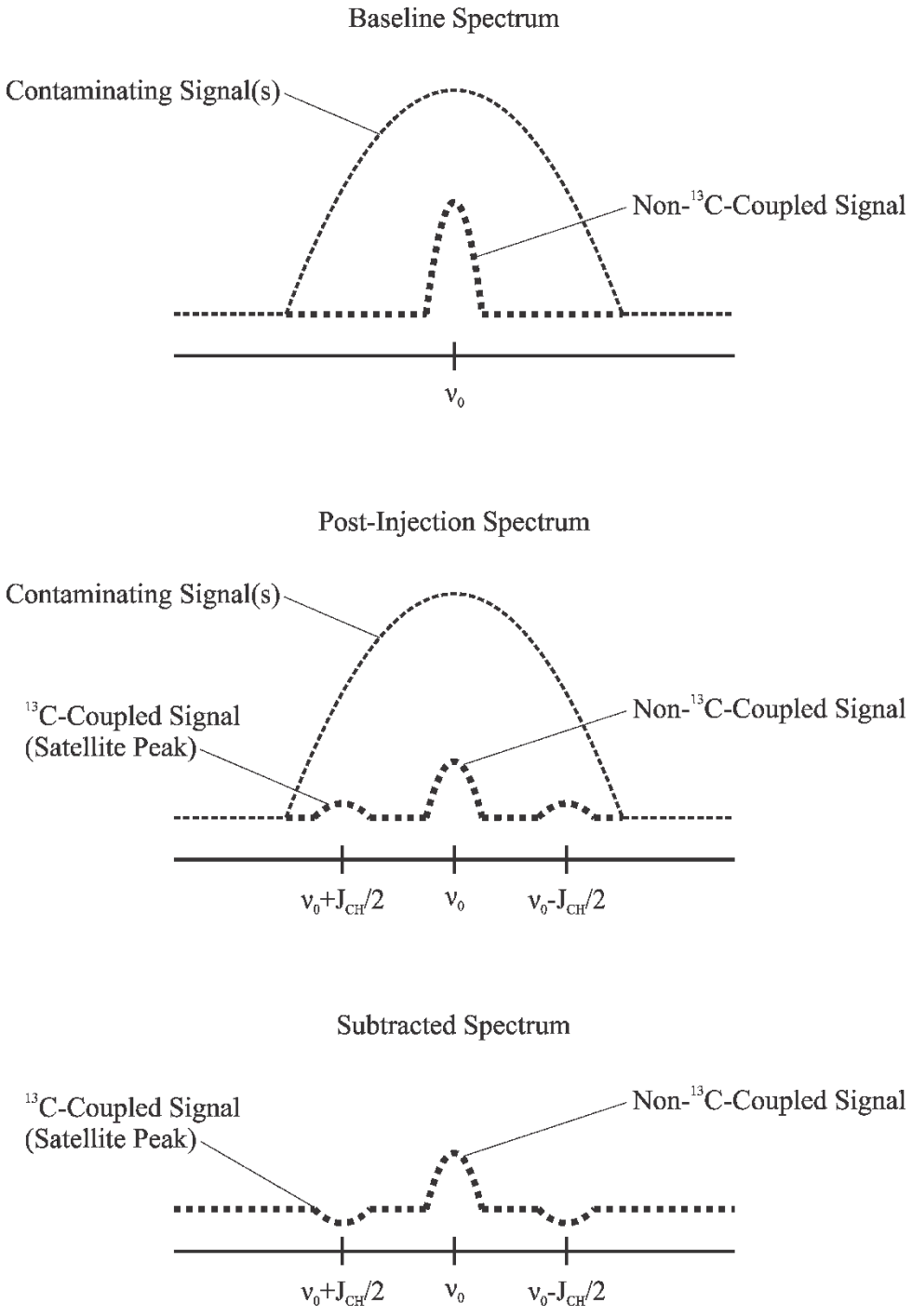

Figure 1.22: Simple example of indirect ^{13}C MRS with ^{1}H PRESS. The post-injection spectrum is subtracted from the baseline spectrum to remove the contaminating signal(s) and visualize the decrease in the non-^{13}C-coupled signal as well as the increase in the ^{13}C-coupled signals or satellite peaks.

When deciding between the various ^{13}C MRS methods, the most important factors are often SNR and spectral resolution. As mentioned, direct ^{13}C detection methods benefit from a better spectral resolution, which decreases overlap of resonances. In particular, direct ^{13}C detection enables better separation between $^{13}C_4$-glutamate and $^{13}C_4$-glutamine, which is important for dynamic studies.[17] However, indirect ^{13}C measurements through ^{1}H detection have the advantage of higher SNR.

1.12 – REFERENCES

1. Ramadan S, Lin A, Stanwell P. Glutamate and glutamine: a review of in vivo MRS in the human brain. *NMR in Biomedicine.* 2013;26(12):1630-1646.

2. Bottomley PA. Selective volume method for performing localized NMR spectroscopy. U.S. patent 4,480,228; 1984.

3. Frahm J, Merboldt K-D, Hänicke W. Localized proton spectroscopy using stimulated echoes. *Journal of Magnetic Resonance.* 1987;72:502-508.

4. Snyder J, Wilman A. Field strength dependence of PRESS timings for simultaneous detection of glutamate and glutamine from 1.5 to 7T. *Journal of Magnetic Resonance.* 2010;203(1):66-72.

5. Ganji SK, An Z, Tiwari V, et al. In vivo detection of 2-hydroxyglutarate in brain tumors by optimized point-resolved spectroscopy (PRESS) at 7T. *Magnetic Resonance in Medicine.* 2017;77(3):936-944.

6. Ganji SK, An Z, Banerjee A, Madan A, Hulsey KM, Choi C. Measurement of regional variation of GABA in the human brain by optimized point-resolved spectroscopy at 7 T in vivo. *NMR in Biomedicine.* 2014;27(10):1167-1175.

7. Choi C, Ganji SK, DeBerardinis RJ, et al. 2-hydroxyglutarate detection by magnetic resonance spectroscopy in IDH-mutated patients with gliomas. *Nature Medicine.* 2012;18(4):624.

8. Choi C, Ganji SK, DeBerardinis RJ, et al. Measurement of glycine in the human brain in vivo by 1H-MRS at 3 T: application in brain tumors. *Magnetic Resonance in Medicine.* 2011;66(3):609-618.

9. Choi C, Douglas D, Hawesa H, Jindal A, Storey C, Dimitrov I. Measurement of glycine in human prefrontal brain by point-resolved spectroscopy at 7.0 tesla in vivo. *Magnetic Resonance in Medicine.* 2009;62:1305-1310.

10. Choi C, Dimitrov IE, Douglas D, et al. Improvement of resolution for brain coupled metabolites by optimized 1H MRS at 7 T. *NMR in Biomedicine.* 2010;23(9):1044-1052.

11. Thompson RB, Allen PS. Sources of variability in the response of coupled spins to the PRESS sequence and their potential impact on metabolite quantification. *Magnetic Resonance in Medicine.* 1999;41(6):1162-1169.

12. Bogner W, Hangel G, Esmaeili M, Andronesi OC. 1D-spectral editing and 2D multispectral in vivo1H-MRS and 1H-MRSI-Methods and applications. *Analytical biochemistry.* 2017;529:48-64.

13. Govindaraju V, Young K, Maudsley AA. Proton NMR chemical shifts and coupling constants for brain metabolites. *NMR in Biomedicine.* 2000;13(3):129-153.
14. Waagepetersen HS, Sonnewald U, Schousboe A. Compartmentation of glutamine, glutamate, and GABA metabolism in neurons and astrocytes: functional implications. *The Neuroscientist.* 2003;9(5):398-403.
15. Meldrum BS. Glutamate as a neurotransmitter in the brain: review of physiology and pathology. *The Journal of Nutrition.* 2000;130(4):1007S-1015S.
16. Horská A, Barker PB. Imaging of brain tumors: MR spectroscopy and metabolic imaging. *Neuroimaging Clinics of North America.* 2010;20(3):293-310.
17. de Graaf RA, Rothman DL, Behar KL. State of the art direct 13C and indirect 1H-[13C] NMR spectroscopy in vivo. A practical guide. *NMR in Biomedicine.* 2011;24(8):958-972.
18. Wijnen JP, Van der Graaf M, Scheenen TW, et al. In vivo 13C magnetic resonance spectroscopy of a human brain tumor after application of 13C-1-enriched glucose. *Magnetic Resonance Imaging.* 2010;28(5):690-697.
19. Maher EA, Marin-Valencia I, Bachoo RM, et al. Metabolism of [U-13C] glucose in human brain tumors in vivo. *NMR in Biomedicine.* 2012;25(11):1234-1244.
20. Boumezbeur F, Besret L, Valette J, et al. NMR measurement of brain oxidative metabolism in monkeys using 13C-labeled glucose without a 13C radiofrequency channel. *Magnetic Resonance in Medicine.* 2004;52(1):33-40.
21. Pfeuffer J, Tkáč I, Choi IY, et al. Localized in vivo 1H NMR detection of neurotransmitter labeling in rat brain during infusion of [1-13C] D-glucose. *Magnetic Resonance in Medicine.* 1999;41(6):1077-1083.
22. Bendall M, Pegg D, Doddrell D, Field J. NMR of protons coupled to carbon-13 nuclei only. *Journal of the American Chemical Society.* 1981;103(4):934-936.
23. Ocali O, Atalar E. Ultimate intrinsic signal-to-noise ratio in MRI. *Magnetic Resonance in Medicine.* 1998;39(3):462-473.
24. Yang S, Hu J, Kou Z, Yang Y. Spectral simplification for resolved glutamate and glutamine measurement using a standard STEAM sequence with optimized timing parameters at 3, 4, 4.7, 7, and 9.4 T. *Magnetic Resonance in Medicine.* 2008;59(2):236-244.
25. Wang WT, Lee P, Yeh HW, Smirnova IV, Choi IY. Effects of acute and chronic hyperglycemia on the neurochemical profiles in the rat brain with streptozotocin-induced diabetes detected using in vivo 1H MR spectroscopy at 9.4 T. *Journal of Neurochemistry.* 2012;121(3):407-417.
26. Tkac I, Dubinsky JM, Keene CD, Gruetter R, Low WC. Neurochemical changes in Huntington R6/2 mouse striatum detected by in vivo 1H NMR spectroscopy. *Journal of Neurochemistry.* 2007;100(5):1397-1406.
27. Rao R, Tkac I, Townsend EL, Gruetter R, Georgieff MK. Perinatal iron deficiency alters the neurochemical profile of the developing rat hippocampus. *The Journal of Nutrition.* 2003;133(10):3215-3221.
28. Raman L, Tkac I, Ennis K, Georgieff MK, Gruetter R, Rao R. In vivo effect of chronic hypoxia on the neurochemical profile of the developing rat hippocampus. *Developmental Brain Research.* 2005;156(2):202-209.
29. Öz G, Nelson CD, Koski DM, et al. Noninvasive detection of presymptomatic and progressive neurodegeneration in a mouse model of spinocerebellar ataxia type 1. *Journal of Neuroscience.* 2010;30(10):3831-3838.
30. Marjanska M, Curran GL, Wengenack TM, et al. Monitoring disease progression in transgenic mouse models of Alzheimer's disease with proton magnetic resonance spectroscopy. *Proceedings of the National Academy of Sciences of the United States of America.* 2005;102(33):11906-11910.

31. Choi IY, Seaquist ER, Gruetter R. Effect of hypoglycemia on brain glycogen metabolism in vivo. *Journal of Neuroscience Research.* 2003;72(1):25-32.

32. Xin L, Gambarota G, Duarte J, Mlynárik V, Gruetter R. Direct in vivo measurement of glycine and the neurochemical profile in the rat medulla oblongata. *NMR in Biomedicine.* 2010;23(9):1097-1102.

33. Van Eijsden P, Behar KL, Mason GF, Braun KP, De Graaf RA. In vivo neurochemical profiling of rat brain by 1H-[13C] NMR spectroscopy: cerebral energetics and glutamatergic/GABAergic neurotransmission. *Journal of Neurochemistry.* 2010;112(1):24-33.

34. Tkáč I, Rao R, Georgieff MK, Gruetter R. Developmental and regional changes in the neurochemical profile of the rat brain determined by in vivo 1H NMR spectroscopy. *Magnetic Resonance in Medicine.* 2003;50(1):24-32.

35. Pfeuffer J, Tkáč I, Provencher SW, Gruetter R. Toward an in vivo neurochemical profile: quantification of 18 metabolites in short-echo-time 1 H NMR spectra of the rat brain. *Journal of Magnetic Resonance.* 1999;141(1):104-120.

36. Gambarota G, Xin L, Perazzolo C, Kohler I, Mlynárik V, Gruetter R. In vivo 1H NMR measurement of glycine in rat brain at 9.4 T at short echo time. *Magnetic Resonance in Medicine.* 2008;60:727-731.

37. Sanaei Nezhad F, Anton A, Parkes LM, Deakin B, Williams SR. Quantification of glutathione in the human brain by MR spectroscopy at 3 Tesla: Comparison of PRESS and MEGA-PRESS. *Magnetic Resonance in Medicine.* 2017;78(4):1257-1266.

38. Gil AM, de Pinho PG, Monteiro MS, Duarte IF. NMR metabolomics of renal cancer: an overview. *Bioanalysis.* 2015;7(18):2361-2374.

39. Gao H, Dong B, Jia J, et al. Application of ex vivo 1 H NMR metabonomics to the characterization and possible detection of renal cell carcinoma metastases. *Journal of Cancer Research and Clinical Oncology.* 2012;138(5):753-761.

40. Terrier F, Lazeyras F, Posse S, et al. Study of acute renal ischemia in the rat using magnetic resonance imaging and spectroscopy. *Magnetic Resonance in Medicine.* 1989;12(1):114-136.

41. Crozier S, Cowin G, Endre ZH. MR microscopy and microspectroscopy of the intact kidney. *Concepts in Magnetic Resonance Part A.* 2004;22(1):50-59.

42. Cowin G, Leditschke I, Crozier S, Brereton I, Endre Z. Regional proton nuclear magnetic resonance spectroscopy differentiates cortex and medulla in the isolated perfused rat kidney. *Magnetic Resonance Materials in Physics, Biology and Medicine.* 1997;5(2):151-158.

43. Xu S, Ji Y, Chen X, Yang Y, Gullapalli RP, Masri R. In vivo high-resolution localized 1H MR spectroscopy in the awake rat brain at 7 T. *Magnetic Resonance in Medicine.* 2013;69(4):937-943.

44. Hofmann L, Slotboom J, Boesch C, Kreis R. Characterization of the macromolecule baseline in localized 1H-MR spectra of human brain. *Magnetic Resonance in Medicine.* 2001;46(5):855-863.

45. Gottschalk M, Troprès I, Lamalle L, Grand S, Le Bas JF, Segebarth C. Refined modelling of the short-T2 signal component and ensuing detection of glutamate and glutamine in short-TE, localised, 1H MR spectra of human glioma measured at 3 T. *NMR in Biomedicine.* 2016.

46. Moonen CT, Kienlin MV, Van Zijl PC, et al. Comparison of single-shot localization methods (STEAM and PRESS) for in vivo proton NMR spectroscopy. *NMR in Biomedicine.* 1989;2(5-6):201-208.

47. Träber F, Block W, Lamerichs R, Gieseke J, Schild HH. 1H metabolite relaxation times at 3.0 tesla: Measurements of T1 and T2 values in normal brain and determination of regional differences in transverse relaxation. *Journal of Magnetic Resonance Imaging.* 2004;19(5):537-545.

48. Helms G. Analysis of 1.5 Tesla proton MR spectra of human brain using LCModel and an imported basis set. *Magnetic Resonance Imaging.* 1999;17(8):1211-1218.

49. De Graaf RA. *In vivo NMR spectroscopy: principles and techniques.* Wiley; 2019.

50. De Graaf RA, Rothman DL. In vivo detection and quantification of scalar coupled 1H NMR resonances. *Concepts in Magnetic Resonance.* 2001;13(1):32-76.

51. Kay LE, McClung R. A product operator description of AB and ABX spin systems. *Journal of Magnetic Resonance.* 1988;77(2):258-273.

52. Yablonskiy DA, Neil JJ, Raichle ME, Ackerman JJ. Homonuclear J coupling effects in volume localized NMR spectroscopy: pitfalls and solutions. *Magnetic Resonance in Medicine.* 1998;39(2):169-178.

53. Hoult D, Lauterbur PC. The sensitivity of the zeugmatographic experiment involving human samples. *Journal of Magnetic Resonance.* 1979;34(2):425-433.

54. Kurhanewicz J, Bok R, Nelson SJ, Vigneron DB. Current and potential applications of clinical 13C MR spectroscopy. *Journal of Nuclear Medicine.* 2008;49(3):341-344.

55. Doddrell D, Pegg D, Bendall MR. Distortionless enhancement of NMR signals by polarization transfer. *Journal of Magnetic Resonance.* 1982;48(2):323-327.

Chapter 2 - Background Information and Methodology

2.1 – METABOLITES

2.1.1 - Glycine

Glycine (Gly) is an amino acid that acts as the primary *inhibitory* neurotransmitter in the spinal cord.[1] That is, it acts to *decrease* the probability of an action potential, which is the mechanism for nervous transmission.[2] As an amino acid, it is involved in protein synthesis.[3] In this form, its molecular structure is NH_2-CH_2-COOH. However, when it exists unbound in solution at physiological pH, it takes a zwitterionic form, which is that of an ion with an overall neutral charge. In this form, its molecular structure is NH_3^+-CH_2-COO^-. From an NMR perspective, Gly has two protons bound to the C_2 carbon that both resonate at ≈ 3.55 ppm.[4] Also of note is that the signal from these protons does not exhibit peak splitting or modulation due to J-coupling.[4] Figure 2.1 illustrates the molecular structure, with the relevant protons highlighted and labelled with their chemical shift. In this thesis, the concentration of Gly is measured in rat brain.

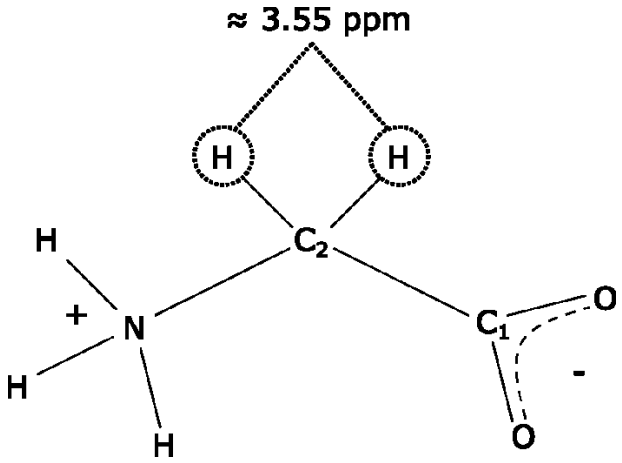

Figure 2.1: The molecular structure of Gly, with the chemical shift of the C_2 protons labelled.

2.1.2 – *myo*-Inositol

myo-Inositol (Ins) is a carbocyclic sugar that is involved in the mediation of cell signal transduction, as well as in osmoregulation, the maintenance of osmotic pressure.[5] It is a six-carbon ring, with each carbon connected to a proton and a hydroxyl (OH) group.[6] It has six protons that contribute to its NMR spectrum, with two of them (C_1 and C_3 protons) resonating at ≈ 3.52 ppm and two (C_4 and C_6 protons) resonating at ≈ 3.61 ppm.[4] The C_2 and C_5 protons resonate at ≈ 4.05 ppm and ≈ 3.27 ppm, respectively.[4] Each of these protons experiences J-coupling interactions with their nearest neighbour protons. The J-coupling constants are 2.889 Hz, 3.006 Hz, 9.997 Hz, 9.485 Hz, 9.482 Hz, and 9.998 Hz for the C_1-C_2, C_2-C_3, C_3-C_4, C_4-C_5, C_5-C_6, and C_6-C_1 protons, respectively.[4] As such, Ins is considered an AM_2N_2X spin system at 9.4 T, with the C_5 proton as the A spin, the C_4 and C_6 protons as the M spins, the C_1 and C_3 protons as the N spins, and the C_2 proton as the X spin. The chemical shift and scalar coupling constants were provided by Govindaraju et al.[4] Figure 2.2 shows the molecular structure, with the relevant protons labelled with their chemical shifts. In this thesis, the relative concentration of Ins is measured in rat kidney.

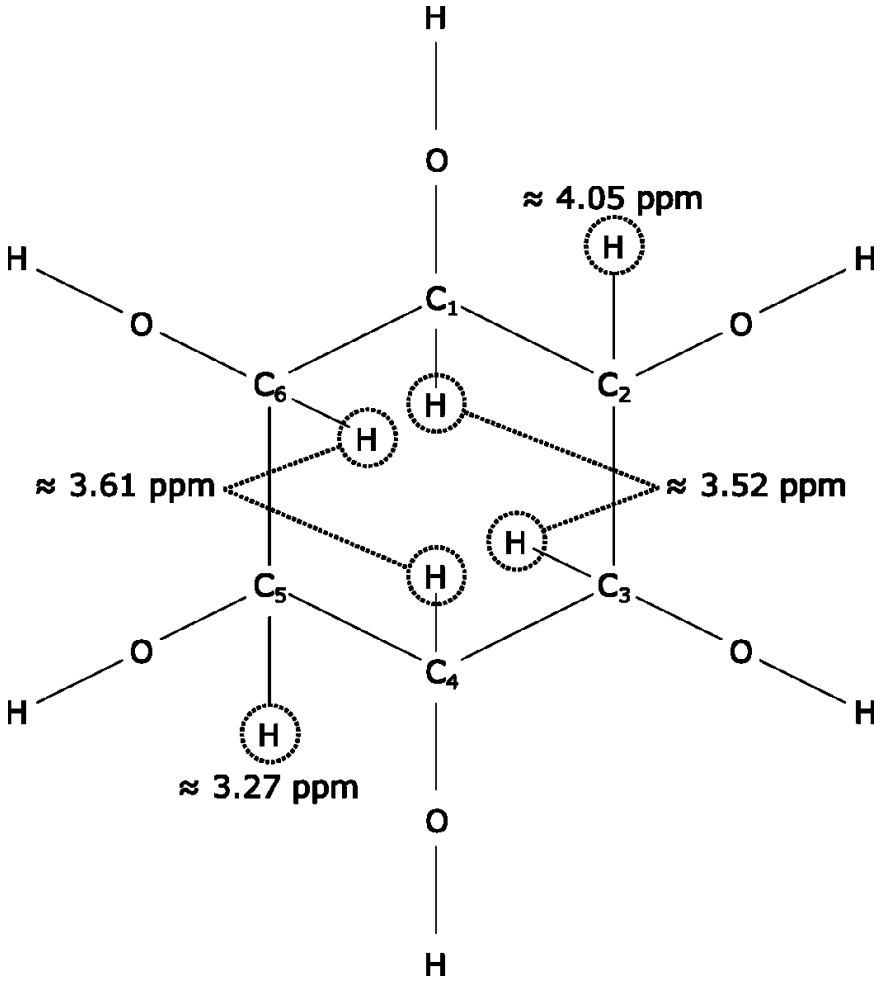

Figure 2.2: The molecular structure of Ins, with the chemical shifts of the protons labelled.

2.1.3 - Glutamate

Glutamate (Glu or ^{12}C-Glu) is an anion of glutamic acid, an amino acid.[7] It is involved in nucleotide synthesis and in energy metabolism, being linked to the tricarboxylic acid (TCA) cycle through transamination with α-ketoglutarate (αKG).[8] Glutamic acid has the form HOOC-$CH(NH_2)$-$(CH_2)_2$-COOH. At physiological pH in solution, Glu has the form $^-$OOC-$CH(NH_3^+)$-$(CH_2)_2$-COO^-. In this form, Glu functions as the primary *excitatory* neurotransmitter in the central

nervous system.[9] As such, it acts to *increase* the probability of an action potential. The NMR signals come from the C_2, C_3, and C_4 protons. The C_2 proton resonates at ≈ 3.74 ppm, the two C_3 protons resonate at ≈ 2.04 ppm (C_3) and ≈ 2.12 ppm (C_3'), and the two C_4 protons resonate at ≈ 2.34 ppm (C_4) and ≈ 2.35 ppm (C_4').[4] These protons all exhibit J-coupling interactions. The C_2 proton is coupled to the C_3 protons with J-coupling constants of 7.331 Hz (C_3) and 4.651 Hz (C_3').[4] The C_3 protons are coupled to the C_4 protons with constants of 8.406 Hz (C_3-C_4'), 6.875 Hz (C_3'-C_4'), 6.413 Hz (C_3-C_4), and 8.478 Hz (C_3'-C_4).[4] The C_3 protons are also coupled to each other with a constant of -14.849 Hz.[4] Similarly, the C_4 protons are coupled to each other with a constant of -15.915 Hz.[4] As such, Glu is considered an AMNPQ spin system at 9.4 T, with the C_2 proton as the A spin, the C_3 protons as the M and N spins, and the C_4 protons as the P and Q spins. The chemical shift and scalar coupling constants were provided by Govindaraju et al.[4] Figure 2.3 shows the molecular structure of Glu, with the relevant protons labelled with their chemical shifts. In this thesis, the concentration of Glu is measured in rat brain, and the relative concentration of Glx (Glu + Gln) is measured in rat kidney.

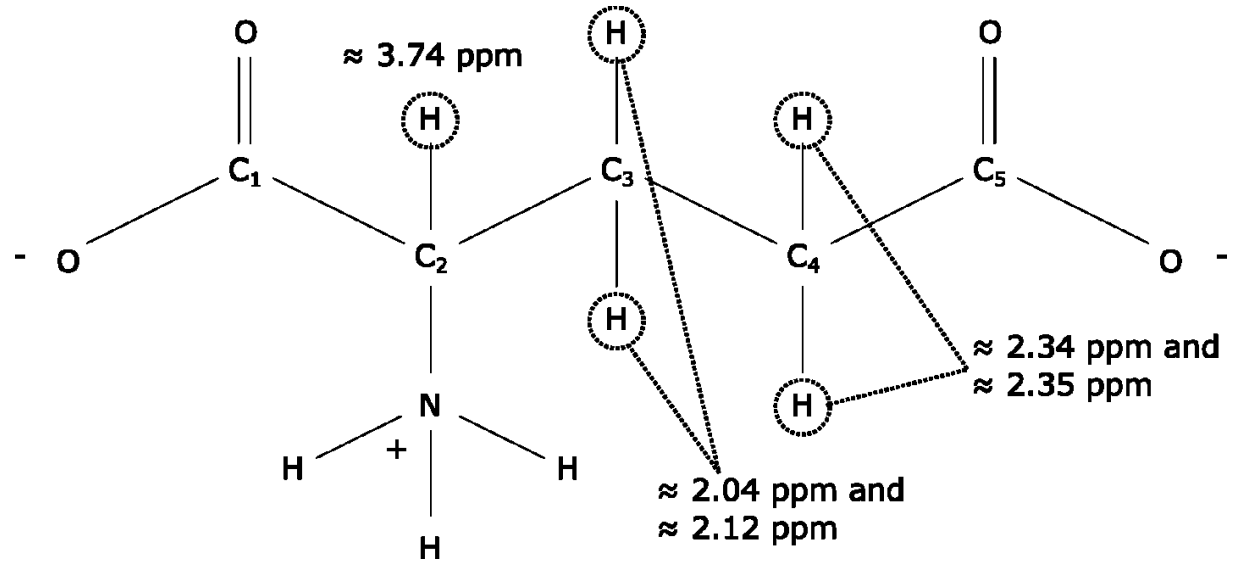

Figure 2.3: The molecular structure of Glu, with the chemical shifts of the protons labelled.

2.1.4 – $^{13}C_4$-Glu

^{13}C-labelled-C4-glutamate ($^{13}C_4$-Glu) is an isotopologue of Glu. That is, it has the same chemical structure, but one or more of the atoms are of a different isotope. In this case, the C_4 of Glu is ^{13}C instead of ^{12}C. This has important relevance to its NMR properties, as ^{13}C has a net spin, and, therefore, an NMR signal, whereas ^{12}C does not. This leads to heteronuclear J-coupling with the neighbouring protons, resulting in peak splitting and signal modulation. This is in addition to the homonuclear J-coupling interactions present between the Glu protons.The heteronuclear J-coupling constant J_{CH} is about 127 Hz, provided by Deelchand et al.[10] Figure 2.4 shows the molecular structure, with ^{13}C on the C_4 carbon, and with the heteronuclear J coupling constant labelled.

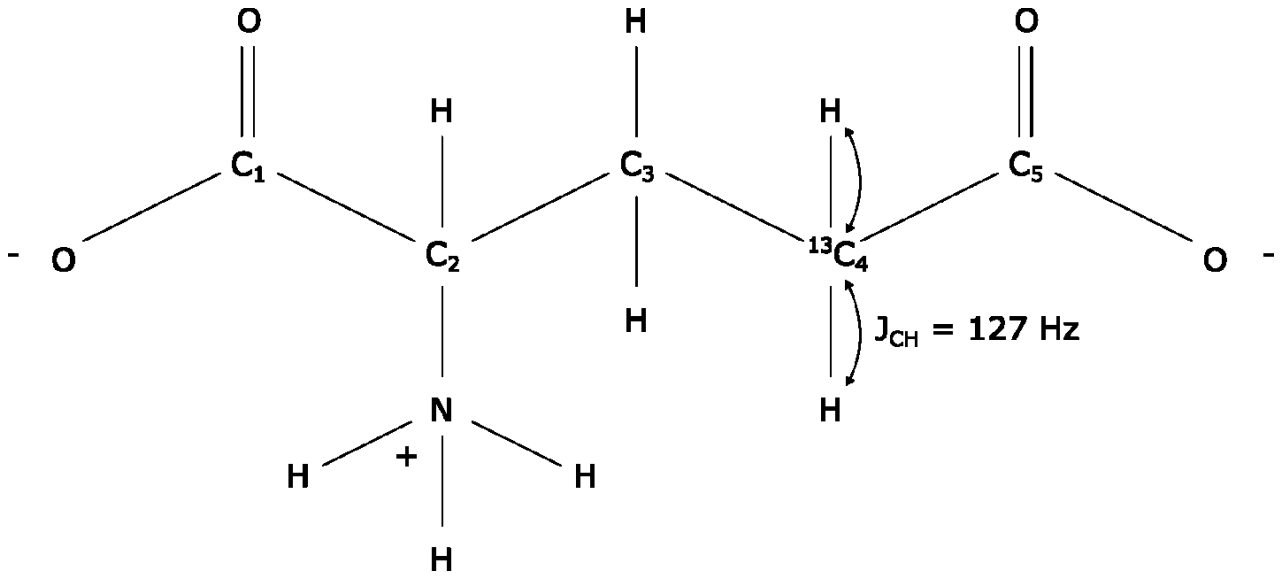

Figure 2.4: The molecular structure of $^{13}C_4$-Glu, with the heteronuclear J-coupling constant J_{CH} labelled.

As mentioned previously, Glu is connected to the TCA cycle.[8] This has special relevance to $^{13}C_4$-Glu. If a ^{13}C-labelled substrate such as glucose is infused in a living system, the products of its metabolism incorporate ^{13}C label.[8] When glucose has ^{13}C labelling on either the C_1 or C_6 carbons, ^{13}C will travel through the TCA cycle and eventually label the C_4 of Glu, turning a portion of the total Glu pool into $^{13}C_4$-Glu.[8] Measuring this change over time can be used to measure V_{TCA}, the rate of the TCA cycle.[8] Figure 2.5 illustrates this. Not shown is additional labelling that occurs on the C_3 of Glu on the second round of the TCA cycle. It has been shown that the C_4 time curve is sufficient for estimating V_{TCA} if V_X, the exchange rate between αKG and Glu, is assumed.[8,11]

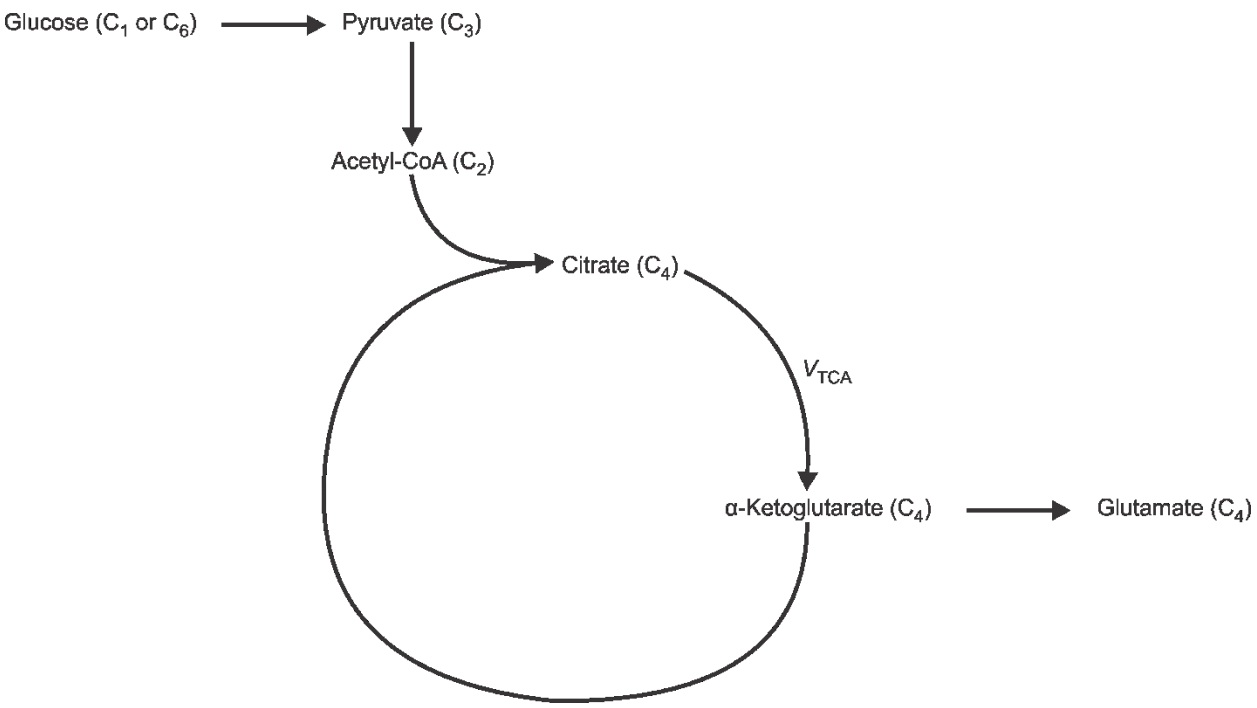

Figure 2.5: Simplified diagram of the tricarboxylic acid cycle showing the incorporation of a ^{13}C label from the C_1 or C_6 of glucose to the C_4 of Glu, adapted from Henry et al.[8]

In this thesis, the fractional enrichment of Glu, namely, the concentration of $^{13}C_4$-Glu relative to the total Glu pool (^{12}C-Glu + $^{13}C_4$-Glu) is measured over time in rat brain.

2.1.5 - Glutamine

Glutamine (Gln) is an amino acid that is involved in protein synthesis.[12] It is linked to Glu through the Glu-Gln cycle, acting as a precursor for Glu in a reaction catalyzed by glutaminase.[13] It is stored in astrocytes, which are support cells in the nervous system.[13] It can also be synthesized from Glu in a reaction catalyzed by glutamine synthetase.[13] In its amino acid form it has the

formula HOOC-CH(NH_2)-(CH_2)$_2$-CO-NH_2, while in solution at physiological pH, it exists as a zwitterion in the form $^-$OOC-CH(NH_3^+)-(CH_2)$_2$-CO-NH_2. The C_2 proton resonates at ≈ 3.75 ppm, the two C_3 protons resonate at ≈ 2.13 ppm (C_3) and ≈ 2.11 ppm (C_3'), and the two C_4 protons resonate at ≈ 2.43 ppm (C_4) and ≈ 2.45 ppm (C_4').[4] The C_2 proton is coupled to the C_3 protons with J-coupling constants of 5.847 Hz (C_3) and 6.500 Hz (C_3').[4] The C_3 protons are coupled to the C_4 protons with constants of 9.165 Hz (C_3-C_4), 6.347 Hz (C_3-C_4'), 6.324 Hz (C_3'-C_4), and 9.209 Hz (C_3'-C_4').[4] The C_3 protons are also coupled to each other with a constant of -14.504 Hz, while the C_4 protons are coupled to each other with a constant of -15.371 Hz.[4] Like Glu, Gln is also considered an AMNPQ spin system at 9.4 T, with the C_2 proton as the A spin, the C_3 protons as the M and N spins, and the C_4 protons as the P and Q spins. The chemical shift and scalar coupling constants were provided by Govindaraju et al.[4] Figure 2.6 shows the molecular structure, with the relevant protons labelled with their chemical shifts. In this thesis, the concentration of Gln is measured in rat brain, and the relative concentration of Glx (Glu + Gln) is measured in rat kidney.

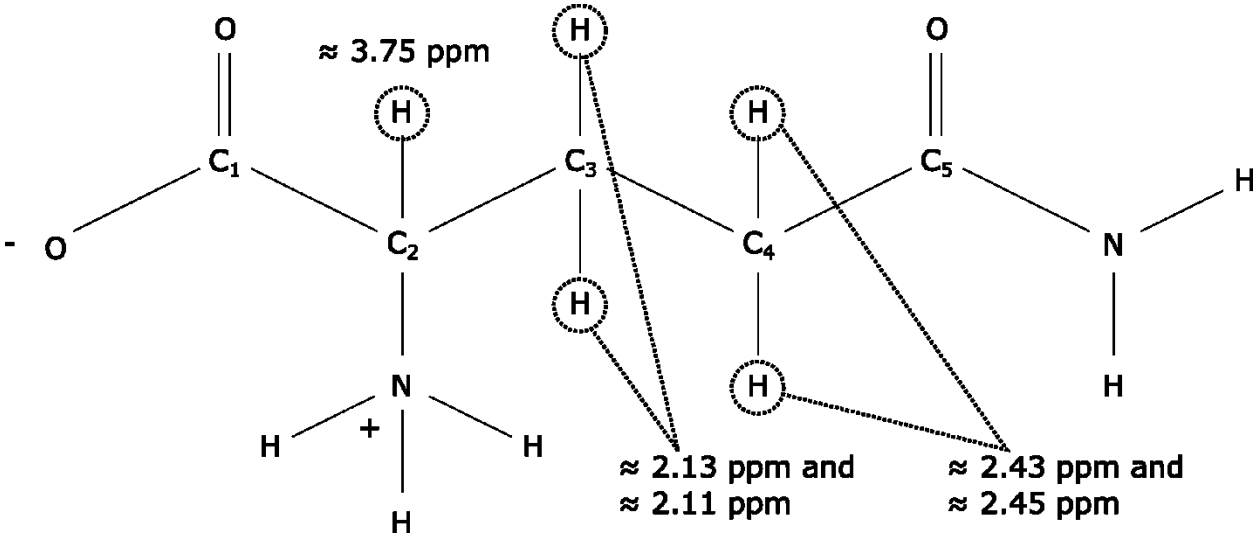

Figure 2.6: The molecular structure of Gln, with the chemical shifts of the protons labelled.

2.1.6 - γ-Aminobutyric Acid

γ-Aminobutyric acid (GABA) is the primary inhibitory neurotransmitter in the brain.[1] It is also linked to the Glu-Gln cycle, being synthesized from Glu via a reaction catalyzed by glutamate decarboxylase.[14] Its molecular formula is $HOOC\text{-}(CH_2)_3\text{-}NH_2$, but it is mostly found in solution at physiological pH as a zwitterion of the form $^{-}OOC\text{-}(CH_2)_3\text{-}NH_3^{+}$. It has two C_2 protons that resonate at ≈ 2.28 ppm, two C_3 protons that resonate at ≈ 1.89 ppm, and two C_4 protons that resonate at ≈ 3.01 ppm.[15] The C_2 protons are coupled to the C_3 protons with a J-coupling constant of 7.352 Hz.[15] The C_3 protons are coupled to the C_4 protons with constants of 6.377 Hz, 7.960 Hz, 8.139 Hz, and 7.495 Hz.[15] As such, GABA is considered an $A_2M_2X_2$ spin system at 9.4 T, with the C_4 protons as the A spins, the C_3 protons as the M spins, and the C_2 protons as the X spins. The chemical shift and scalar coupling constants were provided by Kaiser et al.[15] Figure 2.7 shows the molecular structure, with the relevant protons labelled with their chemical shifts. In this thesis, the concentration of GABA is measured in rat brain.

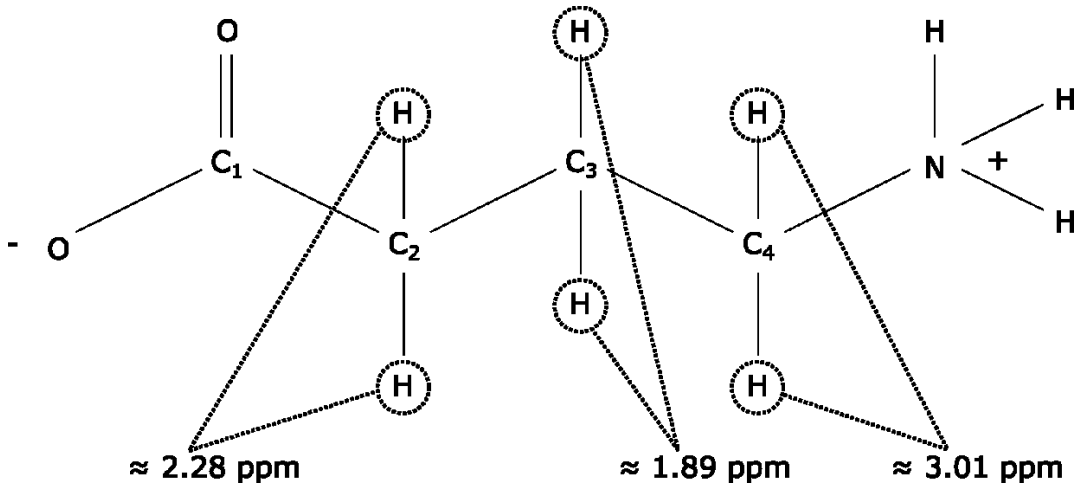

Figure 2.7: The molecular structure of GABA, with the chemical shifts of the relevant protons labelled.

2.1.7 – *N*-Acetylaspartate

N-Acetylaspartate (NAA) is the second most concentrated amino acid derivative in the brain, after only Glu,[16] being present in neurons, oligodendrocytes, and myelin.[17] It may have functions in osmoregulation and myelin synthesis.[17] It is an anion of acetylaspartic acid, which has the form $C_6H_9NO_5$. The structure of NAA in solution is $C_6H_7NO_5^{-2}$. It consists of two moieties, one acetyl and one aspartyl. The acetyl moiety has three protons on the C_2 carbon that resonate at ≈ 2.01 ppm with no J-coupling interactions.[4] The aspartyl moiety has one proton on the C_2 carbon that resonates at ≈ 4.38 ppm.[4] It also has two protons on the C_3 carbon that resonate at ≈ 2.67 ppm (C_3) and ≈ 2.49 ppm (C_3').[4] The C_2 proton is coupled to the C_3 protons with constants of 3.861 Hz (C_2-C_3) and 9.821 Hz (C_2-C_3').[4] The C_3 protons are coupled to each other with a constant of -15.592 Hz.[4] This forms an ABX spin system at 9.4 T, with the C_3 protons as the A and B spins, and the C_2 proton as the X spin. The chemical shift and scalar coupling constants were provided

by Govindaraju et al.[4] Figure 2.8 shows the molecular structure, with two moieties circled, and with the relevant protons highlighted with their chemical shifts.

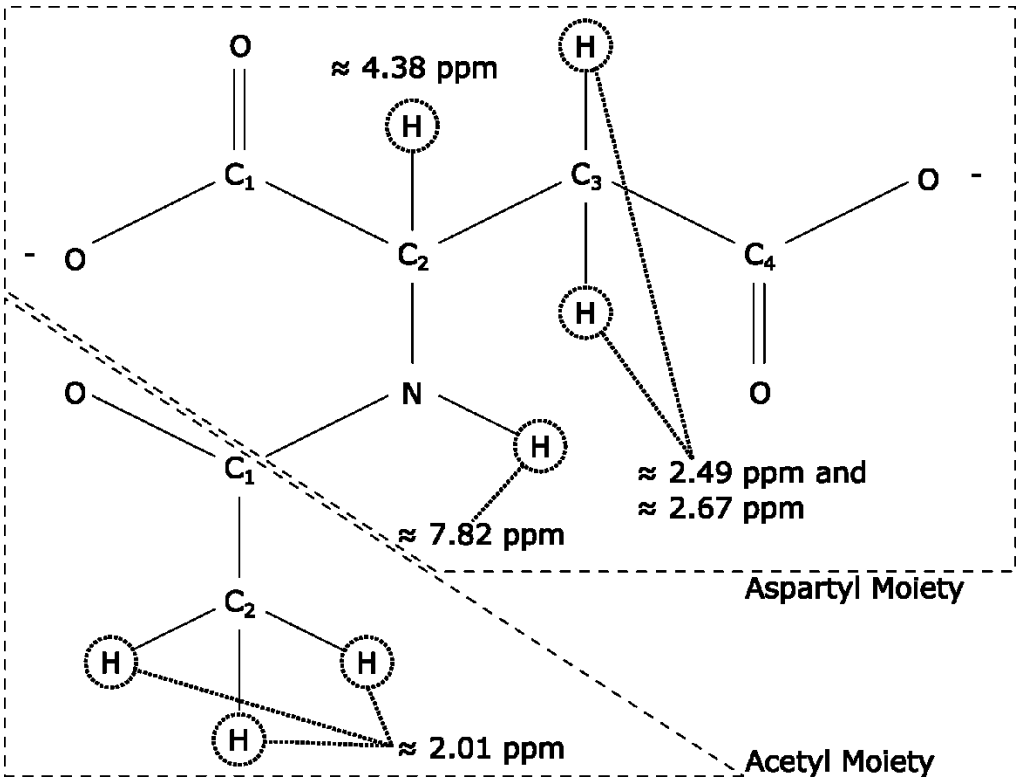

Figure 2.8: The molecular structure of NAA, with the acetyl and aspartyl moieties circled, and with the relevant protons labelled with their chemical shifts.

2.1.8 – Taurine

Taurine (Tau) is a compound that is found in many parts of the body.[18] It is a major constituent of bile, and it is involved in osmoregulation and modulation of neurotransmitters.[18] It has a molecular structure of $HO\text{-}SO_2\text{-}(CH_2)_2\text{-}NH_2$, but it is found in solution at physiological pH

as a zwitterion of the form $^{-}O_3S\text{-}(CH_2)_2\text{-}NH_3^{+}$. It has two C_1 protons that resonate at ≈ 3.42 ppm and two C_2 protons that resonate at ≈ 3.25 ppm.[4] The C_1 protons are coupled to the C_2 protons, with constants of 6.74 Hz, 6.40 Hz, 6.46 Hz, and 6.79 Hz.[4] It can be considered an A_2X_2 spin system at 9.4 T. The chemical shift and scalar coupling constants were provided by Govindaraju et al.[4] Figure 2.9 shows the molecular structure, with the relevant protons labelled with their chemical shifts. In this thesis, the concentration of Tau is measured in rat kidney.

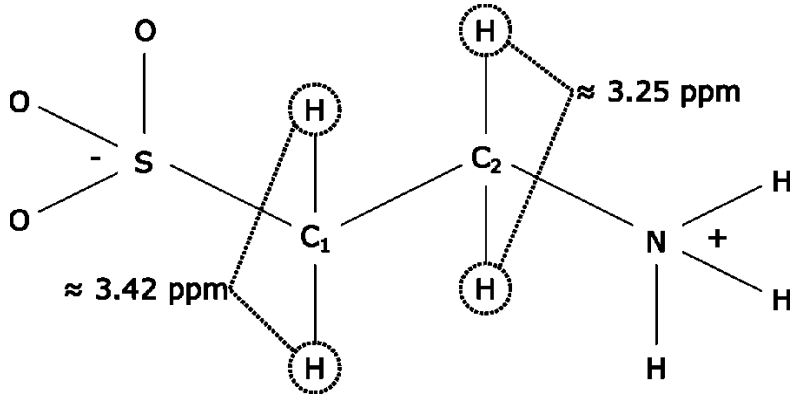

Figure 2.9: The molecular structure of Tau, with the chemical shifts of the relevant protons labelled.

2.1.9 – Betaine

Betaine (Bet), also known as trimethylglycine, is an amino acid derivative that is involved in osmoregulation.[19] In solution at neutral pH, it has the form of a zwitterion with the molecular structure $^{-}OOC\text{-}CH_2\text{-}N(CH_3)_3^{+}$. It has two C_2 protons that resonate at ≈ 3.89 ppm and nine protons from three methyl groups that resonate at ≈ 3.25 ppm.[20] Figure 2.10 shows the molecular structure, with the relevant protons labelled with their chemical shifts.

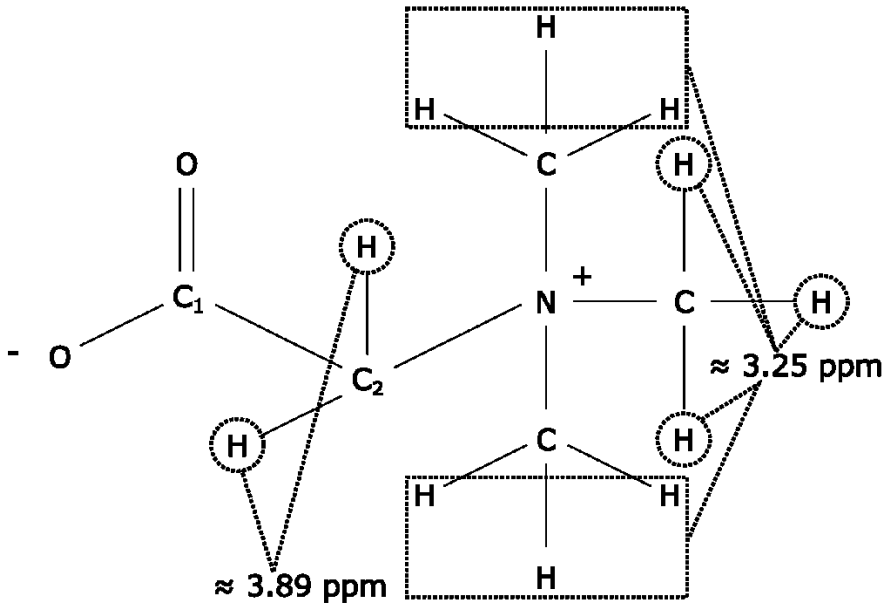

Figure 2.10: The molecular structure of Bet, with the chemical shifts of the relevant protons labelled.

In this thesis, the relative concentration of the sum of choline and Bet (Cho + Bet) is measured in rat kidney.

2.1.10 - Choline

Choline (Cho) is a class of salts containing the *N,N,N*-trimethylammonium cation. In the brain, the two most prominent choline compounds are glycerophosphocholine (GPC) and

phosphoryl choline (PCh).[21] Cholines play a role in structural integrity and signaling for cell membranes, as well as in neurotransmission.[22] The molecular formula of GPC is $C_8H_{20}NO_6P$. It contains two C_1 protons that resonate at ≈ 3.61 ppm (C_1) and ≈ 3.67 ppm (C_1'), one C_2 proton that resonates at ≈ 3.90 ppm, and two C_3 protons that resonate at ≈ 3.87 ppm (C_3) and ≈ 3.95 ppm (C_3').[4] In addition, it contains two C_7 protons that resonate at ≈ 4.31 ppm, two C_8 protons that resonate at ≈ 3.66 ppm, and nine protons from three methyl groups that resonate at ≈ 3.21 ppm.[4] There is coupling between the C_1, C_2, and C_3 protons, with constants of 5.57 Hz (C_1-C_2 and C_2-C_3) and 4.53 Hz (C_1'-C_2 and C_2-C_3').[4] There is also coupling between the C_7 and C_8 protons, with constants of 3.10 Hz and 5.90 Hz.[4] The chemical shift and scalar coupling constants were provided by Govindaraju et al.[4] Figure 2.11 shows the molecular structure, with the relevant protons labelled with their chemical shifts.

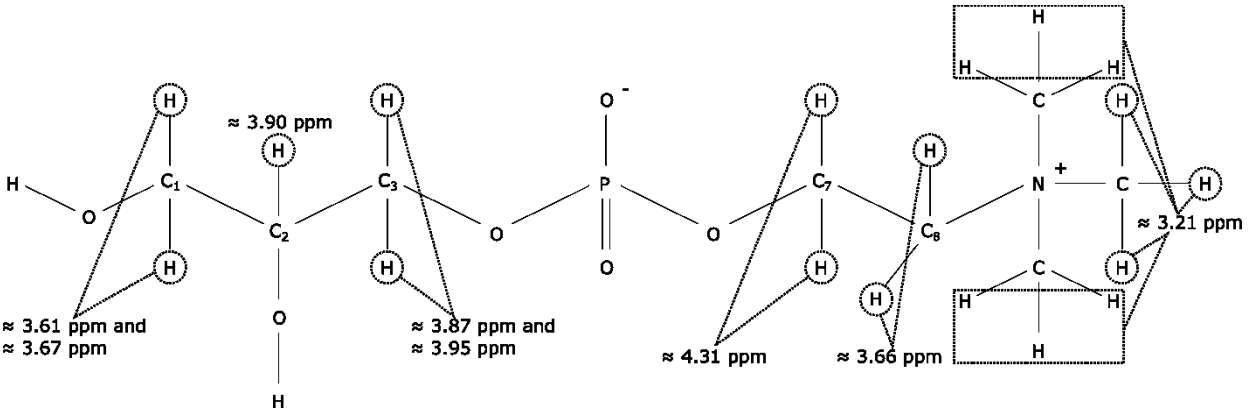

Figure 2.11: The molecular structure of GPC, with the chemical shifts of the relevant protons labelled.

The molecular formula of PCh is $C_5H_{14}NO_4P$. It contains two C_1 protons that resonate at ≈ 4.28 ppm, two C_2 protons that resonate at ≈ 3.64 ppm, and nine protons from three methyl groups that resonate at ≈ 3.21 ppm.[4] There is coupling between the C_1 and C_2 protons with constants of 2.284 Hz, 7.231 Hz, 2.235 Hz, and 7.326 Hz.[4] The chemical shift and scalar coupling constants were provided by Govindaraju et al.[4] Figure 2.12 shows the molecular structure, with the relevant protons labelled with their chemical shifts. In this thesis, the relative concentration of Cho + Bet is measured in rat kidney.

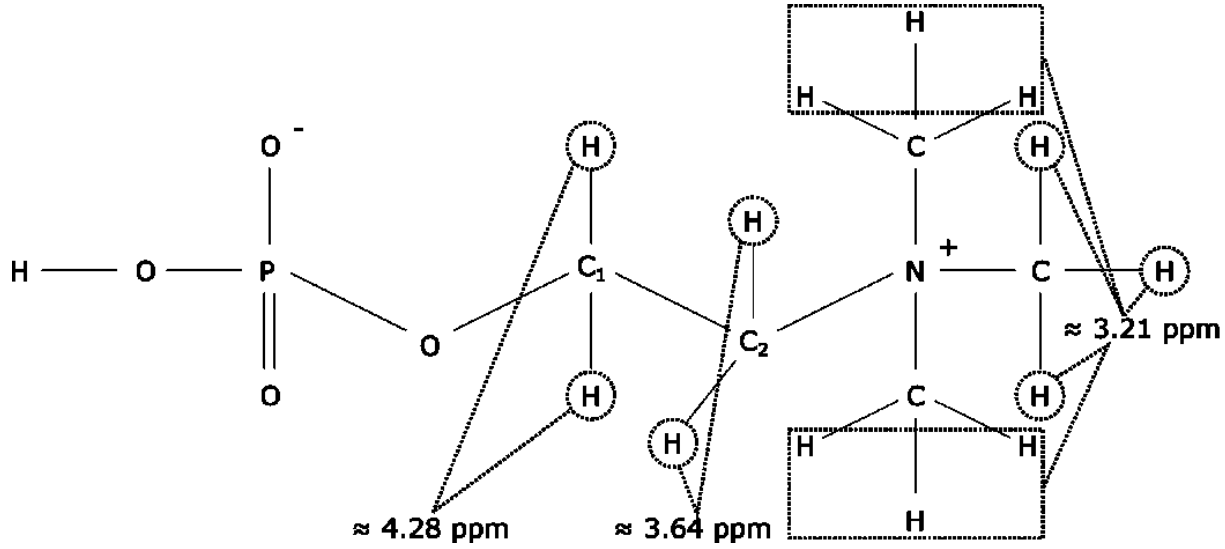

Figure 2.12: The molecular structure of PCh, with the chemical shifts of the relevant protons labelled.

2.1.11 – Glutamate-Glutamine and Tricarboxylic Acid Cycles

As mentioned, Glu and Gln are connected through the Glu-Gln cycle, with GABA being linked as well.[13,14] Neurons and astrocytes are both involved in the cycle, with each exhibiting metabolism in a compartmentalized way. At glutamatergic neurons, a stable supply of the neurotransmitter Glu is required. Neurons are incapable of synthesizing Glu from glucose; therefore, it is necessary for non-neuronal support cells to provide Gln, which acts as a precursor for Glu production in neurons. Astrocytes take on this role, by creating Gln from Glu in the cytosol by amidation via the glutamine synthetase pathway. After it is produced, Gln is released into extracellular space and taken up into the presynaptic terminal, where it is converted to Glu in the inner mitochondrial membrane by phosphate-activated glutaminase. Glu is then released as necessary into the synaptic cleft, and excess Glu is removed via uptake into the astrocyte.[13]

At GABAergic neurons, where GABA is required instead of Glu, the cycle is called the GABA-Gln cycle. Here, in the astrocyte mitochondria, GABA is catabolized via transamination with αKG to produce Glu and succinate-semialdehyde, which is oxidized to form succinate, which, along with αKG, is an intermediate of the TCA cycle. Gln is again synthesized from Glu via glutamine synthetase, with Glu provided from the TCA cycle. Upon release of Gln into the extracellular space and reuptake into the presynaptic neuron, Gln is converted to Glu, which is then metabolized to GABA by Glu decarboxylase. Upon release, excess GABA is taken up into the astrocyte.[14]

2.1.12 – Altered Metabolite Levels in Cancer

The above sections discuss the roles of the various metabolites in healthy tissue function. In addition, metabolites that have been targeted for quantification have shown relevance to the study of cancer.

The levels of Gly are elevated in brain tumours, especially in high grade gliomas compared to low grade gliomas, and it may serve as a biomarker for malignancy.[23] The biological reason for this is unclear.[23]

The concentrations of Glu, Gln, and GABA have all shown relevance to cancer. Glx levels are increased in high grade gliomas relative to low grade gliomas.[24] Some studies have reported high Glx in meningiomas and glioblastomas compared to healthy brain.[24] Glx plays a role as an energy fuel, and it is essential for the creation of purine and pyrimidine bases and is necessary for tumour growth.[24] Glu can also cause excitotoxicity to normal brain, which may facilitate invasion of tumours.[24] GABA and GABA receptors have been detected in a number of different tumour tissues.[25] Receptors play a role in regulating tumour cell proliferation and migration.[25]

The isotopologue of Glu, $^{13}C_4$-Glu, which is labelled *in vivo* upon infusion of ^{13}C-labelled substrates such as glucose, has also shown applicability to cancer.[26] It becomes labelled in glioblastomas upon infusion of [U-^{13}C]-glucose.[26] In addition, TCA cycle flux, which is determined in part by changes in the $^{13}C_4$-Glu signal, was also active in glioblastomas.[26] The Warburg effect states that cancer cells exhibit excess glycolysis and lactate production, which implies a decrease in the TCA cycle flux compared to normal cells.

In kidney, compared to adjacent tissue, the levels of a few metabolites have been shown to be altered compared to renal cell carcinoma (RCC) tumour tissue.[27] Tau, Bet, and Cho are higher,

while Ins is lower.[27] The biological relevance of Ins and Bet to RCC is unclear. Tau, however, is a potential antioxidant, and has been shown to protect against other types of renal injury, such as that caused by oxidative stress.[28] The increase in Cho may be caused by an increased demand for phospholipids during the rapid replication of cancer cells.[29]

2.2 – NUMERICAL METHODS

Numerical simulations were used to calculate the response of spins of proton groups of the relevant metabolites to a standard single-voxel PRESS sequence at 9.4 T, as a function of TE_1 and TE_2. Calculations were performed using a previously-developed MATLAB (Mathworks, Natick, Massachusetts, United States) program (implemented by R.B. Thompson) based on density matrix simulations.[30,31] Where simulations involving ^{13}C were conducted, the program incorporated modifications to include a ^{13}C nucleus (implemented previously as described in Yahya and Allen).[32] The numerical methods solve the Liouville-von Neumann equation, which describes how a quantum system evolves in time[30]:

$$\frac{d}{dt}\rho(t) = -i[H(t), \rho(t)] \tag{2.1}$$

$\rho(t)$ is the density matrix, which is calculated from a density operator and can be used to represent a quantum system of mixed states. It can be represented as a matrix with $2^N \times 2^N$ elements for N spins of spin-½.[30] For spin ½ nuclei, the density matrix is a weighted sum of 2^{2N} product operator basis terms, which were introduced as coherence terms in section 1.7.1. For a single spin-1/2 system I, these are[33]:

$$I_X = \frac{1}{2}\begin{bmatrix} 0 & 1 \\ 1 & 0 \end{bmatrix}, \quad I_Y = \frac{1}{2}\begin{bmatrix} 0 & -i \\ i & 0 \end{bmatrix}, \quad I_Z = \frac{1}{2}\begin{bmatrix} 1 & 0 \\ 0 & -1 \end{bmatrix}, \quad \frac{1}{2}E = \frac{1}{2}\begin{bmatrix} 1 & 0 \\ 0 & 1 \end{bmatrix} \tag{2.2}$$

I_X, I_Y, and I_Z are the spin angular momentum operators along the x-, y-, and z-axis, respectively, and E is referred to as the identity operator. For a two-spin coupled system of I and S, the basis terms will also include S_X, S_Y, S_Z, $2I_XS_Z$, $2I_YS_Z$, $2I_ZS_Z$, $2I_ZS_X$, $2I_ZS_Y$, $2I_XS_X$, $2I_YS_Y$, $2I_XS_Y$, and $2I_YS_X$. A few of these are shown below[33]:

$$I_X = \frac{1}{2}\begin{bmatrix} 0 & 0 & 1 & 0 \\ 0 & 0 & 0 & 1 \\ 1 & 0 & 0 & 0 \\ 0 & 1 & 0 & 0 \end{bmatrix}, \quad I_Y = \frac{1}{2}\begin{bmatrix} 0 & 0 & -i & 0 \\ 0 & 0 & 0 & -i \\ i & 0 & 0 & 0 \\ 0 & i & 0 & 0 \end{bmatrix}, \quad I_Z = \frac{1}{2}\begin{bmatrix} 1 & 0 & 0 & 0 \\ 0 & 1 & 0 & 0 \\ 0 & 0 & -1 & 0 \\ 0 & 0 & 0 & -1 \end{bmatrix},$$

$$S_Z = \frac{1}{2}\begin{bmatrix} 1 & 0 & 0 & 0 \\ 0 & -1 & 0 & 0 \\ 0 & 0 & 1 & 0 \\ 0 & 0 & 0 & -1 \end{bmatrix}, \quad 2I_YS_Z = \frac{1}{2}\begin{bmatrix} 0 & 0 & -i & 0 \\ 0 & 0 & 0 & i \\ i & 0 & 0 & 0 \\ 0 & -i & 0 & 0 \end{bmatrix} \tag{2.3}$$

$H(t)$ is the Hamiltonian under which spin evolution occurs, which represents the energy of the spins. It includes all of the energies corresponding to RF pulses, gradient pulses, chemical shift evolution, and J-coupling interactions. The Zeeman effect is not included, as the simulations are performed in the rotating frame. Relaxation effects are also not included, however, that can be corrected for post-calculations if the T_1 and T_2 values are known. At any moment, $\rho(t)$ can be constructed by the eigenstates of $H(t)$.[33] The total Hamiltonian in the rotating reference frame can be represented as follows:

$$H = H_{CS} + H_G + H_{JC} + H_{RF} \tag{2.4}$$

H_{CS} is for chemical shift evolution, H_G is for the gradient pulses, H_{JC} is for J-coupling, and H_{RF} is for the RF pulses. For a spin $\vec{I}$, coupled to spin $\vec{S}$, H can be expressed as:

$$H = \gamma\hbar\sigma I_Z B_0 + \gamma\hbar I_Z \vec{G}\cdot\vec{r} + 2\pi\hbar J_{IS}\left(\vec{I}\cdot\vec{S}\right) + \gamma\hbar\vec{I}\cdot\vec{B}_1(t)$$

$$H = \gamma\hbar\sigma I_Z B_0 + \gamma\hbar I_Z \vec{G}\cdot\vec{r} + 2\pi\hbar J_{IS}(I_X S_X + I_Y S_Y + I_Z S_Z)$$

$$+\gamma\hbar B_1(t)[(\cos\varphi)I_X + (\sin\varphi)I_Y] \quad (2.5)$$

σ is the shielding coefficient, $\vec{G}$ is the linear gradient field strength, $\vec{r}$ is the distance from the gradient field origin, and φ is the phase of the RF pulses relative to the phase of the excitation pulse. Equation 2.5 is for a single spin. For an ensemble of N spins, H will be equal to the sum of all of the product operator terms over all the spins in the system, as follows:

$$H = \gamma\hbar\sum_{n=1}^{N}\sigma_n I_{Z,n} B_0 + \gamma\hbar\vec{G}\cdot\vec{r}\sum_{n=1}^{N} I_{Z,n} + 2\pi\hbar\sum_{m=1}^{N-1}\sum_{n=m+1}^{N} J_{nm}\left(\vec{I}_n\cdot\vec{I}_m\right)$$

$$+\gamma\hbar B_1(t)\left[(\cos\varphi)\sum_{n=1}^{N} I_{X,n} + (\sin\varphi)\sum_{n=1}^{N} I_{Y,n}\right] \quad (2.6)$$

For time-independent Hamiltonians, $\rho(t)$ can be solved as follows:

$$\rho(t) = e^{-iHt}\rho(0)e^{iHt} \quad (2.7)$$

$\rho(0)$ is the density matrix at time $t = 0$. At thermal equilibrium, it is I_Z for a single spin. For a number of spins, it is the sum of spin angular momentum operators along the z-direction. When the Hamiltonian is time dependent, such as that for an RF pulse, its time evolution can be divided into discrete elements that are short enough for time independence to be assumed.[30] $\rho(t)$ from each calculation becomes $\rho(0)$ for the next one. When the Hamiltonian corresponds to a diagonal matrix, e^{-iHt} can be simply expressed as a diagonal matrix of exponential elements. The Hamiltonian can be diagonalized with a unitary matrix U:

$$\rho(t) = Ue^{-iU^{-1}HUt}U^{-1}\rho(0)Ue^{iU^{-1}HUt}U^{-1} \quad (2.8)$$

U is made up of the eigenvectors of H. To incorporate a ^{13}C nucleus, a spin with an arbitrarily large chemical shift was added to the spin system such that it becomes an $N + 1$ spin system (implemented previously as described in Yahya and Allen).[32] No RF pulses were applied at the ^{13}C frequency so modifications to the RF pulse Hamiltonian were not required. The J-coupling interactions between protons and the ^{13}C spin were explicitly defined as weak. For a weakly coupled system, the J-coupling Hamiltonian simplifies, such that only the $I_Z S_Z$ term remains:

$$H_{JC} = 2\pi\hbar J_{IS}(\vec{I} \cdot \vec{S}) = 2\pi\hbar J_{IS}(I_X S_X + I_Y S_Y + I_Z S_Z) \approx 2\pi\hbar J_{IS} I_Z S_Z \quad (2.9)$$

Heteronuclear J-coupling constants J_{CH} were added.

The chemical shift and scalar coupling constants were based on those provided by Govindaraju et al.[4], except for GABA, for which updated values were provided by Kaiser et al.[15] The $^{13}C_4$-Glu scalar coupling constant was obtained from Deelchand et al.[10] Spectra and peak areas were calculated for spectral regions of interest, with TE_1 and TE_2 varying within the chosen range (typically 2 – 200 ms) in steps of 2 ms. The minimum TE is limited by the 2 ms duration of the refocusing pulses, and the maximum total TE (TE_1 + TE_2) was chosen to limit the effects of T_2 relaxation. The spectral regions of Ins (3.52-3.57 ppm), ^{12}C-Glu (2.30-2.39 ppm for the ≈ 2.35 ppm peak), Gln (2.40-2.49 ppm for the ≈ 2.45 ppm peak), GABA (2.23-2.33 ppm for the ≈ 2.28 ppm peak), NAA (2.40-2.49 ppm and 2.45-2.55 ppm), and $^{13}C_4$-Glu (2.45-2.55 ppm for the the ≈ 2.51 ppm peak) were investigated to find an optimal (TE_1, TE_2) combination to improve quantification of Gly, ^{12}C-Glu, Gln, GABA, and $^{13}C_4$-Glu. Normalized contour plots were created based on peak areas for each individual metabolite, and the peak area relative to the corresponding value at (2 ms, 2 ms) was found for each metabolite at the optimal timing sets. The individual spectra of each metabolite were simulated with a (TE_1, TE_2) of (12 ms, 9 ms), which is the

minimum used experimentally with the MRI scanner, and with the optimal TE candidates. Spectra were line-broadened to match *in-vivo* linewidths (corresponding to a water linewidth of about 20 Hz).

2.3 – EXPERIMENTAL DETAILS

2.3.1 – System Details

Experiments were performed with a 9.4 Tesla, 21.5 cm diameter MRI (magnetic resonance imaging) scanner (Magnex Scientific, Oxford, UK) in conjunction with a TMX console (National Research Council of Canada Institute for Biodiagnostics, West, Calgary, AB, Canada). Figure 2.13 shows the magnet.

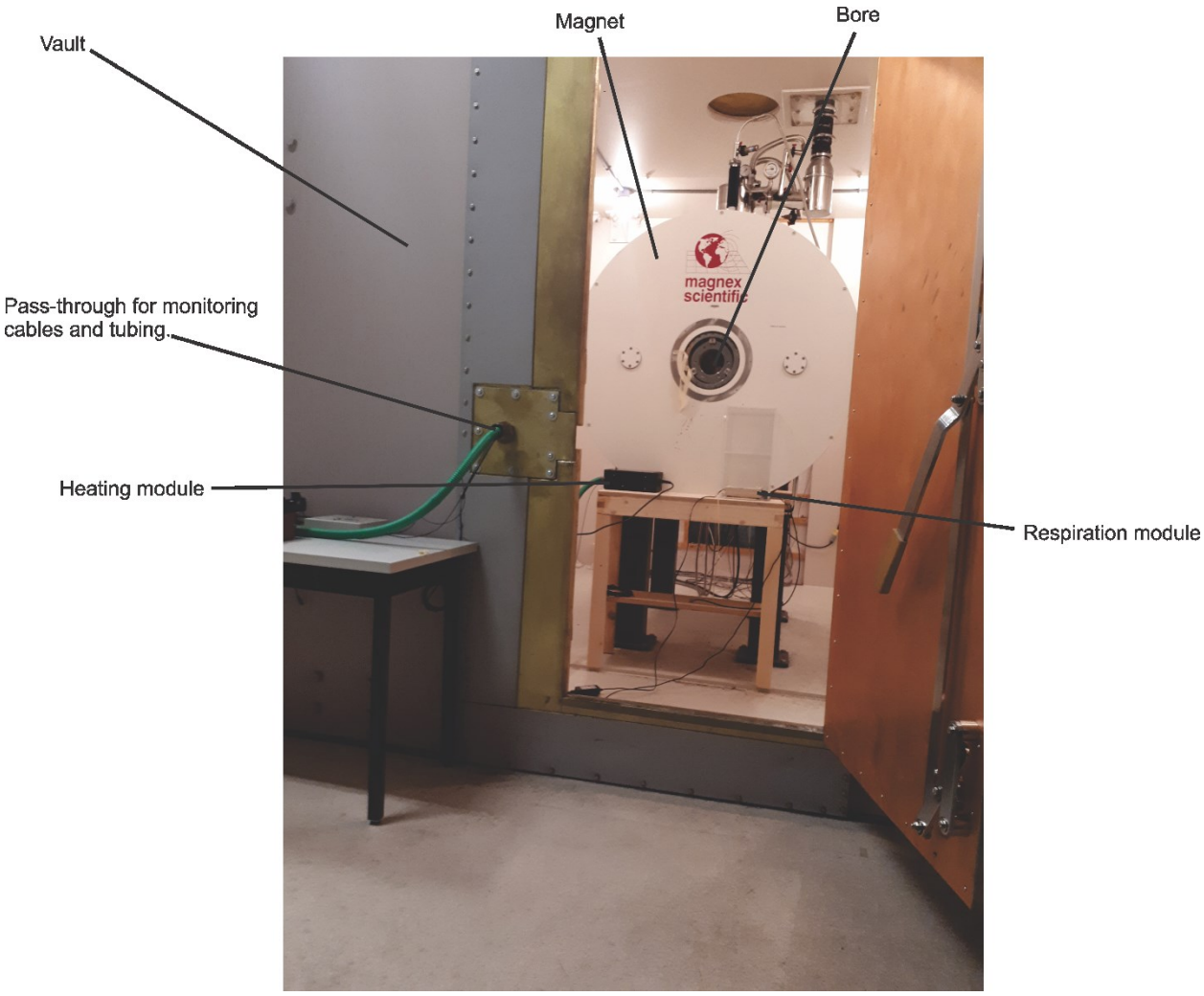

Figure 2.13: The 9.4 T animal magnet, with the vault, magnet, bore, pass-through, animal heating module, and animal respiration module labelled.

It is made up of a 1.47-m-long cylindrical superconducting magnet, along with a system of gradient coils 12.0 cm in diameter. Superconducting shim coils are in place to improve magnetic field homogeneity. When the magnet was commissioned, the B_0 field homogeneity was measured with a magnetometer over a 10 cm sphere of air at the centre of the magnet, yielding a value of 4.56 ppm peak-to-peak. Resistive shim coils are also in place, which are cooled with circulating

water. They are each connected to an external power supply and can be readily adjusted by the user. Gradient coils, also cooled with circulating water, are located within the magnet, connected to an external set of amplifiers. They can achieve a peak gradient strength of 200 mT/m. A steel vault surrounds the magnet for passive shielding. At the back of the vault, there is a filter panel for shim, gradient, RF, and lighting cables, as well as water cooling lines, which can be seen in figure 2.14.

Figure 2.14: Filter panel at the back of the vault for shim, gradient, RF, and lighting cables, as well as water cooling lines.

There are additional pass-throughs at the front and back for animal monitoring, anaesthetic, and injection equipment. Outside of the vault is an electronics rack with 4 kW RF amplifier, three primary gradient amplifiers, and three secondary gradient amplifiers, power supply and shim computer, shown in figure 2.15.

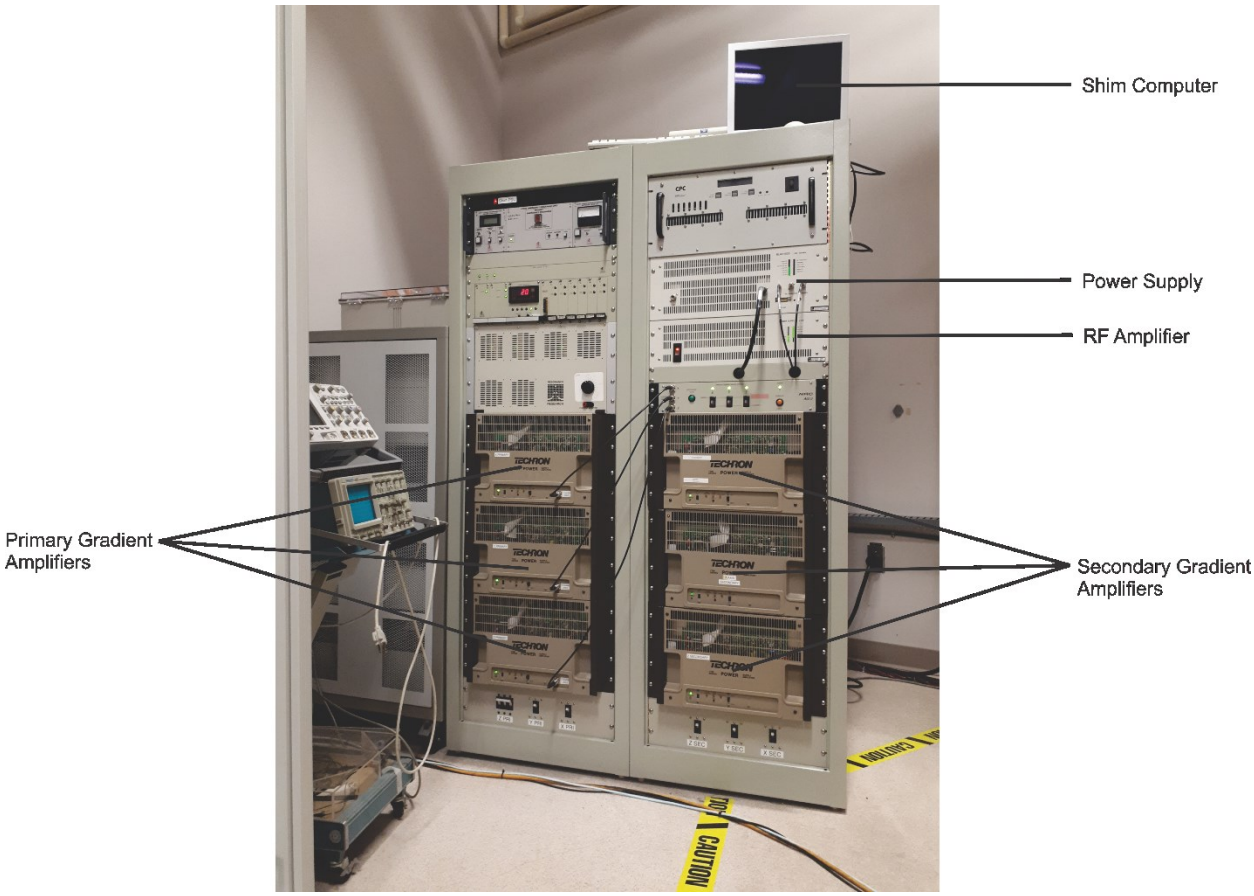

Figure 2.15: Electronics rack with amplifiers, power supply, and shim computer.

Nearby in an adjacent, climate-controlled room is a second rack with additional RF amplifers, frequency synthesizers, and computers that generate pulse shapes and sequence timings.

A computer at the operating station allows the user to change pulse sequence parameters, shims, and RF amplification for both transmission and reception, controlled with a custom graphical user interface (National Research Council of Canada Institute for Biodiagnostics, West, Calgary, AB, Canada).

2.3.2 – Phantom Experiments

Phantom experiments were performed on spherical glass phantoms filled with solutions of interest. The spheres are approximately 30 mm in diameter and 10 mL in volume. A picture of a phantom is shown in figure 2.16.

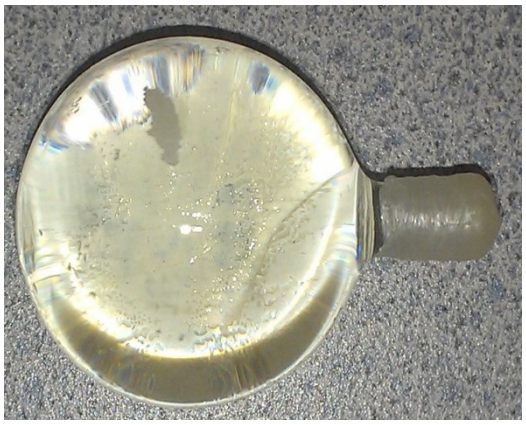

Figure 2.16: Spherical, 30 mm diameter, 10 mL volume, glass phantom used for experiments.

Solutions were prepared beforehand with chemicals purchased from Millipore Sigma (Oakville, ON, Canada). The chemicals were carefully weighed with milligram accuracy and then

placed in a beaker with deionized water. Magnetic stirring and heating were applied to aid in dissolution. The solution was tested for pH with pH test paper, and premade, concentrated solutions of NaOH or HCl were added in small amounts to bring the pH to 7. A syringe was then used to transfer the solution to the phantom. The phantom was placed in the centre of a 4.3 cm diameter birdcage RF coil (National Research Council of Canada Institute for Biodiagnostics, West), which was used for both transmission and reception. This was then transferred into the bore of the magnet in an acrylic cylinder approximately 11 cm in diameter and 100 cm in length, which was designed for the phantom to be in the iso-centre of the magnet.

Spectra were obtained from $5 \times 5 \times 5$ mm^3 voxels placed in the centre of the phantoms. A PRESS sequence, consisting of 2 ms sinc RF pulses of 3000 Hz bandwidth was employed. The spectra were acquired in 32 averages with a repetition time, TR, of 5 s. A total of 8192 complex data points were collected at a sampling frequency of 10,000 Hz and a 4 step phase cycling scheme was applied. A gradient strength of 14.1 mT/m was used. For the voxel size employed, it was found that manual first order shimming was adequate. Shimming was performed on the water signal by manually adjusting the first order shims until the peak amplitude was maximized. A chemical shift selective (CHESS)[34] sequence was used for water suppression. Phantoms containing 50 mM of the metabolite of interest, as well as 10 mM creatine (Cr) to serve as a reference, were scanned with a (TE_1, TE_2) of (12 ms, 9 ms), the shortest used timings experimentally, and with the optimal TE candidates. In addition, mixture phantoms designed to mimic *in vivo* conditions were sometimes scanned. Shims were adjusted until the peak amplitude of the water signal was maximized (phantom water linewidths of less than 5 Hz were achieved).

The spectra were analyzed by manually integrating the peak areas for each metabolite in their respective spectral regions of interest at the optimal TE combinations, and comparing them

to the corresponding areas obtained at the short TE combination of (12 ms, 9 ms). Spectra were processed with software provided by National Research Council of Canada (Spectrum Viewer v. 2.00.002, National Research Council of Canada Institute for Biodiagnostics, West, Calgary, AB, Canada). Processing included filtering, zero-filling, Fourier transformation, phase correction and baseline correction.

2.3.3 – Rat Brain Experiments

Experiments were performed *in vivo* on the brains of female Sprague-Dawley rats. Prior to the experiment, the rat was transported from the on-site vivarium to the magnet room. It was anaesthetized with isoflurane inside of a small acrylic box. Once unconscious, it was transferred to the work bench, where a nose cone device was attached for further anaesthetization. A pneumatic pillow was taped to the abdomen for respiratory monitoring. A thermistor-type temperature probe connected to a fiber optic cable was inserted into the rectum and secured with tape. The rat was then moved to a polystyrene couch and placed in prone position, with the nose cone device secured in place. A single loop 24 mm diameter surface coil (Doty Scientific, Inc., Columbia, South Carolina, United States) was placed on top of the head, behind the eyes, such that the brain was centred in its field of view. It was used for both transmission and reception. Figure 2.17 shows the setup.

Figure 2.17: Rat brain spectroscopy setup with heating tube, nose cone, and temperature and respiration cables, along with the surface coil placed over the rat's head.

The setup was placed inside of the acrylic cylinder and transferred into the bore of the magnet. The rat was positioned such that the brain was at the magnet iso-centre. Connections for monitoring and gating were then made, with lines going through the pass-through of the vault. The small animal monitoring and gating system that was used was model 1025 (SA Instruments Inc., Stony Brook, NY, USA). It monitors temperature and respiration, outputting data to a connected PC outside of the vault. A fan blows air through a tube system, through a heater, and towards the rat to maintain a body temperature of 37 ˚C. The degree of heating is controlled by software running on the PC. The abdominal probe returned a waveform pattern that was used for respiratory monitoring, as well as respiratory gating. The anaesthetic tube also went through a pass-through, such that anaesthetic could be administered throughout the experiment. It was adjusted from outside of the vault to maintain 40-80 breaths per minute.

In addition to the regular *in-vivo* brain scans, some were acquired during an infusion of uniformly-labelled ^{13}C-glucose ([U-$^{13}C_6$]-Glc. Prior to experiment, the rat was weighed. 99 % enriched [U-$^{13}C_6$]-Glc was mixed with a saline solution to create a solution of 0.75 M/(200 g body weight), and was then filtered with a Millex®-GS 0.22 μm syringe filter (Fisher Scientific Company, Ottawa, ON, Canada) for sterilization. The rat underwent overnight fasting (12-16 hours) prior to the experiment. The rat tail vein was cannulated and attached via PE-10 tubing to a BD 3 ml Luer-Lok™ tip syringe (Fisher Scientific Company, Ottawa, ON, Canada), which was filled with the [U-$^{13}C_6$]-Glc solution and placed in a Multi-Phaser™ NE-4000 Double Syringe Pump (New Era Pump Systems Inc., Farmingdale, NY, USA).

Spin echo images were obtained for voxel placement. The imaging sequence employed a TE of 13 ms and a TR of at least 1250 ms. Transverse and coronal slices (2 mm thickness) were obtained of the rat brain. A $5 \times 5 \times 5$ mm^3 voxel was approximately centred in the brain, with its centre a distance of ≈ 6 mm from the surface coil. Typically, a water linewidth of ≈ 20 - 25 Hz was achieved. Two spectra were acquired from each rat, namely, one with a short-TE of (TE_1, TE_2) = (12 ms, 9 ms) and one with the optimized TE combination. Both spectra were measured as 2048 complex data points, sampled at 10,000 Hz, with a TR of at least 3 s. A CHESS sequence was used for water suppression. The pulse sequence played out during the flat respiratory response between breaths. After the experiment, the setup was removed from the magnet, and the rat was allowed to wake up before transportation back to the vivarium.

2.3.4 – Rat Kidney Experiments

Experiments were also performed *in vivo* on rat kidney. The right kidneys were scanned. An in-house, 5 cm diameter single loop surface coil was used for both transmission and reception, shown in figure 2.18.

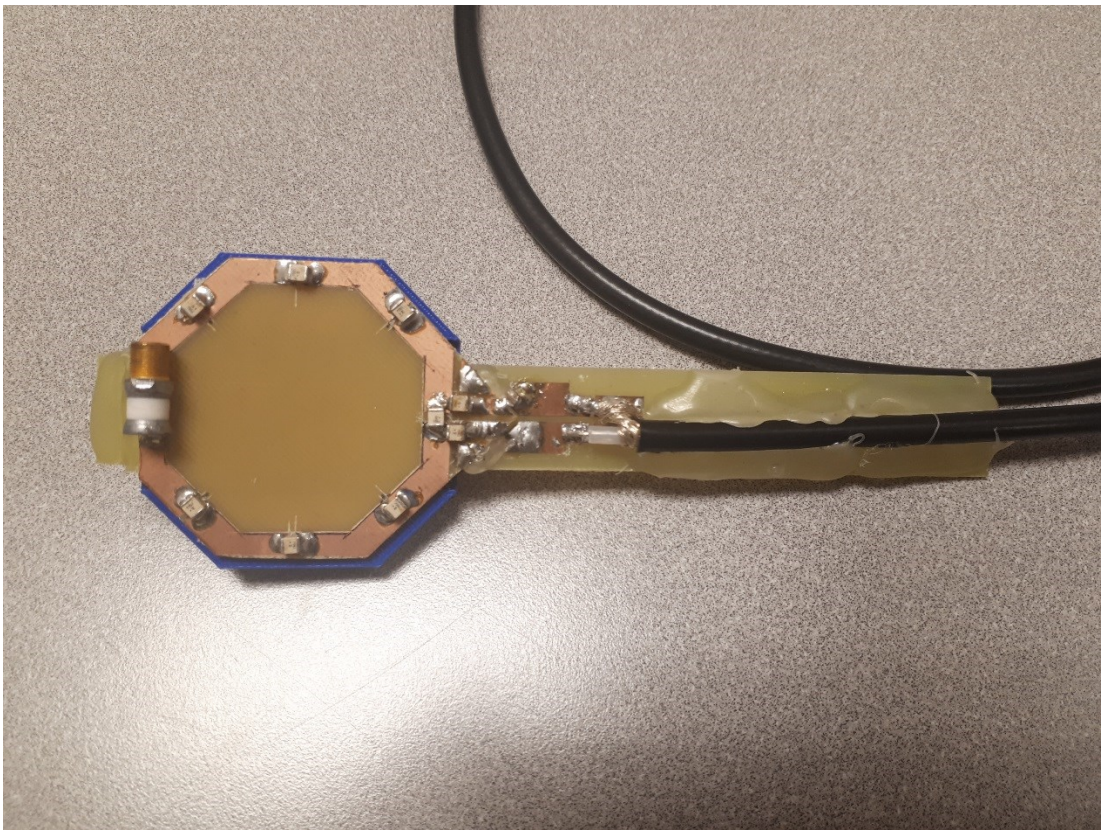

Figure 2.18: In-house, 5 cm diameter surface coil used for rat kidney imaging and spectroscopy.

Rats were anaesthetized with isoflurane and placed on their side with the surface coil positioned over the right kidney region. The setup is shown in figure 2.19.

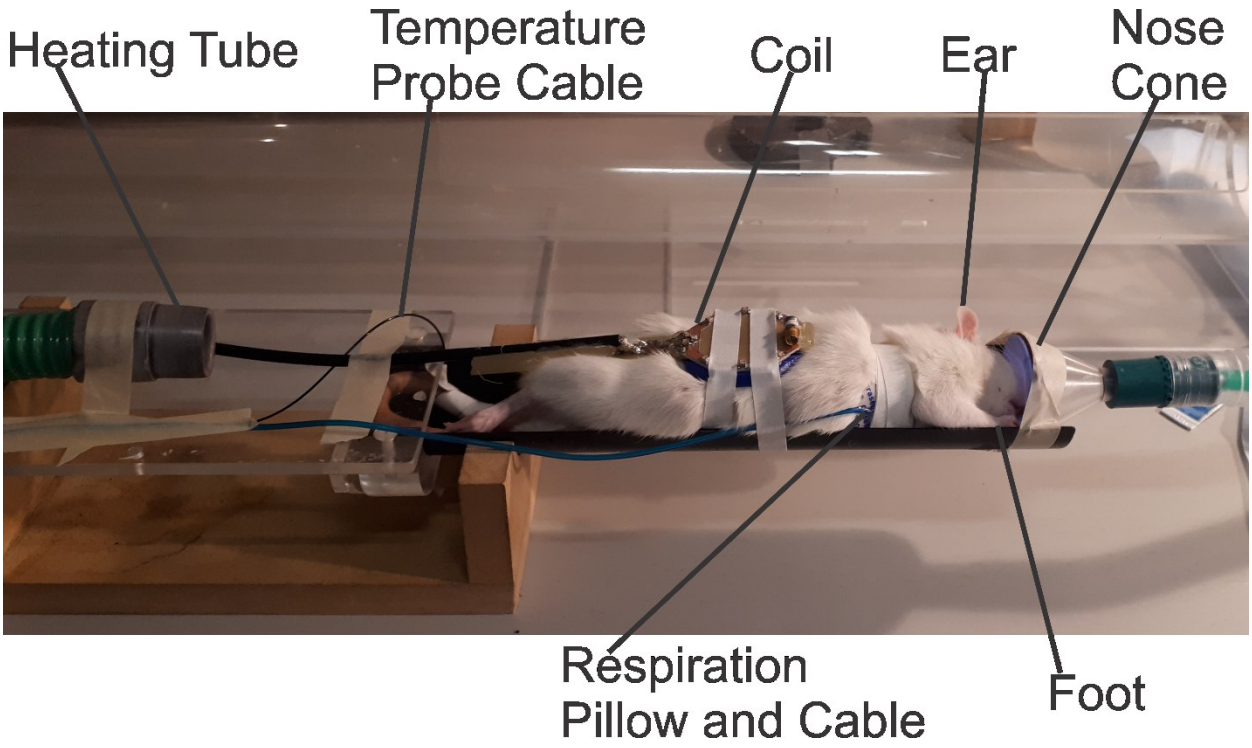

Figure 2.19: Rat kidney spectroscopy setup, with the nose cone system, heating hose, respiratory gating probe, and temperature probe, along with the surface coil placed on top of the rat lying on its left side.

The same small animal temperature and respiratory monitoring, heating and gating system as the brain scans was used. The rat was positioned such that the kidney was at the magnet iso-centre.

Transverse and sagittal spin echo images were acquired with a slice thickness of 2 mm, repetition time of 600 ms, and an echo time of 16.3 ms. These parameters differ from those used for the brain images, as they were found to minimize motion artifacts that occurred due to the

increased motion of the rat abdomen, as compared the head. The images were used to localize a 5 x 5 x 5 mm^3 voxel approximately centred in the right kidney (≈ 1 cm from the coil surface). PRESS spectra were acquired at the short TE combination of (12 ms, 9 ms) for this initial feasibility study.

Respiratory gating was applied with an auto track feature, which is an automatic way to respond to changes in respiration. The desired percentage of the begin delay and max width is specified. When the rat's respiration rate changes, the two parameters automatically track according to the parameter settings. The begin delay was set to 20 - 40 % of the respiration period, and the maximum width was set to 10 – 20 % of the respiration period. An example waveform is shown in figure 2.20.

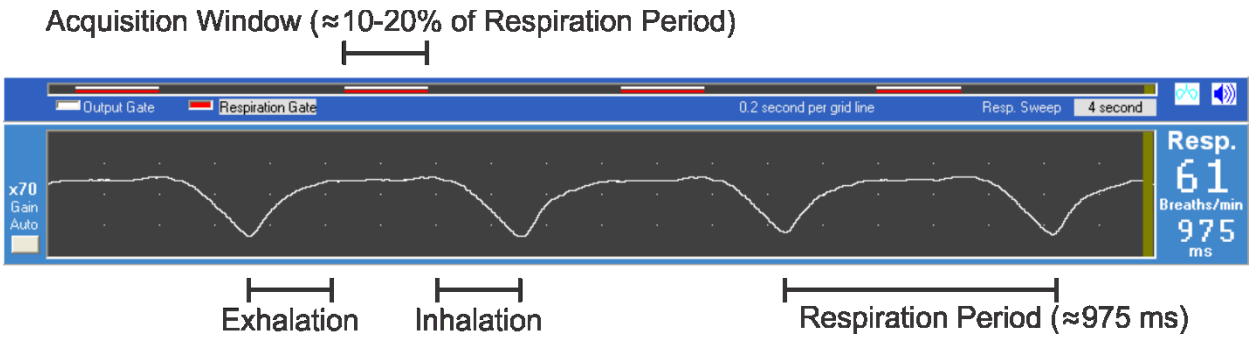

Figure 2.20: Example respiration waveform, with exhalation, inhalation, acquisition window, and respiration period shown.

2.4 – DATA ANALYSIS

LCModel software was used to analyze the *in-vivo* spectra.[35] It works by using a linear combination of predetermined model basis spectra, acquired either *in vitro* or simulated by other

means. Constrained regularization is performed with a Marquardt modification[36] of a constrained Gauss-Newton least-squares analysis to determine the metabolite concentrations and their uncertainties. It accounts for some differences between the basis spectra and *in-vivo* spectra. T_2 broadening and a small frequency shift are applied to account for referencing errors. A convolution is applied to account for field inhomogeneities, eddy currents, and frequency drifts. Baseline corrections, as well as zero- and first-order phase corrections, are also applied. Analysis is done numerically.

The basis sets were specific to 9.4 T and provided by the vendor, with additional macromolecules and lipid signals simulated by LCModel. Each (TE_1, TE_2) combination requires an independent basis set. Some basis files were replaced by us with simulated spectra, using the previously described MATLAB software, to account for the difference in spectral response due to refocusing pulse shape, as described in chapter 1.8. They were converted to the LCModel .RAW format before they were inputted into the MakeBasis program included in the LCModel package. The $^{13}C_4$-Glu basis spectrum was also created this way. Two basis spectra were created for $^{13}C_4$-Glu, one for each of the two satellite peaks. This was done because the 2.19 ppm peak experiences complex overlap with a number of unaccounted signals. The 2.51 ppm peak was used for $^{13}C_4$-Glu quantification.

Fitted spectra were obtained along with tables of Cramér-Rao lower bound (CRLB) values for each metabolite in addition to concentrations. CRLB expresses a lower bound on the variance of an unbiased estimator of a deterministic parameter and is a valuable tool for evaluating quantification. It can provide the best case scenario of the standard deviation of a concentration estimate. It can be described by[37]:

$$\sigma_f \geq CRLB_f = \sqrt{(AF^{-1}A^H)} \tag{2.10}$$

σ_f is the standard deviation of a function f (for example, a concentration) of model parameters p. A is a matrix of the derivatives of f with respect to each p. and F is the Fisher information matrix, which can be conveyed as[37]:

$$F = \frac{1}{\sigma^2} real(P^T D^H DP) \tag{2.11}$$

σ is the standard deviation of the noise. D is the matrix of the derivative of each model function $\hat{x}_n$ with respect to each model parameter p. P is the prior knowledge matrix, which can be computed as the derivative of each model parameter p with respect to the unconstrained parameters p'.[37]

The CRLB is given as a percentage (relative CRLB), and the absolute CRLB can be calculated readily by multiplying by the concentration and dividing by 100. For example, a metabolite with a concentration of 10 mM and a CRLB of 10 % would have an absolute CRLB of (10 %) x (10 mM) / (100) = 1 mM. Twice the absolute CRLB, 2 mM, represents the 95 % confidence interval, implying that the true concentration lies within the range of 10 ± 1 mM 95 % of the time. It is important to note that CRLB is a measure of *precision*, as opposed to *accuracy*. Therefore, it is more useful for evaluating *differences* in concentrations, say, within a disease study. Accuracy is important for absolute concentration estimates and is evaluated by comparison with a "gold standard" if possible. When comparing results obtained with different equipment, or from different laboratories, accuracy is a more useful measure than precision.

Figure 2.21 shows an example of an LCModel-analyzed short-TE PRESS spectrum of rat brain at 9.4 T, along with the table of concentrations and CRLBs labelled.

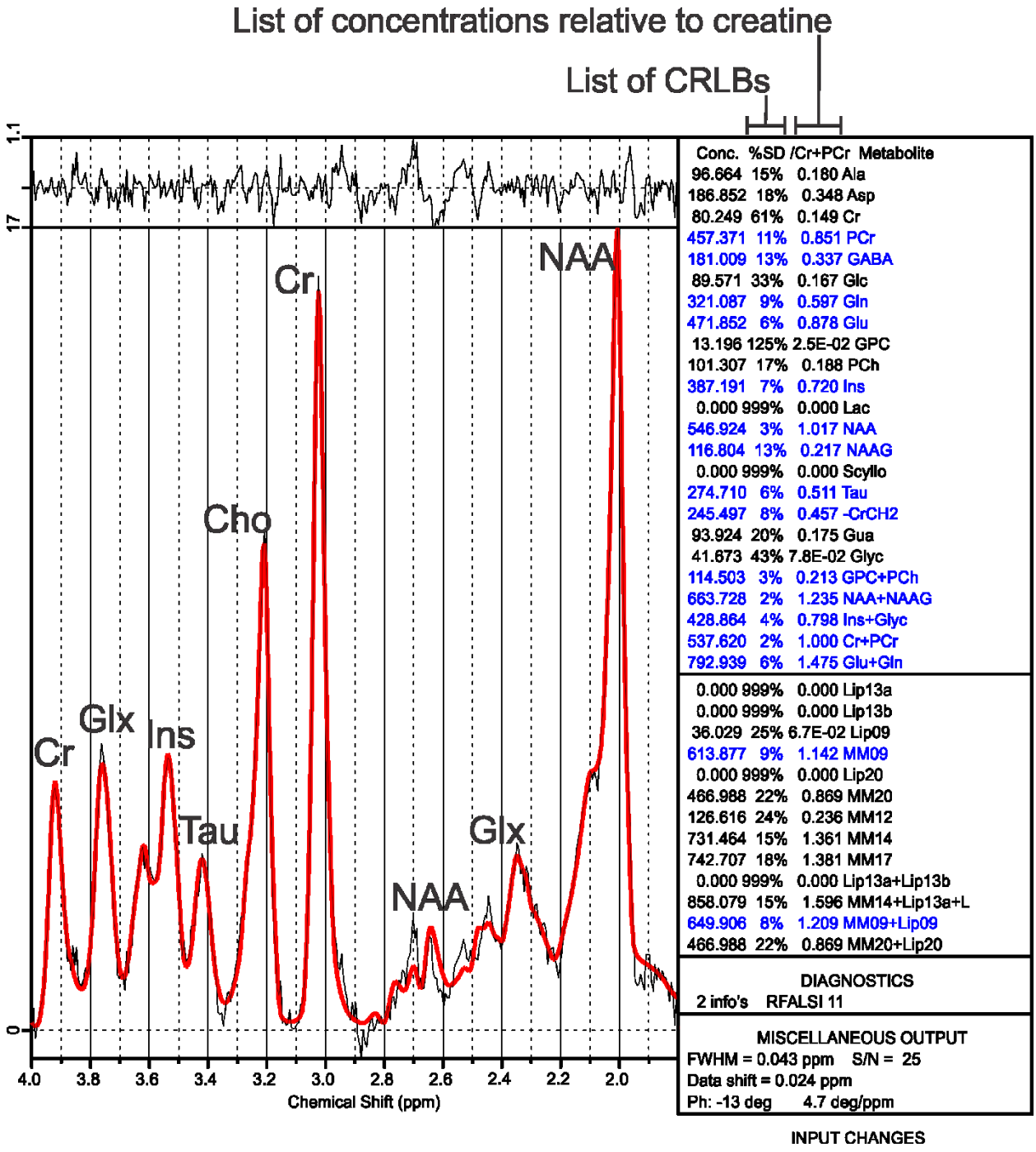

Figure 2.21: LCModel-analyzed short-TE PRESS spectrum of rat brain at 9.4 T, with the list of CRLBs and concentrations (relative to total creatine) labelled.

For the [U-$^{13}C_6$]-Glc infusion experiments, the total Glu pool (^{12}C-Glu + $^{13}C_4$-Glu) was estimated from the baseline spectrum (pre-infusion) by removing $^{13}C_4$-Glu from the basis set (assumed to be zero pre-infusion) and using LCModel to obtain a concentration estimate of ^{12}C-Glu. The concentration of NAA pre-infusion was found as well. The ratio of NAA to total Glu was kept constant throughout the analysis using the nratio and chrato commands in LCModel to maintain a constant sum of total Glu, as follows:

nratio = 13

chrato(13) = 'NAA/Glu+13CGlu = X.XX +- 0.01'

X.XX is the ratio of NAA to total Glu.

For the rat kidney experiments, Bet was not included in the provided basis set but was simulated. It is a simple system without J-coupling interactions and was modeled as such with the LCModel nsimul and chsimu commands, as follows:

nsimul = 15

chsimu(15) = 'Bet @ 3.25 +- 0. FWHM = -9. < 0. +- 0. AMP = 9.
@ 3.89 FWHM = -9. AMP = 2.'

The ncombi and chcomb commands were used to yield the concentration and CRLB of Cho + Bet, as follows:

ncombi = 17

chcomb(17) = 'PCh + GPC + Bet'

2.5 – REFERENCES

1. Bowery N, Smart T. GABA and glycine as neurotransmitters: a brief history. *British journal of pharmacology.* 2006;147(S1):S109-S119.

2. Bean BP. The action potential in mammalian central neurons. *Nature Reviews Neuroscience.* 2007;8(6):451.

3. Razak MA, Begum PS, Viswanath B, Rajagopal S. Multifarious beneficial effect of nonessential amino acid, Glycine: a review. *Oxidative medicine and cellular longevity.* 2017;2017.

4. Govindaraju V, Young K, Maudsley AA. Proton NMR chemical shifts and coupling constants for brain metabolites. *NMR in Biomedicine.* 2000;13(3):129-153.

5. Parthasarathy LK, Ratnam L, Seelan S, Tobias C, Casanova MF, Parthasarathy RN. Mammalian inositol 3-phosphate synthase: its role in the biosynthesis of brain inositol and its clinical use as a psychoactive agent. *Biology of Inositols and Phosphoinositides*: Springer; 2006:293-314.

6. Budavari S, O'Neil M, Smith A, Heckelman P. *The Merck Index: An Encyclopedia of Chemicals, Drugs, and Biologicals.* 11th ed: RSC Publishing; 1989.

7. Young VR, Ajami AM. Glutamate: an amino acid of particular distinction. *The Journal of nutrition.* 2000;130(4):892S-900S.

8. Henry P-G, Adriany G, Deelchand D, et al. In vivo 13C NMR spectroscopy and metabolic modeling in the brain: a practical perspective. *Magnetic resonance imaging.* 2006;24(4):527-539.

9. Meldrum BS. Glutamate as a neurotransmitter in the brain: review of physiology and pathology. *The Journal of nutrition.* 2000;130(4):1007S-1015S.

10. Deelchand DK, Uğurbil K, Henry PG. Investigating brain metabolism at high fields using localized 13C NMR spectroscopy without 1H decoupling. *Magnetic Resonance in Medicine.* 2006;55(2):279-286.

11. Henry PG, Lebon V, Vaufrey F, Brouillet E, Hantraye P, Bloch G. Decreased TCA cycle rate in the rat brain after acute 3-NP treatment measured by in vivo 1H-{13C} NMR spectroscopy. *Journal of neurochemistry.* 2002;82(4):857-866.

12. DeBerardinis RJ, Mancuso A, Daikhin E, et al. Beyond aerobic glycolysis: transformed cells can engage in glutamine metabolism that exceeds the requirement for protein and nucleotide synthesis. *Proceedings of the National Academy of Sciences.* 2007;104(49):19345-19350.

13. Waagepetersen HS, Sonnewald U, Schousboe A. Compartmentation of glutamine, glutamate, and GABA metabolism in neurons and astrocytes: functional implications. *The neuroscientist.* 2003;9(5):398-403.

14. Patel AB, de Graaf RA, Mason GF, Rothman DL, Shulman RG, Behar KL. The contribution of GABA to glutamate/glutamine cycling and energy metabolism in the rat cortex in vivo. *Proceedings of the National Academy of Sciences.* 2005;102(15):5588-5593.

15. Kaiser L, Young K, Meyerhoff D, Mueller S, Matson G. A detailed analysis of localized J-difference GABA editing: theoretical and experimental study at 4 T. *NMR in Biomedicine.* 2008;21(1):22-32.

16. Rigotti D, Inglese M, Babb J, et al. Serial whole-brain N-acetylaspartate concentration in healthy young adults. *American Journal of Neuroradiology.* 2007;28(9):1650-1651.

17. Baslow MH. N-acetylaspartate in the vertebrate brain: metabolism and function. *Neurochemical research.* 2003;28(6):941-953.

18. Ripps H, Shen W. Taurine: a “very essential” amino acid. *Molecular vision.* 2012;18:2673.

19. Cholewa JM, Wyszczelska-Rokiel M, Glowacki R, et al. Effects of betaine on body composition, performance, and homocysteine thiolactone. *Journal of the International Society of Sports Nutrition.* 2013;10(1):39.
20. Kimura S, Hayatsu H, Arimoto-Kobayashi S. Glycine betaine in beer as an antimutagenic substance against 2-chloro-4-methylthiobutanoic acid, the sanma-fish mutagen. *Mutation Research/Genetic Toxicology and Environmental Mutagenesis.* 1999;439(2):267-276.
21. Blüml S, Seymour KJ, Ross BD. Developmental changes in choline-and ethanolamine-containing compounds measured with proton-decoupled 31P MRS in in vivo human brain. *Magnetic Resonance in Medicine.* 1999;42(4):643-654.
22. Sanders LM, Zeisel SH. Choline: dietary requirements and role in brain development. *Nutrition today.* 2007;42(4):181.
23. Choi C, Ganji SK, DeBerardinis RJ, et al. Measurement of glycine in the human brain in vivo by 1H-MRS at 3 T: application in brain tumors. *Magnetic Resonance in Medicine.* 2011;66(3):609-618.
24. Chawla S, Wang S, Wolf R, et al. Arterial spin-labeling and MR spectroscopy in the differentiation of gliomas. *American Journal of Neuroradiology.* 2007;28(9):1683-1689.
25. Zhang X, Du Z, Liu J, He J. Γ-aminobutyric acid receptors affect the progression and migration of tumor cells. *Journal of Receptors and Signal Transduction.* 2014;34(6):431-439.
26. Maher EA, Marin-Valencia I, Bachoo RM, et al. Metabolism of [U-13C] glucose in human brain tumors in vivo. *NMR in Biomedicine.* 2012;25(11):1234-1244.
27. Gao H, Dong B, Jia J, et al. Application of ex vivo 1 H NMR metabonomics to the characterization and possible detection of renal cell carcinoma metastases. *Journal of Cancer Research and Clinical Oncology.* 2012;138(5):753-761.
28. Wang L, Zhang L, Yu Y, Wang Y, Niu N. The protective effects of taurine against early renal injury in STZ-induced diabetic rats, correlated with inhibition of renal LOX-1-mediated ICAM-1 expression. *Renal failure.* 2008;30(8):763-771.
29. Gao H, Dong B, Liu X, Xuan H, Huang Y, Lin D. Metabonomic profiling of renal cell carcinoma: high-resolution proton nuclear magnetic resonance spectroscopy of human serum with multivariate data analysis. *Analytica chimica acta.* 2008;624(2):269-277.
30. Thompson RB, Allen PS. A new multiple quantum filter design procedure for use on strongly coupled spin systems found in vivo: its application to glutamate. *Magnetic resonance in medicine.* 1998;39(5):762-771.
31. Thompson RB, Allen PS. Sources of variability in the response of coupled spins to the PRESS sequence and their potential impact on metabolite quantification. *Magnetic Resonance in Medicine.* 1999;41(6):1162-1169.
32. Yahya A, Allen PS. Effect of strong homonuclear proton coupling on localized 13C detection using PRESS. *Magnetic resonance in medicine.* 2005;54(6):1340-1350.
33. Cavanagh J, Fairbrother WJ, Palmer III AG, Skelton NJ. *Protein NMR spectroscopy: principles and practice.* Elsevier; 1995.
34. Haase A, Frahm J, Hanicke W, Matthaei D. 1H NMR chemical shift selective (CHESS) imaging. *Physics in Medicine & Biology.* 1985;30(4):341.
35. Provencher SW. Estimation of metabolite concentrations from localized in vivo proton NMR spectra. *Magnetic resonance in medicine.* 1993;30(6):672-679.
36. Golub GH, Pereyra V. The differentiation of pseudo-inverses and nonlinear least squares problems whose variables separate. *SIAM Journal on numerical analysis.* 1973;10(2):413-432.
37. Cavassila S, Deval S, Huegen C, Van Ormondt D, Graveron-Demilly D. Cramér–Rao bounds: an evaluation tool for quantitation. *NMR in Biomedicine.* 2001;14(4):278-283.

Chapter 3 - Optimized PRESS Sequence Timings for Measuring Glycine at 9.4 T

A version of this chapter has been published as:

Dobberthien, B. J., Tessier, A. G., Fallone, B. G., & Yahya, A. (2016). Optimized PRESS sequence timings for measuring glycine at 9.4 T: demonstration *in vivo* in rat brain. Biomedical Physics & Engineering Express, 2(2), 027003.

3.1 - INTRODUCTION

Glycine (Gly) is an important brain neurotransmitter whose levels are relevant in the study of a number of disorders including hyperglycinemia,[1] schizophrenia,[2-4] and brain tumours.[5-11] Proton (^{1}H) magnetic resonance spectroscopy (MRS) enables non-invasive measurement of various brain metabolite levels *in vivo*. However, the observation of Gly with MRS is challenging even at high field strengths such as 9.4 T,[12] where spectral resolution is largely improved over that of clinical field strengths. Glycine has two uncoupled protons that resonate at ≈ 3.55 ppm, yielding a singlet peak.[13] The overlapping multiplet signal of *myo*-inositol (mI), which is present in higher concentrations, obscures the Gly peak preventing its observation with standard *in-vivo* short-TE (echo time) PRESS (Point RESolved Spectroscopy)[14] and STEAM (STimulated Echo Acquisition Mode) single-shot localization sequences.[15] Furthermore, with short-TE values, there is macromolecule contamination in the Gly spectral region.[16] Therefore, spectral editing techniques have been implemented for Gly quantification. For example, Gly detection in the human brain has been shown using methods such as TE-optimized triple refocusing at 3 T,[17] optimized long-TE PRESS at 3 T,[6] and TE averaging at 4 T.[18,19] With the recent advancements in high field magnets, Gly has been measured in human brain with an optimized long-TE PRESS sequence at 7 T[20,21] and with an optimized short-TE SPECIAL (SPin ECho full Intensity Acquired Localization)[22] single spin echo technique at 7 T.[23] The latter technique has also been applied to measure Gly levels in rat brain at 9.4 T.[12,24] To our knowledge, the optimized SPECIAL technique is the only spectral editing method implemented for Gly quantification *in vivo* at 9.4 T. However, SPECIAL is not a readily available pulse sequence. In addition, it relies on the addition and subtraction of alternate scans for spatial localization making it prone to subtraction errors. PRESS is a more widely available pulse sequence which has not been optimized for resolving the Gly resonance from that

of mI at 9.4 T. In this work, we optimize the echo times (TE_1 and TE_2) of PRESS to facilitate Gly quantification at 9.4 T. The objective is achieved by exploiting the scalar coupling evolution of the mI protons that resonate in the 3.5 – 3.6 ppm spectral region as has been done at 3 T[6] and at 7 T.[20] The 3.5 – 3.6 ppm protons of mI are strongly-coupled even at 9.4 T rendering their response to PRESS field strength[25,26] dependent and a function of both TE_1 and TE_2 and not just on their sum.[27] The Gly peak can be isolated by determining a (TE_1, TE_2) combination which yields minimal mI signal in the Gly spectral region. The (TE_1, TE_2) combinations that resolved Gly at 3 T[6] and at 7 T[20] were found to be (60 ms, 100 ms) and (101 ms, 51 ms), respectively. Because of the field strength dependence of the evolution of the strongly-coupled mI protons, the determined timings at other field strengths cannot be assumed to be appropriate for the desired purpose at 9.4 T. The objective of this paper is to investigate the response of mI protons in the Gly spectral region to PRESS at 9.4 T to find a (TE_1, TE_2) combination that results in minimal contamination of Gly from mI. The presented work is of value to those who wish to measure Gly in brain at 9.4 T, a field strength widely used for animal magnetic resonance studies, with a readily available pulse sequence. The efficacy of the optimized PRESS sequence is verified on phantom solutions as well as on rat brain *in vivo*.

3.2 – MATERIALS AND METHODS

Experiments were performed with a 9.4 Tesla, 21.5 cm diameter MRI (magnetic resonance imaging) scanner (Magnex Scientific, Oxford, UK) in conjunction with a TMX console (National Research Council of Canada Institute for Biodiagnostics, West, Calgary, AB, Canada). MRI system details are as discussed in section 2.3.1. A 4.3 cm diameter birdcage radiofrequency (RF)

coil (National Research Council of Canada Institute for Biodiagnostics, West) was used for both transmission and reception.

Spectra were acquired from four 10 mL spherical phantom solutions, each prepared in distilled water. One phantom solution consisted of 10 mM creatine (Cr), and 50 mM myo-inositol (mI). Another contained 10 mM Cr and 10 mM Gly, while the third phantom solution was composed of 10 mM Cr, 50 mM mI, and 10 mM Gly. The fourth phantom contained 10 mM Cr, 10 mM Gly, and 10 mM threonine (Thr). Threonine has a spin which resonates at about 3.58 ppm and produces a doublet due to its coupling with a spin at 4.24 ppm.[28] Threonine could potentially contaminate Gly signal.[20] All chemicals were purchased from SigmaAldrich Canada (SigmaAldrich Canada, Oakville, ON, Canada). The Cr/Gly and Cr/mI/Gly phantoms were created from an initial larger 10 mM Cr/10 mM Gly mixture to ensure that the Cr and Gly concentrations were the same in each sphere. Spectra were obtained from $5 \times 5 \times 5$ mm^3 voxels placed in the centre of the phantoms. A PRESS sequence, consisting of 2 ms sinc RF pulses of 3000 Hz bandwidth was employed. The spectra were acquired in 32 averages with a repetition time, TR, of 5 s. A total of 8192 complex data points were collected at a sampling frequency of 10,000 Hz and a 4 step phase cycling scheme was applied. Additional phantom experiment details are included in section 2.3.2.

Numerical calculations of the expected mI signal in response to PRESS as a function of TE_1 and TE_2 were calculated using the previously developed MATLAB program, based on density matrix calculations.[27] The shape of the 2 ms refocusing pulses along with slice selection gradients were included in the calculations and spectra were calculated as 8192 data points with a sampling frequency of 10,000 Hz. Spectra were calculated for TE_1 and TE_2 values ranging from 2 to 120 ms in steps of 2 ms. The minimum TE is limited by the duration of the refocusing pulse. The mI area

in the 3.52 -3.57 ppm spectral region was normalized to the mI area acquired with (TE_1, TE_2) = (2 ms, 2 ms) and a contour plot of the normalized areas as a function of both TE values was generated. Regions between contours were shaded based on the absolute value of the normalized mI signal. The gray scale correlated with the absolute value of the contour level. The chemical shift and scalar coupling constants of mI were based on those provided by Ref. [29]. Additional details about the numerical methods can be found in in section 2.2.

For both phantom and *in-vivo* scans, shimming was performed on the water signal by manually adjusting the first order shims until the peak amplitude was maximized. A chemical shift selective (CHESS)[30] sequence was used for water suppression and the frequency offset of the PRESS RF pulses was set to 3.4 ppm, approximately centred between Cr and Gly resonances.

Measurements were obtained from the 10 mM Cr and 50 mM mI solution with several echo time combinations of (TE_1, TE_2), with the shortest achievable being (12 ms, 9 ms). Spectra were acquired from the sample with a number of TE combinations with TE_1 and TE_2 ranging from 20 ms – 120 ms (in 10 ms increments) and such that the total TE did not exceed 200 ms to avoid excessive signal losses due to T_2 relaxation. Spectra were filtered, zero-filled, Fourier transformed, phase corrected and baseline corrected with software provided by National Research Council of Canada (Spectrum Viewer v. 2.00.002, National Research Council of Canada Institute for Biodiagnostics, West, Calgary, AB, Canada). Processed spectra were assessed in MATLAB (Mathworks, Natick, Massachusetts, United States) by examining the 3.52-3.57 ppm mI spectral region of the Gly resonance. An echo time combination was judged to be suitable for Gly observation based on the numerically generated contour plot and experimental confirmation. Once an optimal TE combination was determined, spectra were acquired from the Cr/Gly and Cr/Gly/mI phantoms (both phantoms were created from the same Cr/Gly solution) and the Gly/Cr area ratios

were compared using the 3.02 ppm Cr peak. A spectrum was also obtained from the Cr/Thr/Gly phantom with the selected optimal TE values. It was evaluated by determining the Thr peak area in the 3.57-3.60 ppm spectral region relative to the area of the Gly resonance.

In-vivo experiments were performed on four female Sprague Dawley rats (ages 4, 5, 5, and 11 months) placed in a prone position. A single loop 24 mm diameter surface coil (Doty Scientific, Inc., Columbia, South Carolina, United States) was used for both transmission and reception. It was placed on top of the rat's head, behind the eyes, such that the brain was centred in its field of view. Temperature was monitored with a rectal probe and a heating module was employed to maintain a rat body temperature of 37 ˚C. A probe placed on the abdomen was used for monitoring respiration and the pattern provided feedback for respiratory gating. Anaesthetic containing 2 % isoflurane was administered to the rat's airway via a plastic tube and nose cone system. Spin echo images were obtained for voxel placement. The imaging sequence employed a TE of 13 ms and a TR of at least 1250 ms. Fifteen transverse slices and 7 coronal slices (2 mm thickness) were obtained of the rat brain. A $5 \times 5 \times 5$ mm^3 voxel was approximately centred in the brain, with its centre a distance of ≈ 6 mm from the surface coil. Typically, a water linewidth of ≈ 30-40 Hz was achieved. Two spectra were acquired from each rat, namely, one with a short-TE of (TE_1, TE_2) = (12 ms, 9 ms) and one with the optimized TE combination. Both spectra were measured as 2048 complex data points with a TR of at least 3 s. The short-TE spectrum and the optimized-TE spectrum were obtained in 128 and 256 averages, respectively. For each TE, a water-unsuppressed scan was acquired with 8 averages for eddy current compensation. A description of the rat brain experiments can be found in section 2.3.3.

LCModel software[31] was used to analyze the *in-vivo* spectra. The basis sets were provided by the vendor, with additional macromolecules and lipid signals simulated by LCModel. Each

(TE_1, TE_2) combination requires an independent basis set; therefore, two sets were used. Each basis set included alanine (Ala), Cr, phosphocreatine (PCr), glutamine (Gln), glutamate (Glu), glycerylphosphorylcholine (GPC), phosphocholine (PCh), glutathione (GSH), mI, lactate (Lac), *N*-acetylaspartate (NAA), *N*-acetylaspartylglutamate (NAAG), *scyllo*-inositol (Scyllo), taurine (Tau), and Gly. Fitted spectra were obtained in the range of 0.2 to 4.0 ppm along with tables of Cramér-Rao lower bound (CRLB) values for each metabolite in addition to concentrations relative to total creatine (Cr + PCr). Total creatine concentration in rat brain was assumed to be 8 mM[32] and relaxation was not taken into account. Additional details regarding data analysis are in section 2.4.

3.3 - RESULTS

Figure 3.1 displays some mI spectra acquired from the 10 mM Cr and 50 mM mI phantom with various TE combinations. The numerically calculated spectra are overlaid in dashed lines; there is clear agreement between experiment and theory and J-modulation of mI signal in the 3.45 to 3.7 ppm spectral region is visible.

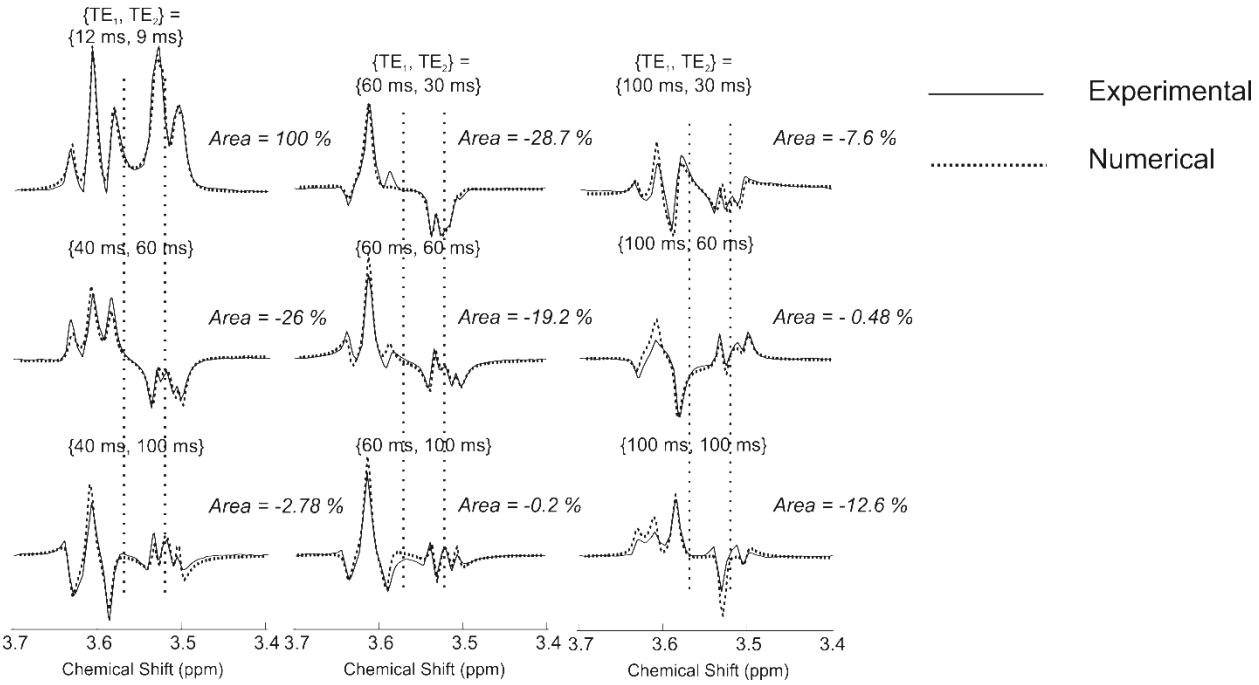

Figure 3.1: Some experimental and calculated spectra acquired from the 50 mM mI phantom with PRESS are shown. (TE_1, TE_2) combinations are indicated above each spectrum. Minimal mI contribution to the Gly spectral region (indicated by the dotted lines) is present when (TE_1, TE_2) = (60 ms, 100 ms). The mI contribution was assessed from the simulated spectra by calculating the area in the indicated Gly spectral region normalized to that obtained from the short-TE spectrum. The normalized areas are indicated for each TE combination.

Figure 3.2 displays the contour plot of the normalized mI signal areas in the Gly spectral region. The bright regions correspond to where the normalized mI signal area is between -0.05 – 0.05. Experimental spectra acquired with (TE_1, TE_2) values of (30 ms, 100 ms), (60 ms, 70 ms), (60ms, 80 ms), (60 ms, 100 ms) and (90 ms, 40 ms) were examined. The TE combinations are indicated on Fig. 3.2. Echo time regions where the total TE exceeded 200 ms were not considered (to avoid excessive T_2 losses) and the first bright zone was also not considered as the timings were

too short to ensure adequate macromolecule suppression *in vivo*. Of the specifically examined TE combinations, an optimal (TE_1, TE_2) combination that minimizes mI signal in the Gly spectral region was found to be (60 ms, 100 ms). The maximum amplitude and total area of the mI signal in the 3.52-3.57 ppm region is 5.2 % and -6.1 %, respectively, of the corresponding values obtained from the (TE_1, TE_2) = (12 ms, 9 ms) short-TE spectrum.

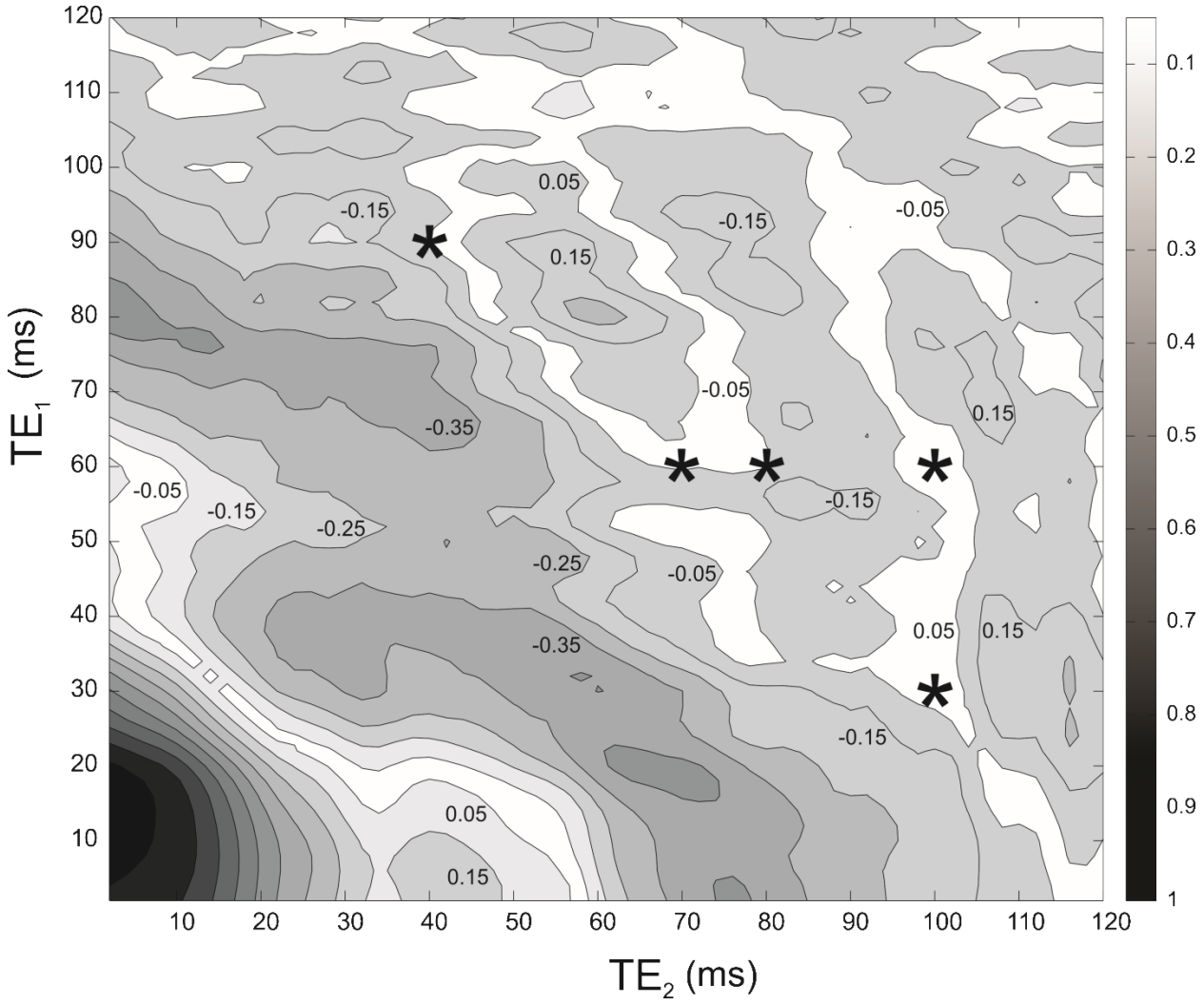

Figure 3.2: Calculated contour plot with mI areas in the Gly spectra region normalized to the area calculated when $TE_1 = TE_2 = 2$ ms. The gray scale corresponds to absolute values of the contour

levels. Some positive and negative contour values are labelled on the plot. The asterisks indicate TE combinations specifically examined as optimal TE candidates.

Figure 3.3(a) shows short-TE spectra acquired from the 10 mM Cr, 10 mM Gly, and 50 mM mI phantom and from the 10 mM Cr and 50 mM mI phantom. The Gly peak is not visible and its contribution can be seen as a broadening and an amplitude increase of the ≈ 3.54 ppm mI peak. With the optimized (TE_1, TE_2) = (60 ms, 100 ms) timing combination, as seen in Fig. 3.3(b), the Gly resonance obtained from the Cr/Gly/mI phantom compares well with that measured from the 10 mM Cr and 10 mM Gly phantom. The Gly/Cr area ratio calculated from the Cr/Gly/mI spectrum is ≈ 11 % less than the ratio obtained from the Cr/Gly phantom spectrum. Figure 3.3(c) displays a spectrum obtained from the 10 mM Cr, 10 mM Gly, and 10 mM Thr phantom with (TE_1, TE_2) = (60 ms, 100 ms). The Gly resonance closely matches that acquired from the Cr/Gly phantom spectrum and the Thr resonance is almost entirely outside the Gly spectral region. The Thr peak area is ≈ -17% of the Gly peak area.

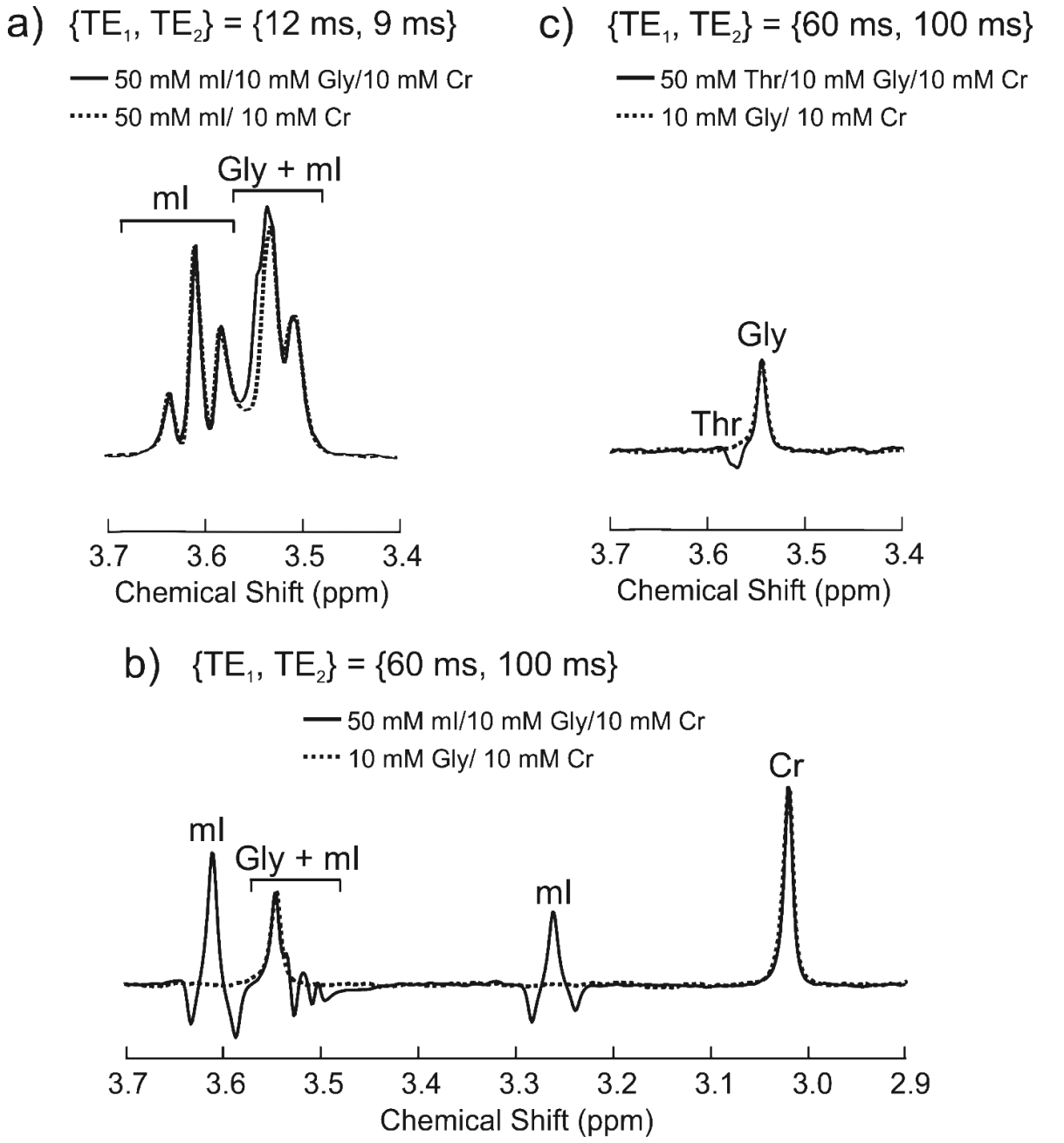

Figure 3.3: Spectra obtained from the various phantoms with PRESS. (TE_1, TE_2) combinations are indicated above each spectrum, along with the phantom constituents. In (a), the short-TE mI/Gly spectrum differs only slightly from the mI spectrum. With the optimized TE combination in (b), the mI/Gly spectrum closely matches that of Gly. The Thr/Gly spectrum in (c) shows the small negative Thr yield at the optimized TE values.

Figure 3.4(a) shows the PRESS voxel placement in a coronal and transverse image of one of the rat brains. Panels (b) and (c) display LCModel eddy-current and baseline corrected spectra acquired from the voxel with (TE_1, TE_2) = (12 ms, 9 ms) and (60 ms, 100 ms), overlapped with their corresponding LCModel fits. Heavy overlap between mI and Gly can be seen in the short-TE spectrum (CRLB of 37 % for Gly) unlike in the optimized long-TE spectrum where there exists a clear distinction between the Gly and mI peaks. When Gly is included in the basis set, as in Fig. 3.4(c), the residual signal in the Gly spectral region is minimized to the noise level. The CRLB of Gly is 15 %, and the relative concentration to total creatine is 0.192, giving an absolute concentration of 1.54 mM, assuming a total creatine concentration of 8 mM. The NAA signal to noise ratio (SNR) provided by LCModel is 16 and the obtained Gly CRLB of 15 % at this level of SNR is consistent with what was determined by Ref. [12] at 9.4 T. The LCModel fit of the (60 ms, 100 ms) *in -vivo* spectrum with a basis set that does not include Gly is shown in Fig. 3.4(d), where a discernable, positive residual can be seen in the Gly spectral region. Figure 3.5 shows processed (TE1, TE2) = (60 ms, 100 ms) spectra obtained from the three other rats along with the LCModel fits. Table 3.1 summarizes the results from all four rats.

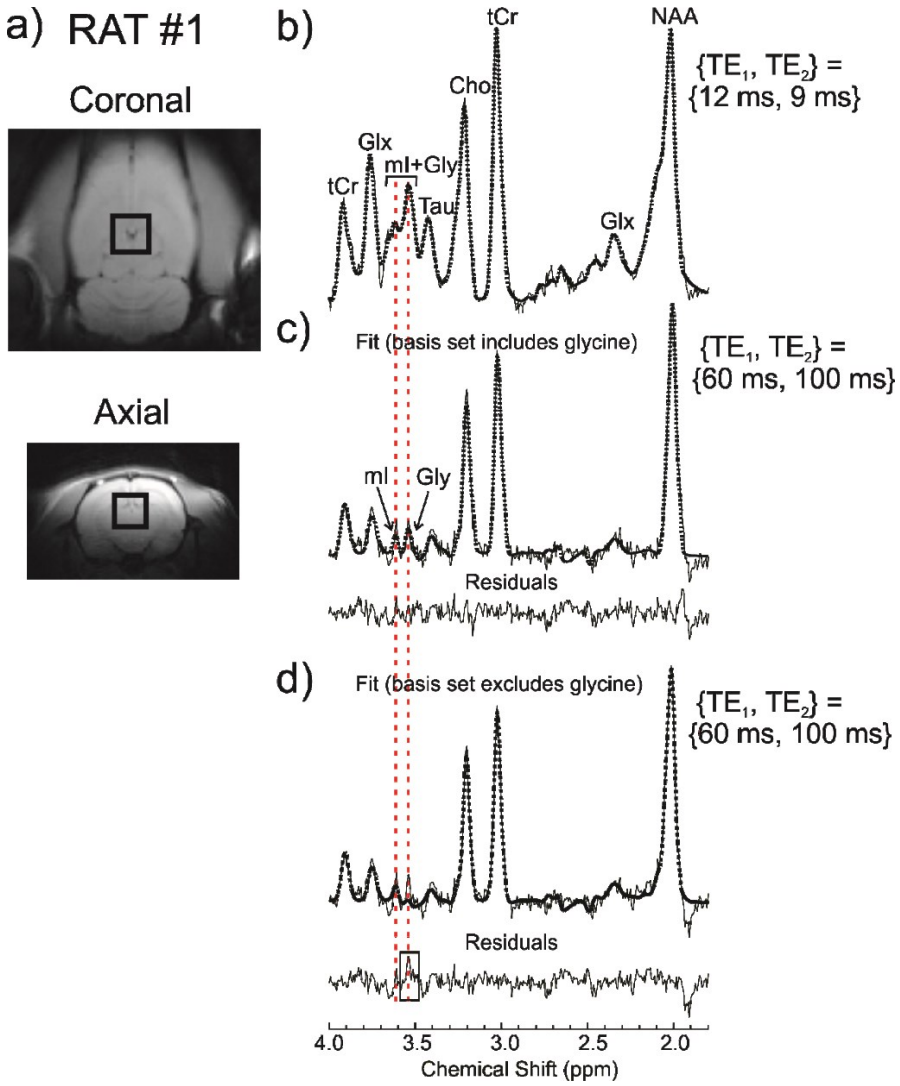

Figure 3.4: Coronal and transverse images of one of the rat brains in (a) shows the location of the voxel used for PRESS. The acquired spectra from the rat are displayed, with the corresponding LCmodel fits overlaid. In (b), a spectrum measured with (TE_1, TE_2) = (12 ms, 9 ms) shows the overlap between mI and Gly, whereas with the optimized (TE_1, TE_2) of (60 ms, 100 ms) the mI and Gly peaks are clearly separated as shown in panel (c); the vertical dotted lines indicate the centre of each peak. The LCmodel fit in (c) includes Gly in the basis set while the fit in (d) does not. Excluding Gly from the basis set results in a clearly visible residual signal in the Gly spectral region (enclosed by the rectangle).

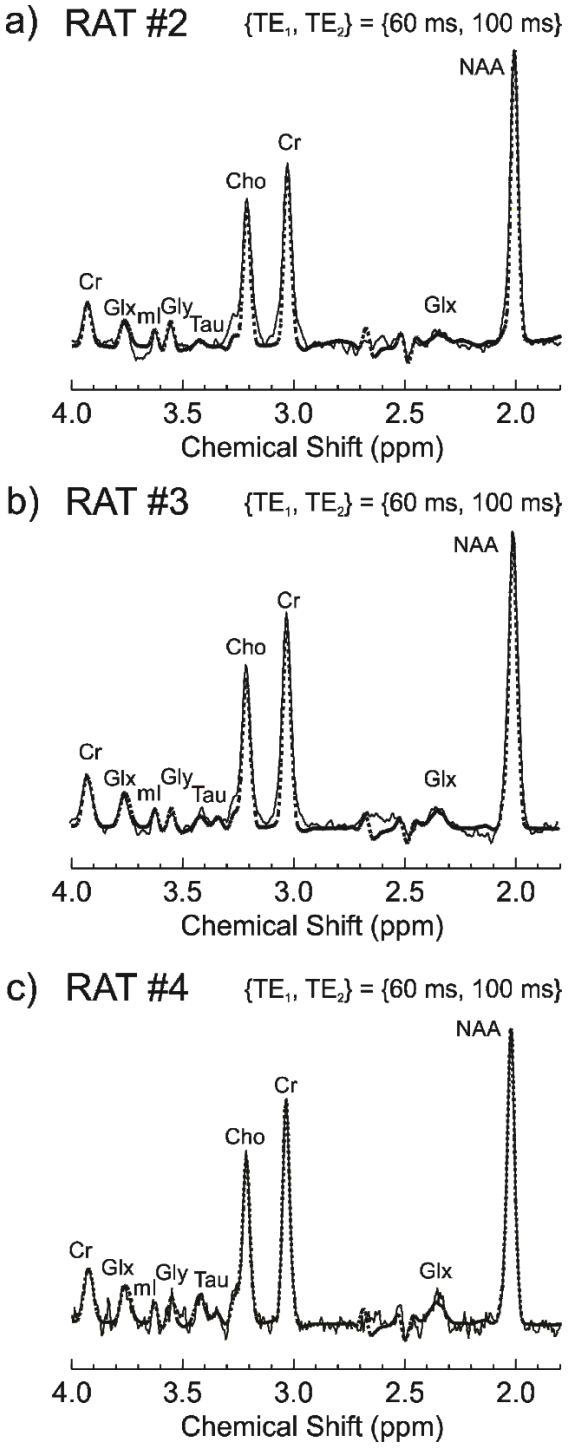

Figure 3.5: Processed *in-vivo* spectra acquired from additional rats with the optimized TE values. Clear resolution between the mI and Gly peaks can be seen. The dashed spectra are the LCModel fits.

Rat number	Gly CRLB (%) (long-TE)	Gly CRLB (%) (short-TE)	Gly/Cr Ratio	Gly Concentration (mM)	LCModel NAA SNR
1	15	37	0.192	1.54	16
2	19	28	0.190	1.52	19
3	20	52	0.129	1.03	20
4	16	31	0.165	1.32	19

Table 3.1: Summary of LCModel results obtained from the three rats. The Cr concentration was assumed to be 8 mM.

3.4 - DISCUSSION

Glycine is an important brain neurotransmitter and its levels can be measured by proton MRS through its singlet resonance at ≈ 3.55 ppm, which arises from two uncoupled protons. However, the peak is overlapped by overwhelming mI signal *in vivo* when acquiring spectra with standard short-TE techniques. To quantify Gly, the signal contribution from mI in the Gly spectral region must be minimized. The readily available PRESS sequence has been previously optimized by others for this purpose at 3 T[6] and 7 T.[20] To our knowledge, PRESS has not been previously optimized for Gly detection at 9.4 T and in the present study, we show that a PRESS sequence with (TE_1, TE_2) = (60 ms, 100 ms) can be used to resolve and detect glycine at 9.4 T *in vivo* in rat brain. It is interesting to note that the determined timings are the same as those found at 3 T[6]; however, the evolution of the mI protons are field strength dependent. In addition, the coupling evolution of the mI protons during the slice selective refocusing pulses affects the outcome to some extent.[27] The differences in evolution can be seen when comparing mI spectra from Fig. 3.1 of Ref. [6] with mI spectra in Fig. 3.1 of this work. As specific examples, it can be seen that the mI

signal around 3.54 ppm is positive at 3 T when (TE_1, TE_2) = (60 ms, 60 ms) and (100 ms, 100 ms) but negative at 9.4 T. The mI protons contributing signal in the Gly spectral region are strongly coupled even at 9.4 T (scalar coupling to chemical shift ratio of 0.28); therefore, a weak-coupling approximation cannot be employed. The complexity of the evolution of strongly-coupled spins renders it difficult to calculate the signal response analytically.[25] We investigated the field strength dependence of mI signal acquired with (TE_1, TE_2) = (60 ms, 100 ms) in the 3.52 – 3.57 ppm spectral region by calculating the response of mI to a PRESS sequence with ideal hard pulses (to remove the dependence on pulse shape). The areas normalized to the corresponding TE = 0 signal area were calculated for 1.5 T, 3 T, 4.5 T, 6 T, 7 T, 9 T and 9.4 T and were found to be 0.47 %, 8.8 %, 3.8 %, 6.2 %, -8.6 %, -19.3 % and -7.3 %, respectively. The difficulty in predicting the response is evident by the significant difference between the 9 T and 9.4 T signal yields. At 7 T the optimal TE for mI suppression in the Gly region was found to be (TE_1, TE_2) = (101 ms, 51 ms).[20] The optimizations at 3 T and 7 T also included the effects of evolution during RF pulses.[6,20]

In this work, with (TE_1, TE_2) = (60 ms, 100 ms), the mI signal area in the 3.52-3.57 ppm region was reduced to ≈ -6 % of the corresponding area obtained with the short–TE sequence. The higher area compared to the contour plot prediction can be attributed to the small deviations between experiment and theory as shown in Fig. 3.1.

The negative mI contribution reduces Gly signal by ≈ 11 % in a phantom solution in which the mI to Gly ratio is 5. On average, the mI concentration was found to be 5.37 mM from LCModel analysis of the short-TE spectra (assuming a Cr concentration of 8 mM). The LCModel basis set for the optimal TE combination accounts for the small mI contributions in the Gly region in the long-TE spectra and an average Gly to Cr concentration ratio of 0.169 (standard deviation 0.030) was obtained from the three rats (CRLB values for Gly ranged between 15 – 20 % which are

considered acceptable[33] and are a significant improvement over the short-TE Gly CRLB range of 28 – 52 %). Assuming a total creatine concentration of 8 mM,[32] this yields an average Gly concentration of 1.35 mM. Threonine was not included in the basis set; a Thr concentration of 0.8 mM has been reported for rat brain.[28] Our phantom experiments indicate that in the worst case where Gly and Thr completely overlap *in vivo* the Gly concentration would be underestimated by less than 10 %, assuming a Thr/Gly concentration ratio of 0.6. The determined average Gly concentration of 1.35 mM is within the range of previously biochemically determined rat brain Gly levels of 1.2 – 1.66 mM[34,35] and somewhat higher than the average Gly concentration of 1.12 mM measured by Ref. [12] with SPECIAL at 9.4 T. Admittedly, T_2 relaxation was not compensated for in this work since to our knowledge, the T_2 value for Gly protons has not been determined at any field strength. References [6,20] assumed the mean T_2 of NAA and 3.02 ppm Cr to be the T_2 value of Gly. At 9.4 T a T_2 of 294.3 ms and 171.1 ms has been determined for NAA and Cr, respectively,[36] yielding a mean of 232.7 ms. If the assumption of Refs. [6,20] is made, then correcting Cr and Gly for T_2 relaxation losses (assuming simple monoexponential decay functions) yields a mean Gly concentration of 1.06 mM for the three rats, which is not within the biochemically determined Gly concentration range but is closer to the average value determined by Ref. [12] with SPECIAL.

The SPECIAL technique optimized for Gly detection at 9.4 T[12] employed a TE of 20 ms, which has the advantage of reduced losses due to T_2 relaxation. However, the technique does not completely resolve Gly from mI and therefore requires LCModel fitting for quantification. The optimized long-TE PRESS sequence enables Gly/Cr levels to be determined by simple peak fitting if necessary (macromolecule signal is also attenuated); the few percent loss due to mI contamination can be compensated for. Furthermore, despite the loss of signal due to T_2 relaxation

an average SNR of 18.5 was obtained for NAA from the four rats with an average Gly CRLB of 17.5 %, which is comparable to the CRLB dependence on SNR which was reported by Ref. [12]. The presented work demonstrates that the commonly employed PRESS sequence is a convenient option for isolating and quantifying the Gly resonance, for example in studies of animal models of brain diseases at 9.4 T.

3.5 - CONCLUSION

A long-TE PRESS sequence with (TE_1, TE_2) = (60 ms, 100 ms) was found to be optimal for resolving Gly signal from that of mI at 9.4 T. The timings minimized mI signal in the Gly spectral region by exploiting the J-coupling evolution of its strongly-coupled protons.

3.6 - REFERENCES

1. Huisman TAGM, Thiel T, Steinmann B, Zeilinger G, Martin E. Proton magnetic resonance spectroscopy of the brain of a neonate with nonketotic hyperglycinemia: in vivo-in vitro (ex vivo) correlation. *Eur Radiol.* 2002;12:858-861.

2. Heresco-Levy U, Ermilov M, Lichtenberg P, Bar G, Javitt DC. High-dose glycine added to olanzapine and risperidone for the treatment of schizophrenia. *Biological Psychiatry.* 2004;55:165-171.

3. Eulenburg V, Armsen W, Betz H, Gomeza J. Glycine transporters: essential regulators of neurotransmission. *Trends in Biochemical Sciences.* 2005;30:325-333.

4. Javitt DC. Glycine transport inhibitors and the treatment of schizophrenia. *Biological Psychiatry.* 2008;63:6-8.

5. Bobek-Billewicz B, Hebda A, Stasik-Pres G, Majchrzak K, Żmuda E, Trojanowska A. Measurement of glycine in a brain and brain tumors by means of 1H MRS. *Folia Neuropathol.* 2010;48:190-199.

6. Choi C, Ganji SK, DeBerardinis RJ, et al. Measurement of glycine in the human brain in vivo by 1H-MRS at 3 T: application in brain tumors. *Magnetic Resonance in Medicine.* 2011;66:609-618.

7. Davies NP, Wilson M, Natarajan K, et al. Non-invasive detection of glycine as a biomarker of malignancy in childhood brain tumours using *in-vivo* 1H MRS at 1.5 Tesla confirmed by *ex-vivo* high-resolution magic-angle spinning NMR. *NMR in Biomedicine.* 2010;23:80-87.

8. Hattingen E, Lanfermann H, Quick J, Franz K, Zanella FE, Pilatus U. 1H MR spectroscopic imaging with short and long echo time to discriminate glycine in glial tumours. *Magn Reson Mater Phy.* 2009;22:33-41.

9. Kinoshita Y, Kajiwara H, Yokota A, Koga Y. Proton magnetic resonance spectrsocopy of brain tumors: an in vitro study. *Neurosurgery.* 1994;35:606-614.

10. Lehnhardt F-G, Bock C, Röhn G, Ernestus R-I, Hoehn M. Metabolic differences between primary and recurrent human brain tumors: a 1H NMR spectroscopic investigation. *NMR in Biomedicine.* 2005;18:371-382.

11. Righi V, Andronesi OC, Mintzopoulos D, Black PM, Tzika AA. High-resolution magic angle spinning magnetic resonance spectroscopy detects glycine as a biomarker in brain tumors. *Int J Oncol.* 2010;36:301-306.

12. Gambarota G, Xin L, Perazzolo C, Kohler I, Mlynárik V, Gruetter R. In vivo 1H NMR measurement of glycine in rat brain at 9.4 T at short echo time. *Magnetic Resonance in Medicine.* 2008;60:727-731.

13. Govindaraju V, Young K, Maudsley AA. Proton NMR chemical shifts and coupling constants for brain metabolites. *NMR in Biomedicine.* 2000;13:129-153.

14. Bottomley PA. Selective volume method for performing localized NMR spectroscopy. U.S. patent 4,480,228; 1984.

15. Frahm J, Merboldt K-D, Hänicke W. Localized proton spectroscopy using stimulated echoes. *Journal of Magnetic Resonance.* 1987;72:502-508.

16. Hofmann L, Slotboom J, Boesch C, Kreis R. Characterization of the macromolecule baseline in localized 1H-MR spectra of human brain. *Magnetic Resonance in Medicine.* 2001;46(5):855-863.

17. Choi C, Bhardwaj PP, Seres P, Kalra S, Tibbo PG, Coupland NJ. Measurement of glycine in human brain by triple refocusing 1H-MRS in vivo at 3.0 T. *Magnetic Resonance in Medicine.* 2008;59:59-64.

18. Kaufman MJ, Prescot AP, Ongur D, et al. Oral glycine administration increases brain glycine/creatine ratios in men: A proton magnetic resonance spectroscopy study. *Psychiatry Research: Neuroimaging.* 2009;173:143-149.

19. Prescot AP, Frederick Bd, Wang L, et al. In vivo detection of brain glycine with echo-time-averaged 1H magnetic resonance spectroscopy at 4.0 T. *Magnetic Resonance in Medicine.* 2006;55:681-686.

20. Choi C, Douglas D, Hawesa H, Jindal A, Storey C, Dimitrov I. Measurement of glycine in human prefrontal brain by point-resolved spectroscopy at 7.0 tesla in vivo. *Magnetic Resonance in Medicine.* 2009;62:1305-1310.

21. Banerjee A, Ganji S, Hulsey K, et al. Measurement of glycine in gray and white matter in the human brain in vivo by 1H MRS at 7.0 T. *Magnetic Resonance in Medicine.* 2012;68:325-331.

22. Mlynárik V, Gambarota G, Frenkel H, Gruetter R. Localized short-echo-time proton MR spectroscopy with full signal-intensity acquisition. *Magnetic Resonance in Medicine.* 2006;56:965-970.

23. Gambarota G, Mekle R, Xin L, et al. In vivo measurement of glycine with short echo-time 1H MRS in human brain at 7 T. *Magn Reson Mater Phy.* 2009;22:1-4.

24. Xin L, Gambarota G, Duarte JMN, Mlynárik V, Gruetter R. Direct *in vivo* measurement of glycine and the neurochemical profile in the rat medulla oblongata. *NMR in Biomedicine.* 2010;23:1097-1102.

25. Kay LE, McClung RED. A product operator description of AB and ABX spin systems. *Journal of Magnetic Resonance.* 1988;77:258-273.

26. Wilman AH, Allen PS. The response of the strongly coupled AB system of citrate to typical ^{1}H MRS localization sequences. *Journal of Magnetic Resonance, Series B.* 1995;107:25-33.

27. Thompson RB, Allen PS. Sources of variability in the response of coupled spins to the PRESS sequence and their potential impact on metabolite quantification. *Magnetic Resonance in Medicine.* 1999;41:1162-1169.

28. Marjanska M, Henry P-G, Uğurbil K, Gruetter R. Editing through multiple bonds: Threonine detection. *Magnetic Resonance in Medicine.* 2008;59:245-251.

29. Govindaraju V, Young K, Maudsley A. Proton NMR chemical shifts and coupling constants for brain metabolites. *NMR in Biomedicine.* 2000;13:129-153.

30. Haase A, Frahm J, Hnicke W, Matthaei D. 1H NMR chemical shift selective (CHESS) imaging. *Physics in Medicine & Biology.* 1985;30:341-344.

31. Provencher SW. Estimation of Metabolite Concentrations from Localized *in Vivo* Proton NMR Spectra. *Magnetic Resonance in Medicine.* 1993;30:672-679.

32. Pfeuffer J, Tkac I, Provencher SW, Gruetter R. Toward an *in vivo* neurochemical profile: quantification of 18 metabolites in short-echo-time 1H NMR spectra of the rat brain. *Journal of Magnetic Resonance.* 1999;141:104-120.

33. Cudalbu C, Mlynárik V, Xin L, Gruetter R. Comparison of T1 Relaxation Times of the Neurochemical Profile in Rat Brain at 9.4 Tesla and 14.1 Tesla. *Magnetic Resonance in Medicine.* 2009;62:862-867.

34. Cutler RWP, Dudzinski DS. Regional changes in amino acid content in developing rat brain. *J Neurochem.* 1974;23:1005-1009.

35. Mandel P, Mark J. The influence of nitrogen deprivation on free amino acids in rat brain. *J Neurochem.* 1965;12:987-992.

36. de Graaf RA, Brown PB, McIntyre S, Nixon TW, Behar KL, Rothman DL. High magnetic field water and metabolite proton T1 and T2 relaxation in rat brain in vivo. *Magnetic Resonance in Medicine.* 2006;56:386-394.

Chapter 4 - Improved Resolution of Glutamate, Glutamine and GABA with Optimized PRESS Sequence Timings for their Simultaneous Quantification at 9.4 T

A version of this chapter has been published as:

Dobberthien, B. J., Tessier, A. G., & Yahya, A. (2018). Improved resolution of glutamate, glutamine and γ-aminobutyric acid with optimized point-resolved spectroscopy sequence timings for their simultaneous quantification at 9.4 T. NMR in Biomedicine, 31(1), e3851.

4.1 - INTRODUCTION

Glutamate (Glu) is the major excitatory neurotransmitter in the central nervous system,[1] while glutamine (Gln) is a precursor to and a storage form of it. Glutamine is created in astrocytes by the enzyme glutamine synthetase from Glu and ammonia, as part of the Glu/Gln cycle.[2] Altered levels of Glu and Gln have been linked to a number of diseases [3], including schizophrenia,[4] depression,[5] epilepsy,[6] MS (Multiple Sclerosis),[7] ALS (Amyotrophic Lateral Sclerosis),[8] Huntington's disease,[9] Alzheimer's disease,[10] brain trauma,[11] and brain tumors.[12] Another product of Glu metabolism is γ-aminobutyric acid (GABA), the primary inhibitory neurotransmitter in the brain and which also contributes to Glu/Gln cycling.[13] Its quantification is relevant to multiple disorders,[14] including schizophrenia,[15] depression,[16] epilepsy,[17] and cancer.[18] *In-vivo* biochemical analysis of the three metabolites is desirable for research involving neuropsychiatric and neurological disorders and for investigating their potential role as diagnostic markers. Proton (^{1}H) Magnetic Resonance Spectroscopy (MRS) enables non-invasive biochemical analysis and measurements of metabolites *in vivo*. Glutamate and Gln can both be described as AMNPQ spin systems, where the P and Q spins refer to the C4 protons and resonate at ≈ 2.35 ppm and ≈ 2.45 ppm for Glu and Gln, respectively.[19] The C4 protons are often employed to quantify Glu and Gln or their collective levels (Glx) by MRS.[20] The concentration of Gln is ≈ 3.0-5.8 mmol/kg$_{ww}$ (less than the Glu concentration of ≈ 6.0-12.5 mmol/kg$_{ww}$) in healthy human brain,[19] and its signal at ≈ 2.45 ppm is overlapped by that of Glu at ≈ 2.35 ppm and by that of *N*-acetylaspartate (NAA) protons resonating at ≈ 2.49 ppm. GABA can be described as an $A_2M_2X_2$ spin system, with the C2 protons (X spins) resonating at ≈ 2.28 ppm. GABA concentrations are low in healthy human brain, namely ≈ 1.3-1.9 mmol/kg$_{ww}$[19]; therefore, the resonance exhibits significant overlap from the ≈ 2.35 ppm Glu proton signal. Quantification of GABA is typically performed by employing the C4

proton (A spins) GABA signal, which resonates at ≈ 3.01 ppm; however, because techniques prone to subtraction errors (variants of the Mescher-Garwood, MEGA, technique)[21] are required to isolate the resonance there is interest in quantification with the C2 GABA signal.[22]

Spectral editing methods have been used to improve Glu and/or Gln quantification, including echo-time (TE)-averaged Point RESolved Spectroscopy (PRESS),[23] optimal-TE PRESS,[20,24] optimal-TE STimulated Echo Acquisition Mode (STEAM),[25,26] MEGA-PRESS,[27,28] constant-TE difference spectroscopy,[29] Carr-Purcell PRESS,[30] spectrally selective refocusing,[31] double quantum filtering,[32] and 2D MRS.[33] Methods that have been used to enhance the detectability of GABA include MEGA-PRESS,[21,27,28,34-36] double-quantum filtering,[37] optimal-TE PRESS[38] and STEAM.[26] Most of the studies focused on the detection of one or two of Glu, Gln, or GABA, but not on all of them simultaneously. An exception is the study by Hu *et al.*,[26] which was done at 4 T with optimal-TE STEAM. However, the detection of Gln and GABA *in vivo* was limited to the case of excess Gln and GABA due to brain trauma. Other exceptions include the study by Choi *et al.*,[24] as well as the follow up study by Ganji *et al.*,[38] which were both conducted at 7 T with optimal-TE PRESS. Stephenson *et al.*[39] also employed long TE STEAM parameters previously determined by Yang *et al.*[25] at 7 T to quantify Gln, Glu and GABA in human brain but with Cramér-Rao Lower Bound (CRLB) values greater than 24 % for Gln and GABA.

Higher field strengths such as 9.4 T offer better spectral resolution and higher signal-to-noise ratio (SNR). A number of animal studies have been performed at 9.4 T for the study of animal models of disease.[40-46] While the Glu and Gln PQ proton signals can be resolved at 9.4 T, their separability depends on their peak linewidths.[25] The number of spectral editing techniques implemented at 9.4 T has been limited perhaps because glutamate, glutamine, and GABA are often quantified at 9.4 T by acquiring short-TE spectra and employing software, such as LCModel,[47] to

fit the detected signal to estimate the levels of each metabolite.[40,41,43-45,48-52] However, in the case of lower concentration resonances that experience significant signal overlap, quantification estimates from the fit may be prone to bias and uncertainty such that it is possible to find a solution with low CRLB values but that yields inaccurate results.[53] Simulations were performed to optimize a STEAM sequence to resolve Glu from Gln at 9.4 T[25] and subtraction editing for quantifying GABA has been implemented at 9.4 T[36]; however, with the latter, only the ≈ 3.75 ppm Glx peak is co-edited with GABA for which Glu and Gln have similar chemical shifts and therefore, cannot be resolved. In that study Glu and Gln were quantified from short-TE spectra; however, spectral editing was required for GABA quantification due its relatively lower concentration and signal contamination from macromolecular signal in the 2.2 – 2.3 ppm spectral region.

The objective of the presented work is to optimize TE_1 and TE_2 of the readily available PRESS sequence, which is commonly employed in *in-vivo* MRS and potentially offers twice the SNR obtainable with STEAM (also commonly employed) to simultaneously quantify Glu, Gln and GABA at 9.4 T. Numerical calculations are performed to evaluate the J-coupling evolution of Glu, Gln, GABA and NAA to find a long TE that minimizes the undesired NAA signal at ≈ 2.49 ppm, while retaining signal from Gln at ≈ 2.45 ppm, Glu at ≈ 2.35 ppm, and GABA at ≈ 2.28 ppm. The longer TE value also enables the suppression of macromolecule (MM) signals, which contaminate the Glu, Gln, and GABA signals at short TE values.[54-56] The efficacy of the timings is verified on phantom solutions and on rat brain *in vivo.* Furthermore, LCModel quantification is assessed on spectra obtained from phantoms of known concentrations with both short-TE PRESS and with the optimal TE combination. Specifically, the use of CRLB as an indicator of LCModel quantification reliability with short-TE spectra where there is a severe overlap of peaks is investigated.

4.2 - MATERIALS AND METHODS

The response of signals from Glu, Gln, GABA, and NAA protons at 9.4 T as a function of TE values of a standard single voxel PRESS sequence were investigated. Numerical simulations, based on density matrix calculations, were performed with a previously developed MATLAB (Mathworks, Natick, Massachusetts, United States) program.[57] Spectra were calculated with 8192 data points and a sampling frequency of 10000 Hz, with the shape of the refocusing pulses (including their offset frequency) and slice selection gradient magnitudes included in the calculations. The refocusing pulses have a duration of 2 ms; therefore, the minimum (TE_1, TE_2) of (2 ms, 2 ms) is limited by this duration. The numerical calculations account for J-coupling interactions but not for T_2 relaxation. The chemical shift and scalar coupling constants were based on those provided by Govindaraju *et al.*,[19] with the exception of GABA, for which values updated by Kaiser *et al.*[35] were used. Spectra were line-broadened to match *in-vivo* linewidths (corresponding to a water linewidth of about 20 Hz). The 2.30-2.39 ppm spectral region of Glu, the 2.40-2.49 ppm region of Gln and NAA, and the 2.23-2.33 ppm region of GABA were investigated to find an optimal (TE_1, TE_2) combination to improve simultaneous quantification of Glu, Gln, and GABA. Peak areas were calculated for each of the spectral regions, with TE_1 and TE_2 varying from 0 - 200 ms in steps of 2 ms. An objective function that subtracts the absolute value of the NAA peak area normalized to its corresponding (2 ms, 2 ms) area from the corresponding normalized peak area of Gln, was used. It was defined as $\text{objective} = \frac{Gln_{PA}}{Gln_{PA,max}} - \left|\frac{NAA_{PA}}{NAA_{PA,max}}\right|$, where Gln_{PA} and NAA_{PA} are the integrated peak areas of Gln and NAA, respectively, in the 2.40-2.49 ppm region. The maximum peak area values, to which all peak areas are

normalized, occur with the minimum (TE_1, TE_2) of (2 ms, 2 ms). By maximizing the objective function, the peak area of Gln is maximized while the absolute peak area of NAA is minimized. The absolute area (as opposed to the real area) for the NAA signal in the Gln spectral region was considered to ensure minimal Gln contamination from NAA. The objective function was normalized to its maximum value, and a contour plot was generated as a function of TE_1 and TE_2. Optimal TE candidates were chosen by maximizing the objective function, choosing values higher than 0.6. Normalized contour plots were also created based on peak areas for each individual metabolite, and the peak area relative to the corresponding value at (2 ms, 2 ms) was found for each metabolite at the optimal timing sets. The individual spectra of NAA, Gln, Glu, and GABA were simulated with a (TE_1, TE_2) of (12 ms, 9 ms), which is the minimum achievable experimentally with the MRI scanner, and with the optimal TE candidates. Numerical calculation details are discussed in section 2.2.

Phantom and *in-vivo* experiments were performed with a 9.4 T, 21.5 cm diameter bore MRI scanner (Magnex Scientific, Oxford, UK) in combination with a TMX console (National Research Council of Canada Institute for Biodiagnostics, West, Calgary, AB, Canada). Additional MRI system details are included in section 2.3.1. For phantom experiments, a 4.3 cm diameter birdcage radiofrequency (RF) coil (National Research Council of Canada Institute for Biodiagnostics, West) was used for both transmission and reception. The optimal (TE_1, TE_2) candidates were verified experimentally on phantom solutions. Chemicals were purchased from SigmaAldrich Canada (SigmaAldrich Canada, Oakville, ON, Canada). A PRESS sequence was employed to obtain spectra from $5 \times 5 \times 5$ mm^3 voxels placed in the centre of the phantoms. Sinc RF pulses of 2 ms duration and 3000 Hz bandwidth were utilized for PRESS, with the frequency offset set to 2.9 ppm (centre of spectrum with NAA at 2 ppm and Glx at $\approx$ 3.8 ppm). Spectra were acquired in 32

averages, with a repetition time (TR) of 5 s and a four-step phase cycling scheme. For each average, 8192 complex data points were collected at a sampling frequency of 10000 Hz. For the voxel size employed, it was found that manual first order shimming was adequate. Shims were adjusted until the peak amplitude of the water signal was maximized (phantom water linewidths of less than 5 Hz were achieved). A chemical shift selective[58] sequence was used for water suppression.

Phantom solutions (in 30 mm diameter glass spheres), each containing 50 mM of one of NAA, Gln, Glu, or GABA, and all containing 10 mM creatine (Cr) to serve as a reference, were scanned with a (TE_1, TE_2) of (12 ms, 9 ms), the shortest achievable timings experimentally, and with the optimal TE candidates. The spectra were analyzed by manually integrating the peak areas for each metabolite in their respective spectral regions of interest at the optimal TE combinations, and comparing them to the corresponding areas obtained at the short TE combination of (12 ms, 9 ms). Spectra were processed with software provided by National Research Council of Canada (Spectrum Viewer v. 2.00.002, National Research Council of Canada Institute for Biodiagnostics, West, Calgary, AB, Canada). Processing included filtering, zero-filling, Fourier transformation, phase correction and baseline correction. Potential TE candidates that yielded an objective function value greater than 0.6 were analyzed to choose the optimal TE combination. The optimal timing decision was based primarily on minimizing the amplitude of the NAA signal in the 2.40-2.49 ppm spectral region in both numerical and phantom spectra. It was verified that the Gln, Glu, and GABA areas were maximized (numerical signal yield greater than 40 %, 50 % and 50 %, respectively, with respect to the corresponding signal when $TE_1 = TE_2 = 2$ ms) in the 2.40-2.49 ppm region, 2.30-2.39 ppm region, and the 2.23-2.33 ppm region, respectively. Additionally, it was verified on phantoms that the Glu, Gln and GABA peaks were sufficiently resolved.

Two spherical phantom solutions, both containing 20 mM Gln and 45 mM Cr, one of which also contained 50 mM Glu, 45 mM NAA, 5 mM glutathione (GSH) and 5 mM GABA, were scanned to analyze the Gln signal with and without the presence of other metabolites. Glutathione (GSH) was included because it has a signal at ≈ 2.51 ppm, which may potentially overlap with and contaminate the Gln signal at ≈ 2.45 ppm. The concentrations were selected to represent typical concentration ratios *in vivo* in rat brain.[48] Spectra from the two phantoms were acquired with a (TE_1, TE_2) of (12 ms, 9 ms) and with the optimal TE combination. For both TE combinations, the peak area of Gln (2.40-2.49 ppm) was manually integrated and normalized to the peak area of the ≈ 3.03 ppm Cr peak for the spectra obtained from both phantoms, and a percent difference was calculated between the values obtained from the two phantoms. A similar analysis was performed for assessing GABA signal with and without the presence of other metabolites. Spectra were acquired with a (TE_1, TE_2) of (12 ms, 9 ms) and with the optimal TE combination from a spherical phantom solution consisting of 5 mM GABA and 45 mM Cr. The spectra were compared to the previously acquired spectra from the 20 mM Gln, 45 mM Cr, 50 mM Glu, 45 mM NAA, 5 mM GSH, and 5 mM GABA phantom. Additional details about the phantom experiments can be found in section 2.3.2.

The optimal timing set was verified *in vivo* on the brains of 5 Sprague Dawley rats, with a mean age and standard deviation of 11.2 and 2.3 months, respectively. For both transmission and reception, a single loop 24 mm diameter surface coil (Doty Scientific, Inc., Columbia, South Carolina, United States) was used. The rat was placed in prone position, and the coil was positioned on top of its head, behind the eyes, in order to centre the brain in the field of view. The body temperature of the rat was maintained at 37 °C by monitoring it with a rectal probe and employing a heating module. Respiratory gating was performed with the use of a probe placed on the

abdomen, the respiratory pattern providing feedback. To sedate the rat, anaesthetic containing 2 % isoflurane was administered via a plastic tube and nose cone system to the rat's airway. Spin echo images, obtained with a TE of 13 ms and a TR of at least 1250 ms, were employed for voxel placement. Twenty transverse slices and twenty coronal slices (2 mm thickness) of the rat brain were acquired. A $5 \times 5 \times 5$ mm^3 voxel, with its centre a distance of ≈ 6 mm from the surface coil, was approximately centred in the brain. Typically, a water linewidth of $\approx 20 - 25$ Hz was achieved. Two spectra, one with a short TE of (TE_1, TE_2) = (12 ms, 9 ms) and one with the optimal TE combination, were acquired from each rat. Both spectra were measured as 2048 complex data points and sampled at 10000 Hz, with a TR of at least 3 s. The short-TE spectrum and the optimal-TE spectrum were obtained in 128 (6.4 minutes) and 256 averages (12.8 minutes), respectively. A chemical shift selective[58] sequence was used for water suppression. Fewer averages were acquired for short-TE spectra to minimize scan time. A short-TE spectrum was acquired in a rat with both 128 and 256 averages to verify that the higher SNR obtained with more averages does not significantly affect LCModel quantification. A description of rat brain experiments can be found in section 2.3.3.

LCModel software[47] was utilized to analyse the *in-vivo* spectra. The basis sets were specific to 9.4 T and were provided by the vendor, with additional macromolecules and lipid signals simulated by LCModel. Each (TE_1, TE_2) combination requires an independent basis set; therefore, two sets were used. Each basis set included alanine (Ala), aspartate (Asp), glucose (Glc), Cr, phosphocreatine (PCr), Gln, Glu, GABA, glycerylphosphorylcholine (GPC), phosphocholine (PCh), GSH, inositol (Ins), lactate (Lac), NAA, N-acetylaspartylglutamate (NAAG), scyllo-inositol (Scyllo), and taurine (Tau). Basis files for Gln, Glu, GABA, and NAA were replaced with simulated spectra to account for the difference in spectral response due to refocusing pulse shape.[57]

Spectra were numerically simulated with the described MATLAB software and converted to the LCModel .RAW format before they were inputted into the MakeBasis program included in the LCModel package. Fitted spectra were obtained in the range of 0.2 – 4.0 ppm along with an LCModel table of relative CRLB values for each metabolite in addition to concentrations relative to total creatine (tCr = Cr + PCr). Concentration ratios were T_2 corrected using T_2 values for Glu, Gln, GABA, NAA and tCr obtained from Xin *et al.*,[59] namely, 89 ms, 116 ms, 105 ms, 202 ms and 113 ms, respectively. Approximate T_1 values for the metabolites from the literature[60] are 1.5 s, 1.44 s, 1.86 s and 1.7 s, respectively. The similarity of the T_1 values yield correction factors $1 - \exp(-\frac{TR}{T_1})$[61] of less than 5 % for Glu, Gln and GABA. Considering the small effect of the correction and the uncertainties associated with the T_1 values,[60] concentration ratios were not corrected for T_1 relaxation. Metabolite concentrations were calculated assuming a total creatine concentration of 8.5 mM in rat brain.[48] In this work, it was approximated that a mM is equivalent to μmol/g and mmol/kg (to convert concentrations obtained from the literature). Additional details regarding data analysis are in section 2.4.

To assess the reliability of Gln quantification with short TE and with the optimal TE, four phantoms of known concentrations of Gln were created, namely, 0, 10, 20 and 30 mM. To mimic *in-vivo* conditions, NAA, Cr, GABA, GSH, and Glu were added to each in consistent concentrations of 45 mM, 45 mM, 5 mM, 5 mM, and 50 mM, respectively. Spectra were acquired with (TE_1, TE_2) = (12 ms, 9 ms) and with the optimal TE combination for each phantom. LCModel analysis of the phantom spectra was performed and concentrations of Gln relative to Cr along with CRLB values were obtained. Measured ratios of Gln concentrations relative to Cr obtained with the (12 ms, 9 ms) TE combination and with the optimal TE combination were T_2-corrected. The Gln concentrations were then calculated by multiplication by the Cr concentration of 45 mM and

plotted against the actual known concentrations. Error bars were created based on reported CRLBs[62] and were calculated as $\pm(\text{CRLB} \times \text{estimated concentration})$ (absolute CRLB).[63] T_2 values were estimated from the phantoms containing individual metabolite components with a least squares fit to a monoexponentially decaying function, using peak areas obtained with (TE_1, TE_2) values of (15 ms, 15 ms), (106 ms, 16 ms), and (130 ms, 130 ms) for Gln and Glu. For Cr, NAA and GABA, additional spectra were obtained with (200 ms, 200 ms) and (400 ms, 400 ms) due to their longer T_2 values. Peak areas were fitted with a least-squares analysis in MATLAB, as specified by the function $M = M_0 \exp(-\frac{TE}{T_2})$, where TE is the total echo time and M_0 is the predicted peak area when TE is equal to 0 ms. J-coupling corrections were included in the T_2 estimates for Glu, Gln, and GABA (Cr protons do not exhibit J-coupling) by dividing each peak area by the numerically determined ratio of the peak area at the specified echo time combination to the peak area at (2 ms, 2 ms) (compensating for the signal loss due to J-coupling). It was verified experimentally that the TR of 5 s used for phantom experiments was sufficiently long to render all metabolite T_1 relaxation effects negligible. Concentrations and corresponding CRLBs were also found for Glu and GABA from the spectra acquired from the 20 mM Gln phantom, with (TE_1, TE_2) = (12 ms, 9 ms) and with the optimal TE combination. To assess the effect of the presence of a larger amount of NAA, a phantom with 90 mM NAA was created while retaining the same concentrations for the other metabolites (45 mM, 5 mM, 5 mM, 20 mM and 50 mM for Cr, GABA, GSH, Gln and Glu, respectively). In addition, a phantom with altered amounts of Gln, Glu and GABA was created to assess quantification efficacy. The phantom contained 45 mM, 45 mM, 12 mM, 5 mM, 30 mM, and 45 mM of NAA, Cr, GABA, GSH, Gln and Glu, respectively. The increase in Gln and GABA and decrease in Glu are consistent with changes seen in epileptic patients treated with Vigabatrin.[64]

4.3 - RESULTS

Figure 4.1 displays a contour plot of the objective function normalized to the maximum value. Contour lines vary from -0.6 to 0.6 in steps of 0.3. The optimal (TE_1, TE_2) value was determined to be (106 ms, 16 ms), represented with an asterisk in Figure 4.1 and which yielded an objective function value of 0.65.

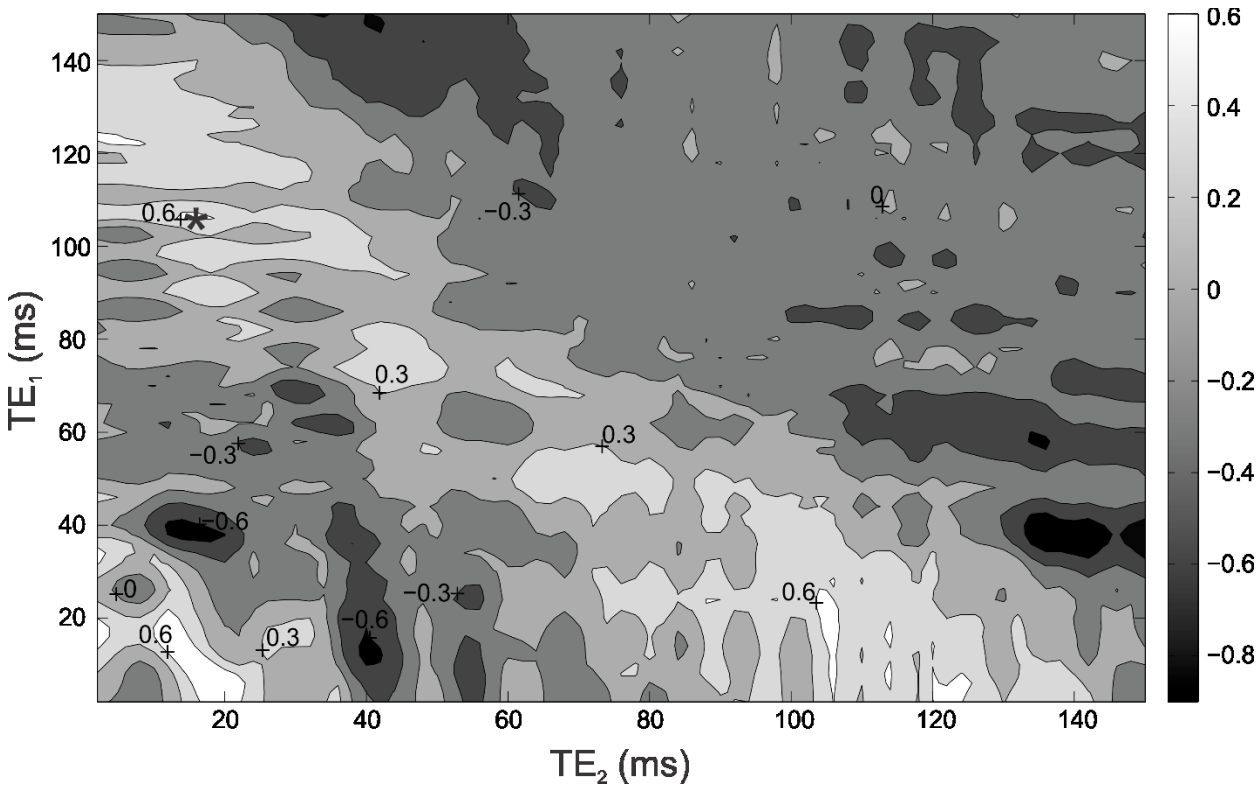

Figure 4.1: Contour plot of the objective function (normalized Gln area – normalized NAA area) normalized to the maximum value, with the optimal (TE_1, TE_2) of (106 ms, 16 ms) represented with an asterisk. Values are displayed for a TE_1 and TE_2 range of 2 – 150 ms. Normalized Gln and NAA values are with respect to values obtained with (TE_1, TE_2) of (2 ms, 2 ms).

Figure 4.2 shows the normalized numerical contour plot for areas of each individual metabolite, including NAA (absolute value; Figure 4.2a), Gln (Figure 4.2b), Glu (Figure 4.2c), and GABA (Figure 4.2d). The values shown for Gln, Glu, and GABA are real values. The optimal timing set, (106 ms, 16 ms), represented again by asterisks, yielded signal areas of 0.02, 0.42, 0.54, and 0.57 for NAA, Gln, Glu, and GABA, respectively, relative to the corresponding value at (2 ms, 2 ms). Relative to the values at (12 ms, 9 ms), the signal areas were 0.03, 0.67, 0.80, and 0.76, respectively.

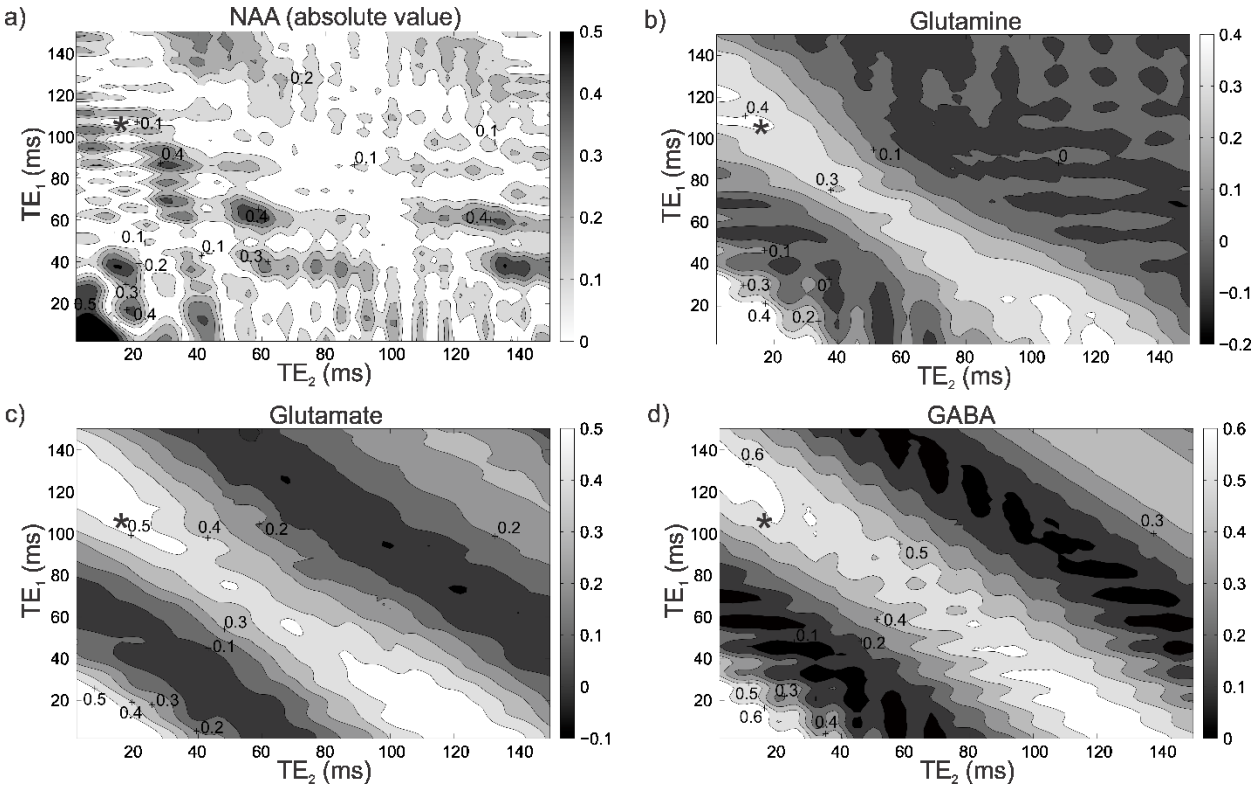

Figure 4.2: Contour plots of individual metabolites, including a) NAA (absolute value and an inverted grayscale), b) Gln, c) Glu, and d) GABA, with the optimal TE of (106 ms, 16 ms)

represented by asterisks. Contour plots for Gln, Glu, and GABA were generated using real values for the areas normalized to their respective values at (2 ms, 2 ms). Values are displayed for a TE_1 and TE_2 range of 2 – 150 ms.

Figure 4.3 shows both theoretical (left) and experimental (right) spectra for each individual metabolite obtained with a (TE_1, TE_2) of (12 ms, 9 ms) (solid line) and (106 ms, 16 ms) (dashed line). Phantom measurements obtained with (106 ms, 16 ms) gave relative NAA, Gln, Glu, and GABA signal areas of <0.05, 0.44, 0.59, and 0.70, respectively, to the corresponding (12 ms, 9 ms) values.

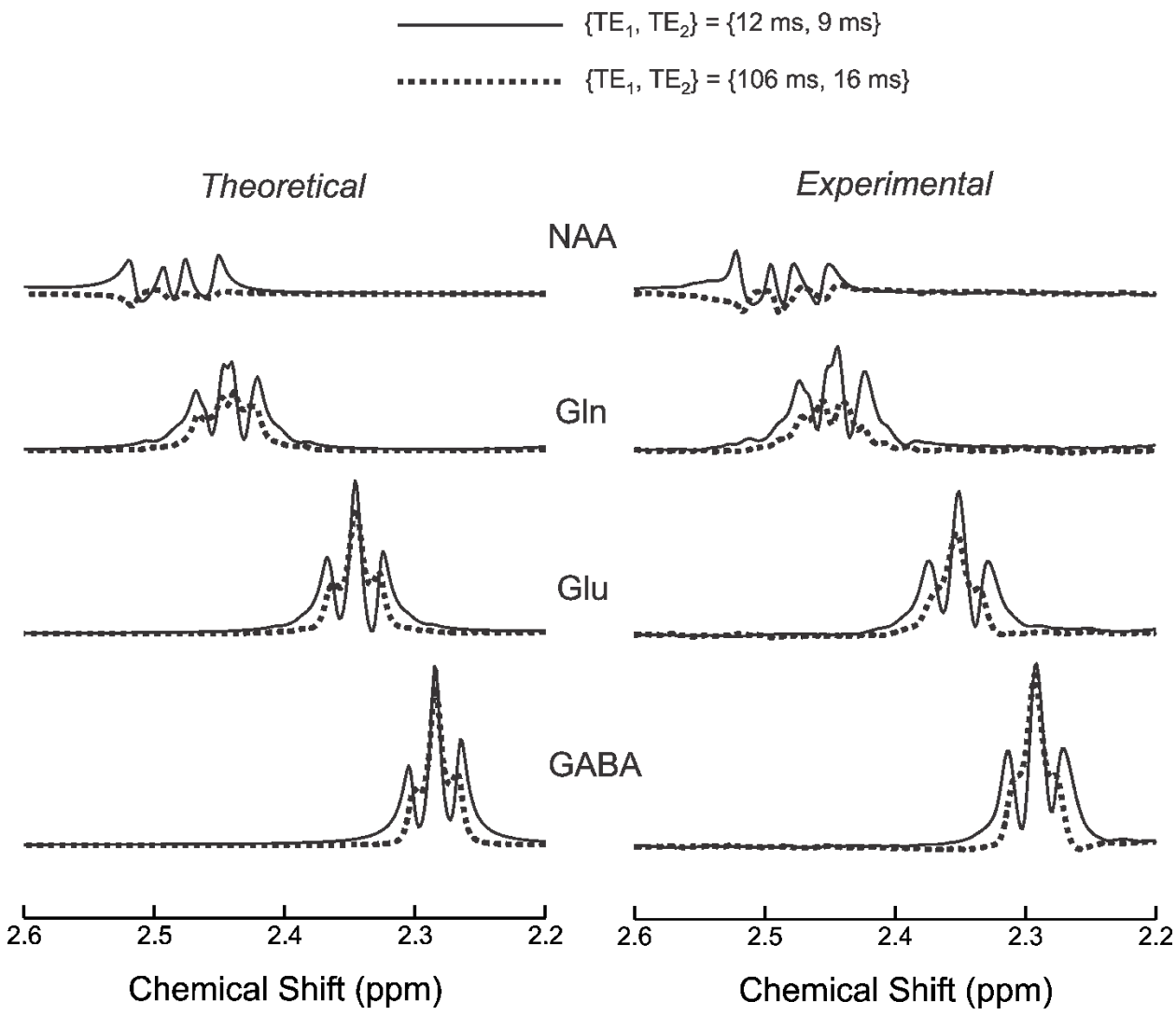

Figure 4.3: Theoretical (left) and experimental (right) spectra obtained for individual metabolites with a TE combination of (12 ms, 9 ms) (solid line) and (106 ms, 16 ms) (dashed line).

Spectra from a phantom containing a mixture of Gln, Glu, NAA, GSH, and GABA are shown in Figure 4.4, where they are overlapped with spectra from a phantom containing Gln only (a, b; dotted line) and GABA only (c, d; dotted line). Spectra were acquired with both a TE combination of (12 ms, 9 ms) (a, c) and (106 ms, 16 ms) (b, d). For both Gln and GABA, the signal

area normalized to that of Cr changed by <10 % in the presence of the other metabolites when the spectra were acquired at the optimal TE. For the short-TE spectra, the signal area normalized to that of Cr was 49 % higher for Gln and 207 % higher for GABA in the presence of the other metabolites. GSH was found to have a negligible impact on the Gln resonance in all cases.

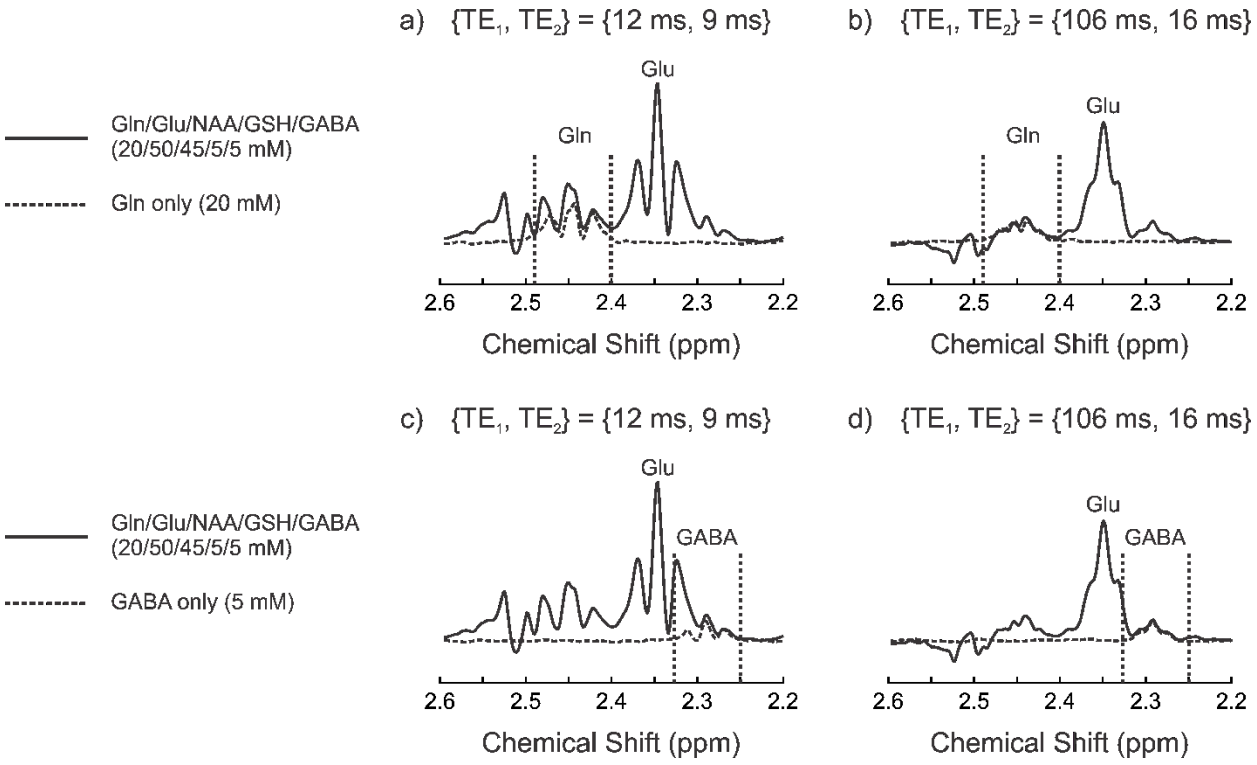

Figure 4.4: Spectra from a phantom containing Cr, Gln, Glu, NAA, GSH, and GABA (solid line), overlapped with spectra (dotted line) from phantoms containing Gln only (a and b) and GABA only (c and d). Spectra from all phantoms were acquired with TE combinations of (12 ms, 9 ms) and (106 ms, 16 ms). The spectral regions of Gln and GABA are indicated by the vertical dashed lines. Overlapped spectra were scaled so that the heights of the Cr peaks matched (each phantom contained 45 mM Cr).

Spectra acquired from one of the rats are shown in Figure 4.5. PRESS voxel placement is shown on a coronal and a transverse image of the rat brain (a). Baseline-corrected *in-vivo* spectra acquired from the voxel with a short (TE_1, TE_2) of (12 ms, 9 ms) (b) and with the optimal TE combination of (106 ms, 16 ms) (c) are shown, overlapped with their corresponding LCModel fits. Heavy overlap between NAA, Glu, Gln, and GABA can be seen in the 2.2 – 2.5 ppm spectral region in the short-TE spectrum, whereas there is a clear resolution of Glu, Gln and GABA peaks in the optimal-TE spectrum. Additionally, the LCModel analysis of the short-TE spectrum included the presence of the "MM20" macromolecular signal, which has a peak at ≈ 2.25 ppm and overlaps with GABA. No macromolecule contribution was reported for the optimal-TE spectrum.

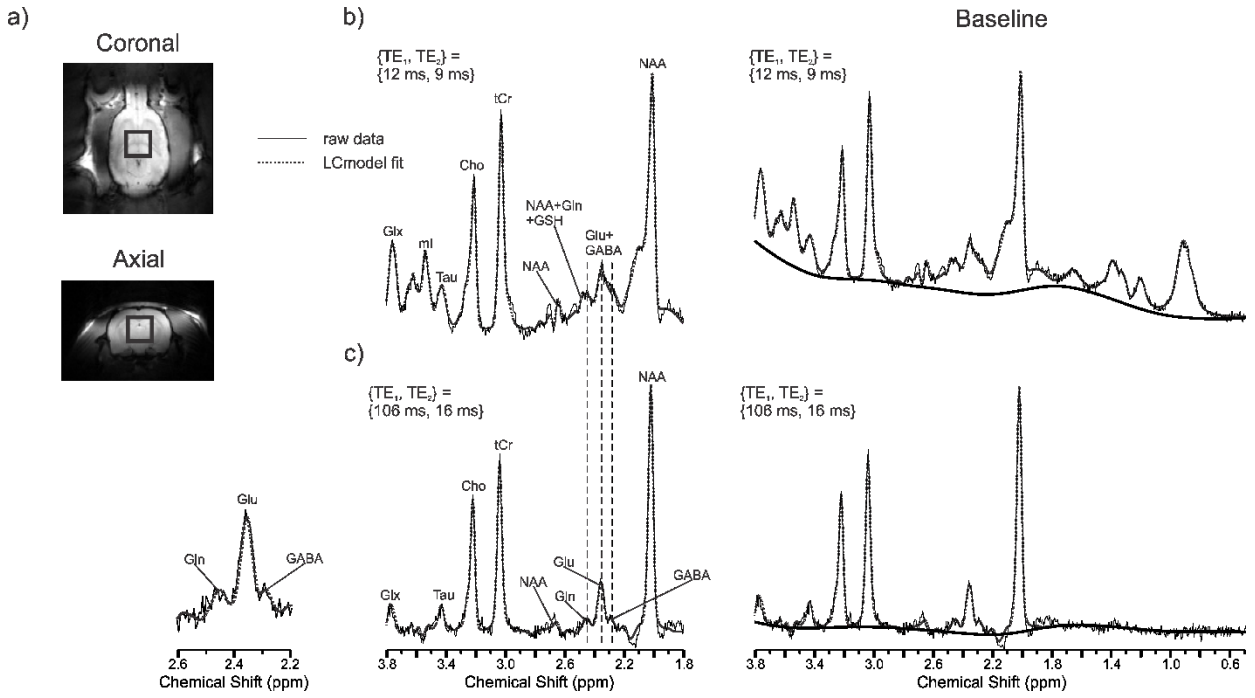

Figure 4.5: *In-vivo* rat brain data acquired at 9.4 T, with a) voxel placement shown in a coronal and a transverse image of one of the rat brains and b) PRESS spectra acquired from the voxel with a short (TE_1, TE_2) of (12 ms, 9 ms) (top) and the optimal TE combination of (106 ms, 16 ms) (bottom), overlapped with their corresponding baseline subtracted LCModel fits. LCModel baselines are shown to the right of the spectra, overlapped with raw data. Water was suppressed to less than 2% of its unsuppressed amplitude.

Figure 4.6 (a) shows a processed (106 ms, 16 ms) spectrum from one of the four other rats, along with its LCModel fit. Table 4.1 summarizes the concentrations, both with and without T_2 correction, and CRLBs determined from the LCModel analysis, for each metabolite, with both TE combinations in each rat, as well as an average for all the rats. Literature values are included for each metabolite, obtained from.[65,66] Figure 4.6(b) reflects the average values summarized in the table. LCModel analysis of the short-TE spectra indicated that reducing the number of averages to

128 resulted in ≈ 10 % less Gln and ≈ 2 % less GABA. The CRLB values for Gln and GABA increased from 8 % to 10 % and from 9 % to 10 %, respectively. The small changes demonstrate that the comparisons in Table 4.1 are acceptable. The higher number of averages for the long-TE spectra explains the similar SNR obtained with short and long-TE spectra. A mean SNR (± standard deviation) based on the NAA peak of 26.90 ± 2.49 was obtained for the short-TE spectra over the five rats. For long TE spectra the mean SNR was 25.00 ± 3.74. The mean full width half maximum (± standard deviation) of the NAA peak was calculated to be 17.60 ± 4.44 Hz and 15.52 ± 1.88 Hz for the short-TE and long-TE spectra, respectively (LCModel yielded average linewidths for all peaks of 13.20 ± 2.25 Hz and 11.04 ± 1.31 Hz for the short-TE and long-TE spectra, respectively). CRLB values for NAA and tCr for both short-TE and long-TE spectra were 2-3 %. Average T_2- corrected NAA concentrations (± average absolute CRLB) over the five rats were 8.94 ± 0.25 mM and 7.64 ± 0.17 mM from short-TE and long-TE spectra, respectively. The standard deviations of the concentrations were 0.85 mM and 0.47 mM, respectively.

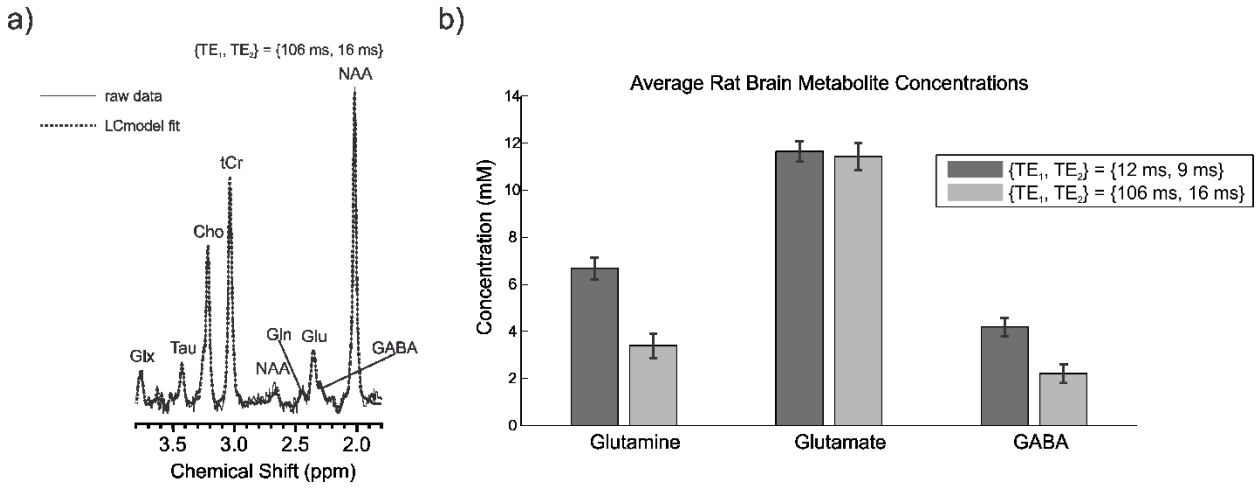

Figure 4.6: *In-vivo* baseline subtracted rat brain PRESS spectrum obtained at 9.4 T with the optimal combination of (106 ms, 16 ms) from one of the other rats, along with the LCModel fit (a). A bar chart shows the T_2-corrected concentrations of Gln, Glu, and GABA, acquired with TE combinations of (12 ms, 9 ms) and (106 ms, 16 ms), and averaged from all five of the rats (b). Error bars are shown with a value of ±(mean absolute CRLB).

Rat Number	Metabolite	Estimated Concentration (mM) (CRLB) (short-TE)	T_2-Corrected Concentration (mM) (short-TE)	Estimated Concentration (mM) (CRLB) (optimal-TE)	T_2-Corrected Concentration (mM) (optimal-TE)	Literature Concentrations (mM)[a]
1	Gln	6.76 (6%)	6.73	2.94 (16%)	2.87	3.91 - 5.59
	Glu	11.24 (3%)	11.82	7.58 (5%)	10.14	9.77 - 12.00
	GABA	4.18 (8%)	4.23	1.85 (18%)	1.89	1.26 - 1.99
2	Gln	7.77 (6%)	7.74	3.93 (14%)	3.83	3.91 - 5.59
	Glu	11.02 (4%)	11.58	9.12 (5%)	12.19	9.77 - 12.00
	GABA	5.15 (8%)	5.23	1.93 (19%)	2.10	1.26 - 1.99
3	Gln	7.43 (7%)	7.40	3.04 (15%)	2.95	3.91 - 5.59
	Glu	11.83 (4%)	12.43	7.68 (5%)	10.29	9.77 - 12.00
	GABA	4.68 (9%)	4.74	1.85 (17%)	1.89	1.26 - 1.99
4	Gln	5.80 (8%)	5.77	2.99 (17%)	2.90	3.91 - 5.59
	Glu	10.65 (4%)	11.20	9.41 (4%)	12.59	9.77 - 12.00
	GABA	3.17 (12%)	3.21	2.16 (16%)	2.35	1.26 - 1.99
5	Gln	5.80 (8%)	5.77	4.51 (15%)	4.39	3.91 - 5.59
	Glu	10.69 (4%)	11.24	8.95 (6%)	11.97	9.77 - 12.00
	GABA	3.49 (10%)	3.54	2.35 (19%)	2.55	1.26 - 1.99
Average	Gln	6.72 (7%)	6.68 ± 0.47	3.49 (15.4%)	3.39 ± 0.52	3.91 - 5.59
	Glu	11.08 (3.8%)	11.65 ± 0.44	8.54 (5%)	11.43 ± 0.57	9.77 - 12.00
	GABA	4.13 (9.4%)	4.19 ± 0.39	2.03 (17.8%)	2.20 ± 0.39	1.26 - 1.99

[a]Literature concentrations are taken from Refs. [65,66].

Table 4.1: Summary of the LCModel analysis performed on the five rats. Concentrations (both uncorrected and T_2 corrected) are calculated from the ratio relative to total creatine (tCr), assuming a tCr concentration of 8.5 mM. Relative Cramér Rao Lower Bounds (CRLBs) are given in brackets. Average, T_2-corrected concentrations are mean ± mean absolute CRLB. Concentration standard deviations over all the rats (not shown in the table) for Gln, Glu and GABA are 0.91 mM, 0.5 mM and 0.83 mM, respectively, for the short-TE spectra. For long-TE spectra, concentration standard deviations are 0.69 mM, 1.14 mM and 0.24 mM. for Gln, Glu and GABA, respectively.

To assess LCModel quantification with the short- and long-TE spectra, LCModel estimated Gln concentrations of the mixture phantoms containing different amounts of Gln are plotted against the actual Gln concentrations in Figure 4.7. Results for both (TE_1, TE_2) combinations of (12 ms, 9 ms) and (106 ms, 16 ms) are shown. The CRLBs for the estimated concentrations are 11 %, 5 %, 3 %, and 3 % for set Gln concentrations of 0 mM, 10 mM, 20 mM, and 30 mM, respectively, at (12 ms, 9 ms). For the optimal TE of (106 ms, 16 ms), the CRLBs are 11 %, 4 %, 3 %, and 2 %, respectively. The T_2 values found for Gln, Glu, Cr, NAA and GABA were 284 ms, 405 ms, 1264 ms, 1363 ms and 905 ms, respectively. Table 4.2 summarizes the concentrations and CRLBs determined from the mixture phantoms containing 20 mM Gln, with both TE combinations of (12 ms, 9 ms) and the optimal TE combination with one of the phantoms containing twice the amount of NAA. Altering the concentrations of Gln, Glu and GABA to 30 mM, 45 mM and 12 mM, respectively, resulted in T_2-corrected long-TE LCModel concentrations of 31.71 mM (CRLB 2 %), 47.99 mM (CRLB 2 %) and 13.23 mM (CRLB 3 %), respectively (NAA concentration was unaltered and the estimated concentration was found to be 49.38 mM in the first phantom and 47.14 mM in the second).

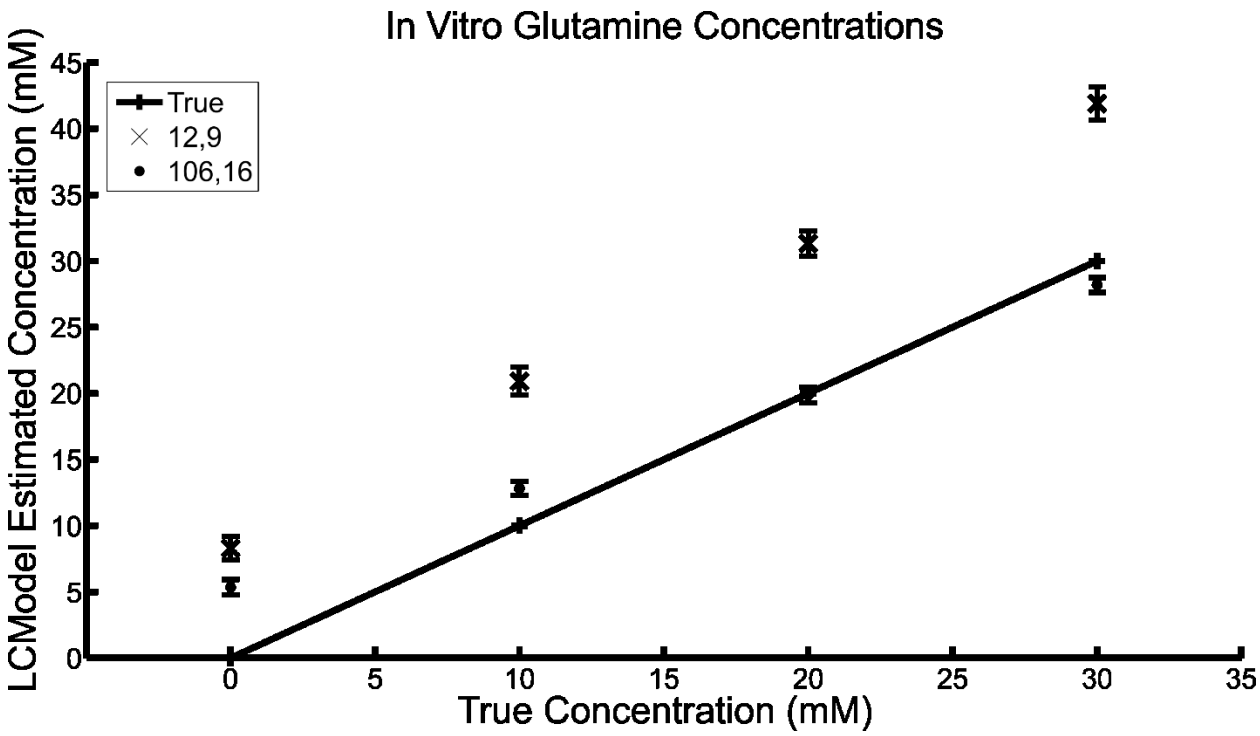

Figure 4.7: LCModel estimated concentrations of phantom Gln plotted against the actual Gln concentrations. Measurements were performed with both (TE_1, TE_2) combinations of (12 ms, 9 ms) and (106 ms, 16 ms). Error bars are ± absolute CRLB (mM). Each phantom contains 45 mM NAA, 45 mM Cr, 5 mM GABA, 5 mM GSH, and 50 mM Glu. The solid line shows the true Gln concentration.

Phantom	Metabolite	Actual Concentration (mM)	Estimated Concentration (mM) (CRLB) (short-TE)	T2-Corrected Concentration (mM) (short-TE)	Estimated Concentration (mM) (CRLB) (optimal-TE)	T2-corrected Concentration (mM) (optimal-TE)
45 mM NAA	NAA	45	50.18 (1%)	50.11	49.73 (1%)	49.38
	Gln	20	29.57 (3%)	31.31	14.27 (3%)	19.90
	Glu	50	57.87 (2%)	59.94	46.08 (1%)	56.54
	GABA	5	10.49 (7%)	10.55	4.82 (6%)	5.00
90 mM NAA	NAA	90	107.33 (1%)	107.20	97.43 (1%)	96.74
	Gln	20	41.13 (3%)	43.56	19.35 (3%)	27.00
	Glu	50	62.10 (2%)	64.33	43.02 (2%)	52.79
	GABA	5	12.42 (9%)	12.50	4.86 (9%)	5.05

Table 4.2: Summary of LCModel quantification of phantom solutions containing known metabolite concentrations. Concentrations (both uncorrected and T_2 corrected) are calculated from the ratio relative to creatine (45 mM). Relative CRLBs are given in brackets.

4.4 - DISCUSSION

Glutamine, Glutamate, and GABA are important metabolites in the brain, and their levels can be estimated with MRS from their resonances at ≈ 2.45 ppm, ≈ 2.35 ppm, and ≈ 2.28 ppm, respectively. However, the Gln signal exhibits overlap with that of NAA at ≈ 2.49 ppm, and both of the Gln and GABA signals display overlap with that of Glu *in vivo* when using typical short-TE methods. To our knowledge, spectral editing for the improved simultaneous quantification of Gln, Glu and GABA has not been previously implemented at 9.4 T. In the presented work, we show that a readily available PRESS sequence with an optimal (TE_1, TE_2) of (106 ms, 16 ms) can be used to resolve and simultaneously measure Gln, Glu, and GABA *in vivo* in rat brain at 9.4 T. The signal contribution from NAA in the 2.40-2.49 ppm Gln spectral region was minimized, and the signals of Gln, Glu, and GABA were retained and narrowed such that they were better resolved

for quantification. Experimentally, with a TE combination of (106 ms, 16 ms), the contaminating 2.40-2.49 ppm NAA signal area was found to be <0.05 of the corresponding value obtained with (12 ms, 9 ms), agreeing with the numerically determined absolute value of 0.03. Areas of Gln, Glu, and GABA obtained with the long TE relative to those acquired with the short TE were found to be 0.44, 0.59, and 0.70, comparing well to the numerically determined ratios of 0.67, 0.80, and 0.76, respectively. The reduced values experimentally are a result of T_2 relaxation. The long-TE combination was determined from calculations performed with metabolite linewidths corresponding to those obtained in our *in-vivo* experiments (water linewidth about 20 Hz). Therefore, the timings may not optimal for different levels of shim.

The efficacy of the determined long TE in removing signal that contaminates the Gln and the GABA spectral regions was verified by measuring the Gln/Cr and GABA/Cr ratios obtained with the long TE from the phantoms containing 20 mM Gln/45 mM Cr and 5 mM GABA/45 mM Cr and comparing them to the corresponding ratios obtained from the 20 mM Gln/45 mM Cr/50 mM Glu/45 mM NAA/5 mM GSH/5 mM GABA phantom. For both Gln and GABA, the ratios differed by less than 10 %. The small difference, compared to the large difference obtained with short TE, demonstrates minimal contamination from NAA and Glu in the Gln 2.40-2.49 ppm spectral region and from Glu in the 2.23–2.33 ppm GABA region.

Average, T_2-corrected concentrations for Gln, Glu, and GABA were assessed from LCModel analysis of the spectra acquired from the five rat brains *in vivo*. The average concentrations for Gln and GABA, determined from the short-TE spectra, are 6.68 ± 0.47 mM (CRLB 7 %) and 4.19 ± 0.39 mM (CRLB 9.4 %), respectively, which are higher than rat brain literature values determined previously with other biochemical analysis methods, including liquid chromatography[65] and enzymatic assay.[66] The values are higher compared to some short-TE

concentrations found in the literature, namely, approximately 2.70 – 4.56 mM for Gln and 0.5 – 1.35 mM for GABA.[36,48,50] Renormalizing (to 8.5 mM Cr) according to Cr concentrations in the references yields ranges of 2.82 – 3.88 mM and 0.43 – 1.64 for Gln and GABA, respectively. However, differences in the employed sequences and the rat ages do not enable an entirely fair comparison. Relative CRLB values obtained from the long-TE spectra for Gln, Glu, and GABA ranged from 14-17 %, 4-6 %, and 16-19 %, with averages of 15.4 %, 5 %, and 17.8 %, respectively. The CRLB values being under 20 % are considered acceptable.[60] The T_2-corrected, determined concentration for Glu, 11.43 ± 0.57 mM, is within the range of literature values 9.77-12.00 mM. The estimated concentration of GABA, 2.20 ± 0.39 mM agrees within error to literature values of 1.26-1.99 mM, and the estimated Gln concentration of 3.39 ± 0.52 mM also agrees within error to the literature values of 3.91-5.59 mM. Compared to the concentrations obtained with short TE, Gln and GABA concentrations obtained with the optimal TE combination are closer to those found in the literature even though the CRLB values are higher for the long-TE spectra. NAA concentrations of 8.94 ± 0.25 mM and 7.64 ± 0.17 mM were obtained from short-TE and long-TE spectra, respectively. Literature NAA values in rat brain are in the range of 8.27 – 8.4 mmol/kg.[36,48,50]

The LCModel basis set, which is specific to the field strength and echo time combination, accounts for the small contributions from overlapping signals from NAA and Glu when measuring Gln, as well as from overlapping signal from Glu when measuring GABA. In addition, J-coupling evolution of the protons relevant to the quantification of Gln, Glu and GABA during the slice selective refocusing pulses[57] are accounted for by replacing Gln, Glu, GABA, and NAA basis set components with numerically calculated spectra.

A number of MRS studies utilize LCModel fitting along with a short-TE acquired spectrum to deduce metabolite concentrations. In this study, the LCModel evaluation with phantom data shows that LCModel estimated concentrations can be inaccurate when combined with short-TE PRESS, for lower concentration metabolites where there is significant overlap between peaks. For example, Figure 4.7 demonstrates that Gln phantom concentrations estimated with (106 ms, 16 ms) are consistently closer to the true values than those estimated with (12 ms, 9 ms), even though the CRLBs are comparable in both cases. The largest deviation with the long-TE sequence occurs for a Gln concentration of 0 mM, where the concentration is estimated at 5.34 mM; however, the short-TE measurement estimates the concentration at 8.29 mM. In addition, for the 20 mM Gln/50 mM Glu/5 mM GABA phantom, LCModel analysis of the short-TE spectrum overestimated all concentrations yielding 31.31 mM, 59.94 mM, and 10.55 mM for Gln, Glu, and GABA, respectively, despite the low CRLBs of 3 %, 2 %, and 7 %, respectively. With the optimized TE combination of (106 ms, 16 ms), the values were 19.90 mM (CRLB 3 %), 56.54 mM (CRLB 1 %), and 5.00 mM (CRLB 6 %), for Gln, Glu, and GABA, respectively, closer to their true values. Quantification of 45 mM NAA with the short-TE and long-TE techniques was similar. The short-TE spectrum yielded an NAA concentration of 50.11 mM (CRLB 1 %) and the long-TE spectrum resulted in a concentration of 49.38 mM (CRLB 1 %). Doubling the concentration of NAA, resulted in Gln being overestimated (27 mM) with the long-TE technique; however, the overestimation was not as significant as that obtained from the short-TE spectrum (≈ 41 mM). Doubling the concentration of NAA had no significant effect on the quantification of Glu and GABA with the long-TE. The long-TE technique also successfully detected alterations in levels of Gln, Glu and GABA. Altering the phantom concentrations to 30 mM Gln/45 mM Glu/12 mM GABA, resulted in T_2-corrected LCModel estimations of 31.71 mM (CRLB 2 %), 47.99 mM

(CRLB 2 %) and 13.23 mM (CRLB 3 %), respectively. The 10 % decrease in Glu concentration (50 mM to 45 mM) resulted in a decreased measured concentration of 15 % (56.54 mM to 47.99 mM). From literature 9.4 T studies performed on rats, statistically significant changes as small as ≈ 10 % have been measured for Glu and Gln in a study on diabetes.[45] Statistically significant changes as low as ≈ 10 % have also been reported for GABA in a study on iron deficiency[40] and one on hypoxia.[41] Further investigation is required to determine the smallest levels of change that can be detected with the timings presented in this work. It is also of interest that in the short-TE PRESS analysis, LCModel yielded a finite amount for the "MM20" macromolecular signal, which has peaks at ≈ 1.95 ppm, ≈ 2.08 ppm, ≈ 2.25 ppm, and ≈ 3.00 ppm, despite there being no macromolecules in the phantom. However, no macromolecular contribution was attributed to the optimal-TE PRESS spectrum LCModel fit. Although it has been suggested that the higher SNR at short-TE provides better quantification because of lower CRLB values,[39] our work suggests that caution should be taken when attempting to quantify lower concentration metabolites from short-TE spectra where there is peak overlap, even at the high field strength of 9.4 T and that CRLB alone cannot be taken as an indicator for quantification reliability, as is commonly assumed,[49] and it would appear that a combination of LCModel peak fitting and spectral editing is a better choice for obtaining more accurate quantification of metabolites that suffer from overlapping peaks. However, a study at 7 T comparing phantom quantification of Gln and Glu obtained with short and long TE STEAM sequences demonstrated that the higher SNR short-TE spectra yielded comparable quantification to that obtained from the long-TE spectra with lower CRLB values.[67] In addition, T_2 values of metabolites can change with disease[68,69]; therefore, if a T_2 cannot be determined, a short-TE method may be a better alternative. For example, the TE combination of (14 ms, 14 ms) with an objective function value of 0.86 could serve as an alternative to the long-

TE technique. It was not selected as the optimal TE in this work due to the larger presence of macromolecules and NAA [≈ 4.5 times more signal area and 8.5 times more signal amplitude compared to that present at the long TE combination of (106 ms, 16 ms)]. In the presented work, admittedly, we simulated individual and groups of macromolecular components rather than using the more time consuming metabolite-nulling technique to obtain a more accurate measure of the short-TE macromolecule signal. The latter method is more representative and improves quantification, particularly at higher field strengths[70]; however, a more accurate measured macromolecular fit may still not be sufficient for accurate quantification of GABA with short TE techniques at 9.4 T.[36] Macromolecule signal was not detected at long-TE due to the short T_2 of macromolecule protons (about 26 ms) at 9.4 T.[48]

The presented optimized PRESS timings resolves Gln, Glu and GABA at 9.4 T while minimizing the macromolecular baseline. It has been demonstrated on phantoms that it provides more accurate concentrations than those obtained with short-TE. The technique provides an alternative to subtraction editing for GABA while having the advantage of enabling simultaneous separate quantification of Gln and Glu. The timings can be translated for human studies at 9.4 T; however, if SAR (specific absorption rate) is a concern, an optimized STEAM sequence may serve as an alternative.

4.5 - CONCLUSION

A PRESS sequence with a TE combination of (106 ms, 16 ms) was found to be suitable for suppressing the NAA signal at ≈ 2.49 ppm and for resolving and quantifying the Gln, Glu, and GABA signals at ≈ 2.45 ppm, ≈ 2.35 ppm, and ≈ 2.28 ppm, respectively, simultaneously in rat

brain *in vivo* at 9.4 T. Particularly for low concentration GABA, it was shown that LCModel analysis of the optimal TE spectrum yielded concentrations that match more closely to values provided in the literature.

4.6 - REFERENCES

1. Meldrum BS. Glutamate as a neurotransmitter in the brain: review of physiology and pathology. *The Journal of nutrition.* 2000;130(4):1007S-1015S.

2. Waagepetersen HS, Sonnewald U, Schousboe A. Compartmentation of glutamine, glutamate, and GABA metabolism in neurons and astrocytes: functional implications. *The neuroscientist.* 2003;9(5):398-403.

3. Ramadan S, Lin A, Stanwell P. Glutamate and glutamine: a review of in vivo MRS in the human brain. *NMR in Biomedicine.* 2013;26(12):1630-1646.

4. Lutkenhoff E, Van Erp T, Thomas M, et al. Proton MRS in twin pairs discordant for schizophrenia. *Molecular psychiatry.* 2010;15(3):308-318.

5. Yüksel C, Öngür D. Magnetic resonance spectroscopy studies of glutamate-related abnormalities in mood disorders. *Biological psychiatry.* 2010;68(9):785-794.

6. Cavus I, Kasoff WS, Cassaday MP, et al. Extracellular metabolites in the cortex and hippocampus of epileptic patients. *Annals of neurology.* 2005;57(2):226-235.

7. Cianfoni A, Niku S, Imbesi S. Metabolite findings in tumefactive demyelinating lesions utilizing short echo time proton magnetic resonance spectroscopy. *American journal of neuroradiology.* 2007;28(2):272-277.

8. Pioro E, Majors A, Mitsumoto H, Nelson D, Ng T. 1H-MRS evidence of neurodegeneration and excess glutamate glutamine in ALS medulla. *Neurology.* 1999;53(1):71-71.

9. Taylor-Robinson S, Weeks R, Bryant D, et al. Proton magnetic resonance spectroscopy in Huntington's disease: Evidence in favour of the glutamate excitotoxic theory? *Movement disorders.* 1996;11(2):167-173.

10. Lin AP, Shic F, Enriquez C, Ross BD. Reduced glutamate neurotransmission in patients with Alzheimer's disease–an in vivo 13C magnetic resonance spectroscopy study. *Magnetic Resonance Materials in Physics, Biology and Medicine.* 2003;16(1):29-42.

11. Shutter L, Tong KA, Holshouser BA. Proton MRS in acute traumatic brain injury: role for glutamate/glutamine and choline for outcome prediction. *Journal of neurotrauma.* 2004;21(12):1693-1705.

12. Horská A, Barker PB. Imaging of brain tumors: MR spectroscopy and metabolic imaging. *Neuroimaging clinics of North America.* 2010;20(3):293-310.

13. Patel AB, de Graaf RA, Mason GF, Rothman DL, Shulman RG, Behar KL. The contribution of GABA to glutamate/glutamine cycling and energy metabolism in the rat cortex in vivo. *Proceedings of the National Academy of Sciences of the United States of America.* 2005;102(15):5588-5593.

14. Puts NA, Edden RA. In vivo magnetic resonance spectroscopy of GABA: a methodological review. *Progress in nuclear magnetic resonance spectroscopy.* 2012;60:29-41.

15. Lewis DA, Volk DW, Hashimoto T. Selective alterations in prefrontal cortical GABA neurotransmission in schizophrenia: a novel target for the treatment of working memory dysfunction. *Psychopharmacology.* 2004;174(1):143-150.
16. Sanacora G, Mason GF, Rothman DL, et al. Reduced cortical γ-aminobutyric acid levels in depressed patients determined by proton magnetic resonance spectroscopy. *Archives of general psychiatry.* 1999;56(11):1043-1047.
17. Petroff OA, Rothman DL, Behar KL, Lamoureux D, Mattson RH. The effect of gabapentin on brain gamma-aminobutyric acid in patients with epilepsy. *Annals of neurology.* 1996;39(1):95-99.
18. Zhang X, Du Z, Liu J, He J. Γ-aminobutyric acid receptors affect the progression and migration of tumor cells. *Journal of Receptors and Signal Transduction.* 2014;34(6):431-439.
19. Govindaraju V, Young K, Maudsley AA. Proton NMR chemical shifts and coupling constants for brain metabolites. *NMR in Biomedicine.* 2000;13(3):129-153.
20. Snyder J, Wilman A. Field strength dependence of PRESS timings for simultaneous detection of glutamate and glutamine from 1.5 to 7T. *Journal of Magnetic Resonance.* 2010;203(1):66-72.
21. Mescher M, Merkle H, Kirsch J, Garwood M, Gruetter R. Simultaneous in vivo spectral editing and water suppression. *NMR in Biomedicine.* 1998;11(EPFL-ARTICLE-177509):266-272.
22. Hanstock CC, Coupland NJ, Allen PS. GABA X2 multiplet measured pre-and post-administration of vigabatrin in human brain. *Magnetic resonance in medicine.* 2002;48(4):617-623.
23. Hurd R, Sailasuta N, Srinivasan R, Vigneron DB, Pelletier D, Nelson SJ. Measurement of brain glutamate using TE-averaged PRESS at 3T. *Magnetic resonance in medicine.* 2004;51(3):435-440.
24. Choi C, Dimitrov IE, Douglas D, et al. Improvement of resolution for brain coupled metabolites by optimized 1H MRS at 7 T. *NMR in Biomedicine.* 2010;23(9):1044-1052.
25. Yang S, Hu J, Kou Z, Yang Y. Spectral simplification for resolved glutamate and glutamine measurement using a standard STEAM sequence with optimized timing parameters at 3, 4, 4.7, 7, and 9.4 T. *Magnetic resonance in medicine.* 2008;59(2):236-244.
26. Hu J, Yang S, Xuan Y, Jiang Q, Yang Y, Haacke EM. Simultaneous detection of resolved glutamate, glutamine, and γ-aminobutyric acid at 4T. *Journal of Magnetic Resonance.* 2007;185(2):204-213.
27. Waddell KW, Zanjanipour P, Pradhan S, et al. Anterior cingulate and cerebellar GABA and Glu correlations measured by 1 H J-difference spectroscopy. *Magnetic resonance imaging.* 2011;29(1):19-24.
28. O'Gorman RL, Michels L, Edden RA, Murdoch JB, Martin E. In vivo detection of GABA and glutamate with MEGA-PRESS: Reproducibility and gender effects. *Journal of Magnetic Resonance Imaging.* 2011;33(5):1262-1267.
29. Snyder J, Thompson RB, Wilman AH. Difference spectroscopy using PRESS asymmetry: application to glutamate, glutamine, and myo-inositol. *NMR in Biomedicine.* 2010;23(1):41-47.
30. Hennig J, Thiel T, Speck O. Improved sensitivity to overlapping multiplet signals in in vivo proton spectroscopy using a multiecho volume selective (CPRESS) experiment. *Magnetic resonance in medicine.* 1997;37(6):816-820.
31. Choi C, Coupland NJ, Bhardwaj PP, Malykhin N, Gheorghiu D, Allen PS. Measurement of brain glutamate and glutamine by spectrally-selective refocusing at 3 tesla. *Magnetic resonance in medicine.* 2006;55(5):997-1005.
32. Thompson RB, Allen PS. A new multiple quantum filter design procedure for use on strongly coupled spin systems found in vivo: its application to glutamate. *Magnetic resonance in medicine.* 1998;39(5):762-771.
33. Schulte RF, Boesiger P. ProFit: two-dimensional prior-knowledge fitting of J-resolved spectra. *NMR in Biomedicine.* 2006;19(2):255-263.
34. Shungu DC, Mao X, Gonzales R, et al. Brain γ-aminobutyric acid (GABA) detection in vivo with the J-editing 1H MRS technique: a comprehensive methodological evaluation of sensitivity

enhancement, macromolecule contamination and test–retest reliability. *NMR in Biomedicine.* 2016;29(7):932-942.

35. Kaiser L, Young K, Meyerhoff D, Mueller S, Matson G. A detailed analysis of localized J-difference GABA editing: theoretical and experimental study at 4 T. *NMR in Biomedicine.* 2008;21(1):22-32.

36. Van Eijsden P, Behar KL, Mason GF, Braun KP, De Graaf RA. In vivo neurochemical profiling of rat brain by 1H-[13C] NMR spectroscopy: cerebral energetics and glutamatergic/GABAergic neurotransmission. *Journal of neurochemistry.* 2010;112(1):24-33.

37. Choi C, Bhardwaj PP, Kalra S, et al. Measurement of GABA and contaminants in gray and white matter in human brain in vivo. *Magnetic resonance in medicine.* 2007;58(1):27-33.

38. Ganji SK, An Z, Banerjee A, Madan A, Hulsey KM, Choi C. Measurement of regional variation of GABA in the human brain by optimized point-resolved spectroscopy at 7 T in vivo. *NMR in Biomedicine.* 2014;27(10):1167-1175.

39. Stephenson MC, Gunner F, Napolitano A, et al. Applications of multi-nuclear magnetic resonance spectroscopy at 7 T. *World journal of radiology.* 2011;28:105-113.

40. Rao R, Tkac I, Townsend EL, Gruetter R, Georgieff MK. Perinatal iron deficiency alters the neurochemical profile of the developing rat hippocampus. *The Journal of nutrition.* 2003;133(10):3215-3221.

41. Raman L, Tkac I, Ennis K, Georgieff MK, Gruetter R, Rao R. In vivo effect of chronic hypoxia on the neurochemical profile of the developing rat hippocampus. *Developmental brain research.* 2005;156(2):202-209.

42. Marjanska M, Curran GL, Wengenack TM, et al. Monitoring disease progression in transgenic mouse models of Alzheimer's disease with proton magnetic resonance spectroscopy. *Proceedings of the National Academy of Sciences of the United States of America.* 2005;102(33):11906-11910.

43. Öz G, Nelson CD, Koski DM, et al. Noninvasive detection of presymptomatic and progressive neurodegeneration in a mouse model of spinocerebellar ataxia type 1. *Journal of Neuroscience.* 2010;30(10):3831-3838.

44. Tkac I, Dubinsky JM, Keene CD, Gruetter R, Low WC. Neurochemical changes in Huntington R6/2 mouse striatum detected by in vivo1H NMR spectroscopy. *Journal of neurochemistry.* 2007;100(5):1397-1406.

45. Wang WT, Lee P, Yeh HW, Smirnova IV, Choi IY. Effects of acute and chronic hyperglycemia on the neurochemical profiles in the rat brain with streptozotocin-induced diabetes detected using in vivo1H MR spectroscopy at 9.4 T. *Journal of neurochemistry.* 2012;121(3):407-417.

46. Choi IY, Seaquist ER, Gruetter R. Effect of hypoglycemia on brain glycogen metabolism in vivo. *Journal of neuroscience research.* 2003;72(1):25-32.

47. Provencher SW. Estimation of metabolite concentrations from localized in vivo proton NMR spectra. *Magnetic resonance in medicine.* 1993;30(6):672-679.

48. Pfeuffer J, Tkáč I, Provencher SW, Gruetter R. Toward an in vivo neurochemical profile: quantification of 18 metabolites in short-echo-time 1 H NMR spectra of the rat brain. *Journal of Magnetic Resonance.* 1999;141(1):104-120.

49. Xin L, Gambarota G, Duarte J, Mlynárik V, Gruetter R. Direct in vivo measurement of glycine and the neurochemical profile in the rat medulla oblongata. *NMR in Biomedicine.* 2010;23(9):1097-1102.

50. Tkáč I, Rao R, Georgieff MK, Gruetter R. Developmental and regional changes in the neurochemical profile of the rat brain determined by in vivo 1H NMR spectroscopy. *Magnetic resonance in medicine.* 2003;50(1):24-32.

51. Tkáč I, Henry PG, Andersen P, Keene CD, Low WC, Gruetter R. Highly resolved in vivo 1H NMR spectroscopy of the mouse brain at 9.4 T. *Magnetic resonance in medicine.* 2004;52(3):478-484.

52. Dou W, Palomero-Gallagher N, Van Tol M-J, et al. Systematic regional variations of GABA, glutamine, and glutamate concentrations follow receptor fingerprints of human cingulate cortex. *The journal of newuroscience.* 2013;33:12698-12704.

53. Sanaei Nezhad F, Anton A, Parkes LM, Deakin B, Williams SR. Quantification of glutathione in the human brain by MR spectroscopy at 3 Tesla: Comparison of PRESS and MEGA-PRESS. *Magnetic resonance in medicine.* DOI: 10.1002/mrm.26532.

54. Hofmann L, Slotboom J, Boesch C, Kreis R. Characterization of the macromolecule baseline in localized 1H-MR spectra of human brain. *Magnetic resonance in medicine.* 2001;46(5):855-863.

55. Gottschalk M, Troprès I, Lamalle L, Grand S, Le Bas JF, Segebarth C. Refined modelling of the short-T2 signal component and ensuing detection of glutamate and glutamine in short-TE, localised, 1H MR spectra of human glioma measured at 3 T. *NMR in Biomedicine.* 2016.

56. Xu S, Ji Y, Chen X, Yang Y, Gullapalli RP, Masri R. In vivo high-resolution localized 1H MR spectroscopy in the awake rat brain at 7 T. *Magnetic resonance in medicine.* 2013;69(4):937-943.

57. Thompson RB, Allen PS. Sources of variability in the response of coupled spins to the PRESS sequence and their potential impact on metabolite quantification. *Magnetic resonance in medicine.* 1999;41(6):1162-1169.

58. Haase A, Frahm J, Hanicke W, Matthaei D. 1H NMR chemical shift selective (CHESS) imaging. *Physics in medicine and biology.* 1985;30(4):341.

59. Xin L, Gambarota G, Mlynárik V, Gruetter R. Proton T2 relaxation time of J-coupled cerebral metabolites in rat brain at 9.4 T. *NMR in Biomedicine.* 2008;21(4):396-401.

60. Cudalbu C, Mlynárik V, Xin L, Gruetter R. Comparison of T1 relaxation times of the neurochemical profile in rat brain at 9.4 tesla and 14.1 tesla. *Magnetic resonance in medicine.* 2009;62(4):862-867.

61. Träber F, Block W, Lamerichs R, Gieseke J, Schild HH. ^{1}H metabolite relaxation times at 3.0 tesla: measurements of T1 and T2 values in normal brain and determination of regional differences in transverse relaxation. *Journal of magnetic resonance imaging.* 2004;19:537-545.

62. Terpstra M, Ugurbil K, Tkac I. Noninvasive quantification of human brain ascorbate concentration using 1H NMR spectroscopy at 7 T. *NMR in Biomedicine.* 2010;23(3):227-232.

63. Kreis R. The trouble with quality filtering based on relative Cramér-Rao lower bounds. *Magnetic resonance in medicine.* 2016;75(1):15-18.

64. Petroff OAC, Rothman DL, Behar KL, Mattson RH. Initial observations on effect of vigabatrin on in vivo ^{1}H spectroscopic measurements of γ-aminobutyric acid, glutamate, and glutamine in human brain. *Epilipsia.* 1995;36:457-464.

65. Gunawan S, Walton NY, Treiman DM. High-performance liquid chromatographic determination of selected amino acids in rat brain by precolumn derivatization with phenylisothiocyanate. *Journal of Chromatography A.* 1990;503:177-187.

66. Mans AM, DeJoseph MR, Hawkins RA. Metabolic abnormalities and grade of encephalopathy in acute hepatic failure. *Journal of neurochemistry.* 1994;63(5):1829-1838.

67. Dou W, Kaufmann J, Li M, Zhong K, Walter M, Speck O. The separation of Gln and Glu in STEAM: a comparison study using short and long TEs/TMs at 3 and 7 T. *Magnetic resonance materials in physics, biology and medicine.* 2015;28:395-405.

68. Lei H, Zhang Y, Zhu X-H, Chen W. Changes in the proton T_2 relaxation times of cerebral water and metabolites during forebrain ischemia in rat at 9.4 T. *Magnetic resonance in medicine.* 2003;49:979-984.

69. Li Y, Srinivasan R, Ratiney H, Lu Y, Chang SM, Nelson SJ. Comparison of T_1 and T_2 metabolite relaxation times in glioma and normal brain at 3 T. *Journal of magnetic resonance imaging.* 2008;28:342-350.

70. Schaller B, Xin L, Gruetter R. Is the macromolecule signal tissue-specific in healthy human brain? A ^{1}H MRS study at 7 tesla in the occipital lobe. *Magnetic resonance in medicine.* 2014;72:934-940.

Chapter 5 - Optimized PRESS Sequence Timings for Improved Spectral Resolution of $^{13}C_4$-Glutamate during a Uniformly-Labelled-^{13}C-Glucose Infusion at 9.4 T

A version of this chapter has been submitted for publication to the journal *NMR in Biomedicine* as:

Dobberthien, B. J., Tessier, A. G., Stanislaus, A. E., Sawyer, M. B, Fallone, B. G., & Yahya, A. PRESS timings for resolving $^{13}C_4$-glutamate ^{1}H signal at 9.4 T: demonstration in rat with uniformly-labelled-^{13}C-glucose.

5.1 - INTRODUCTION

The rate of the tricarboxylic acid (TCA) cycle, also known as the citric acid cycle or the Krebs cycle, has shown to be relevant in the study of cancer,[1,2] Huntington's disease,[3] Alzheimer's disease,[4] epilepsy,[5] Parkinson's disease, and amyotrophic lateral sclerosis.[6] Carbon-13 (^{13}C) magnetic resonance spectroscopy (MRS) in conjunction with the infusion of a ^{13}C-labelled substrate, such as [1-^{13}C]-glucose, enables V_{TCA}, the TCA cycle rate, to be determined.[7,8] Measuring the rate of incorporation of ^{13}C label into the C4 carbon of glutamate ($^{13}C_4$-Glu) has shown to be adequate for estimating V_{TCA} if V_X, the exchange rate between α-ketoglutarate and Glu, is assumed.[3,7] ^{13}C MRS can be performed directly and requires a system with multinuclear capability. The ^{13}C measurements can also be obtained indirectly (^{1}H-[^{13}C] MRS) by measuring signal from the ^{13}C-coupled protons of interest, thereby exploiting the higher sensitivity of the ^{1}H nucleus. Indirect ^{1}H-[^{13}C] MRS techniques, such as Adiabatic Carbon Editing and Decoupling (ACED)-STEAM,[9] a variation of the STimulated Echo Acquisition Mode (STEAM) sequence,[10] and techniques incorporating the Proton-Observed Carbon-Edited (POCE)[11] sequence, have been used *in vivo* to obtain $^{13}C_4$-Glu time courses.[3,9,12-25] The techniques require multinuclear capability because of the application of both ^{13}C and ^{1}H pulses. However, it has been shown that indirect ^{13}C detection can also be performed using a standard proton system without the need for additional ^{13}C hardware.[26-29] A standard short echo time (TE) ^{1}H Point-Resolved Spectroscopy (PRESS)[30] sequence was employed at 3 T to obtain $^{13}C_4$-Glu measures at 3 T from monkey brain during an infusion of uniformly-labelled-^{13}C-glucose ([U-$^{13}C_6$]-Glc).[26] The methodology exploits the satellite peaks that arise as $^{13}C_4$-Glu accumulates. Heteronuclear J-coupling between the $^{13}C_4$ nuclei and the coupled protons causes the $^{12}C_4$-Glu ^{1}H MRS signal at ≈ 2.35 ppm to split into two resonances separated by a coupling constant of about 127 Hz.[31] Quantification of the satellite peaks

over the time course of the infusion yields a measure of $^{13}C_4$-Glu label incorporation. Overlapping signal from other metabolites are removed by subtracting the spectrum at each time point from the initial baseline spectrum.[26]

The high field strength of 9.4 T is used for preclinical MRS studies of animal models.[32-38] 9.4 T studies on glutamatergic energy metabolism in rat brain have been done indirectly with ^{1}H-[^{13}C] MRS methods, such as ACED-STEAM[9] and variations of POCE,[13,19,24,39] as well as with direct ^{13}C MRS methods, such as techniques incorporating Distortionless Enhancement by Polarization Transfer (DEPT).[31,40] All the techniques require a ^{13}C channel. The objective of the presented work is to demonstrate an alternative indirect ^{13}C method at 9.4 T that does not require the application of ^{13}C pulses, based on the technique presented by Boumezbeur et al.,[26] but that does not rely on subtraction, rendering it single-shot. At 9.4 T, the $^{13}C_4$-Glu satellite peaks are located at ≈ 2.51 ppm and ≈ 2.19 ppm. Both the satellites suffer contamination from signal of other metabolites. The *N*-acetylaspartate (NAA) resonance at ≈ 2.49 ppm overlaps the ≈ 2.51 ppm satellite peak, while signals from the $^{12}C_3$-Glu protons (≈ 2.12 ppm), *N*-acetylaspartylglutamate (NAAG) (≈ 2.19 ppm), $^{13}C_3$-Glu (2.20-2.28 ppm), $^{13}C_2$-GABA (γ-aminobutyric acid) (≈ 2.12 ppm, assuming a heteronuclear coupling constant of ≈ 130 Hz.), and macromolecules (MMs) (≈ 2.26 ppm) overlap with the ≈ 2.19 ppm satellite peak.[31,41-44] In this work, we optimize TE_1 and TE_2 of a standard ^{1}H PRESS sequence to suppress the NAA peak at ≈ 2.49 ppm while retaining sufficient 2.51 ppm $^{13}C_4$-Glu proton signal by exploiting differences in J-coupling evolution. The technique resolves the 2.51 ppm resonance without the need for subtraction editing. The ≈ 2.19 ppm satellite peak is obscured by more signals and is, therefore, not targeted for optimization. The longer TE value also enables the suppression of MM signals, which contaminate the entire spectrum, including all $^{13}C_4$-Glu and $^{12}C_4$-Glu signals at short TEs.[42-44] The efficacy of the optimized ^{1}H

PRESS sequence is verified on phantom solutions and *in vivo* on two rat brains during infusion of [U-$^{13}C_6$]-Glc.

5.2 - MATERIALS AND METHODS

The response of NAA, ^{12}C-Glu, $^{13}C_4$-Glu, and Gln proton signals to a standard single-voxel PRESS sequence at 9.4 T was investigated as a function of TE_1 and TE_2. Numerical simulations were based on density matrix calculations using a previously developed MATLAB (Mathworks, Natick, MA, USA) program[45] with modifications to incorporate a ^{13}C nucleus.[46] J-coupling interactions, slice selection gradient strengths, refocusing pulse shape (2 ms, 5-lobe sinc pulses of bandwidth 3000 Hz) and 2.8 ppm offset frequency were taken into account; T_2 relaxation was ignored. The chemical shift and scalar coupling constants were based on those provided by Govindaraju et al.,[41] while the $^{13}C_4$-Glu scalar coupling constant of 127 Hz was obtained from Deelchand et al.[31] A sampling frequency of 10 000 Hz was used, with 8192 data points. The minimum values for (TE_1, TE_2) were (2 ms, 2 ms) due to the refocusing pulse duration of 2 ms. Spectra were line broadened to match *in-vivo* water linewidths of ≈ 20 Hz.

Contour plots were created for the peak areas of each of the metabolites, for TE_1 and TE_2 ranges of 14-116 ms each, in steps of 2 ms. The minimum was chosen to be larger than the minimum achievable experimentally, and the maximum total TE (TE_1 + TE_2) was chosen to be 130 ms to limit the effects of T_2 relaxation. Peak areas were determined in the 2.30-2.39 ppm, the 2.40-2.49 ppm and the 2.45-2.55 ppm spectral regions for the ≈ 2.35 ppm ^{12}C-Glu, the ≈ 2.45 ppm Gln, and the ≈ 2.51 ppm $^{13}C_4$-Glu resonances, respectively. To maximize $^{13}C_4$-Glu and minimize NAA contamination in the latter spectral region, an objective function was created by subtracting

the absolute, normalized peak area of NAA from the normalized peak area of $^{13}C_4$-Glu. Each was normalized to the maximum value at a (TE_1, TE_2) of (2 ms, 2 ms). The function was defined as $objective = \frac{13C_4Glu_{PA}}{13C_4Glu_{PA,max}} - \frac{NAA_{PA}}{NAA_{PA,max}}$, where $13C_4Glu_{PA}$ and NAA_{PA} are the integrated peak areas of $^{13}C_4$-Glu and NAA, respectively. The (TE_1, TE_2) combination that maximized the function was considered optimal for resolving the $^{13}C_4$-Glu resonance. The absolute area of NAA was used instead of the real area to ensure minimal contamination of $^{13}C_4$-Glu. For each metabolite, the peak area relative to the corresponding value at (2 ms, 2 ms) was calculated with the optimal TE combination. The individual spectra of each metabolite were simulated with (TE_1, TE_2) = (12 ms, 9 ms), the minimum echo time combination used experimentally, as well as with the optimal TE combination. Additional numerical calculation details are included in section 2.2.

The efficacy of the optimal TE combination was verified experimentally on ≈ 30 mm diameter spherical phantom solutions, using a 9.4 T animal MRI scanner (Magnex Scientific, Oxford, UK) with a 21.5 cm bore, in combination with a TMX console (National Research Council of Canada Institute for Biodiagnostics, West, Calgary, AB, Canada). Additional details about the MRI system can be found in section 2.3.1. PRESS refocusing pulses consisted of 2 ms, 5-lobe sinc pulses with a bandwidth of 3000 Hz. Pulse frequency offset was set to 2.8 ppm (approximate centre of spectrum). A 4.3 cm diameter birdcage radiofrequency (RF) coil (National Research Council of Canada Institute for Biodiagnostics, West, Calgary, AB, Canada) was used for both transmission and reception. 5 x 5 x 5 mm^3 voxels were placed in the center of the phantoms, and spectra were acquired in 32 averages, with a repetition time (TR) of 5 s and an eight-step phase cycling scheme. 8192 data points were collected with a 10 000 Hz sampling frequency. Manual shimming was performed and shims were adjusted until the peak amplitude of the water was maximized;

linewidths less than 5 Hz were obtained. A chemical shift-selective[47] imaging sequence was used for water suppression.

Individual metabolite phantoms contained 50 mM of each of NAA, ^{12}C-Glu, 99 % enriched $^{13}C_4$-Glu, and Gln. Each phantom also contained 10 mM creatine (Cr) to serve as a reference. All metabolites were purchased from Millipore Sigma (Oakville, ON, Canada). Spectra were acquired with the optimal (TE_1, TE_2) and with the short TE combination of (12 ms, 9 ms). Spectra were processed with software provided by the National Research Council of Canada (Spectrum Viewer v. 2.00.002, National Research Council of Canada Institute for Biodiagnostics, West, Calgary, AB, Canada). Processing included filtering, zero-filling, Fourier transformation, phase correction, and baseline correction. The same software was used for manual integration of peak areas. The spectral regions used for integration were 2.30–2.39 ppm, 2.40–2.49 ppm, and 2.45-2.55 ppm for ^{12}C-Glu, Gln, and $^{13}C_4$-Glu and NAA, respectively.

An additional phantom was created with 45 mM NAA, 25 mM ^{12}C-Glu, 25 mM $^{13}C_4$-Glu, 20 mM Gln, 5 mM GABA, and 45 mM Cr ("*in-vivo* phantom") to mimic typical ratios in rat brain,[42] with Glu split evenly into ^{12}C-Glu and $^{13}C_4$-Glu. All metabolites were purchased from Millipore Sigma (Oakville, ON, Canada). The phantom was scanned with the optimal TE combination and with (12 ms, 9 ms), and spectra were compared to those of the $^{13}C_4$-Glu-only phantom. The ratio of $^{13}C_4$-Glu to Cr differed between the phantoms; therefore, a scaling factor of 9 ([45 mM Cr/10 mM Cr] x [50 mM $^{13}C_4$-Glu/25 mM $^{13}C_4$-Glu]) was applied to the "*in-vivo* phantom" spectra after the two phantom spectra were adjusted such that the Cr peaks were equal in height. The scaling was performed for both the short-TE and the long-TE spectra. Phantom experiment details are discussed in section 2.3.2.

In vivo spectra were acquired from the brains of two Sprague-Dawley rats (about 10 months of age) during an infusion of 99 % enriched [U-$^{13}C_6$]-Glc solution. Prior to experiment, the rat was weighed. The 99 % enriched [U-$^{13}C_6$]-Glc was mixed with a saline solution to create a solution of 0.75 M/(200 g body weight),[13,24] and was then filtered with a Millex®-GS 0.22 µm syringe filter (Fisher Scientific Company, Ottawa, ON, Canada) for sterilization. The rat underwent overnight fasting (12-16 hours) and was anaesthetized with isoflurane for the duration of the experiment. It was placed in a prone position, with a single-loop 24-mm-diamater surface RF coil (Doty Scientific, Inc., Columbia, SC, USA) placed on top of its head for both RF transmission and reception. A respiration pillow was attached to the abdomen for respiration monitoring and gating, and a temperature probe was inserted in the rectum for temperature monitoring during the experiment. Temperature was maintained at 37 °C with a heating module. The rat tail vein was cannulated and attached via PE-10 tubing to a BD 3 ml Luer-Lok™ tip syringe (Fisher Scientific Company, Ottawa, ON, Canada), which was filled with the [U-$^{13}C_6$]-Glc solution and placed in a Multi-Phaser™ NE-4000 Double Syringe Pump (New Era Pump Systems Inc., Farmingdale, NY, USA). Spin echo imaging scans were used to localize a 5 x 5 x 5 mm^3 PRESS voxel with its center ≈ 6 mm from the surface coil and approximately centered in the brain. Images were acquired with a TE of 13 ms and a TR of at least 1250 ms.

First order shimming was adjusted manually until the peak amplitude of the water was maximized, resulting in a linewidth of ≈ 20-25 Hz. A baseline pre-injection PRESS spectrum was acquired with the optimal TE combination, in 256 averages, with a TR of at least 3 s in 2048 complex data points, sampled at 10,000 Hz. Following that, the [U-$^{13}C_6$]-Glc injection was initiated. The injection protocol was designed to estimate a decreasing exponential in 10 steps, each 30 s in duration, starting at 500 µl/min and ending at 13.7 µl/min, followed by a constant

injection rate of 13.7 µl/min for the rest of the experiment. The protocol is similar but not identical to those described in the literature.[13,24] Six post-injection spectra were acquired, spaced 20 minutes apart, with midpoints at 10, 30, 50, 70, 90, and 110 minutes after injection. The 90-minute scan was acquired with a short TE combination of (12 ms, 9 ms), while the rest were acquired with the optimal TE combination. Additional details regarding rat brain experiments are in section 2.3.3.

To obtain a measure of blood ^{13}C fractional enrichment, a third rat was prepared according to the described procedure. Two 250 µL venous blood samples were taken, one before (pre-injection) and one after 120 minutes of infusion (post-injection), to determine plasma glucose ^{13}C FE with mass spectrometry. Blood samples were centrifuged at 8000 rpm for 2 min, and the supernatant (plasma) was removed. Plasma samples were prepared by adding 20 µL of plasma and 10 µL of an internal standard (final concentration 5 mM), namely, deuterated-uniformly-labelled ^{13}C-glucose ($^{13}C_6$-d_7-Glc (Millipore Sigma, Oakville, ON, Canada), to 170 µL acetonitrile. The mixture was vortexed for 2 min and then centrifuged at 12,700 rpm for 10 minutes at 4 °C. The supernatant was transferred to a high-performance liquid chromatography vial for analysis. Mobile phase consisted of 15 % 20 mM ammonium acetate, with a pH of 9, and 85% acetonitrile. The flow rate was 400 µL/min, the column temperature was 65 °C, and the autosampler temperature was 4 °C. The run time was 6 minutes. The mass spectrometer was operated in the negative mode, and the acquisition was performed in multiple reaction monitoring mode. Three replicates each of both pre- and post-injection acquisition plasma were assessed, and an average and standard deviation was determined for regular glucose and [U-$^{13}C_6$]-Glc. Plasma FE was calculated by dividing the concentration of [U-$^{13}C_6$]-Glc by the sum of [U-$^{13}C_6$]-Glc and regular glucose in the post-injection blood sample.

LCModel software[48] was utilized to fit and analyze the *in-vivo* spectra. The basis sets were specific to the combination of field strength and (TE_1, TE_2) and were provided by the vendor, with additional MMs and lipids signals simulated by LCModel. A separate basis set was used for each of the two echo time combinations. Each basis set included alanine (Ala), aspartate (Asp), Glc, Cr, phosphocreatine (PCr), Gln, Glu, GABA, glycerylphosphorylcholine (GPC), phosphocholine (PCh), glutathione (GSH), myo-inositol (mI), lactate (Lac), NAA, NAAG, scyllo-inositol (Scyllo), and taurine (Tau). Basis files for Gln, Glu, GABA, GSH, NAA, and NAAG were replaced with simulated spectra with our MATLAB software to account for differences in spectral response due to the refocusing pulse shape.[45] In addition, we simulated $^{13}C_4$-Glu spectra for each TE combination and incorporated them into the corresponding basis sets. Because of the complex overlap of a number of unaccounted signals that influence the 2.19 ppm peak, the two satellite peaks were separated into two different basis spectra, and $^{13}C_4$-Glu quantification was based on LCModel fits of the 2.51 ppm peak. The individual groups of NAA (acetyl [≈ 2.01 ppm] and aspartyl [≈ 2.49 and ≈ 2.67 ppm]) and NAAG (acetyl [≈ 2.04 ppm], aspartyl [≈ 2.52 and ≈ 2.72 ppm], and glutamyl [≈ 1.88, ≈ 2.05 and ≈ 2.19 ppm]) were separated in the basis set to allow for some flexibility in LCModel fitting, should differences in T_2 values between the different proton groups lead to LCModel errors in quantification with the longer TE.[49] Fitted spectra were obtained in the range 0.2-4.0 ppm, together with an LCModel table of relative Cramér-Rao Lower Bound (CRLB) values for each metabolite in addition to concentrations relative to total creatine.

The total Glu pool (^{12}C-Glu + $^{13}C_4$-Glu) was estimated from the baseline spectrum (pre-infusion) by removing $^{13}C_4$-Glu from the basis set (assumed to be zero pre-infusion) and using LCModel to obtain a concentration estimate of ^{12}C-Glu. The concentration of NAA pre-infusion was found as well. The ratio of NAA to total Glu was kept constant throughout the analysis using

the nratio and chrato commands in LCModel to maintain a constant sum of total Glu. Glu C4 fractional enrichment (FE) values were determined at each *in vivo* time point by dividing the estimated $^{13}C_4$-Glu concentration by the total Glu amount. ^{12}C-Glu and $^{13}C_4$-Glu concentrations were calculated assuming a tCr (total creatine = creatine + phosphocreatine) concentration of 8.5 mM in rat brain.[42] A description of the data analysis can be found in section 2.4.

Estimated V_{TCA} values were determined based on the mathematical model that only uses $^{13}C_4$-Glu labelling[3] with modifications made to account for using [U-$^{13}C_6$]-Glc (instead of $^{13}C_1$-Glc).[50] All assumptions were as with Ref. [3] with the following additions: initial brain glucose of 1.7 µmol/g,[51] V_X of 5.5 µmol/min/g,[24] and a plasma glucose FE as determined by our blood sample analysis. Calculations were performed in MATLAB.

5.3 - RESULTS

Figure 5.1 shows the contour plot of the objective function, normalized to the maximum value, with each TE varying from 14 ms to 116 ms. Contour line values range from -1.2 to 0.8 in steps of 0.4. The optimal (TE_1, TE_2) combination was determined to be (20 ms, 106 ms), as indicated with an asterisk on the plot and that provides an objective function value of 0.811. $^{13}C_4$-Glu and NAA have peak areas of 59 % and -2 % at TE values of (20 ms, 106 ms), relative to their respective values at (2 ms, 2 ms).

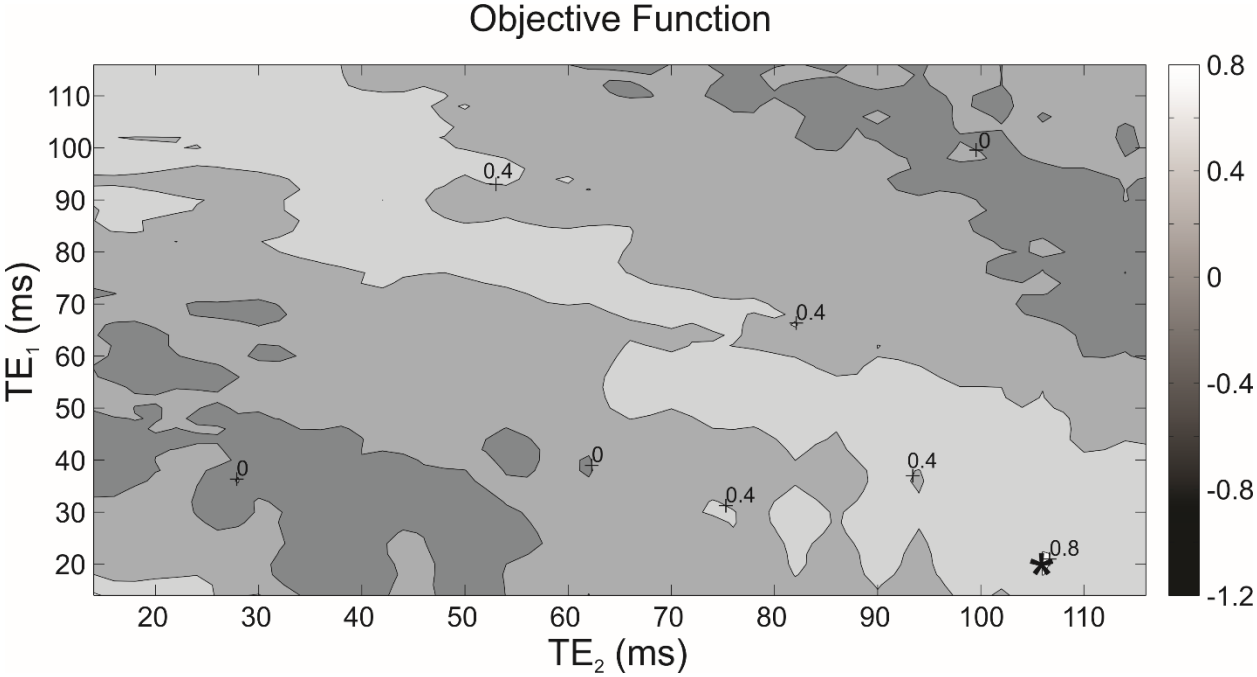

Figure 5.1: Contour plot of the objective function (normalized $^{13}C_4$-Glu area – normalized NAA area), normalized to the maximum value, with the optimal (TE_1, TE_2) of (20 ms, 106 ms) represented with an asterisk. TE_1 values are displayed on the y-axis, while TE_2 values are on the x-axis, each varying from 14–116 ms in steps of 2 ms. Normalized $^{13}C_4$-Glu and NAA values are with respect to values obtained with (TE_1, TE_2) of (2 ms, 2 ms).

Figure 5.2 presents both theoretical (left) and experimental (right) spectra for NAA, $^{13}C_4$-Glu, Gln, and ^{12}C-Glu. The solid line shows the short-TE spectra, while the dashed line displays the long-TE spectra. The figure demonstrates close agreement between numerically calculated and experimentally acquired phantom spectra. The theoretical peak areas at (20 ms, 106 ms) were 75 %, -4 %, 69 % and 80 %, for $^{13}C_4$-Glu, NAA, Gln, and ^{12}C-Glu, relative to their corresponding (12 ms, 9 ms) values. Phantom measurements with (TE_1, TE_2) = (20 ms, 106 ms) resulted in peak areas

of 54 %, -14 %, 51 %, and 62 % for $^{13}C_4$-Glu, NAA, Gln, and ^{12}C-Glu, respectively, relative to their corresponding (12 ms, 9 ms) values.

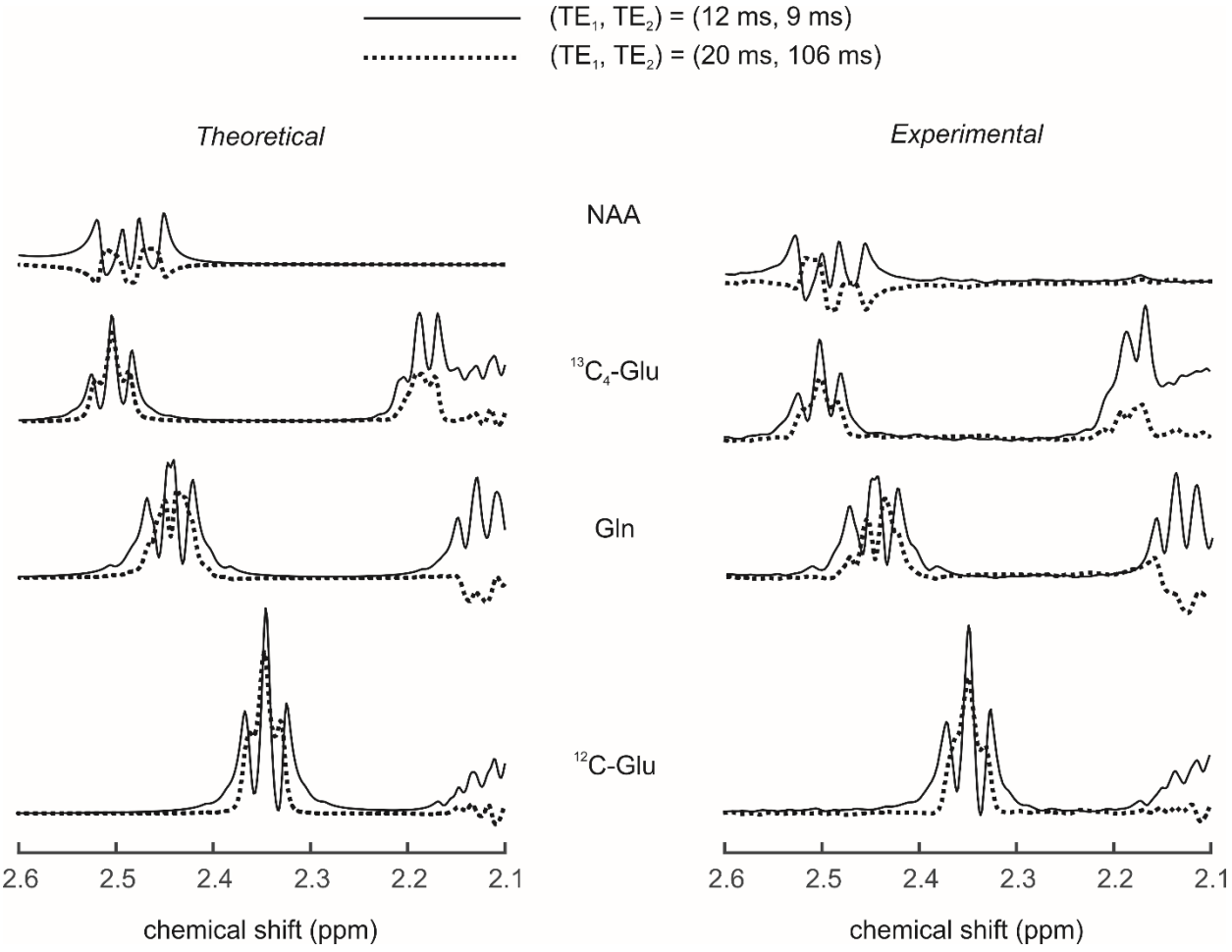

Figure 5.2: Theoretical (simulated, left) and experimental phantom (right) spectra obtained for individual metabolites with a (TE_1, TE_2) of (12 ms, 9 ms) (solid line) and (20 ms, 106 ms) (dashed line).

Figure 5.3 shows an overlap of spectra acquired from the "*in-vivo* phantom" (solid line) and the $^{13}C_4$-Glu only phantom (dashed line). The peak area in the $^{13}C_4$-Glu 2.45 – 2.55 ppm spectral region was 176 % higher in the "*in-vivo* phantom" with (TE_1, TE_2) = (12 ms, 9 ms) and 36 % higher with (TE_1, TE_2) = (20 ms, 106 ms), compared to the corresponding areas found from the $^{13}C_4$-Glu only phantom spectra.

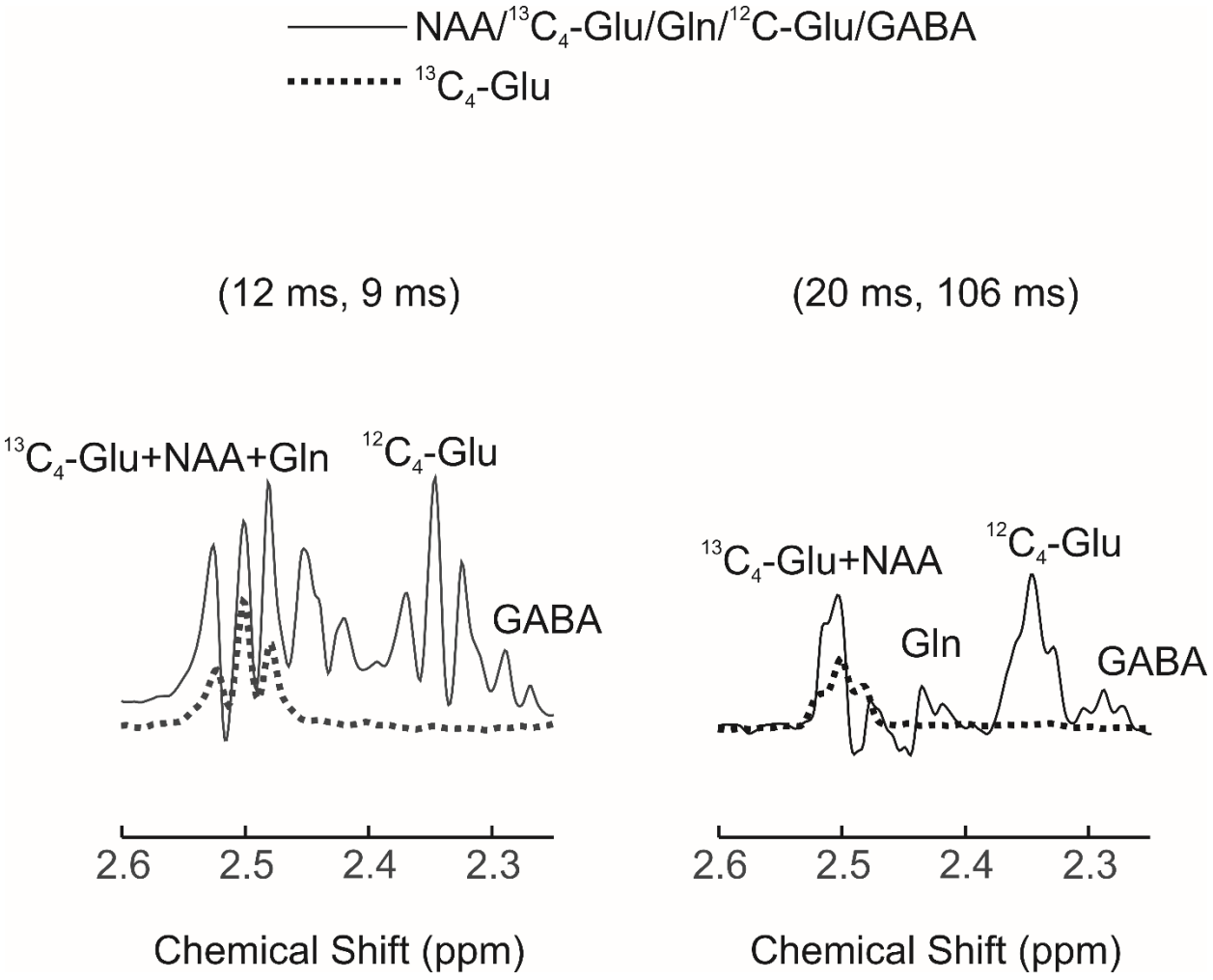

Figure 5.3: Spectra from the "*in-vivo* phantom", containing 45 mM Cr, 45 mM NAA, 25 mM $^{13}C_4$-Glu, 20 mM Gln, 25 mM Glu, and 5 mM GABA (solid line), overlapped with spectra from a

phantom containing 50 mM $^{13}C_4$-Glu only (dashed line) in addition to 10 mM Cr. Spectra were acquired with a (TE_1, TE_2) of (12 ms, 9 ms) (left) and (20 ms, 106 ms) (right). The spectra were adjusted such that the Cr peaks were equal in height, following which the "*in-vivo* phantom" spectra were multiplied by a scaling factor of 9 to compensate for differences in the ratio of $^{13}C_4$-Glu to Cr between the phantoms.

Proton spectra acquired from one of the rats before and at various time points during [U-$^{13}C_6$]-Glc infusion are shown in Figure 5.4. The midpoints of the scans are as indicated on the figure. Baseline-corrected *in vivo* spectra acquired with (20 ms, 106 ms) are overlapped with LCModel fits. PRESS voxel placement is shown on transverse and coronal images of the rat brain.

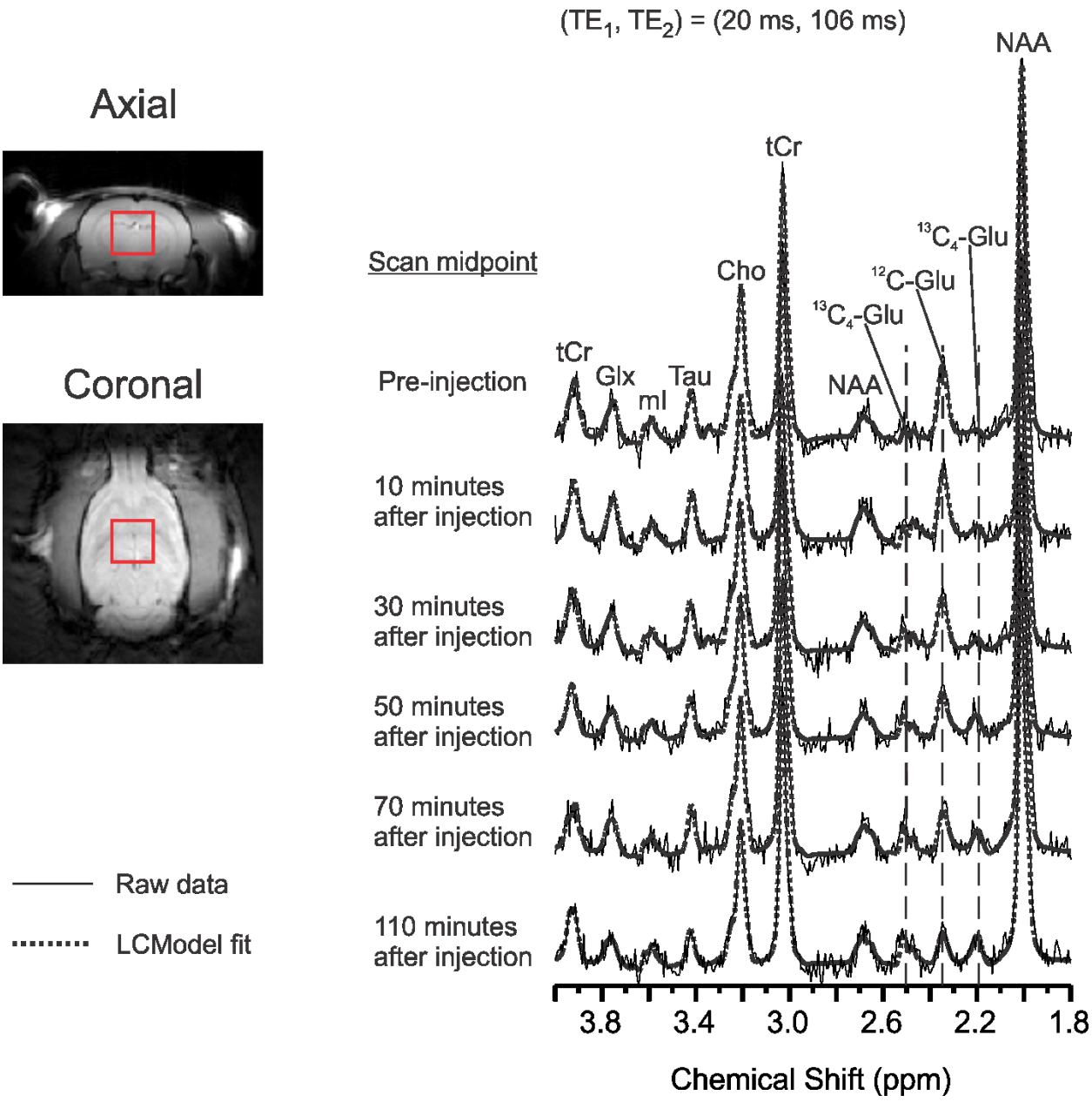

Figure 5.4: *In vivo* rat brain spectra acquired at 9.4 T, with voxel placement shown in an axial and coronal image (left) and PRESS spectra acquired during a [U-$^{13}C_6$]-Glc infusion with the optimal (TE_1, TE_2) of (20 ms, 106 ms) (right), overlapped with their corresponding baseline corrected LCModel fits. Spectra are labelled with the time acquired post-injection, based on the midpoint of the scan.

Two *in vivo* spectra acquired at the end of the infusion are shown for one of the rats in Figure 5.5 (same rat as Figure 5.4). One was acquired with a short TE of (TE_1, TE_2) = (12 ms, 9 ms) (top, midpoint of acquisition 90 minutes) and the other with the long TE of (TE_1, TE_2) = (20 ms, 106 ms) (bottom, midpoint of acquisition 110 minutes). As in Figure 5.4, the spectra include baseline-corrected *in vivo* data, overlapped with LCModel fits. The CRLB values of the 2.51 ppm $^{13}C_4$-Glu protons peak were 15 % and 21 % for the two rats with a (TE_1, TE_2) of (12 ms, 9 ms), and 7 % and 8 % with a (TE_1, TE_2) of at (20 ms, 106 ms).

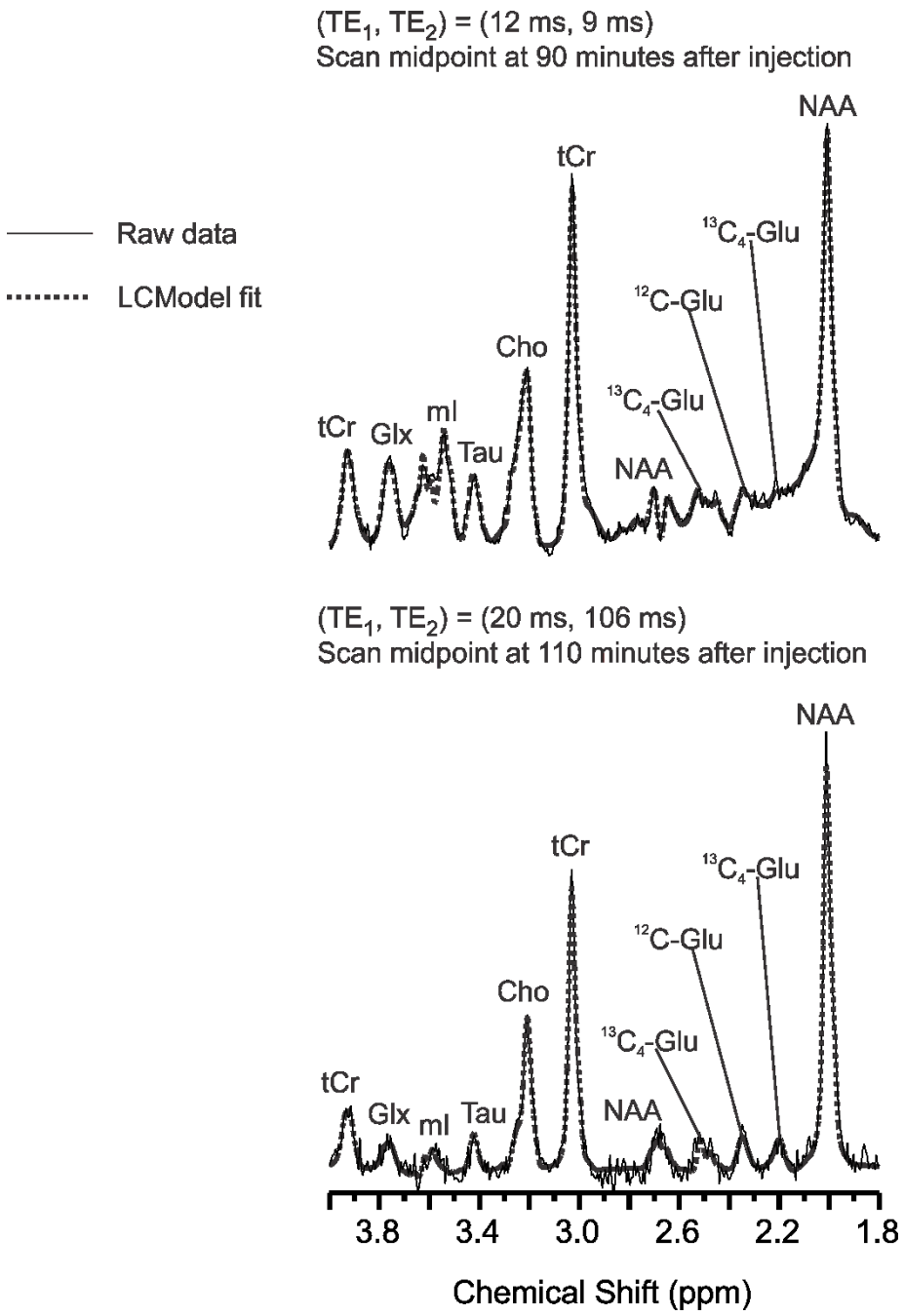

Figure 5.5: *In vivo* rat brain PRESS spectra acquired at 9.4 T with a (TE_1, TE_2) of (12 ms, 9 ms) (top) and (20 ms, 106 ms) (bottom), overlapped with their corresponding baseline corrected LCModel fits. The spectra were acquired towards the end of a [U-$^{13}C_6$]-Glc infusion, with the midpoint of the (12 ms, 9 ms) spectrum acquired 90 minutes post-injection and the (20 ms, 106 ms) spectrum acquired 110 minutes post-injection.

Figure 5.6 presents the Glu C4 FE time courses averaged from the *in-vivo* spectra acquired from the two rats. Table 5.1 lists $^{13}C_4$-Glu and ^{12}C-Glu concentrations, their CRLB values, and Glu C4 FEs for each scan. The calculated Glu ^{13}C FE for the two rats were found to be 0.58 and 0.60, at 110 minutes post-injection.

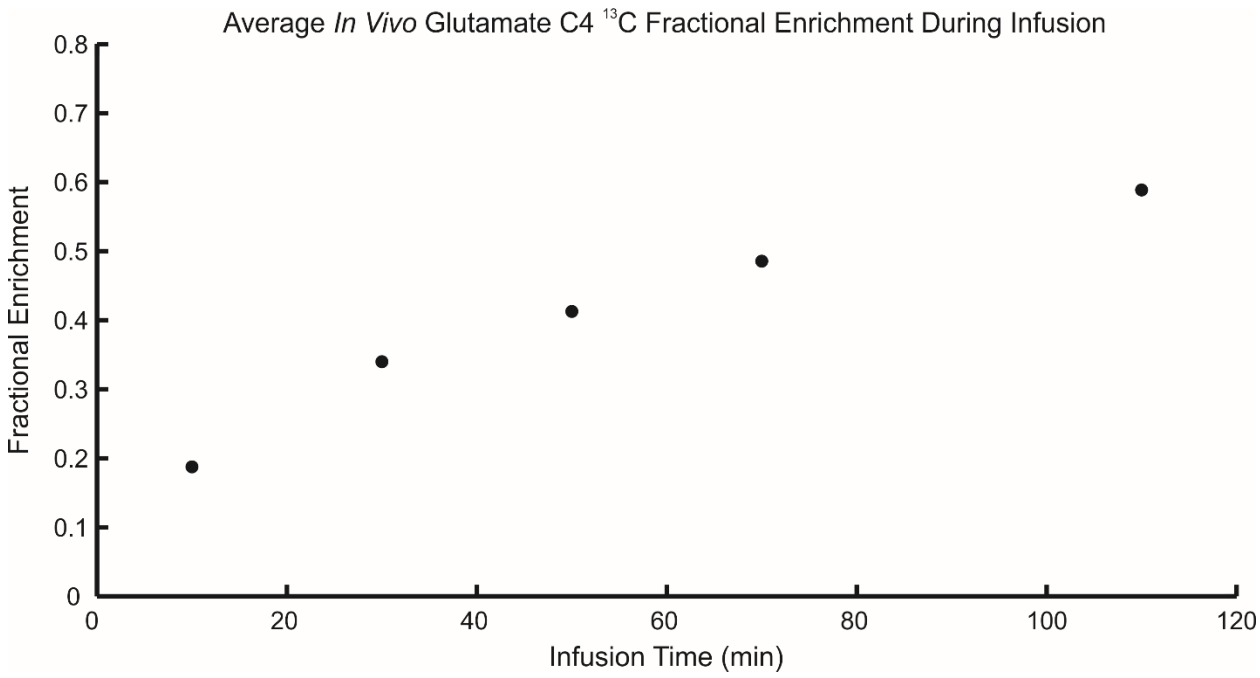

Figure 5.6: Glu C4 ^{13}C FE time course, with FE quantification acquired from LCModel analysis of the (20 ms, 106 ms) spectra, averaged from the first two rats. Infusion time is listed as the midpoint of each scan and is displayed on the x-axis.

Rat Number	Infusion Time (min)	TE_1 (ms), TE_2 (ms)	Estimated $^{13}C_4$-Glu Concentration (mM) (CRLB)	Estimated ^{12}C-Glu Concentration (mM) (CRLB)	Fractional Enrichment
1	0	20, 106	0	10.04 (5 %)	0
	10	20, 106	1.63 (27 %)	8.45 (5 %)	0.16
	30	20, 106	3.13 (12 %)	6.82 (5 %)	0.31
	50	20, 106	3.75 (11 %)	6.00 (7 %)	0.38
	70	20, 106	4.64 (8 %)	5.13 (7 %)	0.47
	90	12, 9	2.66 (15 %)	5.50 (7 %)	0.33
	110	20, 106	5.67 (7 %)	4.18 (9 %)	0.58
2	0	20, 106	0	8.41 (6 %)	0
	10	20, 106	1.85 (19 %)	6.83 (5 %)	0.21
	30	20, 106	3.10 (12 %)	5.40 (7 %)	0.37
	50	20, 106	3.90 (10 %)	4.95 (8 %)	0.44
	70	20, 106	4.26 (9 %)	4.33 (9 %)	0.50
	90	12, 9	1.61 (21 %)	4.66 (7 %)	0.26
	110	20, 106	5.13 (8 %)	3.40 (11 %)	0.60

Table 5.1: Summary of the LCModel analysis performed on the spectra acquired from the two rats during their respective [U-$^{13}C_6$]-Glc infusions. Infusion times are listed as the time from the start of injection to the midpoint of each scan. Concentrations are calculated from the ratio relative to total creatine (tCr), assuming a tCr concentration of 8.5 mM. Relative Cramér Rao Lower Bounds (CRLBs) are given in brackets. Fractional Enrichment is calculated by dividing the estimated $^{13}C_4$-Glu concentration by the sum of the $^{13}C_4$-Glu and ^{12}C-Glu concentrations.

The plasma glucose ^{13}C FE obtained from the third rat was and 68.0 % at 120 minutes after infusion initiation. Determined V_{TCA} values for were 0.61 and 0.58 μmol/min/g for the two rats.

5.4 - DISCUSSION

Measuring brain $^{13}C_4$-Glu with MRS during an infusion of a ^{13}C-labelled substrate such as [U-$^{13}C_6$]-Glc provides a measure of the TCA cycle rate, V_{TCA}, from the Glu C4 FE time course.[7,8]

Such measures have been performed in rat brain at 9.4 T.[9,13,19,24,31,39,40] Techniques that require system multinuclear capability were used. In this work, we show that the readily available ^{1}H PRESS pulse sequence with an optimized (TE_1, TE_2) of (20 ms, 106 ms) can be used for detection and quantification of $^{13}C_4$-Glu in rat brain at 9.4 T during a [U-$^{13}C_6$]-Glc infusion, without the need for ^{13}C hardware or the subtraction of scans. The determined TE timings resolved the ≈ 2.51 ppm $^{13}C_4$-Glu proton satellite peak from the overlapping 2.49 ppm NAA proton peak, while also enabling short-T_2 MM signals to decay. The numerically calculated NAA contamination in the $^{13}C_4$-Glu spectral region of 2.45-2.55 ppm was reduced to -4 % of the (12 ms, 9 ms) peak area. Relatively high numerical signal yields of 75 %, 80 % and 69 %, were obtained from the long-TE spectra of $^{13}C_4$-Glu (2.45-2.55 ppm), ^{12}C-Glu (2.30-2.39 ppm) and Gln (2.40-2.49 ppm), respectively. Gln, a potential contaminant at ≈ 2.45 ppm was found to have minimal overlap with the $^{13}C_4$-Glu resonance, with a reduction in peak width and area at the longer TE. Signal areas obtained from long-TE phantom spectra compared to those acquired with the short-TE of (12 ms, 9 ms) were comparable to those calculated numerically, namely -14 %, 54 %, 62 %, and 51 %, for NAA, $^{13}C_4$-Glu, ^{12}C-Glu, and Gln, respectively. Differences are likely due to T_2 relaxation in the phantoms, which was not accounted for in the numerical simulations.

The efficacy of the optimal timing in removing contaminating signal was tested with an "*in-vivo* phantom" that contained NAA, ^{12}C-Glu, $^{13}C_4$-Glu, Gln, GABA, and Cr in relative concentrations found *in vivo*.[42] Peak areas in the $^{13}C_4$-Glu spectral region were compared to the corresponding areas obtained from the $^{13}C_4$-Glu only phantom. The "*in-vivo* phantom" had a 176 % higher peak area with (TE_1, TE_2) = (12 ms, 9 ms); this was reduced to 36% with (TE_1, TE_2) = (20 ms, 106 ms). Figure 5.3 shows significant contamination of the ≈ 2.51 ppm $^{13}C_4$-Glu resonance from NAA and Gln in the short TE spectrum and a simplified peak in the long TE spectrum with

reduced contamination. The phantom NAA concentration is comparable to that of total Glu (45 mM vs. 50 mM). However, our previous study[52] found *in-vivo* rat brain concentrations of 11.43 mM and 7.64 mM, for Glu and NAA, respectively. A similar average Glu/NAA ratio (12.46 mM/8.45 mM) was obtained in this study from the baseline long-TE spectrum. Therefore, a 33 mM NAA phantom concentration may have been more appropriate for *in-vivo* representation, and a lower residual NAA contamination than that shown in Figure 5.3 is expected in our long-TE *in-vivo* spectra.

The resolved 2.51 ppm satellite peak can be seen in the *in-vivo* spectra displayed in Figures 5.4 and 5.5. LCModel was relied upon to account for residual NAA signal in the 2.45-2.55 ppm region. In addition to reduced contamination from NAA, MM signals, which generally have shorter T_2 values, are reduced at longer TEs.[42] Figure 5.5 compares a short-TE spectrum acquired from one of the rats (the same rat as in Figure 5.4) towards the end of the infusion with the long-TE spectrum obtained following it. The short-TE spectrum shows contamination in the 2.51 ppm $^{13}C_4$ glu region from NAA, while the long-TE spectrum shows a better resolved peak at 2.51 ppm. The improved quantification of the 2.51 ppm satellite peak with the long-TE PRESS sequence is reflected by the LCModel reported CRLBs values which improved for the two rats from 15 % and 21 % with the short-TE to 7 % and 8 %, with the long-TE, respectively. Admittedly, there is a small time difference between the acquisition times of the two spectra to enable an accurate comparison. However, lower CRLB values of 8 % and 9 % were also obtained at the 70 min time point with the long-TE sequence. Both the ≈ 2.51 ppm and ≈ 2.19 ppm peaks can be seen to increase throughout the infusion in Figure 5.4, while the ≈ 2.35 ppm $^{12}C_4$-Glu peak decreases over time. Although the ≈ 2.19 ppm peak also appears resolved, it is potentially contaminated by NAAG (≈ 2.19 ppm), ^{12}C-Glu (≈ 2.12 ppm), $^{13}C_3$-Glu (2.20-2.28 ppm) and $^{13}C_2$-GABA (≈ 2.12 ppm), the

responses of which were not investigated. Therefore, the two $^{13}C_4$-Glu satellite peaks were kept in separate basis spectra, and quantification was based on the ≈ 2.51 ppm resonance.

The sum of total glutamate was constrained to be a constant in our LCModel analysis and Glu C4 FE time courses were measured for the two rats, resulting in final C4-Glu FEs of 0.58 and 0.60 at 110 minutes post-injection. One oversight is that blood plasma FE was not measured for the two rats from which spectra were acquired. However, to confirm that the C4-Glu FE values are reasonable, an identical infusion protocol was employed for a third rat to obtain an estimate of final plasma glucose ^{13}C FE. This was found to be 68.0 %, as measured by mass spectrometry. Our final Glu C4 FE is comparable to that obtained by Duarte et al.,[14] where a final Glu C4 ^{13}C FE of ≈ 0.60 was found ≈ 120 minutes post [1,6-$^{13}C_2$]-Glc infusion, with a plasma glucose FE of 70 %. The anaesthetic employed in that study was α-chloralose. However, our Glu C4 FE is higher than those obtained by de Graaf et al.[13] and van Eijsden et al.,[24] who obtained final FEs of ≈ 0.40 at ≈ 120 minutes post infusion using a similar infusion protocol, with the former using [1,6-$^{13}C_2$]-Glc, and the latter using [U-$^{13}C_6$]-Glc. One reason for the difference in FE could be our somewhat differing infusion protocol where we used 0.75 M/(200 g body weight) (rats weighing about 400-500 g) for the glucose concentration after the bolus, as opposed to 0.75 M,[13,24] which likely resulted in our higher glucose plasma FE, compared to the reported value of ≈ 50 %.[13] Another potential explanation may be the choice of anaesthetic used in those studies, namely, halothane, which can affect brain glucose levels.[53] In particular, isoflurane (used in this study) has been shown to result in higher cerebral glucose levels compared to halothane.[53] Differences in T_2 decay between ^{12}C-Glu and $^{13}C_4$-Glu, if they exist, may also result in some error in Glu C4 FE determination. The determined V_{TCA} values are within the range of values reported for rat brain using ^{13}C MRS techniques, namely, 0.35 – 0.71 μmol/g/min.[3,13,24,54]

5.5 - CONCLUSION

A standard proton PRESS sequence with a (TE_1, TE_2) combination of (20 ms, 106 ms) is suitable for resolving the ≈ 2.51 ppm $^{13}C_4$-Glu proton peak from contaminating NAA signal at 9.4 T. The technique does not require additional ^{13}C hardware nor does it rely on subtracting scans. The efficacy of the technique was demonstrated *in vivo* in rat brain for quantifying $^{13}C_4$-Glu signal during a [U-$^{13}C_6$]-Glc infusion.

5.6 - REFERENCES

1. Wijnen JP, Van der Graaf M, Scheenen TW, et al. In vivo 13C magnetic resonance spectroscopy of a human brain tumor after application of 13C-1-enriched glucose. *Magnetic resonance imaging.* 2010;28(5):690-697.

2. Maher EA, Marin-Valencia I, Bachoo RM, et al. Metabolism of [U-13C] glucose in human brain tumors in vivo. *NMR in biomedicine.* 2012;25(11):1234-1244.

3. Henry PG, Lebon V, Vaufrey F, Brouillet E, Hantraye P, Bloch G. Decreased TCA cycle rate in the rat brain after acute 3-NP treatment measured by in vivo 1H-{13C} NMR spectroscopy. *Journal of neurochemistry.* 2002;82(4):857-866.

4. Bubber P, Haroutunian V, Fisch G, Blass JP, Gibson GE. Mitochondrial abnormalities in Alzheimer brain: mechanistic implications. *Annals of Neurology.* 2005;57(5):695-703.

5. Petroff OA, Errante LD, Rothman DL, Kim JH, Spencer DD. Glutamate–glutamine cycling in the epileptic human hippocampus. *Epilepsia.* 2002;43(7):703-710.

6. Zacharias NM, Chan HR, Sailasuta N, Ross BD, Bhattacharya P. Real-time molecular imaging of tricarboxylic acid cycle metabolism in vivo by hyperpolarized 1-13C diethyl succinate. *Journal of the American Chemical Society.* 2011;134(2):934-943.

7. Henry P-G, Adriany G, Deelchand D, et al. In vivo 13C NMR spectroscopy and metabolic modeling in the brain: a practical perspective. *Magnetic resonance imaging.* 2006;24(4):527-539.

8. de Graaf RA, Rothman DL, Behar KL. State of the art direct 13C and indirect 1H-[13C] NMR spectroscopy in vivo. A practical guide. *NMR in Biomedicine.* 2011;24(8):958-972.

9. Pfeuffer J, Tkáč I, Choi IY, et al. Localized in vivo 1H NMR detection of neurotransmitter labeling in rat brain during infusion of [1-13C] D-glucose. *Magnetic Resonance in Medicine.* 1999;41(6):1077-1083.

10. Frahm J, Merboldt K-D, Hänicke W. Localized proton spectroscopy using stimulated echoes. *Journal of Magnetic Resonance.* 1987;72(3):502-508.

11. Bendall M, Pegg D, Doddrell D, Field J. NMR of protons coupled to carbon-13 nuclei only. *Journal of the American Chemical Society.* 1981;103(4):934-936.
12. De Feyter HM, Herzog RI, Steensma BR, et al. Selective proton-observed, carbon-edited (selPOCE) MRS method for measurement of glutamate and glutamine 13C-labeling in the human frontal cortex. *Magnetic resonance in medicine.* 2018;80(1):11-20.
13. de Graaf RA, Brown PB, Mason GF, Rothman DL, Behar KL. Detection of [1, 6-13C2]-glucose metabolism in rat brain by in vivo 1H-[13C]-NMR spectroscopy. *Magnetic Resonance in Medicine.* 2003;49(1):37-46.
14. Duarte JM, Gruetter R. Glutamatergic and GABA ergic energy metabolism measured in the rat brain by 13C NMR spectroscopy at 14.1 T. *Journal of neurochemistry.* 2013;126(5):579-590.
15. Fitzpatrick SM, Hetherington HP, Behar KL, Shulman RG. The Flux from Glucose to Glutamate in the Rat Brain in vivo as Determined by 1-Observed, 13C-Edited NMR Spectroscopy. *Journal of Cerebral Blood Flow & Metabolism.* 1990;10(2):170-179.
16. Mason GF, Pan JW, Chu W-J, et al. Measurement of the tricarboxylic acid cycle rate in human grey and white matter in vivo by 1H-[13C] magnetic resonance spectroscopy at 4.1 T. *Journal of Cerebral Blood Flow & Metabolism.* 1999;19(11):1179-1188.
17. Mason GF, Rothman DL, Behar KL, Shulman RG. NMR determination of the TCA cycle rate and α-ketoglutarate/glutamate exchange rate in rat brain. *Journal of Cerebral Blood Flow & Metabolism.* 1992;12(3):434-447.
18. Patel AB, de Graaf RA, Mason GF, Rothman DL, Shulman RG, Behar KL. The contribution of GABA to glutamate/glutamine cycling and energy metabolism in the rat cortex in vivo. *Proceedings of the National Academy of Sciences.* 2005;102(15):5588-5593.
19. Patel AB, de Graaf RA, Rothman DL, Behar KL. Effects of γ-Aminobutyric acid transporter 1 inhibition by tiagabine on brain glutamate and γ-Aminobutyric acid metabolism in the anesthetized rat In vivo. *Journal of neuroscience research.* 2015;93(7):1101-1108.
20. Rothman D, Behar K, Hetherington H, et al. 1H-Observe/13C-decouple spectroscopic measurements of lactate and glutamate in the rat brain in vivo. *Proceedings of the National Academy of Sciences.* 1985;82(6):1633-1637.
21. Rothman D, Novotny E, Shulman G, et al. 1H-[13C] NMR measurements of [4-13C] glutamate turnover in human brain. *Proceedings of the National Academy of Sciences.* 1992;89(20):9603-9606.
22. Shen J, Petersen KF, Behar KL, et al. Determination of the rate of the glutamate/glutamine cycle in the human brain by in vivo 13C NMR. *Proceedings of the National Academy of Sciences.* 1999;96(14):8235-8240.
23. Sonnay S, Duarte JM, Just N, Gruetter R. Compartmentalised energy metabolism supporting glutamatergic neurotransmission in response to increased activity in the rat cerebral cortex: A 13C MRS study in vivo at 14.1 T. *Journal of Cerebral Blood Flow & Metabolism.* 2016;36(5):928-940.
24. Van Eijsden P, Behar KL, Mason GF, Braun KP, De Graaf RA. In vivo neurochemical profiling of rat brain by 1H-[13C] NMR spectroscopy: cerebral energetics and glutamatergic/GABAergic neurotransmission. *Journal of neurochemistry.* 2010;112(1):24-33.
25. Xin L, Lanz B, Lei g, Gruetter R. Assessment of metabolic fluxes in the mouse brain in vivo using 1H-[13C] NMR spectroscopy at 14.1 Tesla. *Journal of Cerebral Blood Flow & Metabolism.* 2015;35(5):759-765.
26. Boumezbeur F, Besret L, Valette J, et al. NMR measurement of brain oxidative metabolism in monkeys using 13C-labeled glucose without a 13C radiofrequency channel. *Magnetic Resonance in Medicine.* 2004;52(1):33-40.

27. Boumezbeur F, Besret L, Valette J, et al. Glycolysis versus TCA cycle in the primate brain as measured by combining 18F-FDG PET and 13C-NMR. *Journal of Cerebral Blood Flow & Metabolism.* 2005;25(11):1418-1423.
28. Valette J, Chaumeil M, Guillermier M, Bloch G, Hantraye P, Lebon V. Diffusion-weighted NMR spectroscopy allows probing of 13C labeling of glutamate inside distinct metabolic compartments in the brain. *Magnetic Resonance in Medicine.* 2008;60(2):306-311.
29. Chaumeil MM, Valette J, Guillermier M, et al. Multimodal neuroimaging provides a highly consistent picture of energy metabolism, validating 31P MRS for measuring brain ATP synthesis. *Proceedings of the National Academy of Sciences.* 2009;106(10):3988-3993.
30. Bottomley PA. Selective volume method for performing localized NMR spectroscopy. U.S. patent 4,480,228; 1984.
31. Deelchand DK, Uğurbil K, Henry PG. Investigating brain metabolism at high fields using localized 13C NMR spectroscopy without 1H decoupling. *Magnetic Resonance in Medicine.* 2006;55(2):279-286.
32. Choi IY, Seaquist ER, Gruetter R. Effect of hypoglycemia on brain glycogen metabolism in vivo. *Journal of neuroscience research.* 2003;72(1):25-32.
33. Tkac I, Dubinsky JM, Keene CD, Gruetter R, Low WC. Neurochemical changes in Huntington R6/2 mouse striatum detected by in vivo 1H NMR spectroscopy. *Journal of neurochemistry.* 2007;100(5):1397-1406.
34. Öz G, Nelson CD, Koski DM, et al. Noninvasive detection of presymptomatic and progressive neurodegeneration in a mouse model of spinocerebellar ataxia type 1. *Journal of Neuroscience.* 2010;30(10):3831-3838.
35. Rao R, Tkac I, Townsend EL, Gruetter R, Georgieff MK. Perinatal iron deficiency alters the neurochemical profile of the developing rat hippocampus. *The Journal of nutrition.* 2003;133(10):3215-3221.
36. Raman L, Tkac I, Ennis K, Georgieff MK, Gruetter R, Rao R. In vivo effect of chronic hypoxia on the neurochemical profile of the developing rat hippocampus. *Developmental brain research.* 2005;156(2):202-209.
37. Marjanska M, Curran GL, Wengenack TM, et al. Monitoring disease progression in transgenic mouse models of Alzheimer's disease with proton magnetic resonance spectroscopy. *Proceedings of the National Academy of Sciences.* 2005;102(33):11906-11910.
38. Wang WT, Lee P, Yeh HW, Smirnova IV, Choi IY. Effects of acute and chronic hyperglycemia on the neurochemical profiles in the rat brain with streptozotocin-induced diabetes detected using in vivo 1H MR spectroscopy at 9.4 T. *Journal of neurochemistry.* 2012;121(3):407-417.
39. Doan B-T, Autret G, Mispelter J, et al. Simultaneous two-voxel localized 1H-observed 13C-edited spectroscopy for in vivo MRS on rat brain at 9.4 T: Application to the investigation of excitotoxic lesions. *Journal of Magnetic Resonance.* 2009;198(1):94-104.
40. Henry PG, Tkáč I, Gruetter R. 1H-localized broadband 13C NMR spectroscopy of the rat brain in vivo at 9.4 T. *Magnetic Resonance in Medicine.* 2003;50(4):684-692.
41. Govindaraju V, Young K, Maudsley AA. Proton NMR chemical shifts and coupling constants for brain metabolites. *NMR in Biomedicine.* 2000;13(3):129-153.
42. Pfeuffer J, Tkáč I, Provencher SW, Gruetter R. Toward an in vivo neurochemical profile: quantification of 18 metabolites in short-echo-time 1H NMR spectra of the rat brain. *Journal of magnetic resonance.* 1999;141(1):104-120.
43. Behar KL, Ogino T. Characterization of macromolecule resonances in the 1H NMR spectrum of rat brain. *Magnetic resonance in medicine.* 1993;30(1):38-44.

44. Xu S, Ji Y, Chen X, Yang Y, Gullapalli RP, Masri R. In vivo high-resolution localized 1H MR spectroscopy in the awake rat brain at 7 T. *Magnetic resonance in medicine.* 2013;69(4):937-943.
45. Thompson RB, Allen PS. Sources of variability in the response of coupled spins to the PRESS sequence and their potential impact on metabolite quantification. *Magnetic Resonance in Medicine.* 1999;41(6):1162-1169.
46. Yahya A, Allen PS. Effect of strong homonuclear proton coupling on localized 13C detection using PRESS. *Magnetic resonance in medicine.* 2005;54(6):1340-1350.
47. Haase A, Frahm J, Hanicke W, Matthaei D. 1H NMR chemical shift selective (CHESS) imaging. *Physics in Medicine & Biology.* 1985;30(4):341.
48. Provencher SW. Estimation of metabolite concentrations from localized in vivo proton NMR spectra. *Magnetic resonance in medicine.* 1993;30(6):672-679.
49. Xin L, Gambarota G, Mlynárik V, Gruetter R. Proton T2 relaxation time of J-coupled cerebral metabolites in rat brain at 9.4 T. *NMR in Biomedicine.* 2008;21(4):396-401.
50. Valette J, Boumezbeur F, Hantraye P, Lebon V. Simplified 13C metabolic modeling for simplified measurements of cerebral TCA cycle rate in vivo. *Magnetic Resonance in Medicine.* 2009;62(6):1641-1645.
51. Choi I-Y, Lee S-P, Kim S-G, Gruetter R. In vivo measurements of brain glucose transport using the reversible Michaelis–Menten model and simultaneous measurements of cerebral blood flow changes during hypoglycemia. *Journal of Cerebral Blood Flow & Metabolism.* 2001;21(6):653-663.
52. Dobberthien BJ, Tessier AG, Yahya A. Improved resolution of glutamate, glutamine and γ-aminobutyric acid with optimized point-resolved spectroscopy sequence timings for their simultaneous quantification at 9.4 T. *NMR in Biomedicine.* 2018;31(1):e3851.
53. Kofke WA, Hawkins RA, Davis DW, Biebuyck JF. Comparison of the effects of volatile anesthetics on brain glucose metabolism in rats. *Anesthesiology.* 1987;66(6):810-813.
54. Choi I-Y, Lei H, Gruetter R. Effect of deep pentobarbital anesthesia on neurotransmitter metabolism in vivo: on the correlation of total glucose consumption with glutamatergic action. *Journal of Cerebral Blood Flow & Metabolism.* 2002;22(11):1343-1351.

Chapter 6 - Magnetic Resonance Spectroscopy of Rat Kidney *In Vivo* at 9.4 T

A version of this chapter has been provisionally accepted for publication by the journal *Biomedical Physics and Engineering Express* as:

Dobberthien, B. J., Volotovskyy, V., Tessier, A. G., & Yahya, A. Magnetic Resonance Spectroscopy of Rat Kidney *In Vivo* at 9.4 T.

6.1 - INTRODUCTION

Renal cell carcinoma (RCC) is the most common and fatal urologic malignancy, comprising ≈ 90 % of kidney malignancies.[1] RCC is also among the ten most common human malignancies, making up ≈ 3 % of them.[1,2] It often develops asymptomatically, resulting in 50-60% of patients being diagnosed incidentally, with approximately a third of cases being at an advanced stage at the time of diagnosis when treatment is less effective.[1,2] The current system for clinical staging classifies renal tumours according to size, spread, nodal involvement, and presence of metastases.[2] New techniques for early detection of RCC are essential, yet no dependable biomarkers are currently available.[2] With early detection, it is possible to cure RCC through surgery, as it is resistant to chemotherapy and radiation therapy.[1-3]

Metabolomics, a strategy for the analysis of molecules involved in metabolism, is a promising methodology for discovering biomarkers,[2] which for cancer, can have potential use in diagnosis, assessment and prediction of prognosis, therapeutic effectiveness, and follow-up. While metabolomics research for RCC has been increasing, it is limited compared to other cancers.[1,2] Proton (^{1}H) Nuclear Magnetic Resonance (NMR) is a popular technique for metabolomics and has been used to study kidney tissue extracts[3] and plasma[4] of RCC patients, with some metabolites showing relevance. For example, compared with adjacent tissues, RCC tumour tissue contains more glutamate (Glu), glutamine (Gln), total choline (Cho), betaine (Bet), and taurine (Tau), and less *myo*-inositol (Ins).[3]

Glutamate is necessary for nucleotide synthesis in most dividing cells, and Gln is intrinsically linked to Glu, generating Glu in a reaction catalyzed by glutaminase.[5] Glutamate and Gln levels, the sum of which in MRS is often denoted as Glx, have also been shown to be relevant

in studies of other types of tumours, such as those in liver[6] and brain.[7] Choline is involved in cell membrane synthesis, and its level is altered in cancer development[8] with tumor tissues often containing elevated levels of choline. The increases may be caused by an increased demand for phospholipids during the rapid replication of cancer cells.[9] Betaine, Ins, Tau, and Cho are osmolytes, helping to maintain cell volume and fluid balance in the mammalian renal medulla.[10] Ins has also been showed to have increased levels in brain tumours.[11] Tau is a potential antioxidant, and has been shown to protect against other types of renal injury, such as that caused by oxidative stress.[12]

Preclinical animal models offer ways to investigate disease, gathering information to further fuel research in humans. Serkova et al.[13] performed ^{1}H NMR metabolomics on rat kidney extracts and found that Glu, Gln, Ins, Tau, Cho, and Bet were all prominent metabolites in normal kidney and ischemia reperfusion injury in a rat kidney transplant model. This is supported by other *ex vivo* ^{1}H NMR studies.[14,15] While ^{1}H NMR of plasma and tissue extracts *in vitro* is valuable, *in vivo* studies would enable us to understand disease processes in a living organism. *In vivo* magnetic resonance spectroscopy (MRS) offers a non-invasive way to measure the levels of Glx, Cho, Bet, Ins, and Tau *in vivo*. It is commonly employed in brain studies, but its application in abdominal regions such as in the kidney is complicated by respiratory motion which leads to artifacts. Previous rat kidney MRS studies have been performed on surgically exposed kidneys,[16-18] which allows the kidney to be fixed in placed, alleviating issues due to motion, and, in addition, improving the signal to noise ratio (SNR) by increasing proximity of the radiofrequency (RF) coil to the kidney. Two of the studies were performed at 7 T,[16,17] and one at 2.0 T.[18] Recently, there has been an increase in the use of higher field strengths, such as 9.4 T, for preclinical studies of animal models,[19-25] offering the advantages of higher SNR and spectral resolution. Point-Resolved

Spectroscopy (PRESS)[26] is a widely available pulse sequence that is commonly used in *in vivo* MRS. It potentially offers twice the SNR compared to Stimulated Echo Acquisition Mode,[27] another commonly used MRS pulse sequence.

The resonances of Glu and Gln, are difficult to resolve in standard short TE spectra, even at 9.4 T, depending on their peak linewidths,[28] because they have closely related proton chemical shifts, namely, ≈ 2.12 ppm, ≈ 2.35 ppm, and ≈ 3.74 ppm for Glu, and ≈ 2.11 ppm, ≈ 2.45 ppm, and ≈ 3.75 ppm for Gln.[29] Choline and Bet, which have resonances at ≈ 3.20 ppm and ≈ 3.25 ppm, respectively, can also be difficult to resolve. The objective of the presented study is to obtain *in-vivo* MRS spectra from rat kidney non-invasively by exploiting the higher SNR obtained with the high field strength of 9.4 T, from which levels of Glx (Glu + Gln), Ins, and Tau, relative to Cho + Bet, can be quantified. To our knowledge, this is the first rat *in-vivo* MRS study of kidney that does not rely on invasive procedures.

6.2 - MATERIALS AND METHODS

Experiments were performed with a 21.5 cm bore 9.4 T animal MRI scanner (Magnex Scientific, Oxford, UK), in conjunction with a TMX console (National Research Council of Canada Institute for Biodiagnostics, West, Calgary, AB, Canada) using an in-house, 5 cm diameter single loop surface coil for both transmission and reception. Additional details about the MRI system can be found in section 2.3.1. The right kidney of four Sprague-Dawley rats (aged 7-9 months) were scanned. Rats were fed a standard diet and had access to autoclaved tap water, both *ad libitum*. They were housed in cages under controlled conditions of light (12 h / 12 h cycle of light / dark, with lights on from 8:00 a.m. - 8:00 pm), temperature (19 - 21 °C), and humidity (30

- 40 %). Prior to scanning, rats were anaesthetized with isoflurane and placed on their side with the surface coil positioned over the right kidney region. The animal setup is shown in Figure 6.1. A small animal temperature and respiratory monitoring, heating and gating system (SA Instruments Inc., Stony Brook, NY, USA) was used with the respiratory pillow attached to the thorax. A rectal probe monitored temperature during the experiment, which was maintained at 37 °C with a heating module. The rat was positioned such that the kidney was at the magnet iso-centre.

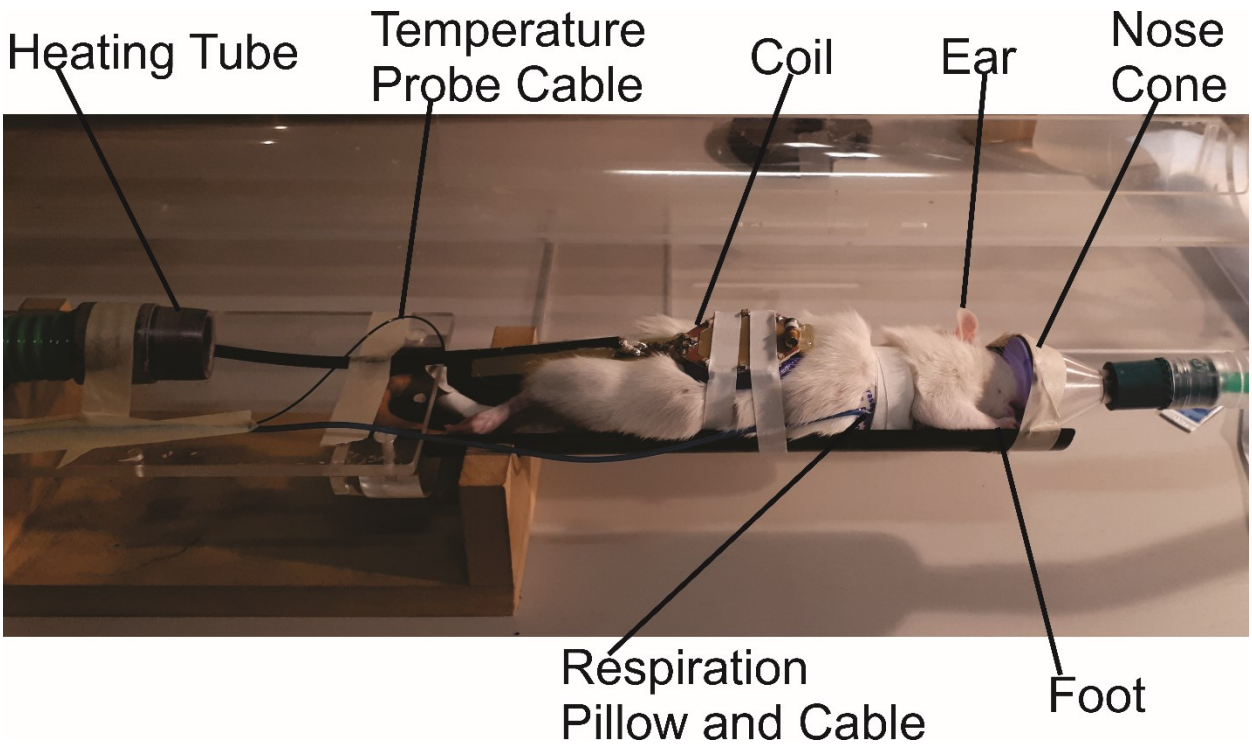

Figure 6.1: Experimental setup showing the rat, placed on its left side, with the surface coil laid over top of its right kidney; the nose cone system, heating hose, respiratory gating cable, and temperature probe cable can all be seen.

Transverse and sagittal spin echo images were acquired with a slice thickness of 2 mm, repetition time of at least 600 ms, and an echo time of 16.3 ms. The images were used to localize a 5 x 5 x 5 mm^3 voxel approximately centred in the right kidney (≈ 1 cm from the coil surface).

A PRESS sequence was utilized for spectral acquisition. The sequence consisted of 2 ms, 5-lobe sinc pulses, with RF bandwidths of 3000 Hz and a frequency offset of 2.8 ppm (approximate centre of spectrum). Spectra were acquired in 256 averages, with a repetition time of at least 3 s and first and second PRESS echo times of (TE_1, TE_2) = (12 ms, 9 ms), the shortest achievable with the choice of pulses. First-order shimming was adjusted manually until the peak amplitude of the water signal was maximized, resulting in a linewidth of ≈ 20-25 Hz. Chemical Shift-Selective Imaging[30] was used for water suppression.

Respiratory gating was applied with the acquisition window (gate position) chosen by adjusting the begin delay and maximum width so that the pulse sequence played out during the flat respiratory response between breaths. The begin delay was set to 20 - 40 % of the respiration period, and the maximum width was set to 10 – 20 % of the respiration period. An auto track feature was also enabled, which is an automatic way to respond to changes in respiration. An example of the respiration waveform along with the acquisition window is shown in Figure 6.2. Rat kidney experiment details are discussed in section 2.3.4.

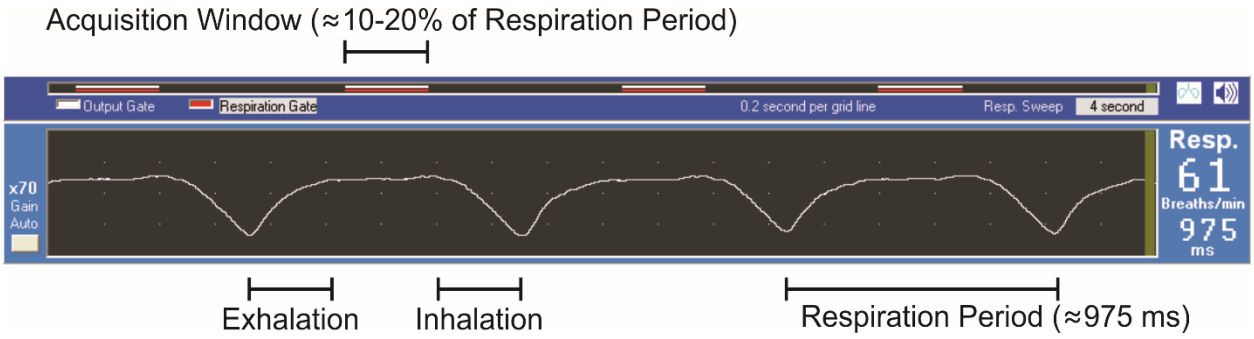

Figure 6.2: Example of the respiration waveform, along with the acquisition window; the width of the acquisition window is set to ≈ 10-20 % of the respiration period, which is ≈ 975 ms.

LCModel software[31] was employed for peak quantification. The basis set, provided by the vendor, was specific to the field strength and the PRESS echo times (TE_1, TE_2). The basis set included Cho (made up of glycerophosphocholine and phosphocholine), creatine (Cr), phosphocreatine (PCr), Glu, Gln, Ins, and Tau. Betaine was not included in the provided basis set but was simulated as a simple system without J-coupling interactions with the LCModel nsimul and chsimu commands. Betaine contains two resonance signals, one at 3.25 ppm that arises from the signals of 9 protons (three CH_3 molecular groups), and one at 3.89 ppm that results from 2 protons (CH_2). LCModel returned a spectral fit and concentration estimates, as well as Cramér-Rao Lower Bound (CRLB) values for each metabolite concentration. The ncombi and chcomb commands were used to yield the concentration and CRLB of Cho + Bet. The sum of glutamate and glutamine, Glx, which is also specified with the same commands, was provided by default. Since we do not have prior knowledge of any of the metabolite concentrations, quantification was performed relative to Cho + Bet, the largest peak. Additional data analysis details are included in section 2.4.

6.3 - RESULTS

Figure 6.3 displays the spin echo images of the right kidney acquired from one of the rats. The cubic voxel from which the PRESS spectra are obtained is overlaid on the images.

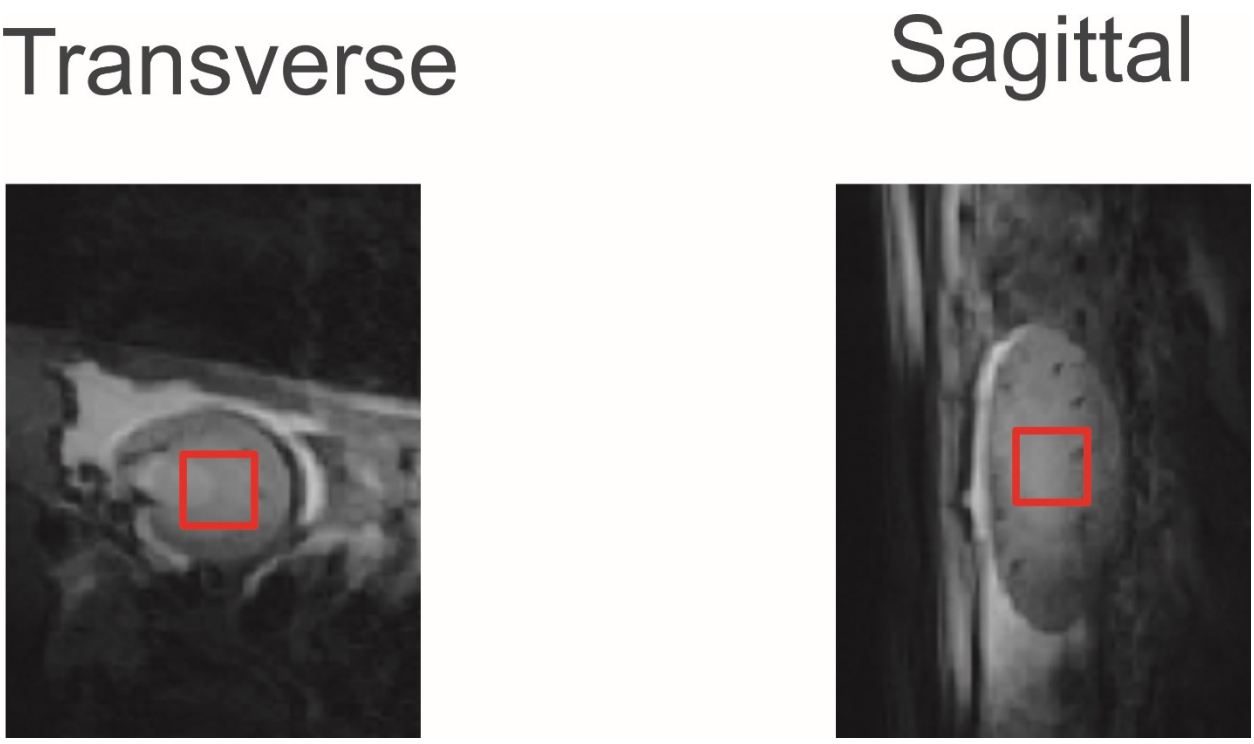

Figure 6.3: Spin echo images of the rat kidney, one transverse and one sagittal, overlaid with the cubic voxel from which the PRESS spectra are acquired.

Figure 6.4 shows *in-vivo* PRESS spectra obtained from voxels like the one shown in Fig. 6.3 from the other three rats. The LCModel fit is overlaid on the raw data. The spectral components consisting of Bet, Cho, Glu, Gln, Ins, and Tau are also displayed for rat 3. Table 6.1 summarizes

the concentration ratios of each metabolite, to Cho + Bet, with corresponding CRLB values. The spectrum acquired from rat 3 is shown in Fig. 6.4.

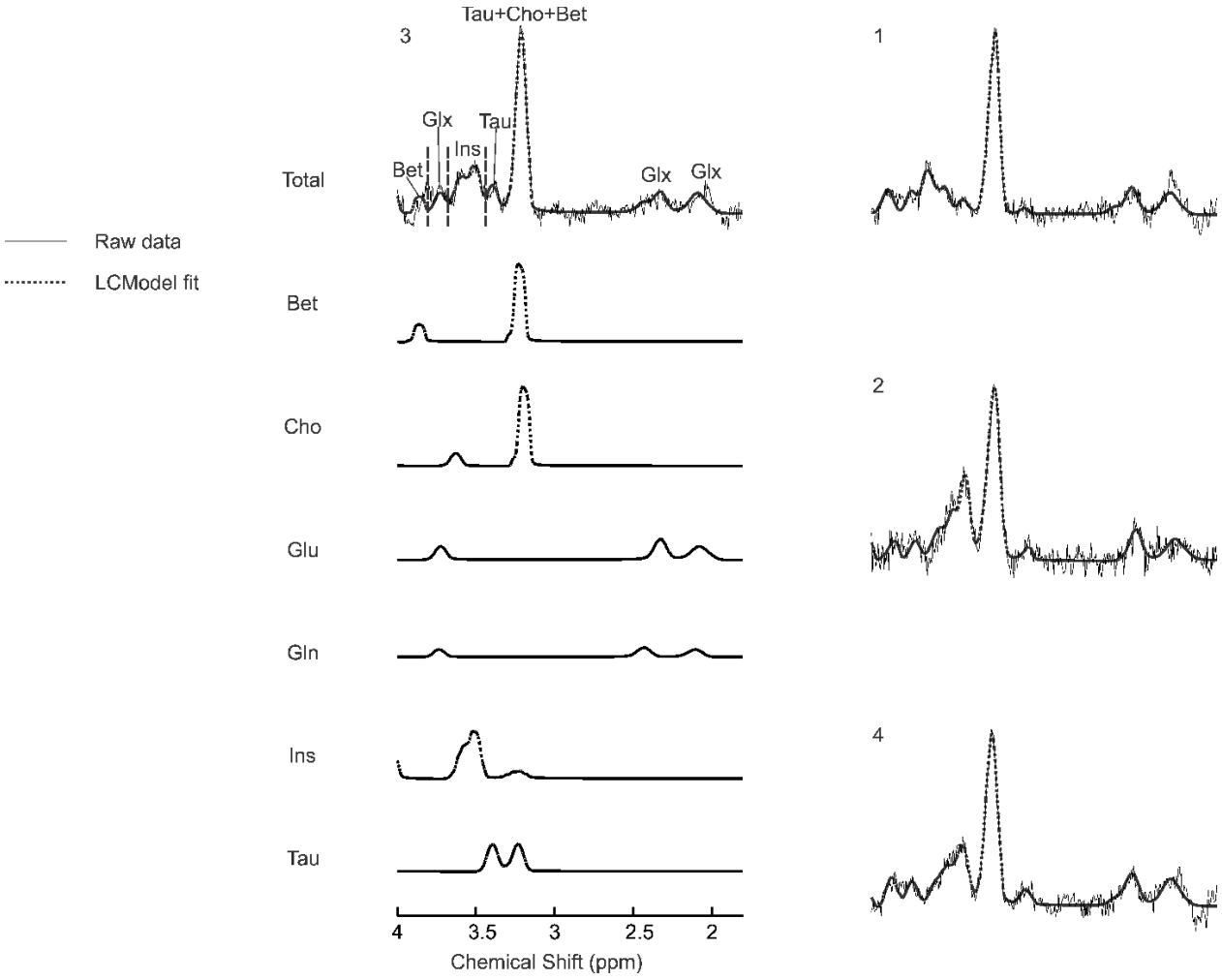

Figure 6.4: *In-vivo* PRESS spectra, acquired at 9.4 T from the kidneys of each rat (rat number indicated above spectrum); the LCModel fit is overlaid on the raw data. A breakdown, showing each component spectrum of Bet, Cho, Glu, Gln, Ins, and Tau is displayed beneath the spectrum of rat 3.

Rat	Age (Months)	Metabolite	Concentration ratio normalized to that of Cho + Bet	CRLB (%)
1	9	Glx	1.54	11
		Ins	0.63	17
		Tau	0.42	32
		Cho + Bet	1	3
2	7	Glx	2.46	18
		Ins	1.90	15
		Tau	4.33	10
		Cho + Bet	1	8
3	7.25	Glx	1.68	11
		Ins	1.39	8
		Tau	0.94	16
		Cho + Bet	1	3
4	7.5	Glx	2.94	10
		Ins	1.66	11
		Tau	2.97	9
		Cho + Bet	1	5
Average	7.69	Glx	2.16 ± 0.66	12.5 ± 3.7
		Ins	1.40 ± 0.55	12.8 ± 4.0
		Tau	2.17 ± 1.81	16.8 ± 10.6
		Cho + Bet	1	4.8 ± 2.4

Table 6.1: Summary of LCModel results of the four rats, along with their age in months. Concentration ratios obtained from LCModel (to Cho + Bet) along with corresponding CRLB values (%) are quoted for Glx, Ins, and Tau. Average values are mean ± st. dev. of the four rats. The spectrum from rat 3 is shown in Fig. 6.4.

6.4 - DISCUSSION

Levels of Glu, Gln, Ins, Tau, Cho, and Bet are relevant to the study of RCC. The ability to quantify their levels *in vivo* in animal studies, such as in rats, is valuable in translating knowledge to humans. Previous rat kidney studies, which involved surgical exposure, detected a metabolite peak from lactate at 2 T during renal ischemia (none is visible in the control kidneys).[18] At 7 T,

peaks from glycerophosphocholine (major component of Cho), Bet, Glu, Gln, and Ins were detected *in vivo*, but not quantified.[16,17] In this work, we exploited the higher SNR obtainable from the higher field strength of 9.4 T to obtain *in-vivo* rat kidney spectra non-invasively. In addition to the metabolites that were detected at 7 T, we also obtained signal from Tau, and quantified concentrations of Glx, Ins, and Tau, relative to Cho + Bet. The readily available PRESS sequence was used in conjunction with respiratory gating to minimize motion artifacts. LCModel was employed to quantify the levels of the six mentioned metabolites, which have previously been found to be prominent in NMR spectra of rat kidney extracts.[13] The ratios of Glx, Ins, and Tau, to Cho + Bet, in that *in-vitro* study, were found to be 0.26, 0.18, and 0.32, respectively. In this work, they were found to be, on average (± standard deviation), 2.16 ± 0.66, 1.40 ± 0.55, and 2.17 ± 1.81, respectively, with average CRLBs of 12.5 ± 3.7 %, 12.8 ± 4.0 %, and 16.8 ± 10.6 %. The average CRLB of Cho + Bet was 4.8 ± 2.4 %. The average CRLB for each metabolite is lower than 20 %, which is considered acceptable.[32] While the concentrations relative to Cho + Bet in this study differs from what was found in the extracts, the relative amounts of Glx, Ins, and Tau to each other are similar. Differences may be explained by the fact that this study was done *in vivo*, where the concentrations of Glx, Ins, and Tau may be higher, or the concentration of Cho + Bet may be lower. In addition to interstudy differences, there was a fair amount of variability in the relative metabolite concentrations between rats within this study. In particular, the concentration of Tau, relative to Cho + Bet, varied from 0.42 - 4.33, despite a low average CRLB of 16.8 ± 10.6 %. The concentration of Ins, relative to Cho + Bet, also varied substantially, from 0.63 – 1.90, again with a low average CRLB of 12.8 ± 4.0 %. The sources of variability should be investigated in future work. Diet may also play a role in affecting kidney metabolite concentrations, as has been shown in human studies.[33,34] The concentration of Bet might also be altered due to variance in temperature

conditions, as its role as an osmolyte protects cells from stress due to extreme temperatures.[33] It is also important to note that the effects of T_2 relaxation were not taken into account, as we do not have prior knowledge of relative T_2 values. However, the relatively short total TE of 21 ms should render T_2 effects minimal.

Trimethylamine *N*-oxide (TMAO) is another metabolite that is present in kidney tissue,[13,15] but it was not considered in this study (nor in previous *in-vivo* work) due to its heavy spectral overlap with Cho + Bet. It is likely that the Cho + Bet resonance signal also contains amounts of TMAO. TMAO is a biomarker of renal disease in humans.[35]

The study reports relative *in-vivo* concentrations of Glx, Ins, Tau, and Cho + Bet in rat kidney. *In-vivo* MRS studies on rat kidney models of RCC or other disorders in which the metabolite concentrations are relevant can be investigated for any metabolic changes. The knowledge obtained can potentially be translated to humans.

6.5 - CONCLUSION

Rat kidney MRS spectra were acquired non-invasively at 9.4 T. LCModel was employed for peak fitting and quantification. Average concentration ratios and standard deviations (over 4 rats) of Glx, Ins, and Tau, relative to Cho + Bet, were found to be 2.16 ± 0.66, 1.40 ± 0.55, and 2.17 ± 1.81, respectively, with CRLB values of 12.5 ± 3.7, 12.8 ± 4.0, and 16.8 ± 10.6, respectively. The CRLB of Cho + Bet was 4.8 ± 2.4.

6.6 - REFERENCES

1. Monteiro MS, Carvalho M, de Lourdes Bastos M, de Pinho PG. Biomarkers in renal cell carcinoma: a metabolomics approach. *Metabolomics.* 2014;10(6):1210-1222.

2. Gil AM, de Pinho PG, Monteiro MS, Duarte IF. NMR metabolomics of renal cancer: an overview. *Bioanalysis.* 2015;7(18):2361-2374.

3. Gao H, Dong B, Jia J, et al. Application of ex vivo 1 H NMR metabonomics to the characterization and possible detection of renal cell carcinoma metastases. *Journal of cancer research and clinical oncology.* 2012;138(5):753-761.

4. Zira AN, Theocharis SE, Mitropoulos D, Migdalis V, Mikros E. 1H NMR metabonomic analysis in renal cell carcinoma: a possible diagnostic tool. *Journal of proteome research.* 2010;9(8):4038-4044.

5. Newsholme P, Procopio J, Lima MMR, Pithon-Curi TC, Curi R. Glutamine and glutamate—their central role in cell metabolism and function. *Cell biochemistry and function.* 2003;21(1):1-9.

6. Yang Y, Li C, Nie X, et al. Metabonomic studies of human hepatocellular carcinoma using high-resolution magic-angle spinning 1H NMR spectroscopy in conjunction with multivariate data analysis. *Journal of proteome research.* 2007;6(7):2605-2614.

7. Horská A, Barker PB. Imaging of brain tumors: MR spectroscopy and metabolic imaging. *Neuroimaging Clinics.* 2010;20(3):293-310.

8. Glunde K, Bhujwalla ZM, Ronen SM. Choline metabolism in malignant transformation. *Nature Reviews Cancer.* 2011;11(12):835.

9. Gao H, Dong B, Liu X, Xuan H, Huang Y, Lin D. Metabonomic profiling of renal cell carcinoma: high-resolution proton nuclear magnetic resonance spectroscopy of human serum with multivariate data analysis. *Analytica chimica acta.* 2008;624(2):269-277.

10. Burg MB, Ferraris JD. Intracellular organic osmolytes: function and regulation. *Journal of Biological Chemistry.* 2008;283(12):7309-7313.

11. Hattingen E, Raab P, Franz K, Zanella FE, Lanfermann H, Pilatus U. Myo-inositol: a marker of reactive astrogliosis in glial tumors? *NMR in Biomedicine.* 2008;21(3):233-241.

12. Wang L, Zhang L, Yu Y, Wang Y, Niu N. The protective effects of taurine against early renal injury in STZ-induced diabetic rats, correlated with inhibition of renal LOX-1-mediated ICAM-1 expression. *Renal failure.* 2008;30(8):763-771.

13. Serkova N, Fuller TF, Klawitter J, Freise CE, Niemann CU. 1H-NMR–based metabolic signatures of mild and severe ischemia/reperfusion injury in rat kidney transplants. *Kidney international.* 2005;67(3):1142-1151.

14. Jun-Sheng T, Lei Z, Xiao-Li S, Huan L, Xue-Mei Q. 1H NMR-based metabolomics approach to investigating the renal protective effects of Genipin in diabetic rats. *Chinese journal of natural medicines.* 2018;16(4):261-270.

15. Garrod S, Humpfer E, Spraul M, et al. High-resolution magic angle spinning 1H NMR spectroscopic studies on intact rat renal cortex and medulla. *Magnetic Resonance in Medicine.* 1999;41(6):1108-1118.

16. Cowin G, Leditschke I, Crozier S, Brereton I, Endre Z. Regional proton nuclear magnetic resonance spectroscopy differentiates cortex and medulla in the isolated perfused rat kidney. *Magnetic Resonance Materials in Physics, Biology and Medicine.* 1997;5(2):151-158.

17. Crozier S, Cowin G, Endre ZH. MR microscopy and microspectroscopy of the intact kidney. *Concepts in Magnetic Resonance Part A.* 2004;22(1):50-59.

18. Terrier F, Lazeyras F, Posse S, et al. Study of acute renal ischemia in the rat using magnetic resonance imaging and spectroscopy. *Magnetic resonance in medicine.* 1989;12(1):114-136.

19. Choi IY, Seaquist ER, Gruetter R. Effect of hypoglycemia on brain glycogen metabolism in vivo. *Journal of neuroscience research.* 2003;72(1):25-32.
20. Tkac I, Dubinsky JM, Keene CD, Gruetter R, Low WC. Neurochemical changes in Huntington R6/2 mouse striatum detected by in vivo 1H NMR spectroscopy. *Journal of neurochemistry.* 2007;100(5):1397-1406.
21. Marjanska M, Curran GL, Wengenack TM, et al. Monitoring disease progression in transgenic mouse models of Alzheimer's disease with proton magnetic resonance spectroscopy. *Proceedings of the National Academy of Sciences.* 2005;102(33):11906-11910.
22. Öz G, Nelson CD, Koski DM, et al. Noninvasive detection of presymptomatic and progressive neurodegeneration in a mouse model of spinocerebellar ataxia type 1. *Journal of Neuroscience.* 2010;30(10):3831-3838.
23. Raman L, Tkac I, Ennis K, Georgieff MK, Gruetter R, Rao R. In vivo effect of chronic hypoxia on the neurochemical profile of the developing rat hippocampus. *Developmental brain research.* 2005;156(2):202-209.
24. Rao R, Tkac I, Townsend EL, Gruetter R, Georgieff MK. Perinatal iron deficiency alters the neurochemical profile of the developing rat hippocampus. *The Journal of nutrition.* 2003;133(10):3215-3221.
25. Wang WT, Lee P, Yeh HW, Smirnova IV, Choi IY. Effects of acute and chronic hyperglycemia on the neurochemical profiles in the rat brain with streptozotocin-induced diabetes detected using in vivo 1H MR spectroscopy at 9.4 T. *Journal of neurochemistry.* 2012;121(3):407-417.
26. Bottomley PA. Selective volume method for performing localized NMR spectroscopy. US Patent 4,480,228; 1984.
27. Frahm J, Merboldt K-D, Hänicke W. Localized proton spectroscopy using stimulated echoes. *Journal of Magnetic Resonance.* 1987;72(3):502-508.
28. Yang S, Hu J, Kou Z, Yang Y. Spectral simplification for resolved glutamate and glutamine measurement using a standard STEAM sequence with optimized timing parameters at 3, 4, 4.7, 7, and 9.4 T. *Magnetic Resonance in Medicine.* 2008;59(2):236-244.
29. Govindaraju V, Young K, Maudsley AA. Proton NMR chemical shifts and coupling constants for brain metabolites. *NMR in Biomedicine.* 2000;13(3):129-153.
30. Haase A, Frahm J, Hanicke W, Matthaei D. 1H NMR chemical shift selective (CHESS) imaging. *Physics in Medicine & Biology.* 1985;30(4):341.
31. Provencher SW. Estimation of metabolite concentrations from localized in vivo proton NMR spectra. *Magnetic resonance in medicine.* 1993;30(6):672-679.
32. Cudalbu C, Mlynárik V, Xin L, Gruetter R. Comparison of T1 relaxation times of the neurochemical profile in rat brain at 9.4 tesla and 14.1 tesla. *Magnetic Resonance in Medicine.* 2009;62(4):862-867.
33. Craig SA. Betaine in human nutrition. *The American journal of clinical nutrition.* 2004;80(3):539-549.
34. Heather LC, Wang X, West JA, Griffin JL. A practical guide to metabolomic profiling as a discovery tool for human heart disease. *Journal of molecular and cellular cardiology.* 2013;55:2-11.
35. Fogelman AM. TMAO is both a biomarker and a renal toxin. *Circulation Research.* 2015;116(3):396-397.

Chapter 7 - Conclusion

7.1 - CONCLUDING REMARKS

The hypothesis of this thesis is that the detection and quantification of oncologically relevant rat brain metabolites with *in-vivo* magnetic resonance spectroscopy at 9.4 T is improved via spectral editing with optimal-TE PRESS. In addition, the high magnetic field strength of 9.4 T can be exploited to enable *in-vivo* magnetic resonance spectroscopy of rat kidney non-invasively. This was investigated in this thesis by addressing a number of specific research goals. The first goal was to use spectral editing to improve the detection of some brain metabolites relevant to cancer at 9.4 T, namely, glycine (Gly), glutamine (Gln), glutamate (Glu), and γ-aminobutyric acid (GABA). Measurements of the metabolites were performed in rat brain after optimizing the echo times (TE_1 and TE_2) of the commonly employed *in-vivo* MRS sequence, Point-RESolved Spectroscopy (PRESS). Another goal was to optimize ^{1}H PRESS for the dynamic measures of $^{13}C_4$-Glu by indirect ^{13}C detection, during [U-$^{13}C_6$]-Glc infusions. Rat kidney magnetic resonance spectroscopy (MRS) was the final goal, which was investigated with short-TE PRESS at 9.4 T to non-invasively obtain *in-vivo* spectra of the kidney and quantify levels of Glx (Glu + Gln), *myo*-inositol (Ins), and taurine (Tau), relative to choline (Cho) + betaine (Bet). The significance of the presented work lies in the improvement of the detection and quantification of some metabolites relevant to the study of cancer. It adds to the collection of literature that seeks to use measures of metabolism to advance the understanding and diagnosis of cancer, among other diseases, in biological sites that include the brain and kidney.

7.2 - BRAIN MRS

In chapter 3, PRESS TE_1 and TE_2 were optimized for the detection of the ≈ 3.55 ppm Gly peak at 9.4 T. J-coupling evolution of the strongly-coupled Ins protons, which overwhelm Gly in its spectral region (3.52 – 3.57 ppm), was characterized with numerical calculations and verified with phantom spectra. A (TE_1, TE_2) combination of (60 ms, 100 ms) minimized the Ins signal in this region, and its efficacy was verified on phantom solutions and on rat brain *in vivo*. LCModel was employed to analyze *in-vivo* spectra. The average Gly concentration from three rat brains was found to be 1.35 mM, with LCModel CRLB (Cramér-Rao Lower Bound) values ranging from 15 to 20 %. Previous work for Gly quantification at 9.4 T used a technique (SPECIAL)[1] not readily available on all scanners and that relies on the addition and subtraction of scans for localization.

The work discussed in chapter 4 showed how PRESS TE_1 and TE_2 can be optimized for the simultaneous detection and quantification of Gln, Glu, and GABA at 9.4 T, which have proton resonances at ≈ 2.45 ppm, ≈ 2.35 ppm, and ≈ 2.28 ppm, respectively. J-coupling evolution of the protons was characterized numerically and verified experimentally. Signal from the strongly coupled protons of *N*-acetylaspartate (NAA), which resonate at ≈ 2.49 ppm, contaminate the Gln peak. In addition, Glu exhibits overlap with both Gln and GABA. A (TE_1, TE_2) combination of (106 ms, 16 ms) minimized NAA signal in the Gln spectral region, while retaining Gln, Glu, and GABA peaks, and its efficacy was verified on phantom solutions and on rat brain *in vivo*. LCModel was again employed to analyse *in-vivo* spectra. The average T_2-corrected Gln, Glu, and GABA concentrations were found to be 3.39 mM, 11.43 mM, and 2.20 mM, respectively. LCModel CRLB values for Gln, Glu, and GABA ranged from 14-17 %, 4-6 %, and 16-19 %, respectively. Previous work for quantifying GABA at 9.4 T used a subtraction technique that removed the Glu and Gln resonances, except for the ≈ 3.75 ppm Glx peak, for which Glu and Gln cannot be resolved.[2]

Phantom solutions of known metabolite concentrations of Glu, Gln, and GABA were also used to evaluate LCModel estimations, showing that they can be inaccurate when combined with short-TE PRESS, where there is peak overlap, even when low CRLBs are reported. Specifically, concentrations were estimated from phantoms of known varying glutamine (Gln) concentrations, with other metabolites present in fixed known physiological concentration ratios, and it was found that errors in estimation were >39 %. The phantom work demonstrates that the commonly used approach of using short-TE techniques and relying on spectral fitting can lead to erroneous concentrations when there is spectral overlap from metabolite and macromolecule peaks.

Chapter 5 presented an optimized ^{1}H PRESS sequence that can be used to measure $^{13}C_4$-Glu during an infusion of [U-$^{13}C_6$]-Glc. It is a single-shot, indirect ^{13}C detection technique that can quantify the ≈ 2.51 ppm $^{13}C_4$-Glu satellite proton peak at 9.4 T without the need for additional ^{13}C hardware. PRESS TE_1 and TE_2 were optimized to minimize signal contamination from NAA. J-coupling evolution of protons were again characterized numerically and verified experimentally. A (TE_1, TE_2) combination of (20 ms, 106 ms) was found to be suitable for minimizing NAA signal in the ≈ 2.51 ppm $^{13}C_4$-Glu proton spectral region, while retaining the $^{13}C_4$-Glu proton satellite peak. The efficacy of the technique was verified on phantom solutions and on two rat brains *in vivo* during an infusion of [U-$^{13}C_6$]-Glc. LCModel was employed for analysis of the *in-vivo* spectra to quantify the ≈ 2.51 ppm proton $^{13}C_4$-Glu signal to obtain Glu C4 fractional enrichment time courses during the infusions. CRLBs of about 8 % were obtained for the ≈ 2.51 ppm $^{13}C_4$-Glu proton satellite peak with the optimal TE combination.

7.3 - KIDNEY MRS

Chapter 6 examined the non-invasive acquisition of PRESS spectra from rat kidney *in vivo* at 9.4 T, and the quantification of Glu, Gln, Ins, Tau, relative to Cho + Bet. Spectra were acquired from the kidneys of four rats. LCModel was utilized for peak fitting and spectral analysis of the *in-vivo* spectra. The concentrations of Glx, Ins, and Tau, relative to Cho + Bet, were found to be, on average, 2.16, 1.40, and 2.17, with average CRLBs of 12.5 %, 12.8 %, and 16.8 %, respectively. The average CRLB of Cho + Bet was 4.8 %. Previous work that measured *in-vivo* MRS spectra from rat kidney relied on invasive techniques such as surgical exposure.[3-5]

7.4 - LIMITATIONS

There are a number of limitations to the work in this thesis. Errors in localization were not addressed. The sources of localization errors, which were not estimated, include voxel shift effects and the use of a surface coil *in vivo*. Effects on quantification are further exacerbated by B_1^+ inhomogeneity, which was also not measured. These effects can be mitigated by the choice of pulses, pulse sequences, and coils. In particular, surface coils, which were used predominantly in this thesis *in vivo*, experience more B_1^+ inhomogeneity than other types of coils. A volume coil would have a more homogenous B_1^+ field. Larger bandwidth pulses reduce voxel shift effects. Adiabatic pulses especially, such as those used in the Localization by Adiabatic SElective Refocusing (LASER) and semi-LASER pulse sequences, are less susceptible to voxel shift effects and B_1^+ inhomogeneity effects.[6] Another limitation is the general challenge of performing absolute quantification with *in-vivo* MRS; all work in this thesis was based on relative quantification of metabolite concentrations.

The kidney MRS work in particular has a number of limitations, since the research is at a preliminary stage. As mentioned in chapter 6, in addition to interstudy differences, there was a fair amount of variability in the relative metabolite concentrations between rats within the study. In addition, trimethylamine *N*-oxide is another kidney metabolite that was not considered in the study.

7.5 - FUTURE DIRECTIONS

The research presented in this thesis can be applied to study tumours in animal models at 9.4 T. Measures of Gly, Glu, Gln and GABA in tumour and in response to treatment can aid in the understanding of cancer. The ^{13}C work in conjunction with incorporating the Glu C4 FE curves into a mathematical model to estimate V_{TCA} in rat brain will enable glucose metabolism to be assessed in tumours compared to healthy tissue. The preliminary kidney MRS work will be furthered by investigating spectral editing in rat kidney to separately quantify Gln and Glu. The techniques can be applied to study renal cancer in animal models. The knowledge gained from the animal model studies can aid in our understanding of human disease. Beyond cancer, other disease states that can be investigated with these methods include hyperglycinemia, schizophrenia, depression, epilepsy, multiple sclerosis, amyotrophic lateral sclerosis, Huntington's disease, Alzheimer's disease, Parkinson's disease, and brain trauma. In addition, future studies can investigate specific regions in the brain or kidney such as the hippocampus or medulla, respectively. The voxels in this work were chosen to be in the centre of the brain or kidney, but smaller voxels could be used with alternate locations. For studies on disease models, a power analysis should be done to determine a required sample size. The analysis includes measurement variability in the sample size determination. The CRLBs were shown to decrease with the methods

investigated in this thesis, thus a reduction in the required sample size can be expected. The presented methods can also be applied to other field strengths; however, the timings would have to be re-optimized, as J-coupling effects are affected by field strength, particularly for the strongly-coupled spin systems considered in this thesis. Future work can also explore the use of other pulse sequences such as LASER and semi-LASER; however, care would need to be taken to ensure that tissue specific absorption rate is within an acceptable level, as it is higher with LASER-based techniques. In addition, J-coupling effects have been shown to be mitigated with LASER, a consideration that would have to be accounted for in the optimization.[6]

7.6 - REFERENCES

1. Gambarota G, Xin L, Perazzolo C, Kohler I, Mlynárik V, Gruetter R. In vivo 1H NMR measurement of glycine in rat brain at 9.4 T at short echo time. *Magnetic Resonance in Medicine.* 2008;60:727-731.

2. Van Eijsden P, Behar KL, Mason GF, Braun KP, De Graaf RA. In vivo neurochemical profiling of rat brain by 1H-[13C] NMR spectroscopy: cerebral energetics and glutamatergic/GABAergic neurotransmission. *Journal of Neurochemistry.* 2010;112(1):24-33.

3. Cowin G, Leditschke I, Crozier S, Brereton I, Endre Z. Regional proton nuclear magnetic resonance spectroscopy differentiates cortex and medulla in the isolated perfused rat kidney. *Magnetic Resonance Materials in Physics, Biology and Medicine.* 1997;5(2):151-158.

4. Crozier S, Cowin G, Endre ZH. MR microscopy and microspectroscopy of the intact kidney. *Concepts in Magnetic Resonance Part A.* 2004;22(1):50-59.

5. Terrier F, Lazeyras F, Posse S, et al. Study of acute renal ischemia in the rat using magnetic resonance imaging and spectroscopy. *Magnetic Resonance in Medicine.* 1989;12(1):114-136.

6. Wilson M, Andronesi O, Barker PB, et al. Methodological consensus on clinical proton MRS of the brain: Review and recommendations. *Magnetic resonance in medicine.* 2019.

Bibliography

- Ramadan S, Lin A, Stanwell P. Glutamate and glutamine: a review of in vivo MRS in the human brain. *NMR in Biomedicine.* 2013;26(12):1630-1646.
- Bottomley PA. Selective volume method for performing localized NMR spectroscopy. U.S. patent 4,480,228; 1984.
- Frahm J, Merboldt K-D, Hänicke W. Localized proton spectroscopy using stimulated echoes. *Journal of Magnetic Resonance.* 1987;72:502-508.
- Snyder J, Wilman A. Field strength dependence of PRESS timings for simultaneous detection of glutamate and glutamine from 1.5 to 7T. *Journal of Magnetic Resonance.* 2010;203(1):66-72.
- Ganji SK, An Z, Tiwari V, et al. In vivo detection of 2-hydroxyglutarate in brain tumors by optimized point-resolved spectroscopy (PRESS) at 7T. *Magnetic Resonance in Medicine.* 2017;77(3):936-944.
- Ganji SK, An Z, Banerjee A, Madan A, Hulsey KM, Choi C. Measurement of regional variation of GABA in the human brain by optimized point-resolved spectroscopy at 7 T in vivo. *NMR in Biomedicine.* 2014;27(10):1167-1175.
- Choi C, Ganji SK, DeBerardinis RJ, et al. 2-hydroxyglutarate detection by magnetic resonance spectroscopy in IDH-mutated patients with gliomas. *Nature Medicine.* 2012;18(4):624.
- Choi C, Ganji SK, DeBerardinis RJ, et al. Measurement of glycine in the human brain in vivo by 1H-MRS at 3 T: application in brain tumors. *Magnetic Resonance in Medicine.* 2011;66(3):609-618.
- Choi C, Douglas D, Hawesa H, Jindal A, Storey C, Dimitrov I. Measurement of glycine in human prefrontal brain by point-resolved spectroscopy at 7.0 tesla in vivo. *Magnetic Resonance in Medicine.* 2009;62:1305-1310.
- Choi C, Dimitrov IE, Douglas D, et al. Improvement of resolution for brain coupled metabolites by optimized 1H MRS at 7 T. *NMR in Biomedicine.* 2010;23(9):1044-1052.
- Thompson RB, Allen PS. Sources of variability in the response of coupled spins to the PRESS sequence and their potential impact on metabolite quantification. *Magnetic Resonance in Medicine.* 1999;41(6):1162-1169.
- Bogner W, Hangel G, Esmaeili M, Andronesi OC. 1D-spectral editing and 2D multispectral in vivo 1H-MRS and 1H-MRSI-Methods and applications. *Analytical biochemistry.* 2017;529:48-64.
- Govindaraju V, Young K, Maudsley AA. Proton NMR chemical shifts and coupling constants for brain metabolites. *NMR in Biomedicine.* 2000;13(3):129-153.
- Waagepetersen HS, Sonnewald U, Schousboe A. Compartmentation of glutamine, glutamate, and GABA metabolism in neurons and astrocytes: functional implications. *The Neuroscientist.* 2003;9(5):398-403.
- Meldrum BS. Glutamate as a neurotransmitter in the brain: review of physiology and pathology. *The Journal of Nutrition.* 2000;130(4):1007S-1015S.
- Horská A, Barker PB. Imaging of brain tumors: MR spectroscopy and metabolic imaging. *Neuroimaging Clinics of North America.* 2010;20(3):293-310.
- de Graaf RA, Rothman DL, Behar KL. State of the art direct 13C and indirect 1H-[13C] NMR spectroscopy in vivo. A practical guide. *NMR in Biomedicine.* 2011;24(8):958-972.
- Wijnen JP, Van der Graaf M, Scheenen TW, et al. In vivo 13C magnetic resonance spectroscopy of a human brain tumor after application of 13C-1-enriched glucose. *Magnetic Resonance Imaging.* 2010;28(5):690-697.
- Maher EA, Marin-Valencia I, Bachoo RM, et al. Metabolism of [U-13C] glucose in human brain tumors in vivo. *NMR in Biomedicine.* 2012;25(11):1234-1244.

- Boumezbeur F, Besret L, Valette J, et al. NMR measurement of brain oxidative metabolism in monkeys using 13C-labeled glucose without a 13C radiofrequency channel. *Magnetic Resonance in Medicine.* 2004;52(1):33-40.
- Pfeuffer J, Tkáč I, Choi IY, et al. Localized in vivo 1H NMR detection of neurotransmitter labeling in rat brain during infusion of [1-13C] D-glucose. *Magnetic Resonance in Medicine.* 1999;41(6):1077-1083.
- Bendall M, Pegg D, Doddrell D, Field J. NMR of protons coupled to carbon-13 nuclei only. *Journal of the American Chemical Society.* 1981;103(4):934-936.
- Ocali O, Atalar E. Ultimate intrinsic signal-to-noise ratio in MRI. *Magnetic Resonance in Medicine.* 1998;39(3):462-473.
- Yang S, Hu J, Kou Z, Yang Y. Spectral simplification for resolved glutamate and glutamine measurement using a standard STEAM sequence with optimized timing parameters at 3, 4, 4.7, 7, and 9.4 T. *Magnetic Resonance in Medicine.* 2008;59(2):236-244.
- Wang WT, Lee P, Yeh HW, Smirnova IV, Choi IY. Effects of acute and chronic hyperglycemia on the neurochemical profiles in the rat brain with streptozotocin-induced diabetes detected using in vivo 1H MR spectroscopy at 9.4 T. *Journal of Neurochemistry.* 2012;121(3):407-417.
- Tkac I, Dubinsky JM, Keene CD, Gruetter R, Low WC. Neurochemical changes in Huntington R6/2 mouse striatum detected by in vivo 1H NMR spectroscopy. *Journal of Neurochemistry.* 2007;100(5):1397-1406.
- Rao R, Tkac I, Townsend EL, Gruetter R, Georgieff MK. Perinatal iron deficiency alters the neurochemical profile of the developing rat hippocampus. *The Journal of Nutrition.* 2003;133(10):3215-3221.
- Raman L, Tkac I, Ennis K, Georgieff MK, Gruetter R, Rao R. In vivo effect of chronic hypoxia on the neurochemical profile of the developing rat hippocampus. *Developmental Brain Research.* 2005;156(2):202-209.
- Öz G, Nelson CD, Koski DM, et al. Noninvasive detection of presymptomatic and progressive neurodegeneration in a mouse model of spinocerebellar ataxia type 1. *Journal of Neuroscience.* 2010;30(10):3831-3838.
- Marjanska M, Curran GL, Wengenack TM, et al. Monitoring disease progression in transgenic mouse models of Alzheimer's disease with proton magnetic resonance spectroscopy. *Proceedings of the National Academy of Sciences of the United States of America.* 2005;102(33):11906-11910.
- Choi IY, Seaquist ER, Gruetter R. Effect of hypoglycemia on brain glycogen metabolism in vivo. *Journal of Neuroscience Research.* 2003;72(1):25-32.
- Xin L, Gambarota G, Duarte J, Mlynárik V, Gruetter R. Direct in vivo measurement of glycine and the neurochemical profile in the rat medulla oblongata. *NMR in Biomedicine.* 2010;23(9):1097-1102.
- Van Eijsden P, Behar KL, Mason GF, Braun KP, De Graaf RA. In vivo neurochemical profiling of rat brain by 1H-[13C] NMR spectroscopy: cerebral energetics and glutamatergic/GABAergic neurotransmission. *Journal of Neurochemistry.* 2010;112(1):24-33.
- Tkáč I, Rao R, Georgieff MK, Gruetter R. Developmental and regional changes in the neurochemical profile of the rat brain determined by in vivo 1H NMR spectroscopy. *Magnetic Resonance in Medicine.* 2003;50(1):24-32.
- Pfeuffer J, Tkáč I, Provencher SW, Gruetter R. Toward an in vivo neurochemical profile: quantification of 18 metabolites in short-echo-time 1 H NMR spectra of the rat brain. *Journal of Magnetic Resonance.* 1999;141(1):104-120.
- Gambarota G, Xin L, Perazzolo C, Kohler I, Mlynárik V, Gruetter R. In vivo 1H NMR measurement of glycine in rat brain at 9.4 T at short echo time. *Magnetic Resonance in Medicine.* 2008;60:727-731.

- Sanaei Nezhad F, Anton A, Parkes LM, Deakin B, Williams SR. Quantification of glutathione in the human brain by MR spectroscopy at 3 Tesla: Comparison of PRESS and MEGA-PRESS. *Magnetic Resonance in Medicine.* 2017;78(4):1257-1266.
- Gil AM, de Pinho PG, Monteiro MS, Duarte IF. NMR metabolomics of renal cancer: an overview. *Bioanalysis.* 2015;7(18):2361-2374.
- Gao H, Dong B, Jia J, et al. Application of ex vivo 1 H NMR metabonomics to the characterization and possible detection of renal cell carcinoma metastases. *Journal of Cancer Research and Clinical Oncology.* 2012;138(5):753-761.
- Terrier F, Lazeyras F, Posse S, et al. Study of acute renal ischemia in the rat using magnetic resonance imaging and spectroscopy. *Magnetic Resonance in Medicine.* 1989;12(1):114-136.
- Crozier S, Cowin G, Endre ZH. MR microscopy and microspectroscopy of the intact kidney. *Concepts in Magnetic Resonance Part A.* 2004;22(1):50-59.
- Cowin G, Leditschke I, Crozier S, Brereton I, Endre Z. Regional proton nuclear magnetic resonance spectroscopy differentiates cortex and medulla in the isolated perfused rat kidney. *Magnetic Resonance Materials in Physics, Biology and Medicine.* 1997;5(2):151-158.
- Xu S, Ji Y, Chen X, Yang Y, Gullapalli RP, Masri R. In vivo high-resolution localized 1H MR spectroscopy in the awake rat brain at 7 T. *Magnetic Resonance in Medicine.* 2013;69(4):937-943.
- Hofmann L, Slotboom J, Boesch C, Kreis R. Characterization of the macromolecule baseline in localized 1H-MR spectra of human brain. *Magnetic Resonance in Medicine.* 2001;46(5):855-863.
- Gottschalk M, Troprès I, Lamalle L, Grand S, Le Bas JF, Segebarth C. Refined modelling of the short-T2 signal component and ensuing detection of glutamate and glutamine in short-TE, localised, 1H MR spectra of human glioma measured at 3 T. *NMR in Biomedicine.* 2016.
- Moonen CT, Kienlin MV, Van Zijl PC, et al. Comparison of single-shot localization methods (STEAM and PRESS) for in vivo proton NMR spectroscopy. *NMR in Biomedicine.* 1989;2(5-6):201-208.
- Träber F, Block W, Lamerichs R, Gieseke J, Schild HH. 1H metabolite relaxation times at 3.0 tesla: Measurements of T1 and T2 values in normal brain and determination of regional differences in transverse relaxation. *Journal of Magnetic Resonance Imaging.* 2004;19(5):537-545.
- Helms G. Analysis of 1.5 Tesla proton MR spectra of human brain using LCModel and an imported basis set. *Magnetic Resonance Imaging.* 1999;17(8):1211-1218.
- De Graaf RA. *In vivo NMR spectroscopy: principles and techniques.* Wiley; 2019.
- De Graaf RA, Rothman DL. In vivo detection and quantification of scalar coupled 1H NMR resonances. *Concepts in Magnetic Resonance.* 2001;13(1):32-76.
- Kay LE, McClung R. A product operator description of AB and ABX spin systems. *Journal of Magnetic Resonance.* 1988;77(2):258-273.
- Yablonskiy DA, Neil JJ, Raichle ME, Ackerman JJ. Homonuclear J coupling effects in volume localized NMR spectroscopy: pitfalls and solutions. *Magnetic Resonance in Medicine.* 1998;39(2):169-178.
- Hoult D, Lauterbur PC. The sensitivity of the zeugmatographic experiment involving human samples. *Journal of Magnetic Resonance.* 1979;34(2):425-433.
- Kurhanewicz J, Bok R, Nelson SJ, Vigneron DB. Current and potential applications of clinical 13C MR spectroscopy. *Journal of Nuclear Medicine.* 2008;49(3):341-344.
- Doddrell D, Pegg D, Bendall MR. Distortionless enhancement of NMR signals by polarization transfer. *Journal of Magnetic Resonance.* 1982;48(2):323-327.
- Bowery N, Smart T. GABA and glycine as neurotransmitters: a brief history. *British journal of pharmacology.* 2006;147(S1):S109-S119.
- Bean BP. The action potential in mammalian central neurons. *Nature Reviews Neuroscience.* 2007;8(6):451.

- Razak MA, Begum PS, Viswanath B, Rajagopal S. Multifarious beneficial effect of nonessential amino acid, Glycine: a review. *Oxidative medicine and cellular longevity.* 2017;2017.
- Parthasarathy LK, Ratnam L, Seelan S, Tobias C, Casanova MF, Parthasarathy RN. Mammalian inositol 3-phosphate synthase: its role in the biosynthesis of brain inositol and its clinical use as a psychoactive agent. *Biology of Inositols and Phosphoinositides*: Springer; 2006:293-314.
- Budavari S, O'Neil M, Smith A, Heckelman P. *The Merck Index: An Encyclopedia of Chemicals, Drugs, and Biologicals.* 11th ed: RSC Publishing; 1989.
- Young VR, Ajami AM. Glutamate: an amino acid of particular distinction. *The Journal of nutrition.* 2000;130(4):892S-900S.
- Henry P-G, Adriany G, Deelchand D, et al. In vivo 13C NMR spectroscopy and metabolic modeling in the brain: a practical perspective. *Magnetic resonance imaging.* 2006;24(4):527-539.
- Deelchand DK, Uğurbil K, Henry PG. Investigating brain metabolism at high fields using localized 13C NMR spectroscopy without 1H decoupling. *Magnetic Resonance in Medicine.* 2006;55(2):279-286.
- Henry PG, Lebon V, Vaufrey F, Brouillet E, Hantraye P, Bloch G. Decreased TCA cycle rate in the rat brain after acute 3-NP treatment measured by in vivo 1H-{13C} NMR spectroscopy. *Journal of neurochemistry.* 2002;82(4):857-866.
- DeBerardinis RJ, Mancuso A, Daikhin E, et al. Beyond aerobic glycolysis: transformed cells can engage in glutamine metabolism that exceeds the requirement for protein and nucleotide synthesis. *Proceedings of the National Academy of Sciences.* 2007;104(49):19345-19350.
- Patel AB, de Graaf RA, Mason GF, Rothman DL, Shulman RG, Behar KL. The contribution of GABA to glutamate/glutamine cycling and energy metabolism in the rat cortex in vivo. *Proceedings of the National Academy of Sciences.* 2005;102(15):5588-5593.
- Kaiser L, Young K, Meyerhoff D, Mueller S, Matson G. A detailed analysis of localized J-difference GABA editing: theoretical and experimental study at 4 T. *NMR in Biomedicine.* 2008;21(1):22-32.
- Rigotti D, Inglese M, Babb J, et al. Serial whole-brain N-acetylaspartate concentration in healthy young adults. *American Journal of Neuroradiology.* 2007;28(9):1650-1651.
- Baslow MH. N-acetylaspartate in the vertebrate brain: metabolism and function. *Neurochemical research.* 2003;28(6):941-953.
- Ripps H, Shen W. Taurine: a “very essential” amino acid. *Molecular vision.* 2012;18:2673.
- Cholewa JM, Wyszczelska-Rokiel M, Glowacki R, et al. Effects of betaine on body composition, performance, and homocysteine thiolactone. *Journal of the International Society of Sports Nutrition.* 2013;10(1):39.
- Kimura S, Hayatsu H, Arimoto-Kobayashi S. Glycine betaine in beer as an antimutagenic substance against 2-chloro-4-methylthiobutanoic acid, the sanma-fish mutagen. *Mutation Research/Genetic Toxicology and Environmental Mutagenesis.* 1999;439(2):267-276.
- Blüml S, Seymour KJ, Ross BD. Developmental changes in choline-and ethanolamine-containing compounds measured with proton-decoupled 31P MRS in in vivo human brain. *Magnetic Resonance in Medicine.* 1999;42(4):643-654.
- Sanders LM, Zeisel SH. Choline: dietary requirements and role in brain development. *Nutrition today.* 2007;42(4):181.
- Thompson RB, Allen PS. A new multiple quantum filter design procedure for use on strongly coupled spin systems found in vivo: its application to glutamate. *Magnetic resonance in medicine.* 1998;39(5):762-771.
- Yahya A, Allen PS. Effect of strong homonuclear proton coupling on localized 13C detection using PRESS. *Magnetic resonance in medicine.* 2005;54(6):1340-1350.
- Cavanagh J, Fairbrother WJ, Palmer III AG, Skelton NJ. *Protein NMR spectroscopy: principles and practice.* Elsevier; 1995.

- Haase A, Frahm J, Hanicke W, Matthaei D. 1H NMR chemical shift selective (CHESS) imaging. *Physics in Medicine & Biology.* 1985;30(4):341.
- Provencher SW. Estimation of metabolite concentrations from localized in vivo proton NMR spectra. *Magnetic resonance in medicine.* 1993;30(6):672-679.
- Golub GH, Pereyra V. The differentiation of pseudo-inverses and nonlinear least squares problems whose variables separate. *SIAM Journal on numerical analysis.* 1973;10(2):413-432.
- Huisman TAGM, Thiel T, Steinmann B, Zeilinger G, Martin E. Proton magnetic resonance spectroscopy of the brain of a neonate with nonketotic hyperglycinemia: in vivo-in vitro (ex vivo) correlation. *Eur Radiol.* 2002;12:858-861.
- Heresco-Levy U, Ermilov M, Lichtenberg P, Bar G, Javitt DC. High-dose glycine added to olanzapine and risperidone for the treatment of schizophrenia. *Biological Psychiatry.* 2004;55:165-171.
- Eulenburg V, Armsen W, Betz H, Gomeza J. Glycine transporters: essential regulators of neurotransmission. *Trends in Biochemical Sciences.* 2005;30:325-333.
- Javitt DC. Glycine transport inhibitors and the treatment of schizophrenia. *Biological Psychiatry.* 2008;63:6-8.
- Bobek-Billewicz B, Hebda A, Stasik-Pres G, Majchrzak K, Żmuda E, Trojanowska A. Measurement of glycine in a brain and brain tumors by means of 1H MRS. *Folia Neuropathol.* 2010;48:190-199.
- Davies NP, Wilson M, Natarajan K, et al. Non-invasive detection of glycine as a biomarker of malignancy in childhood brain tumours using *in-vivo* 1H MRS at 1.5 Tesla confirmed by *ex-vivo* high-resolution magic-angle spinning NMR. *NMR in Biomedicine.* 2010;23:80-87.
- Hattingen E, Lanfermann H, Quick J, Franz K, Zanella FE, Pilatus U. 1H MR spectroscopic imaging with short and long echo time to discriminate glycine in glial tumours. *Magn Reson Mater Phy.* 2009;22:33-41.
- Kinoshita Y, Kajiwara H, Yokota A, Koga Y. Proton magnetic resonance spectrsocopy of brain tumors: an in vitro study. *Neurosurgery.* 1994;35:606-614.
- Lehnhardt F-G, Bock C, Röhn G, Ernestus R-I, Hoehn M. Metabolic differences between primary and recurrent human brain tumors: a 1H NMR spectroscopic investigation. *NMR in Biomedicine.* 2005;18:371-382.
- Righi V, Andronesi OC, Mintzopoulos D, Black PM, Tzika AA. High-resolution magic angle spinning magnetic resonance spectroscopy detects glycine as a biomarker in brain tumors. *Int J Oncol.* 2010;36:301-306.
- Choi C, Bhardwaj PP, Seres P, Kalra S, Tibbo PG, Coupland NJ. Measurement of glycine in human brain by triple refocusing 1H-MRS in vivo at 3.0 T. *Magnetic Resonance in Medicine.* 2008;59:59-64.
- Kaufman MJ, Prescot AP, Ongur D, et al. Oral glycine administration increases brain glycine/creatine ratios in men: A proton magnetic resonance spectroscopy study. *Psychiatry Research: Neuroimaging.* 2009;173:143-149.
- Prescot AP, Frederick Bd, Wang L, et al. In vivo detection of brain glycine with echo-time-averaged 1H magnetic resonance spectroscopy at 4.0 T. *Magnetic Resonance in Medicine.* 2006;55:681-686.
- Banerjee A, Ganji S, Hulsey K, et al. Measurement of glycine in gray and white matter in the human brain in vivo by 1H MRS at 7.0 T. *Magnetic Resonance in Medicine.* 2012;68:325-331.
- Mlynárik V, Gambarota G, Frenkel H, Gruetter R. Localized short-echo-time proton MR spectroscopy with full signal-intensity acquisition. *Magnetic Resonance in Medicine.* 2006;56:965-970.
- Gambarota G, Mekle R, Xin L, et al. In vivo measurement of glycine with short echo-time 1H MRS in human brain at 7 T. *Magn Reson Mater Phy.* 2009;22:1-4.
- Wilman AH, Allen PS. The response of the strongly coupled AB system of citrate to typical ^{1}H MRS localization sequences. *Journal of Magnetic Resonance, Series B.* 1995;107:25-33.

- Marjanska M, Henry P-G, Uğurbil K, Gruetter R. Editing through multiple bonds: Threonine detection. *Magnetic Resonance in Medicine.* 2008;59:245-251.
- Cudalbu C, Mlynárik V, Xin L, Gruetter R. Comparison of T1 Relaxation Times of the Neurochemical Profile in Rat Brain at 9.4 Tesla and 14.1 Tesla. *Magnetic Resonance in Medicine.* 2009;62:862-867.
- Cutler RWP, Dudzinski DS. Regional changes in amino acid content in developing rat brain. *J Neurochem.* 1974;23:1005-1009.
- Mandel P, Mark J. The influence of nitrogen deprivation on free amino acids in rat brain. *J Neurochem.* 1965;12:987-992.
- de Graaf RA, Brown PB, McIntyre S, Nixon TW, Behar KL, Rothman DL. High magnetic field water and metabolite proton T1 and T2 relaxation in rat brain in vivo. *Magnetic Resonance in Medicine.* 2006;56:386-394.
- Lutkenhoff E, Van Erp T, Thomas M, et al. Proton MRS in twin pairs discordant for schizophrenia. *Molecular psychiatry.* 2010;15(3):308-318.
- Yüksel C, Öngür D. Magnetic resonance spectroscopy studies of glutamate-related abnormalities in mood disorders. *Biological psychiatry.* 2010;68(9):785-794.
- Cavus I, Kasoff WS, Cassaday MP, et al. Extracellular metabolites in the cortex and hippocampus of epileptic patients. *Annals of neurology.* 2005;57(2):226-235.
- Cianfoni A, Niku S, Imbesi S. Metabolite findings in tumefactive demyelinating lesions utilizing short echo time proton magnetic resonance spectroscopy. *American journal of neuroradiology.* 2007;28(2):272-277.
- Pioro E, Majors A, Mitsumoto H, Nelson D, Ng T. 1H-MRS evidence of neurodegeneration and excess glutamate glutamine in ALS medulla. *Neurology.* 1999;53(1):71-71.
- Taylor-Robinson S, Weeks R, Bryant D, et al. Proton magnetic resonance spectroscopy in Huntington's disease: Evidence in favour of the glutamate excitotoxic theory? *Movement disorders.* 1996;11(2):167-173.
- Lin AP, Shic F, Enriquez C, Ross BD. Reduced glutamate neurotransmission in patients with Alzheimer's disease–an in vivo 13C magnetic resonance spectroscopy study. *Magnetic Resonance Materials in Physics, Biology and Medicine.* 2003;16(1):29-42.
- Shutter L, Tong KA, Holshouser BA. Proton MRS in acute traumatic brain injury: role for glutamate/glutamine and choline for outcome prediction. *Journal of neurotrauma.* 2004;21(12):1693-1705.
- Puts NA, Edden RA. In vivo magnetic resonance spectroscopy of GABA: a methodological review. *Progress in nuclear magnetic resonance spectroscopy.* 2012;60:29-41.
- Lewis DA, Volk DW, Hashimoto T. Selective alterations in prefrontal cortical GABA neurotransmission in schizophrenia: a novel target for the treatment of working memory dysfunction. *Psychopharmacology.* 2004;174(1):143-150.
- Sanacora G, Mason GF, Rothman DL, et al. Reduced cortical γ-aminobutyric acid levels in depressed patients determined by proton magnetic resonance spectroscopy. *Archives of general psychiatry.* 1999;56(11):1043-1047.
- Petroff OA, Rothman DL, Behar KL, Lamoureux D, Mattson RH. The effect of gabapentin on brain gamma-aminobutyric acid in patients with epilepsy. *Annals of neurology.* 1996;39(1):95-99.
- Zhang X, Du Z, Liu J, He J. Γ-aminobutyric acid receptors affect the progression and migration of tumor cells. *Journal of Receptors and Signal Transduction.* 2014;34(6):431-439.
- Mescher M, Merkle H, Kirsch J, Garwood M, Gruetter R. Simultaneous in vivo spectral editing and water suppression. *NMR in Biomedicine.* 1998;11(EPFL-ARTICLE-177509):266-272.
- Hanstock CC, Coupland NJ, Allen PS. GABA X2 multiplet measured pre-and post-administration of vigabatrin in human brain. *Magnetic resonance in medicine.* 2002;48(4):617-623.

- Hurd R, Sailasuta N, Srinivasan R, Vigneron DB, Pelletier D, Nelson SJ. Measurement of brain glutamate using TE-averaged PRESS at 3T. *Magnetic resonance in medicine.* 2004;51(3):435-440.
- Hu J, Yang S, Xuan Y, Jiang Q, Yang Y, Haacke EM. Simultaneous detection of resolved glutamate, glutamine, and γ-aminobutyric acid at 4T. *Journal of Magnetic Resonance.* 2007;185(2):204-213.
- Waddell KW, Zanjanipour P, Pradhan S, et al. Anterior cingulate and cerebellar GABA and Glu correlations measured by 1 H J-difference spectroscopy. *Magnetic resonance imaging.* 2011;29(1):19-24.
- O'Gorman RL, Michels L, Edden RA, Murdoch JB, Martin E. In vivo detection of GABA and glutamate with MEGA-PRESS: Reproducibility and gender effects. *Journal of Magnetic Resonance Imaging.* 2011;33(5):1262-1267.
- Snyder J, Thompson RB, Wilman AH. Difference spectroscopy using PRESS asymmetry: application to glutamate, glutamine, and myo-inositol. *NMR in Biomedicine.* 2010;23(1):41-47.
- Hennig J, Thiel T, Speck O. Improved sensitivity to overlapping multiplet signals in in vivo proton spectroscopy using a multiecho volume selective (CPRESS) experiment. *Magnetic resonance in medicine.* 1997;37(6):816-820.
- Choi C, Coupland NJ, Bhardwaj PP, Malykhin N, Gheorghiu D, Allen PS. Measurement of brain glutamate and glutamine by spectrally-selective refocusing at 3 tesla. *Magnetic resonance in medicine.* 2006;55(5):997-1005.
- Schulte RF, Boesiger P. ProFit: two-dimensional prior-knowledge fitting of J-resolved spectra. *NMR in Biomedicine.* 2006;19(2):255-263.
- Shungu DC, Mao X, Gonzales R, et al. Brain γ-aminobutyric acid (GABA) detection in vivo with the J-editing 1H MRS technique: a comprehensive methodological evaluation of sensitivity enhancement, macromolecule contamination and test–retest reliability. *NMR in Biomedicine.* 2016;29(7):932-942.
- Choi C, Bhardwaj PP, Kalra S, et al. Measurement of GABA and contaminants in gray and white matter in human brain in vivo. *Magnetic resonance in medicine.* 2007;58(1):27-33.
- Stephenson MC, Gunner F, Napolitano A, et al. Applications of multi-nuclear magnetic resonance spectroscopy at 7 T. *World journal of radiology.* 2011;28:105-113.
- Tkáč I, Henry PG, Andersen P, Keene CD, Low WC, Gruetter R. Highly resolved in vivo 1H NMR spectroscopy of the mouse brain at 9.4 T. *Magnetic resonance in medicine.* 2004;52(3):478-484.
- Dou W, Palomero-Gallagher N, Van Tol M-J, et al. Systematic regional variations of GABA, glutamine, and glutamate concentrations follow receptor fingerprints of human cingulate cortex. *The journal of newuroscience.* 2013;33:12698-12704.
- Xin L, Gambarota G, Mlynárik V, Gruetter R. Proton T2 relaxation time of J-coupled cerebral metabolites in rat brain at 9.4 T. *NMR in Biomedicine.* 2008;21(4):396-401.
- Terpstra M, Ugurbil K, Tkac I. Noninvasive quantification of human brain ascorbate concentration using 1H NMR spectroscopy at 7 T. *NMR in Biomedicine.* 2010;23(3):227-232.
- Kreis R. The trouble with quality filtering based on relative Cramér-Rao lower bounds. *Magnetic resonance in medicine.* 2016;75(1):15-18.
- Petroff OAC, Rothman DL, Behar KL, Mattson RH. Initial observations on effect of vigabatrin on in vivo ^{1}H spectroscopic measurements of γ-aminobutyric acid, glutamate, and glutamine in human brain. *Epilipsia.* 1995;36:457-464.
- Gunawan S, Walton NY, Treiman DM. High-performance liquid chromatographic determination of selected amino acids in rat brain by precolumn derivatization with phenylisothiocyanate. *Journal of Chromatography A.* 1990;503:177-187.
- Mans AM, DeJoseph MR, Hawkins RA. Metabolic abnormalities and grade of encephalopathy in acute hepatic failure. *Journal of neurochemistry.* 1994;63(5):1829-1838.

- Dou W, Kaufmann J, Li M, Zhong K, Walter M, Speck O. The separation of Gln and Glu in STEAM: a comparison study using short and long TEs/TMs at 3 and 7 T. *Magnetic resonance materials in physics, biology and medicine.* 2015;28:395-405.
- Lei H, Zhang Y, Zhu X-H, Chen W. Changes in the proton T_2 relaxation times of cerebral water and metabolites during forebrain ischemia in rat at 9.4 T. *Magnetic resonance in medicine.* 2003;49:979-984.
- Li Y, Srinivasan R, Ratiney H, Lu Y, Chang SM, Nelson SJ. Comparison of T_1 and T_2 metabolite relaxation times in glioma and normal brain at 3 T. *Journal of magnetic resonance imaging.* 2008;28:342-350.
- Schaller B, Xin L, Gruetter R. Is the macromolecule signal tissue-specific in healthy human brain? A ^{1}H MRS study at 7 tesla in the occipital lobe. *Magnetic resonance in medicine.* 2014;72:934-940.
- Bubber P, Haroutunian V, Fisch G, Blass JP, Gibson GE. Mitochondrial abnormalities in Alzheimer brain: mechanistic implications. *Annals of Neurology.* 2005;57(5):695-703.
- Petroff OA, Errante LD, Rothman DL, Kim JH, Spencer DD. Glutamate–glutamine cycling in the epileptic human hippocampus. *Epilepsia.* 2002;43(7):703-710.
- Zacharias NM, Chan HR, Sailasuta N, Ross BD, Bhattacharya P. Real-time molecular imaging of tricarboxylic acid cycle metabolism in vivo by hyperpolarized 1-13C diethyl succinate. *Journal of the American Chemical Society.* 2011;134(2):934-943.
- De Feyter HM, Herzog RI, Steensma BR, et al. Selective proton-observed, carbon-edited (selPOCE) MRS method for measurement of glutamate and glutamine 13C-labeling in the human frontal cortex. *Magnetic resonance in medicine.* 2018;80(1):11-20.
- de Graaf RA, Brown PB, Mason GF, Rothman DL, Behar KL. Detection of [1, 6-13C2]-glucose metabolism in rat brain by in vivo 1H-[13C]-NMR spectroscopy. *Magnetic Resonance in Medicine.* 2003;49(1):37-46.
- Duarte JM, Gruetter R. Glutamatergic and GABA ergic energy metabolism measured in the rat brain by 13C NMR spectroscopy at 14.1 T. *Journal of neurochemistry.* 2013;126(5):579-590.
- Fitzpatrick SM, Hetherington HP, Behar KL, Shulman RG. The Flux from Glucose to Glutamate in the Rat Brain in vivo as Determined by 1-Observed, 13C-Edited NMR Spectroscopy. *Journal of Cerebral Blood Flow & Metabolism.* 1990;10(2):170-179.
- Mason GF, Pan JW, Chu W-J, et al. Measurement of the tricarboxylic acid cycle rate in human grey and white matter in vivo by 1H-[13C] magnetic resonance spectroscopy at 4.1 T. *Journal of Cerebral Blood Flow & Metabolism.* 1999;19(11):1179-1188.
- Mason GF, Rothman DL, Behar KL, Shulman RG. NMR determination of the TCA cycle rate and α-ketoglutarate/glutamate exchange rate in rat brain. *Journal of Cerebral Blood Flow & Metabolism.* 1992;12(3):434-447.
- Patel AB, de Graaf RA, Rothman DL, Behar KL. Effects of γ-Aminobutyric acid transporter 1 inhibition by tiagabine on brain glutamate and γ-Aminobutyric acid metabolism in the anesthetized rat In vivo. *Journal of neuroscience research.* 2015;93(7):1101-1108.
- Rothman D, Behar K, Hetherington H, et al. 1H-Observe/13C-decouple spectroscopic measurements of lactate and glutamate in the rat brain in vivo. *Proceedings of the National Academy of Sciences.* 1985;82(6):1633-1637.
- Rothman D, Novotny E, Shulman G, et al. 1H-[13C] NMR measurements of [4-13C] glutamate turnover in human brain. *Proceedings of the National Academy of Sciences.* 1992;89(20):9603-9606.
- Shen J, Petersen KF, Behar KL, et al. Determination of the rate of the glutamate/glutamine cycle in the human brain by in vivo 13C NMR. *Proceedings of the National Academy of Sciences.* 1999;96(14):8235-8240.

- Sonnay S, Duarte JM, Just N, Gruetter R. Compartmentalised energy metabolism supporting glutamatergic neurotransmission in response to increased activity in the rat cerebral cortex: A 13C MRS study in vivo at 14.1 T. *Journal of Cerebral Blood Flow & Metabolism.* 2016;36(5):928-940.
- Xin L, Lanz B, Lei g, Gruetter R. Assessment of metabolic fluxes in the mouse brain in vivo using 1H-[13C] NMR spectroscopy at 14.1 Tesla. *Journal of Cerebral Blood Flow & Metabolism.* 2015;35(5):759-765.
- Boumezbeur F, Besret L, Valette J, et al. Glycolysis versus TCA cycle in the primate brain as measured by combining 18F-FDG PET and 13C-NMR. *Journal of Cerebral Blood Flow & Metabolism.* 2005;25(11):1418-1423.
- Valette J, Chaumeil M, Guillermier M, Bloch G, Hantraye P, Lebon V. Diffusion-weighted NMR spectroscopy allows probing of 13C labeling of glutamate inside distinct metabolic compartments in the brain. *Magnetic Resonance in Medicine.* 2008;60(2):306-311.
- Chaumeil MM, Valette J, Guillermier M, et al. Multimodal neuroimaging provides a highly consistent picture of energy metabolism, validating 31P MRS for measuring brain ATP synthesis. *Proceedings of the National Academy of Sciences.* 2009;106(10):3988-3993.
- Doan B-T, Autret G, Mispelter J, et al. Simultaneous two-voxel localized 1H-observed 13C-edited spectroscopy for in vivo MRS on rat brain at 9.4 T: Application to the investigation of excitotoxic lesions. *Journal of Magnetic Resonance.* 2009;198(1):94-104.
- Henry PG, Tkáč I, Gruetter R. 1H-localized broadband 13C NMR spectroscopy of the rat brain in vivo at 9.4 T. *Magnetic Resonance in Medicine.* 2003;50(4):684-692.
- Behar KL, Ogino T. Characterization of macromolecule resonances in the 1H NMR spectrum of rat brain. *Magnetic resonance in medicine.* 1993;30(1):38-44.
- Dobberthien BJ, Tessier AG, Yahya A. Improved resolution of glutamate, glutamine and γ-aminobutyric acid with optimized point-resolved spectroscopy sequence timings for their simultaneous quantification at 9.4 T. *NMR in Biomedicine.* 2018;31(1):e3851.
- Kofke WA, Hawkins RA, Davis DW, Biebuyck JF. Comparison of the effects of volatile anesthetics on brain glucose metabolism in rats. *Anesthesiology.* 1987;66(6):810-813.
- Monteiro MS, Carvalho M, de Lourdes Bastos M, de Pinho PG. Biomarkers in renal cell carcinoma: a metabolomics approach. *Metabolomics.* 2014;10(6):1210-1222.
- Zira AN, Theocharis SE, Mitropoulos D, Migdalis V, Mikros E. 1H NMR metabonomic analysis in renal cell carcinoma: a possible diagnostic tool. *Journal of proteome research.* 2010;9(8):4038-4044.
- Newsholme P, Procopio J, Lima MMR, Pithon-Curi TC, Curi R. Glutamine and glutamate—their central role in cell metabolism and function. *Cell biochemistry and function.* 2003;21(1):1-9.
- Yang Y, Li C, Nie X, et al. Metabonomic studies of human hepatocellular carcinoma using high-resolution magic-angle spinning 1H NMR spectroscopy in conjunction with multivariate data analysis. *Journal of proteome research.* 2007;6(7):2605-2614.
- Glunde K, Bhujwalla ZM, Ronen SM. Choline metabolism in malignant transformation. *Nature Reviews Cancer.* 2011;11(12):835.
- Gao H, Dong B, Liu X, Xuan H, Huang Y, Lin D. Metabonomic profiling of renal cell carcinoma: high-resolution proton nuclear magnetic resonance spectroscopy of human serum with multivariate data analysis. *Analytica chimica acta.* 2008;624(2):269-277.
- Burg MB, Ferraris JD. Intracellular organic osmolytes: function and regulation. *Journal of Biological Chemistry.* 2008;283(12):7309-7313.
- Hattingen E, Raab P, Franz K, Zanella FE, Lanfermann H, Pilatus U. Myo-inositol: a marker of reactive astrogliosis in glial tumors? *NMR in Biomedicine.* 2008;21(3):233-241.

- Wang L, Zhang L, Yu Y, Wang Y, Niu N. The protective effects of taurine against early renal injury in STZ-induced diabetic rats, correlated with inhibition of renal LOX-1-mediated ICAM-1 expression. *Renal failure.* 2008;30(8):763-771.
- Serkova N, Fuller TF, Klawitter J, Freise CE, Niemann CU. 1H-NMR–based metabolic signatures of mild and severe ischemia/reperfusion injury in rat kidney transplants. *Kidney international.* 2005;67(3):1142-1151.
- Jun-Sheng T, Lei Z, Xiao-Li S, Huan L, Xue-Mei Q. 1H NMR-based metabolomics approach to investigating the renal protective effects of Genipin in diabetic rats. *Chinese journal of natural medicines.* 2018;16(4):261-270.
- Garrod S, Humpfer E, Spraul M, et al. High-resolution magic angle spinning 1H NMR spectroscopic studies on intact rat renal cortex and medulla. *Magnetic Resonance in Medicine.* 1999;41(6):1108-1118.
- Craig SA. Betaine in human nutrition. *The American journal of clinical nutrition.* 2004;80(3):539-549.
- Heather LC, Wang X, West JA, Griffin JL. A practical guide to metabolomic profiling as a discovery tool for human heart disease. *Journal of molecular and cellular cardiology.* 2013;55:2-11.
- Fogelman AM. TMAO is both a biomarker and a renal toxin. *Circulation Research.* 2015;116(3):396-397.
- Cavassila S, Deval S, Huegen C, Van Ormondt D, Graveron-Demilly D. Cramér–Rao bounds: an evaluation tool for quantitation. *NMR in Biomedicine.* 2001;14(4):278-283.
- Chawla S, Wang S, Wolf R, et al. Arterial spin-labeling and MR spectroscopy in the differentiation of gliomas. *American Journal of Neuroradiology.* 2007;28(9):1683-1689.
- Valette J, Boumezbeur F, Hantraye P, Lebon V. Simplified 13C metabolic modeling for simplified measurements of cerebral TCA cycle rate in vivo. *Magnetic Resonance in Medicine.* 2009;62(6):1641-1645.
- Choi I-Y, Lee S-P, Kim S-G, Gruetter R. In vivo measurements of brain glucose transport using the reversible Michaelis–Menten model and simultaneous measurements of cerebral blood flow changes during hypoglycemia. *Journal of Cerebral Blood Flow & Metabolism.* 2001;21(6):653-663.
- Choi I-Y, Lei H, Gruetter R. Effect of deep pentobarbital anesthesia on neurotransmitter metabolism in vivo: on the correlation of total glucose consumption with glutamatergic action. *Journal of Cerebral Blood Flow & Metabolism.* 2002;22(11):1343-1351.
- Wilson M, Andronesi O, Barker PB, et al. Methodological consensus on clinical proton MRS of the brain: Review and recommendations. *Magnetic resonance in medicine.* 2019.